Università degli Studi di Pavia

Dipartimento di Scienze della Terra e dell'Ambiente

SCUOLA DI ALTA FORMAZIONE DOTTORALE

MACRO-AREA SCIENZE E TECNOLOGIE

DOTTORATO DI RICERCA IN SCIENZE DELLA TERRA E DELL'AMBIENTE

Roberta Bonì

Ground motion identification, monitoring and modelling through multi-sensor A-DInSAR data

Anno Accademico 2015-2016
Ciclo XXIX

Coordinatore
Prof. Annamaria Picco

Tutore
Prof.ssa Claudia Meisina

"Il divertimento della ricerca scientifica è anche trovare sempre altre frontiere da superare, costruire mezzi più potenti d'indagine, teorie più complesse, cercare sempre di progredire pur sapendo che probabilmente ci si avvicinerà sempre di più a comprendere la realtà, senza arrivare mai a capirla completamente."

Margherita Hack

Abstract

Ground motion represents the main reaction to superficial and deep deformations induced by multiple natural and anthropic phenomena (i.e. vadose zone processes as swelling/shrinkage of clay soils, soil consolidation, aquifer compaction, solid and fluid extraction and load-induced compaction) which take place at different spatio-temporal scale. This kind of hazard affects an increasing number of worldwide regions, densely populated, causing damage to the environment and infrastructures.

Recent advanced ground deformation investigations make use of satellite Synthetic-Aperture Radar (SAR) data, a new remote sensing tool, to examine the mechanisms of ground motion around the world. In particular, Advanced Differential Synthetic-Aperture Radar (A-DInSAR) techniques which are based on the processing of multiple interferograms derived from a large set (at least 20 images) of SAR images. These techniques allow to obtain the displacement time series of measuring points over wide areas at millimiters resolution. The techniques have already been successfully applied to monitor the evolution of different processes.

In the last two decades, A-DInSAR techniques have experienced a major development, which is mainly related to (i) the progress of the SAR data acquired by the COSMO-SkyMed satellites and the recent ESA Sentinel missions, that act at higher spatio-temporal resolution, and to (ii) the development of advanced processing algorithms. The improvements in the A-DInSAR technique need of an appropriate methodology to analyse extremely large datasets which consist of huge amounts of measuring points with high temporal resolution.

This work contributes to address to these problems by exploiting the great potential contained in the A-DInSAR time series.

The project aims are:

1. Development of a methodology to analyse multi-sensor and multi-temporal A-DInSAR dataset for the geological interpretation of areas affected by ground motion;
2. Analysis of the mechanisms of ground motion mainly due to groundwater level change;
3. Integration of A-DInSAR data with numerical models.

The study has been carried out in areas representative of moderate rates of displacement (the valley bottom of the Oglio river, in Italy), of swelling-shrinkage of clayey soils (Oltrepo Pavese, in Italy), of coastal subsidence (Ravenna, in Italy), of slope instabilities (Piemonte Region, in Italy), of high rate of pumping-induced subsidence (Alto Guadalentín Basin, in Spain) and of ground motion due to groundwater level change (London Basin, in United Kingdom).

Abstract

In the first step of the study, a novel methodology was developed to analyse multi-sensors and multi-temporal A-DInSAR data for the geological interpretation of areas affected by ground motion. The procedure was implemented using open source software and it consists of three main phases. In the first phase, the vertical and E-W components of motion are disentangled, and the displacements time series (TS) accuracy assessment is performed. In the second phase, different statistic tests are applied in order to find the spatio-temporal pattern of the principal components of movement, and the kinematic model of the targets. The result of this step is the identification of areas with significant movement, so-called "ground motion areas". Ground motion areas correspond to a cluster of a minimum 3 of targets, with a maximum distance of 50 meters, characterized by the same trends (linear, non-linear, seasonal). Finally, the third step consists of a data fusion of the A-DInSAR data and the geological data to determine the causes of ground motion processes.

In the second step of the study, a multi-disciplinary approach has been chosen to identify the driving mechanisms. More precisely, the procedure implemented by Tomas *et al.* (2010b) was applied, by including cross-comparisons between A-DInSAR time series and different factors such as geological factors (i.e. geological age and lithologies, soft soil thickness); hydrogeological factors (i.e. piezometric levels of different aquifer layers) and geotechnical factors (i.e. engineering geological unit map).

Finally, in the third step of the study, A-DInSAR data were integrated with 1D numerical model. The ground motion changes due to groundwater level variations were simulated using the approach introduced by Tomás *et al.* (2010a). Therefore, the A-DInSAR data was included in the phase of calibration and validation of the numerical model.

In the investigation site of the Oltrepo Pavese, the developed methodology allowed the disentanglement of natural and man-induced processes through the analyses of ERS-1/2 and RADARSAT data. The results were useful to gain insight into three deformational behaviours: linear, non-linear (accelerations and decelerations of the movements), and seasonal components of motion. The cross-comparisons with the geological, geotechnical and hydrogeological data gave insights into different geohazards such as swelling–shrinkage of clayey soils, land subsidence due to the load of new buildings, moderate tectonic uplift, and seasonal ground motion due to seasonal groundwater level variations.

In the valley bottom of the Oglio river, a Pre-Alpine valley located upstream the Iseo Lake, the application of the methodology, through ERS-1/2 and RADARDAT data, highlighted the geomorphologic control of the subsidence pattern.

Multiple datasets have been employed for the Ravenna case-study such as: ERS-1/2, Envisat, TerraSAR-X and Sentinel-1. The application of the methodology in this site confirms the capability to

recognize ground motion areas. Different components of motion have been recognized in the period from 1992 to 2016 in the Ravenna, such as multi-year and seasonal component of motion, through the A-DInSAR analysis and the priority areas for further investigations were identified.

The reproducibility of the methodology was assessed for investigations at regional scale in the Piemonte Region. The SAR images acquired by C-Band (ERS-1/2, ENVISAT and Sentinel-1) and X-Band (COSMO-SkyMed) sensors were exploited to identify and interpret slope instabilities.

The main advantages of the methodology's application in landslides investigations were the identification of different portions of the landslide characterized by various behaviours (linear and non-linear trend) and the detection of large unstable area that can be considered as a predisposing factor for the activation of phenomena.

The analysis of the mechanisms, mainly due to groundwater level change, was performed in the Alto Guadalentín Basin in Spain. In this basin, the land subsidence due to the groundwater overexploitation reaches the higher values measured of Europa (>10 cm/yr). In this case, the combined analysis of geological and hydrological information with displacement maps and time-series retrieved from multi-sensor and multi-temporal SAR images had provided new insights about mechanisms of ground motion due to groundwater level change. The approach allowed to understand that very thick soft soil layer with low permeability that has been drained since the 1960s, are involved in slow consolidation process, where the maximum settlement has yet to be reached.

Finally, London Basin was chosen to model ground motion due to groundwater level change; by applying 1D model, since the large availability of geological, hydrogeological and geotechnical data. In this case the integration of A-DInSAR data in the modelling permitted to analyse the spatio-temporal variability of the ground motion response to groundwater levels variations across the London Basin.

Overall, the study demonstrates how a better knowledge of ground deformations and the occurrence, measurement, mechanics and prediction can be reached by combining A-DInSAR with geological, geotechnical and hydrogeological data. The results could be used for land use planning and civil protection purposes, providing fundamental information to adopt mitigation measures in order to reduce the social, environmental, infrastructural and economic impacts of this silent hazard.

The research project has been carried out at the University of Pavia, including periods of research abroad spent in the Spain (January 2015-March 2015), at the Geohazards InSAR laboratory and Modelling Group, Geological Survey of Spain (IGME) under the supervision of Dr. Gerardo Herrera and in United Kingdom (June 2015-July 2015 and September 2015), at the British Geological Survey (BGS) under the supervision of Dr. Francesca Cigna.

Acknowledgements

This PhD thesis is the result of a beautiful journey, upon which many people and many research collaborations have contributed and given their support. I am deeply gratefully to all of them.

I would first like to thank my advisor Prof.ssa Claudia Meisina for the constant support for my PhD project. She consistently helped me and encouraged my research, allowing me to grow as a research scientist. Her dedication for the scientific research was truly inspiring for my PhD.

A very special thank goes out to advisors of my research abroad periods, respectively, at the IGME (Spain) and BGS (UK): Dr. Gerardo Herrera and Dr. Francesca Cigna. I really appreciated the guidance of Dr. Gerardo Herrera and his high professional technical competences.

I would like to thank Prof. Roberto Tomás, Dr. Carolina Guardiola-Albert and the IGME team for their support and patience.

With pleasure, I remember the experience at the BGS, thanks to Dr. Francesca Cigna for her important high professional support in UK and her kindness and willingness. I would like to extend thanks to the BGS team and in particular Dr. Stephanie Bricker for the kind assistance she provided.

Thank to Prof. Giorgio Pilla for his knowledge and skill in the hydrogeological investigation. I would like to acknowledge Prof. Michele Saroli of the University of Cassino and Southern Lazio and Prof.ssa Francesca Bozzano of the Sapienza University of Rome, as the second readers of this thesis, and I am gratefully to theirs very valuable comments on this thesis.

Thanks to all who had collaborated to the research project including the ARPA Piemonte team, the University of Padova team and the University of Napoli Federico II team.

A special thanks to all of my friends in Pavia and in Alcamo for all the wonderful and carefree moments spent together. I would also like to thank my sweet ex-roommates who supported me in writing, and incented me to strive towards my goal.

Thanks to my PhD colleagues and UNIPV research team to be always patiently available to solve all the occurred issues.

Finally, I would like express my very profound gratitude to my family and to my boyfriend for providing me with unfailing and lovely support and continuous encouragement throughout my years of study and through the process of researching and writing this thesis. This accomplishment would not have been possible without them. Thank you.

Table of contents

Chapter I. Introduction

In this chapter, the framework of this thesis is presented, providing an overview to remote sensing data and their main applications on natural and human-induced processes. Furthermore, the questions unanswered and the main objectives and novel contributions are described.

1.1. Background

Ground motion can be the surface evidence of shallow or deep-seated deformation induced by different natural and human-induced processes. This phenomenon can imply surface deformation with 3D displacement components, negative and positive vertical movements and/or horizontal (E-W) movements.

More precisely, the negative vertical displacement corresponds to lowering of the ground surface named land subsidence, induced by a wide variety of processes (Figure 1) such as: aquifer-system compaction, drainage of organic soils, underground mining, hydrocompaction, natural compaction, sinkholes, and thawing permafrost (National Research Council, 1991).

The positive displacement is mainly due to isostatic or tectonic activity and poroelastic rebound following recovery of hydraulic heads.

Another kind of ground motion is a surface movement characterized by a seasonal component of motion that can be triggered by poroelastic deformations of aquifer-system in response to changes in aquifer head or swelling shrinkage of clayey soils.

The impacts of ground motion can be infrastructural, economic, environmental and social (Abidin *et al.* 2015), including impacts on the natural heritage, natural surficial drainage system, agricultural activities, building foundations and transportation network, alteration of irrigation network, and it enhances the risk of floods, affecting the human life and activities. The increasing factors of risk are mainly due to the rapid urban development, the relatively young alluvium soils and the relatively weak mitigation and adaptation strategies.

Therefore, in the pre-mitigation investigation phase, the identification of ground motion areas and the understanding of driving factors is fundamental in order to adopt suitable land use planning and sustainable management of the available resources. Then, ground motion investigations are essential to delineate the magnitude and type of deformation related to the temporal evolution of surface

displacements (i.e. linear or non-linear), the spatial extension of the affected areas, and the mechanism of ground motion.

In many cases, the ground motion evidences are the result of superimposed processes that act at different spatio-temporal scale that makes it difficult to discern, and to map the different processes and to evaluate the associated triggering factors. The complexity of the mechanism recognition requires a multidisciplinary approach including the expertise of engineering geologists, hydrogeologists, geotechnical engineers. Up to now, the scientific community carried out in many areas of the world different strategies and a combination of different methods including field measurements, remote sensing tools and integrated approaches to solve the complexity of the problem.

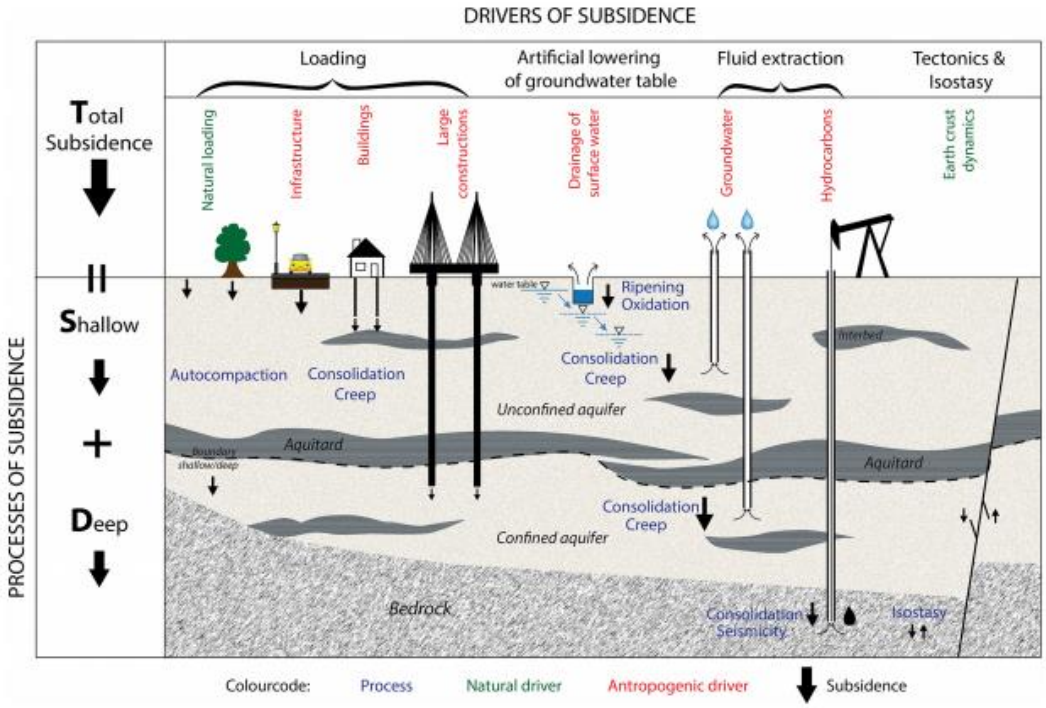

Figure 1. Example of various processes of subsidence (from Minderhoud *et al.*, 2015).

Since the early 1990s, advanced subsidence studies exploited Satellite radar interferometry technique to investigate ground deformation phenomena. The technique is a remote sensing tool capable of mapping displacements over wide areas at very high spatial resolution. The tool allows to obtain the displacement time series by sending a beam of electromagnetic microwaves from a sensor on board of a satellite to the earth surface. The distance between sensor and targets (named Persistent Scatterers, PS) on the earth surface (i.e. the outcrop of rocks, the roof of buildings, metallic structures) can be measured. The different satellites pass over the same area with a revisit time in the range of 35 to 6

days and if slow surface deformation occurs, the sensor allows to detect the movement along the line of sight of the satellite (LOS) with a millimeter accuracy.

Advanced Differential Synthetic Aperture Radar Interferometry (A-DInSAR) techniques belongs to a family of algorithms based on the simultaneous processing of multiple interferograms derived from a large set of Synthetic Aperture Radar (SAR) images that had to be a powerful tool for the detection and monitoring of different geological hazards including earthquakes, volcanic activity, landslides and land subsidence and nowadays widely used to map ground deformations due to natural and anthropogenic processes in different environments.

In this framework, the advances in the remote sensing tools provide new possibilities for (i.) mapping, (ii.) analysing the mechanisms and (iii.) modelling the ground motion processes to precede the design and implementation of appropriate mitigation methods.

In this thesis, the relevant contribution of the scientist community involved in the ground deformation investigations is presented distinguishing three main topics (Table 1.):

1. Detection of ground motion areas;
2. Analysis of the mechanism of ground motion;
3. Modelling ground motion.

Table 1. Review of literature contributions to the main topics in the ground deformation investigations.

Topic	Author	Area	Type of ground motion
Detection of ground motion areas	Meisina *et al.* (2008)	Piemonte Region (Italy)	Landslides and subsidence
	Bianchini *et al.* (2012)	Central Calabria (Italy)	Landslides
	Lu *et al.* (2012)	Arno river Basin (Italy)	Landslides
	Bateson *et al.* (2012)	Large cities in Europe	Geohazards
	Peduto *et al.* (2015)	Campania Region (Italy)	Subsidence
	Di Martire *et al.* (2016)	Palermo province (Italy)	Landslides
Analysis of the mechanism of ground motion	Galloway et al. (1999)	United States	Pumping-induced subsidence
	Tomás *et al.* (2010b)	Orihuela (Spain)	Pumping-induced subsidence
	Cigna *et al.* (2012)	Morelia (Mexico)	Pumping-induced subsidence
	Chaussard *et al.* (2013)	Indonesia	Subsidence due to groundwater and gas extraction
	Tosi *et al.* (2013)	Venice (Italy)	Natural and human-induced processes
	Hu *et al.* (2013)	Beijing (China)	Pumping-induced subsidence
	Higgings *et al.* (2014)	Ganges-Brahmaputra Delta (Bangladesh)	Natural and human-induced processes
	Liu *et al.* (2015)	Yellow river delta (China)	Pumping-induced subsidence
	Bozzano *et al.* (2015)	Acque Albule Plain (Italy)	Pumping-induced subsidence
Modelling ground motion	Hoffmann *et al.* (2003)	Antelope Valley (California)	Pumping-induced subsidence
	Herrera *et al.* (2009)	Murcia (Spain)	Pumping-induced subsidence
	Tomás *et al.* (2010a)	Murcia (Spain)	Pumping-induced subsidence
	Teatini *et al.* (2011)	Po river Basin (Italy)	Ground motion due to seasonal gas storage
	Calderhead *et al.* (2011)	Toluca Valley (Mexico)	Pumping-induced subsidence
	Modoni *et al.* (2013)	Bologna (Italy)	Pumping-induced subsidence
	Raspini *et al.* (2014)	Delta municipality Region (Greece)	Pumping-induced subsidence
	Fokker *et al.* (2016)	Bergermeer gas field (Netherlands)	Ground motion due to gas field management

1.1.1. Detection of ground motion areas

Various geohazard-mapping methodologies were previously implemented by the use of A-DInSAR techniques (Meisina *et al.*, 2008, Lu *et al.*, 2009, Bianchini *et al.*, 2012, Bateson *et al.*, 2012, Peduto *et al.*, 2015, Di Martire *et al.*, 2016). Up to now, all the strategies to detect and to map the ground motion areas are based on the spatial distribution of the average velocities and on statistic approaches to automatically detect clusters with significant movements.

For instance, Meisina *et al.* (2008) implemented a methodology for detecting ground deformations, the so-called "anomalous areas" by the use of velocities measurements obtained by data processed by PSInSAR™ technique in the Piemonte Region (Italy). The approach is based on selecting clusters of minimum 3 Persistent Scatterers (PS) with a maximum distance of 50 meters among, characterized by displacement rates over to ± 2 mm/yr that are above a significant threshold background related to the technique precision. The identification of the movement areas was done through an automatic procedure in a G.I.S. environment. The results highlight the capabilities to detect a great variability of geological processes at regional scale. The success of the technique depends on the typology of processes and their related kinematics, proving to be suitable for assessing the temporal evolution of slow and extremely slow landslides with constant velocity deformations, but some difficulties were observed to detect landslides with intermittent behaviour, such as that triggered by rainfall (rock block slides in the Langhe, complex movements in Apennines) and to distinguish ground deformation due to different processes, as local settlement of man-made structure (i.e. Apennine and Langhe) or the shallow deformations caused by seasonal processes in debris (Alps).

Bianchini *et al.* (2012) introduced a methodology to detect extremely slow and very slow landslides, called Landslide HotSpot Mapping (LHSM). The procedure of the hotspot mapping was tested in the Central Calabria (Italy) proving to be useful to identify landslides at regional scale, by means of Persistent Scatterer Interferometry. LHSM methodology is based on the Line of Sight (LOS) average velocities clustering and limitations were recognized in the areas where the geometry of the satellite acquisitions implicates underestimation of the real movements.

Lu *et al.* (2012) proposed a spatial statistical approach for Persistent Scatterers Interferometry (PSI) Hotspot and Cluster Analysis (PSI-HCA) to automatically detect extremely slow-moving landslides in the Arno river Basin (Italy). The PSI-HCA approach shows a high potential for detecting extremely slow-moving landslide taking into account the PS velocity and spatial distribution. Some PSI-HCA limitations were recognized in differentiating various geo-processes.

In 2011, a 3-year Collaborative Project of the European Commission started, the so-called PanGeo. The aim of the project PanGeo was to provide geohazard information for 52 of the largest towns in Europe, mapping geohazards by the use of Earth Observation (EO) data. In this framework, the

detection of the geohazards was performed using the average velocity, selecting and clustering targets with average velocity higher than a threshold; which varies depending on the town and phenomena (Bateson et al., 2012).

Peduto *et al.* (2015) implemented a methodology to detect subsidence areas using radar interferometry in the Campania Region (Italy). In particular, the authors proposed to adopt a grid analysis which cells size depending on the scale analysis. For each covered cell, the average velocity was computed along the LOS direction by weighting PS LOS velocity values on their coherence values.

Then, a velocity threshold was chosen according to the sensor used and the temporal sampling. The procedure allows to map moving areas by a multiscale approach, providing the distribution of cells that can be appointed as moving (average velocity value exceeding the threshold), not moving (average velocity value lower than the threshold) and not covered (if no PS were found in the singular grid cell).

Recently, Di Martire *et al.* (2015) according to Lu *et al.* (2012), mapped landslides using the kernel density of PS data in Palermo Province (Italy). Even in this case, the approach shows the advantage to map landslides with slow movements and some limitations in areas where the geometry of the satellite acquisitions implicates underestimation of the real movements.

1.1.2. Analysis of the mechanism of ground motion

The second topic of the ground deformation investigations deals with the analysis of the mechanisms of ground motion to assess the drivers of the processes. Most common man-induced cause of ground motion is the groundwater level change and, for this reason, this is the process that was mainly analysed and modelled in this thesis. Obviously to deeper understand the mechanisms of ground motion, we also have to analyse the others physical processes that partially affect the areas of interest.

With reference to this topic, land subsidence was included in the United Nations Educational, Scientific and Cultural Organization (UNESCO) programme of the International Hydrological Decade (IHD), 1965–1974 and an ad hoc working group on land subsidence was assembled, and codified as the Working Group on Land Subsidence (WGLS). Galloway *et al.* (1999) described the role of underground water in human-induced land subsidence through illustrative case histories in United States. These case histories provide information on the role of the extraction and drainage of groundwater in land subsidence by causing the compaction of susceptible aquifer systems and the dewatering of organic soils. Furthermore, it deals with the influence of the ground-water-level declines caused by pumping, or by infiltration from reservoir impoundments on the catastrophic formation of sinkholes in susceptible earth materials. The use of radar interferometry data in the Antelope Valley, Mojave Desert, California allowed to detect residual (time-delayed) aquifer-system

compaction due to the presence of thick aquitards. Following, several works were performed by means of satellite data to investigate ground motion due to hydrological processes. Among previous studies, Tomás *et al.* (2010b) addressed about the analysis of subsidence conditioning and triggering factors by means of PSI data in Orihuela (Spain). It distinguished various conditioning and triggering factors such as:

- Geological factors (i.e. geological age and lithologies, soft soil thickness);
- Hydrogeological factors (i.e. piezometric levels of different aquifer layers);
- Geotechnical factors (i.e. soil deformability).

These factors can be divided into two main groups:

1. Conditioning or passive factors, which are inherent to the materials of the aquifer system,
2. Triggering or active factors that cause subsidence once certain conditions concur.

The calculation of subsidence-induced ground settlement (δ) triggered by groundwater abstraction is usually performed with consideration of three parameters: (a) the thickness of deformable soils (H), which is spatially correlated with the calculated settlements; (b) the variation in the stress state due to groundwater drawdown (Δh), which is responsible for the effective stress increase, causing the consolidation of deformable soils; and (c) the deformability of the soil (D), which mainly depends on the nature of the different layers that constitute the aquifer system and its geological history.
This relationship can be written as:

$$\delta = H \times \Delta h \times D \qquad (1.1)$$ (Tomás et al. 2010)

The mechanisms of ground motion were detected by a spatial comparison of the deformation distribution with the factors. The relationship between accumulated deformation and soft soil thickness, were performed by plotting the mean and the standard deviation of the subsidence versus the different compressible thickness areas. The analysis of the geological factors was performed by computing the mean, the standard deviation and the extreme values (i.e. maximum and minimum) of deformation for each unit. To understand the role of the hydrogeological factors, the authors plotted the time series of A-DInSAR ground deformations versus the piezometric level time series to assess a visual inspection of the correlation between these measurements. The results highlight the improve of knowledge of the mechanisms governing this phenomenon by combining radar-derived deformation data and pre-existing geo-information.

Cigna *et al.* (2012) investigated the ground deformations in Morelia, (Mexico) by the use of A-DInSAR data. The authors observed that the variance of the subsidence signal can be explained by the location of major wells, the thickness of the underlying Quaternary sedimentary fill (the main aquifer) that overlies a faulted Miocene basement, and proximity to major faults. The method to analyse the mechanisms of ground motion is mainly based on scatter diagrams, which plotted the deformation versus the controlling and triggering factors (i.e. thickness of compressible sediments, water extraction) and by means of the computation of the Coefficient of determination, R^2 for the linear regression between the two variables (i.e. deformation and thickness of compressible sediments). In addition, deformation profiles, obtained using the Inverse Distance Weighting spatial interpolation, were compared with geological cross-sections to assess the geological contribute of motion.

Chaussard *et al.* (2013) studied the land subsidence in Indonesia, using A-DInSAR time-series analysis. The authors correlated the observed subsidence with surface geology and land use by a visual inspection of the average velocity, and by reporting for the different land use (i.e. forest, agricultural, residential, industrial, and mixed such as residential and industrial) the displacement time series.

Tosi *et al.* (2013) distinguished natural land subsidence and movements induced by anthropogenic activities at Venice (Italy) using the long- and short-term displacements processed by means of PSI technique and acquired by d by C- and X-band sensors, respectively. X-band satellites revealed a high effectiveness to monitor short-time movements as those induced by human activities, conversely, C-band sensors was used to quantify the long-term movements, i.e. the subsidence component primarily ascribed to natural processes. By interpolating the two datasets and by removing the C-band from the X-band map, the natural and anthropogenic components of the subsidence were distinguished. The proposed approach requires the use of A-DInSAR data acquired by C and X sensors, over the same period.

Another exemplificative study was performed by Hu *et al.* (2013) in order to analyse the mechanism of ground motion affecting Beijing in China. More precisely, the authors investigated the excessive groundwater withdrawal by comparing the average velocity map, obtained by means of A-DInSAR technique, with the groundwater depression cone.

In the last years, a group of researchers assessed the state of the world's major river deltas in order to investigate their subsidence. Taking into account that many of the world's deltas are hydrocarbon producers, including those of the Yukon, Lena, Irrawaddy, Po, Rhine, Burdekin, Red, Niger, Magdalena, Mahakam, Mackenzie, Yellow, Sacramento and Mississippi, the complicated subsurface geology, the variable extraction depths and the delayed reactions make more difficult the analysis of the mechanisms of ground motion (Syvitski and Higgins, 2012).

Higgings *et al.* (2014) detected the role of the local stratigraphy on the subsidence affecting the Ganges-Brahmaputra delta (Bangladesh) by a visual inspection of the average velocity obtained by means of A-DInSAR techniques and the soil class distribution.

Liu *et al.* (2015) investigated the mechanism of ground motion in the Yellow river delta (China) by means of A-DInSAR data, retrieving a correlation with the groundwater level change and with the seasonal rainfall rates.

Bozzano *et al.* (2015) implemented a 3D groundwater flow model, which was developed using Visual MODFLOW 4.2 in the Acque Albule Plain (Italy) and compared the results with A-DInSAR data. By combining the detailed information of the 3D geological and hydrogeological model, the mechanism of ground motion was deeper understood. The results highlight that in the Acque Albule Plain the groundwater level variations drive the timing of subsidence, whereas the local geological conditions (e.g. the thickness of the compressible deposits overlaying the exploited aquifer) drive the magnitude of the ground motion process.

Therefore, the literature overview, here presented, highlights how the A-DInSAR analysis has provided new insights about the complexity of the mechanisms of ground motion, nowadays representing the unique tool to analyse the drivers of the movements over large areas.

1.1.3. Modelling ground motion

The third topic concerns the modelling of ground motion caused by groundwater level change, by the use of A-DInSAR data.

Hoffmann *et al.* (2003) exploited InSAR-derived subsidence observations to implement the inverse model of the compaction time constant and inelastic skeletal storage coefficient of compacting interbeds in a coupled regional groundwater flow and aquifer-system compaction model in Antelope Valley (California). In this case, the InSAR data were used for calibrating the parameters to be used for a subsidence model implemented using the MODFLOW code and for validating the results.

Herrera *et al.* (2009) demonstrates the potential of A-DInSAR techniques to validate subsidence prediction models by comparing the temporal evolution of the displacements observed in Murcia (Spain) with the values computed using the GEHOMADRID finite element code.

Following, Tomás *et al.* (2010a) presented the usefulness of the A-DInSAR not only to validate but also to calibrate the numerical models of ground subsidence due to aquifer overexploitation for the same city (Murcia). In this cases, the authors proposed a one-dimensional model to simulate the subsidence due to piezometric level changes. This model assumes that deformations are directly caused by vertical effective stress changes derived from piezometric level changes and that aquitard pore pressure equilibrates instantaneously with the piezometric level changes of the gravels layer.

Teatini *et al.* (2011) describes the improved results obtained by the use of A-DInSAR data to calibrate a 3D fluid-dynamic model and to develop a 3D transversally isotropic geomechanical model in order to simulate the expected displacements for the underground gas storage (UGS) in depleted hydrocarbon reservoirs. The vertical and east-west components of ground motion in the Lombardia gas field (Po river basin, Italy) were extracted exploiting A-DInSAR data acquired in ascending and descending modes and then, were included into the geomechanical model.

Calderhead *et al.* (2011) extends the approach introduced by Hoffmann *et al.* (2003) by using A-DInSAR subsidence data and further constrains the groundwater flow-compaction model with a 3D geologic model in the Toluca Valley (Mexico).

Modoni *et al.* (2013) performed the 1D modelling of the seepage induced by pumping and of the soil deformation induced by the changes of overburden effective stress regime in the area of Bologna (Italy) and then, the results were compared with the settlements observed by in situ and satellite-based measurements. The comparisons between observed and simulated displacements highlight areas (in particular, the north area of the alluvial fan of the Reno River) where the adopted model underestimates the settlements and local conditions require a further refinement of the investigation campaign.

Raspini *et al.* (2014) compared the results achieved with a 2D finite element model simulating the pumping-induced subsidence in the Kalochori area (Greece), with the A-DInSAR observed displacements.

With reference to the calibration of parameters to be used for subsidence model, Fokker *et al.* (2016) described the application of A-DInSAR data to estimate subsurface model parameters of the Bergermeer gas field (Netherlands).

In this framework, the integration of A-DInSAR technique proved a valuable contribution for calibrating and validating reasonable models implemented by different approaches.

1.2. Significance of the problem / Questions unanswered

The literature overview described in the Section 1.1. highlights the gaps and the necessities to be addressed in the ground motion investigations.

With reference to the first topic, the previous methodologies were mainly based on the average LOS velocity analysis, constrained by the fact that in the past A-DInSAR data allowed to obtain noisy time series difficult to interpret. Furthermore, some limitations were recognized for distinguishing the ground deformation due to different processes, or to detect shallow deformations caused by seasonal processes.

One of the challenges for the scientific community involved in the ground deformation investigations is to disentangle the different processes and to assess their relative contributions. Understanding ground motion processes requires appropriate methodology and contributions from the geotechnical, geological/geophysical and hydrological communities.

With reference to the second topic, it is clear the necessities to provide a great number of case histories in order to provide information to be used for mitigation strategies by local authorities and to interchange the observations carried out from the different mechanisms of ground motion in the worldwide. Additionally, the combination of A-DInSAR data with hydrogeological and geotechnical data have to be strengthened for characterizing the hydrogeological and geotechnical properties of soils over wide areas.

Finally, with reference to the third topic, the key role of A-DInSAR technique has to be reinforced, proving exemplificative applications in areas of interest.

More specifically, in this work the purpose is to address the following questions:

1. How can we identify a potential area to suffer ground motion processes by the use of A-DInSAR data acquired by different sensors and processed using different algorithms?

2. How can we distinguish the different components of motion?

3. Can we use the temporal pattern of the deformation to map various natural and human-induced processes characterized by different rate of motion?

4. Can temporal and spatial evolution of ground motion processes be obtained reliably for small and large areas and over different contexts including slope and flat areas?

5. Can we use A-DInSAR data to characterize the hydrogeological and geotechnical properties of the soils?

6. How can we integrate the A-DInSAR technique in the modelling of ground deformation?

1.3. Structure of the thesis

The thesis is organized in seven Chapters. In the first Chapter, the problem is introduced, by reviewing the relevant literature and by defining the appropriate concepts and issues.

Most common man-induced cause of ground motion is the groundwater level change and this is the process that was mainly analysed and simulated by a 1D model in this thesis. Therefore, in Chapter II the theory of the aquifer-system compaction was described in detail.

Next, Chapter III is dedicated to A-DInSAR techniques by providing detailed information about the basic concepts of these remote sensing tools, by distinguishing the different sensors and processing techniques which were exploited in this thesis.

In Chapter IV the methodological approach is presented, taking into account three main objectives of the research that are: (i) the identification of ground motion areas, (ii) the identification of the driving mechanisms and (iii) the prediction of the development of the surface movements.

In Chapter V, the six study areas, where the research was carried out, are described. The criteria for selection the areas were explained and for each study area, information on the geological and hydrogeological setting were provided. Additional details about the available A-DInSAR data for each study area are also summarized.

In Chapter VI, the results of the research are presented. More precisely, four published and one submitted papers are included. The first paper is published in the Special Issue "Earth Observations for Geohazards" of the Remote Sensing journal and the work deals with the development of a methodology for detection and interpretation of Ground Motion Areas with the A-DInSAR time series analysis. The methodology was implemented in the Oltrepo Pavese (Italy). The second work is published in the Proceedings of the International Association of Hydrological Sciences and it deals with the preliminary methodology development applied in the Oltrepo Pavese and along the valley bottom of the Oglio river (Italy). The third work has been submitted to the Proceedings of the 4th World Landslide Forum and it concerns the application of the methodology at regional scale in the Piemonte Region (Italy) to investigate slope instabilities. Afterwards, the analyses carry out on the mechanism of ground motion in the Alto Guadalentín Basin (Spain) were presented. The achieved results about the analysis of land subsidence due to the groundwater overexploitation were published in the Engineering Geology journal. Finally, the London Basin was chosen to model ground motion

due to groundwater level change; by applying 1D model, since the large availability of geological, hydrogeological and geotechnical data. The results were successfully published in the Journal of Hydrology.

Finally, in Chapter VII the conclusions were drawn by listing the main results obtained and the contributions to answering the questions listed in Section 1.2.

In the Appendix, the study of the Ravenna area is presented, by including the results presented in the 2nd International Workshop on Coastal Subsidence (May 30th – June 1st, 2016; ISMAR-CNR; Venice, Italy). Furthermore, in this section has been described the main activities performed during the Erasmus traineeship (12/01/15-13/03/15) at the Geological Survey of Spain (IGME), in Spain, in the framework of the AQUARISK Project.

1.4. Objectives and novel contribution

The project objectives are:

1. Development of a methodology to analyse multi-sensor and multi-temporal A-DInSAR dataset for the geological interpretation of areas affected by ground motion, in order to:
   - to overcoming limitations such as the analysis of large datasets
   - to exploit the great potential contained in the A-DInSAR time series;
   - to improve the detection of ground motion areas;
   - to support the interpretation of driving-force mechanisms.
2. Analysis of the mechanisms of ground motion mainly due to groundwater level change
   - to provide detailed information about specific areas;
   - to provide insight for further research in others case histories.
3. Integration of A-DInSAR data with numerical models
   - to improve predictions of ground motion;
   - to calibrate and validate numerical models of ground motion;
   - to characterize the geotechnical and hydrogeological properties of deposits.

The research project has been carried out at the University of Pavia, including external collaborations such as:

- Geohazards InSAR Laboratory and Modelling group, Geoscience Research Dept., Geological Survey of Spain (IGME) [Dr. G. Herrera]
- British Geological Survey (BGS), Environmental Science Centre, Keyworth, Nottingham (United Kingdom) [Dr. F. Cigna]
- Dipartimento di Geoscieze–Università degli Studi di Padova [Dr. M. Floris]

- Dipartimento di Scienze della Terra, dell'Ambiente e delle Risorse dell'Università di Napoli [Prof. D. Calcaterra]

- Dipartimento di Ingegneria Civile, Edile e Ambientale (DICEA) dell'Università di Napoli [Prof. M. Ramondini]

- Istituto Nazionale di Geofisica e Vulcanologia (INGV), Sezione di Napoli [Dr. Sven Borgstrom].

Attendee to Scientific Projects:

- Investigator attendee of the "PanGeo" project. PanGeo provides free access to ground instability geohazard information for many of Europe's largest cities. Design of the PanGeo Report: Geohazard Description for Zaragoza 2013.

- External Investigator attendee of the Project "DORIS" project (Ground Deformation Risk Scenarios: An Advanced Assessment Service) for the analysis of the land subsidence in the Alto Guadalentín Basin (Spain) – IGME, 2015.

- Investigator attendee of the "AQUARISK" project - Estudio de riesgos geológico-geotécnicos por explotación de acuíferos mediante técnicas espaciales y terrestres. Aplicaciones a estructuras e Aplicaciones a estructuras e infraestructuras urbanas - Geohazards InSAR laboratory and Modeling Group (IGME), 2014-2017.

- Principal Investigator of the Project "Land subsidence monitoring and understanding from space: The Ravenna area (Northern Italy) case history" - Proposal "GEO3016" for the TSX archive, 2015.

- Investigator attendee of the Project:"Servizio di aggiornamento del SifraP (Sistema Informativo Frane in Piemonte) finalizzato alla definizione della pericolosità da frana mediante analisi di dati d'archivio, fotointerpretazione ed analisi di dati di interferometria satellitare" - ARPA Piemonte, 2016.

Chapter II. Mechanic of ground motion due to groundwater level change

In this chapter, the theory of aquifer-system compaction is explained. The mechanic of ground motion due to groundwater level change is examined in detail, being the process that was simulated using a 1D model and described in Sections 5.3 and 6.5.

2.1. Principles of the aquifer-system compaction

The relation between changes in pore fluid pressure and compression of the aquifer-system is based on the principles of Effective Stress introduced by Terzaghi (1925)

$\sigma_e = \sigma_T - \rho$ (2.1) (Terzaghi *et al.* 1925)

where σ_e is the effective or intergranular stress, σ_T is the total stress that represents the geostatic load and ρ is the pore fluid pressure (Figure 2).

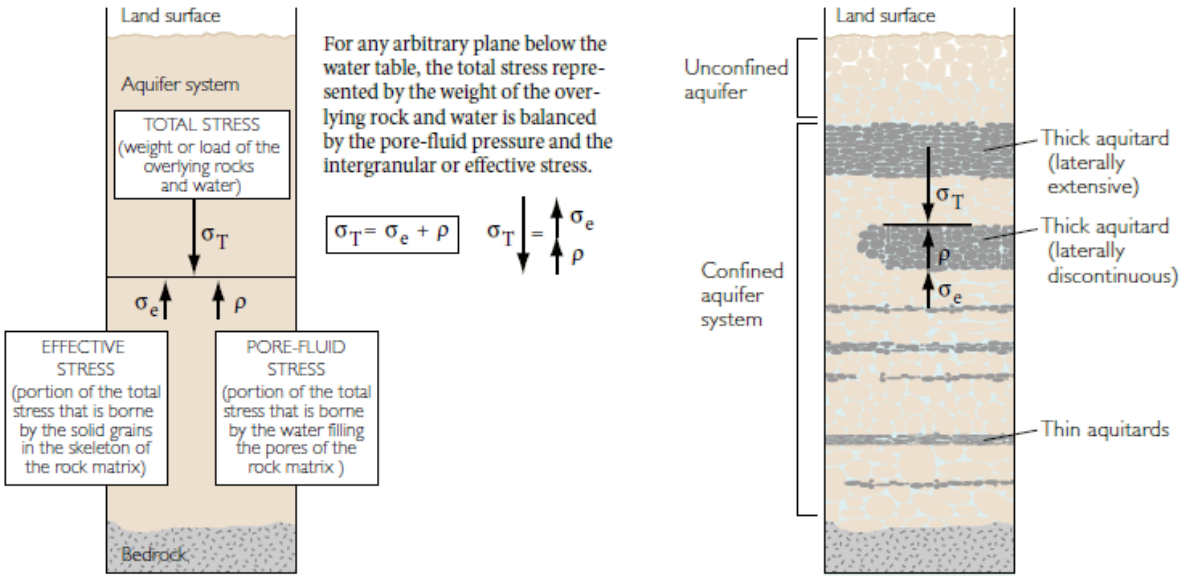

Figure 2. Schematic representation of the Principle of Effective Stress (from Galloway *et al.*, 1999).

According to this principle, if the total stress σ_T remains constant, a change in pore fluid pressure ρ implicates a proportional change in effective stress σ_e within the aquifer-system, causing a small

change in volume in the aquifer-system skeleton. The aquifer-system deformation (compaction or expansion) under the new load is conditioned by the compressibility of the aquifer-system skeleton.
Aquifer consolidation is commonly calculated based on Terzaghi's consolidation theory (Terzaghi 1943). When the effective stress does not exceed the maximum effective stress that the system has experienced in the past (i.e. pre-consolidation stress), the fluctuations in the water level create small elastic deformation of the aquifer-system and small land surface displacement. On the contrary, if the effective stress exceeds the pre-consolidation stress, the pore structure of susceptible fine-grained aquitards in the system may undergo significant rearrangement and the deformation is mainly inelastic (Galloway *et al.*, 1999). Vertical ground motion can therefore be the effect of the elastic and/or inelastic compaction which depends on the hydraulic head changes and the thickness of the unconsolidated deposits (Riley 1969; Helm 1975, 1976). Consequently, both the aquifers and aquitards that constitute the aquifer-system undergo deformation, but according to different behaviours.

2.2. Aquitard drainage and aquifer-system compaction

According to equation (2.1), when ground-water levels are lowered, the pore-fluid pressure is transferred to the skeleton of the aquifer system, which compresses to a degree. Conversely, when ground-water levels are raised (such as when ground water recharges the aquifer-system) and the pore-fluid pressure is increased, support previously provided by the skeleton is transferred to the fluid and the skeleton expands. Therefore, the skeleton alternately undergoes compression and expansion as the pore-fluid pressure oscillates in response to the aquifer-system discharge and recharge (Figure 3).
If the load on the skeleton not exceeds the previous maximum load (preconsolidation stress), the fluctuations causes small elastic deformation of the aquifer system and small displacement results at the land surface. In this case the deformations are fully recoverable, commonly resulting in seasonal, reversible displacements in land surface as effect of the seasonal changes in groundwater level (Galloway *et al.* 1999).

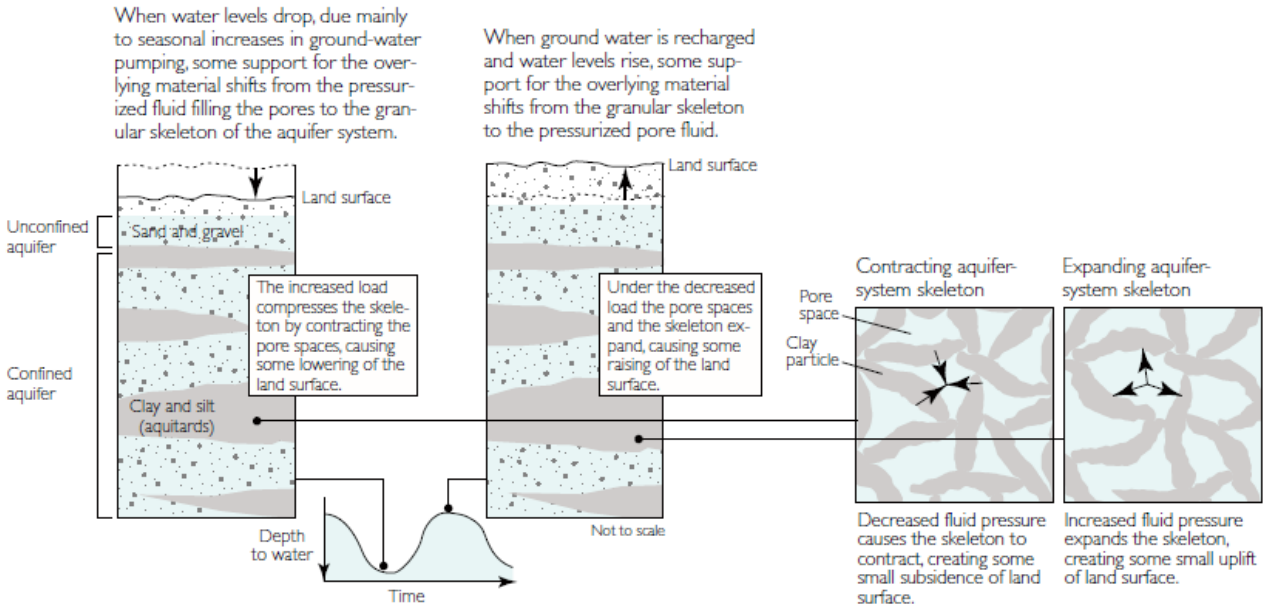

Figure 3. Schematic representation of the reversible deformation in an aquifer-system (from Galloway *et al.*, 1999).

If the load on the aquitard skeleton exceeds the previous maximum load (preconsolidation stress), the aquitard skeleton may undergo evident permanent deformation, resulting in irreversible compaction (Figure 4). Consequently, this results in a permanent reduction of pore volume and a small permanent reduction in the storage capacity of the aquifer system (Galloway *et al.*, 1999).

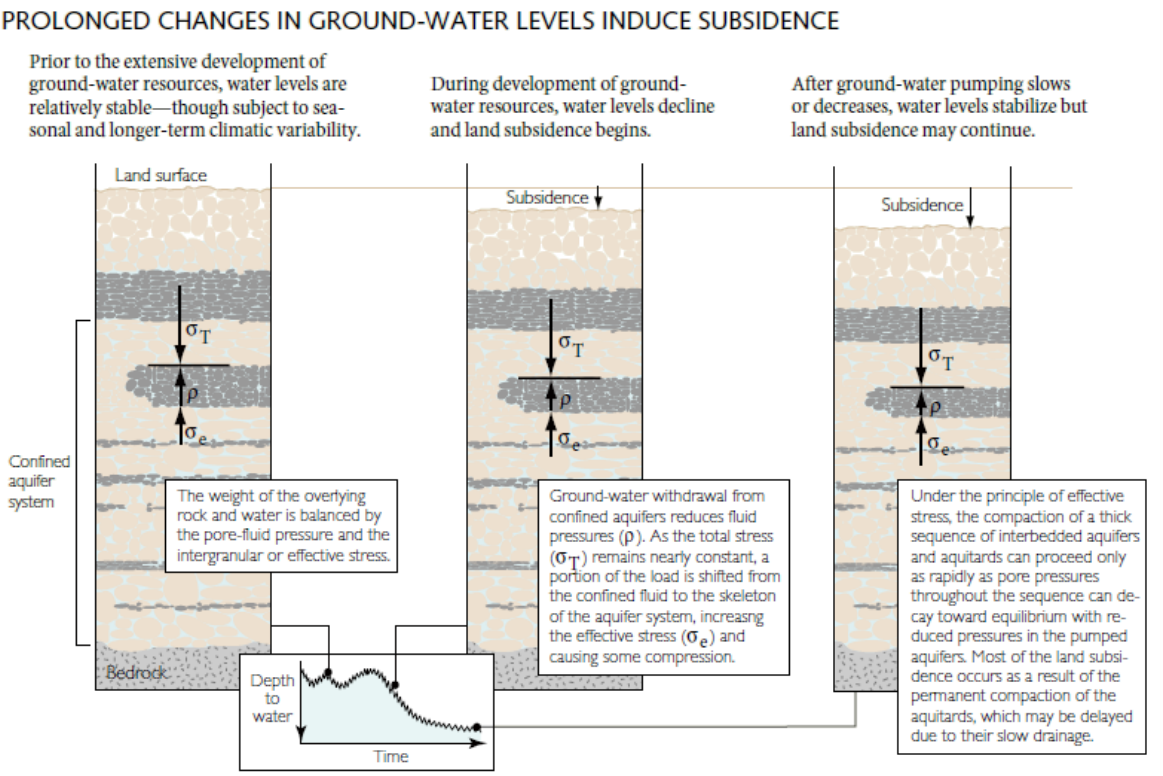

Figure 4. Schematic representation of the irreversible deformation in an aquifer-system (from Galloway *et al.*, 1999).

Tolman and Poland (1940) first realized the conceptual aquitard-drainage model by investigating the aquifer-system in Santa Clara Valley, California. In particular, they suggested that the observed subsidence was not only caused by the compaction of the permeable sands in response to the declining of the hydraulic head, but primarily due to the non-recoverable slow-drainage of the clay layers in the confining units. Successively, Helm (1975,1976) used the insights of previous authors (Terzaghi, 1925; Tolman and Poland, 1940; Riley, 1969) introduced a one-dimensional code to compute the time-delayed aquitard drainage. The theory of hydrodynamic consolidation (Terzaghi, 1925), and the aquitard-drainage model, explains the delay involved in draining aquitards when hydraulic heads are lowered in adjacent aquifers and the residual compaction that may continue long after aquifer heads are initially lowered.

2.3. Stress-strain analysis

Land subsidence studies commonly exploit the subsidence and groundwater level measurements to analyses the relationship stress-strain in confined and semi-confined aquifer-system (Lofgren, 1969; Riley, 1969; Poland et al., 1976; Helm, 1976; Holzer, 1981; Burbey, 2001; Burbey, 2003; Zhang *et al.*, 2007a, 2007b; Tomas *et al.*, 2010a; Ezquerro *et al.*, 2014; Chen *et al.*, 2016). By plotting applied stress (hydraulic head) on the y-axis and either vertical strain or displacement (compaction) on the x-axis, the mechanical behaviours of the hydrostratigraphic units can be investigated in detail. A change in water level (head) represents a change in applied stress, which is equivalent to the change in effective stress on a confined aquifer system with a constant total stress.

The previous works highlight that the same aquifer-system can determine different deformation responses, according to the stratigraphic characteristic and the amount of groundwater pumped. Indeed, firstly the deformation characteristics of hydrostratigraphic units depend on the types and properties of soil within the units and secondly depend on the histories of groundwater-level change that the units have experienced. The complexity of the deformation responses to the applied stress is due to the different composition of the hydrostratigraphic units and the different changing patterns of groundwater levels that the units have experienced.

Zhang *et al.* (2007a, b) described the features of the aquifer-system compaction in Shanghai. The authors compared the compaction measurements of individual strata detected by extensometers with pore water pressure changes measurements detected by observation wells.

The aquifer-system in Shanghai exhibits deformations:

- Elastic;
- elasto-plastic;
- plastic;
- visco-elasto-plastic.

As shown in Figure 5 the second confined aquifer is characterized by an elastic deformation during the period 1965-1989; the cumulative compaction closely follows the change in groundwater level. In the period 1989-2002, the groundwater level fell slowly but the fall was higher than the previous lowest value that the aquifer unit had ever experienced and the aquifer compaction is elasto-plastic.

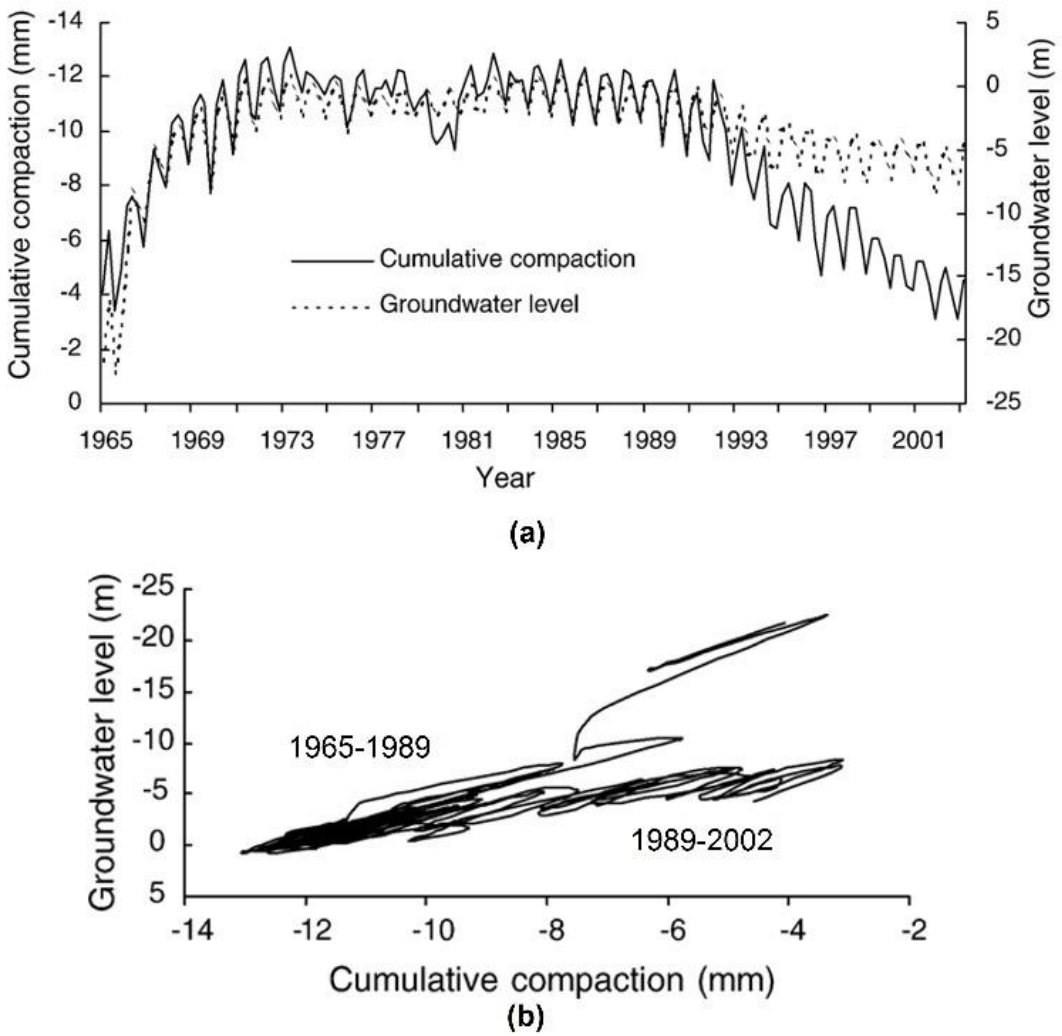

Figure 5. (**a)** Compaction variation and groundwater level change in the second confined aquifer in Shanghai (China) **(b)** Stress-strain curve. The deformation of the aquifer is primarily elastic in the period 1965-1989 and elasto-plastic in the period 1989-2002 (from Zhang *et al.*, 2007a).

Soft clay layers one and two in the same aquifer shows a different deformation response (Figure 6). In this case, the hydrostratigraphic units exhibited a visco-elasto-plastic deformation. In fact, even when the groundwater level raised in yearly cycles, the strata compacted continuously. Dissipation of pore water pressure is slow and lags in these units due to their low permeability and their deformation is primarily plastic.

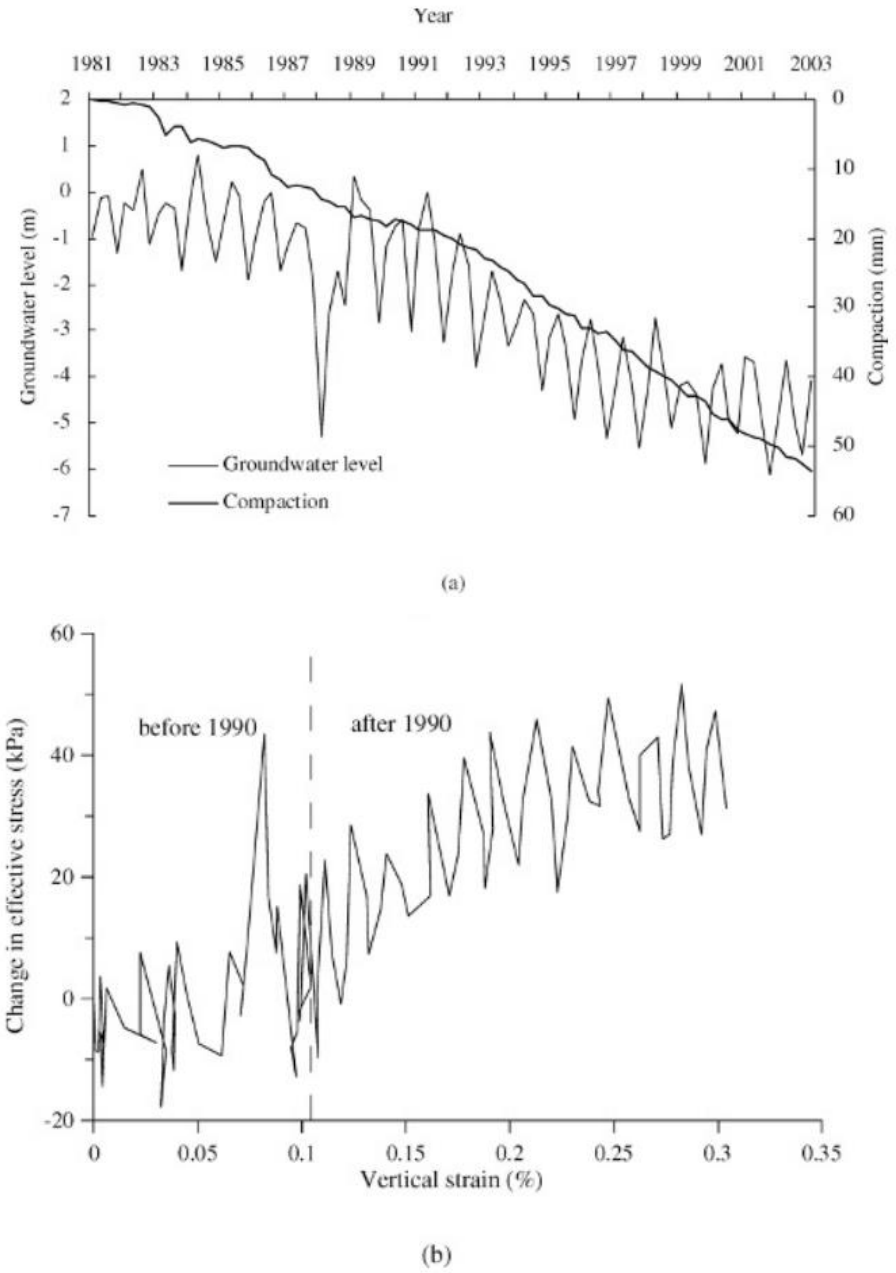

Figure 6. (**a)** Compaction variation of soft clay layers one and two and groundwater level change in confined aquifer one in Shanghai (China). **(b)** Stress-strain curve from January 1981 to December 2002. The deformation of soft clays is visco-elasto-plastic (from Zhang *et al.*, 2007b).

Another feature of the aquifer-system compaction was observed in the soft clay three. When the groundwater level rose, the stratum apparently rebounded, conversely when the groundwater level fell, the stratum compacted. Furthermore, the variation of the deformation is synchronized with groundwater level changes. However, there was an irrecoverable deformation in each yearly stress cycle, and for this reason the deformation was defined as elasto-plastic.

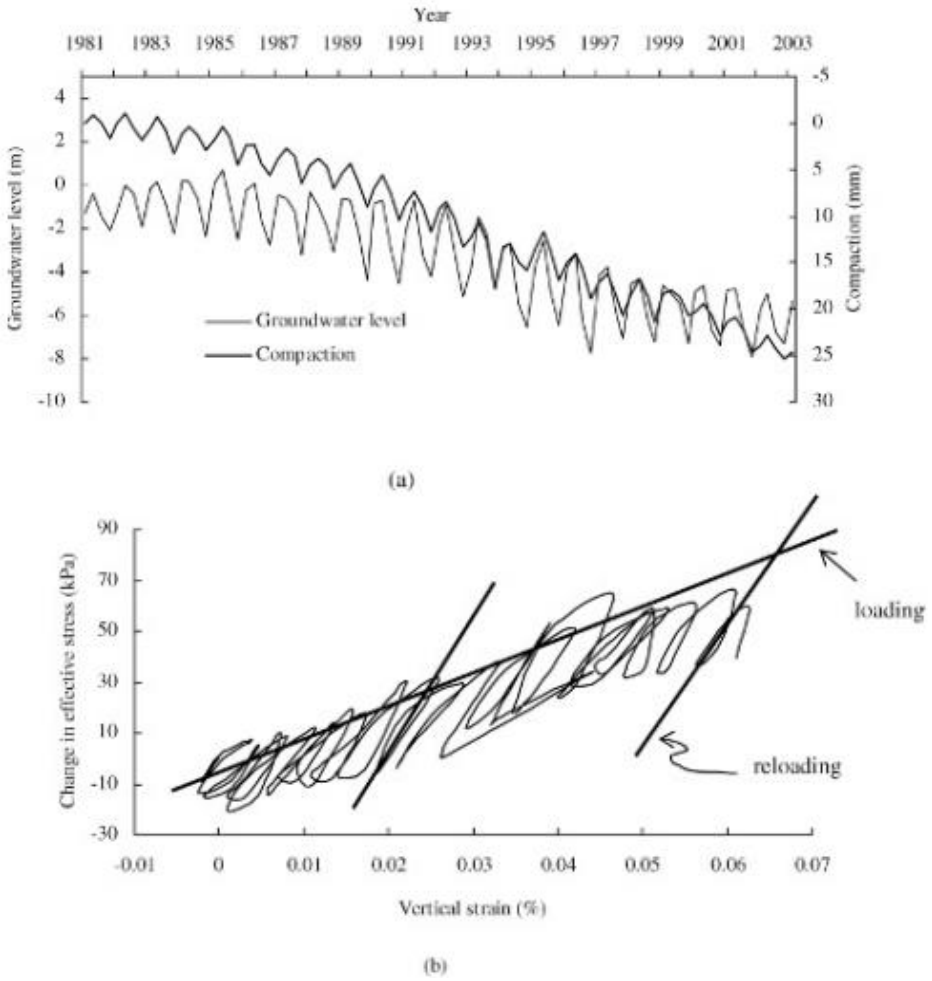

Figure 7. (a) Compaction variation of soft clay three and groundwater level change in confined aquifer two in Shanghai (China). **(b)** Stress-strain curve of soft clay three from January 1981 to December 2002. The deformation of soft clays is primarily elasto-plastic (from Zhang et al., 2007b).

In summary, the spatial variation in hydrostratigraphic units and the spatio-temporal variation in groundwater level change influence the complexity of aquifer-system deformation. Therefore, the stress-analysis represents a crucial step for constructing reasonable mathematic models of aquifer-system deformation.

Chapter III. SAR techniques

Earth Observations (EO) from space combined with complementary terrestrial observations and with physical models, have been used to monitor various geohazards and are enabling our understanding of how the Earth dynamic-system acts (Tralli *et al.,* 2005). A relevant aspect of space-based earth observations is that we can investigate the occurrence of different hazards, addressing the operational requirements of decision support systems used by policy makers and emergency managers.
Active remote sensing techniques are a class of Earth Observation tools which have the potential to provide accurate information about land surface by imaging Synthetic Aperture Radar (SAR) from airborne or spaceborne platforms. It is an active system providing its own energy source for illumination using microwave imaging system sensors and consist of an antenna with a day and night operational capability.

3.1. Synthetic Aperture Radar (SAR)

The antenna transmits electromagnetic (EM) waves from an antenna to the Earth's surface where they are backscattered. Electromagnetic waves with wavelengths between 1 cm and 1 m, have the advantage to penetrate clouds and are independent of atmospheric conditions.
The main advantages of the use of active sensors are (Kerle *et al.,* 2004):

- the possibility to acquire the data at any time and since the waves are actively propagated,
- the control of the signal characteristics (e.g. wavelength, polarization, incidence angle, etc.).

Radar signals are characterized by two fundamental properties: *amplitude* and *phase*.
Amplitude is related to the energy of the backscattered signal. Therefore, the signal of target characterized by high reflective quality such as metal and hard objects (natural or artificial) determines higher amplitude signal.
Phase is related to the distance between sensor and target. It is a crucial property of the radar signal used in estimating displacement in interferometric applications.

As shown in Figure 8, Radar (Ratio Detection And Ranging) transmitted the microwaves (radio signal) directed into a beam towards an area on the earth surface called *swath* with a certain inclination respect to the *nadir* direction. The signal enlightens twice the distance between target and

antenna, and, knowing the speed of light, the distance (*range*) between sensor and target can be measured. The platform moves along the orbit in the *flight direction*. The direction along the trajectory is called along-track or *azimuth range*, while the perpendicular direction is called across-track or *ground range.* The angle between the radar beam and the local vertical is defined as *incidence angle*. Furthermore, it is important to distinguish the *local incidence angle*, which depends on the terrain slope. The measurements are acquired along that Line of Sigh (LOS) of the satellite.

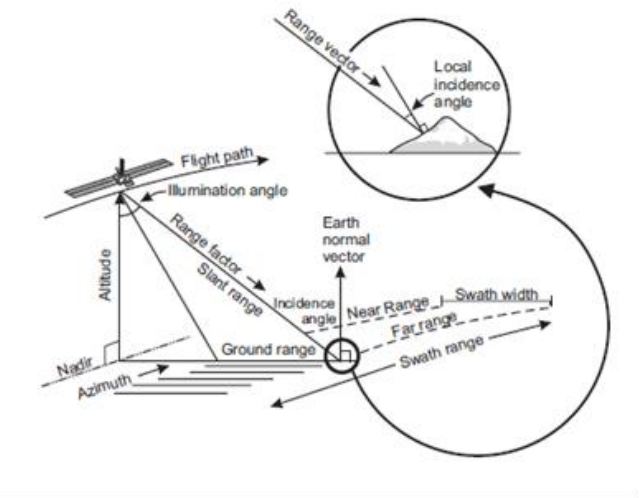

Figure 8. SAR acquisition geometry (from Kerle et al., 2004).

Furthermore, SAR sensors can acquire data in different acquisition modes that correspond to different beam footprint extensions (Figure 9):

- StripMap (SM): antenna maps large areas with low resolution, moving along a strip of terrain parallel to the path motion. The flexibility of the system is given by changing the incidence angle.
- ScanSAR: antenna beam can be electronically steerable in elevation. Radar images can be mapped by scanning the incidence angle and then synthesizing images for the different beam positions. The principle of the ScanSAR is to share the radar operation time between two or more separate sub-swaths in such a way as to obtain full image coverage of each with a medium-resolution data.
- Spotlight: antenna beam continuously enlightens predetermined targets (spot) or terrain patch being imaged with multiple viewing angles during a single pass. The spotlight allows to collect high-resolution data from one or more localized areas.
- Interferometric Wide Swath Mode (IW): the system implements a new type of ScanSAR mode called Terrain Observation with Progressive Scan (TOPS) SAR aimed at reducing the

drawbacks of the ScanSAR mode. The basic principle of TOPSAR is the shrinking of the azimuth antenna pattern (along track direction) as seen by a spot target on the ground. This is obtained by steering the antenna in the opposite direction as for Spotlight support. TOPSAR mode aims to achieve the same coverage and resolution as ScanSAR, but with a nearly uniform Signal-to-Noise Ratio (SNR) and Distributed Target Ambiguity Ratio (DTAR).

- Extra Wide Swath Mode (EW): the acquisition mode uses the TOPSAR technique to cover a very wide area of 400 km at medium resolution of 20 m by 40 m on the ground.
- Wave Mode (WV), a stripmap image is acquired with an alternating elevation beam at a fixed on/off duty cycle, detecting vignettes 20 by 20 km in size at regular intervals of 100 km. Swaths alternate incidence angles between 23° and 36.5° as shown in Figure 9.

In this thesis, the SAR images were mainly acquired using StripMap (SM), whereas the SAR images acquired by the Sentinel-1 sensor in Ravenna were acquired using Interferometric Wide swath (IW) mode.

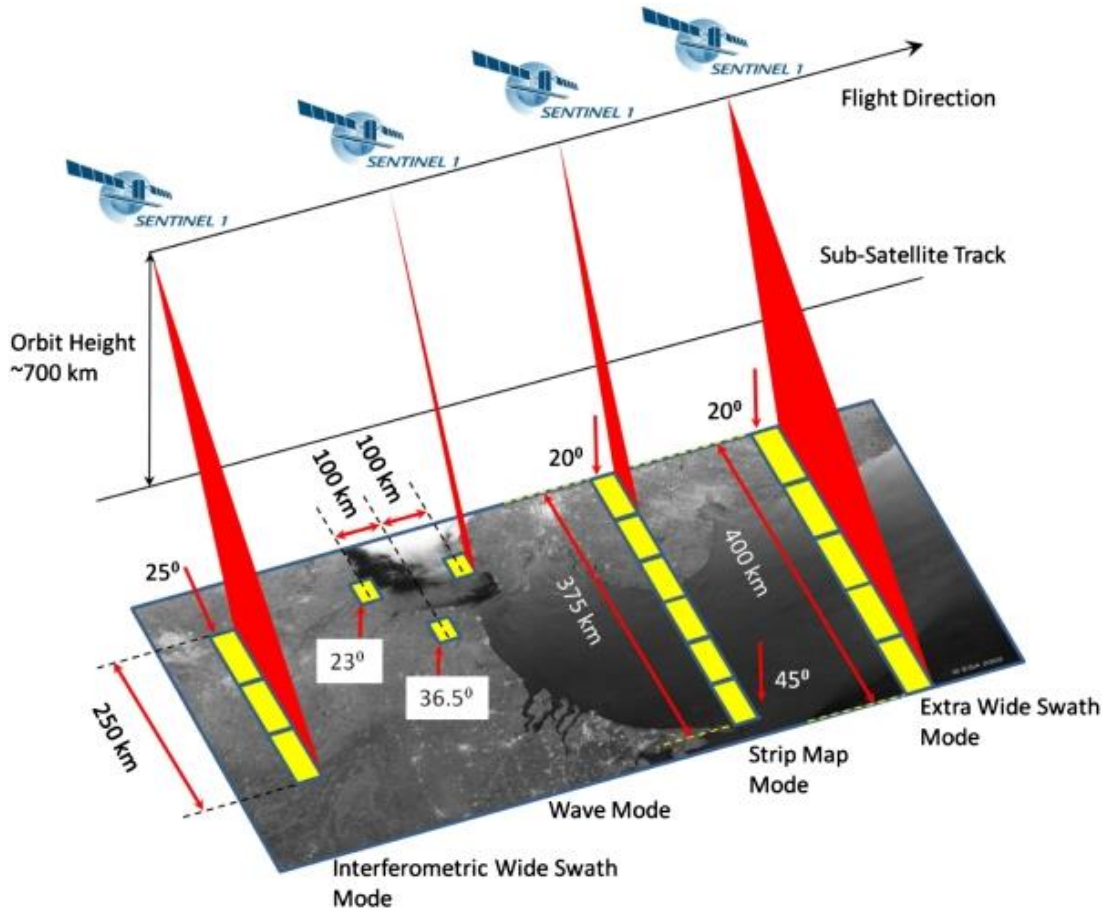

Figure 9. SENTINEL-1 acquisition Modes (from ESA).

3.2. Radar missions and SAR Sensors

All Satellites are able to achieved a complete Earth's surface coverage by combination of the orbital satellite motion travelling from South pole to North pole (ascending passes) and from North pole to South pole (descending passes). As consequence, ascending and descending images can be collected over the same area (Figure 10).

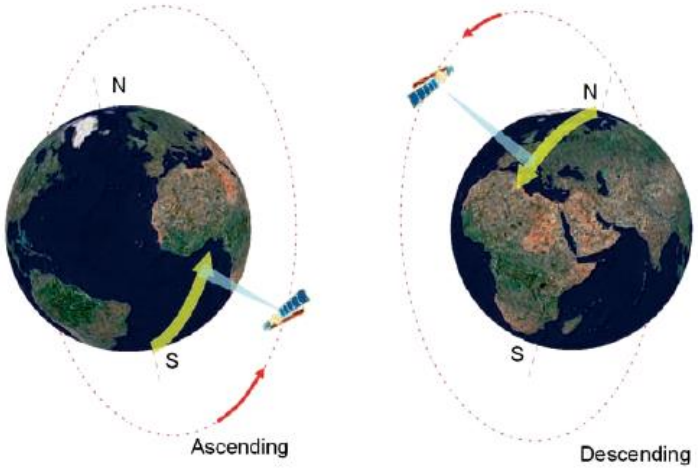

Figure 10. Ascending and descending geometry of acquisition (from TRE)

Since the 1990s various radar mission started collecting data acquired by using different sensors. Commonly used sensors in radar interferometry techniques are listed in Table 2. All the sensors provided data used in the thesis, are X-, C- and L-Band.

Table 2. Frequency and Wavelength of Radar Remote Sensing Bands used in the thesis.

Band	Frequency	Wavelength	Key Characteristics
X-Band	12.5-8 GHz	2.4-3.75 cm	Widely used for military reconnaissance, mapping and surveillance (TerraSAR-X, TanDEM-X, COSMO-SkyMed)
C-Band	8-4 GHz	3.75-7.5 cm	Penetration capability of vegetation or solids is limited and restricted to the top layers. Useful for sea-ice surveillance (RADARSAT, ERS-1/2, Envisat, Sentinel-1).
L-Band	2-1 GHz	15-30 cm	Penetrates vegetation to support observation applications over vegetated surfaces and for monitoring ice sheet and glacier dynamics (ALOS PALSAR)

(http://www.intelligence-airbusds.com/files/pmedia/edited/r15796_9_eij_radarimagery_finalarticle.pdf)

Many satellite constellations were launched by the various Spatial Agency. Figure 11 shows the satellite platforms available for the historical analysis of the surface displacements.

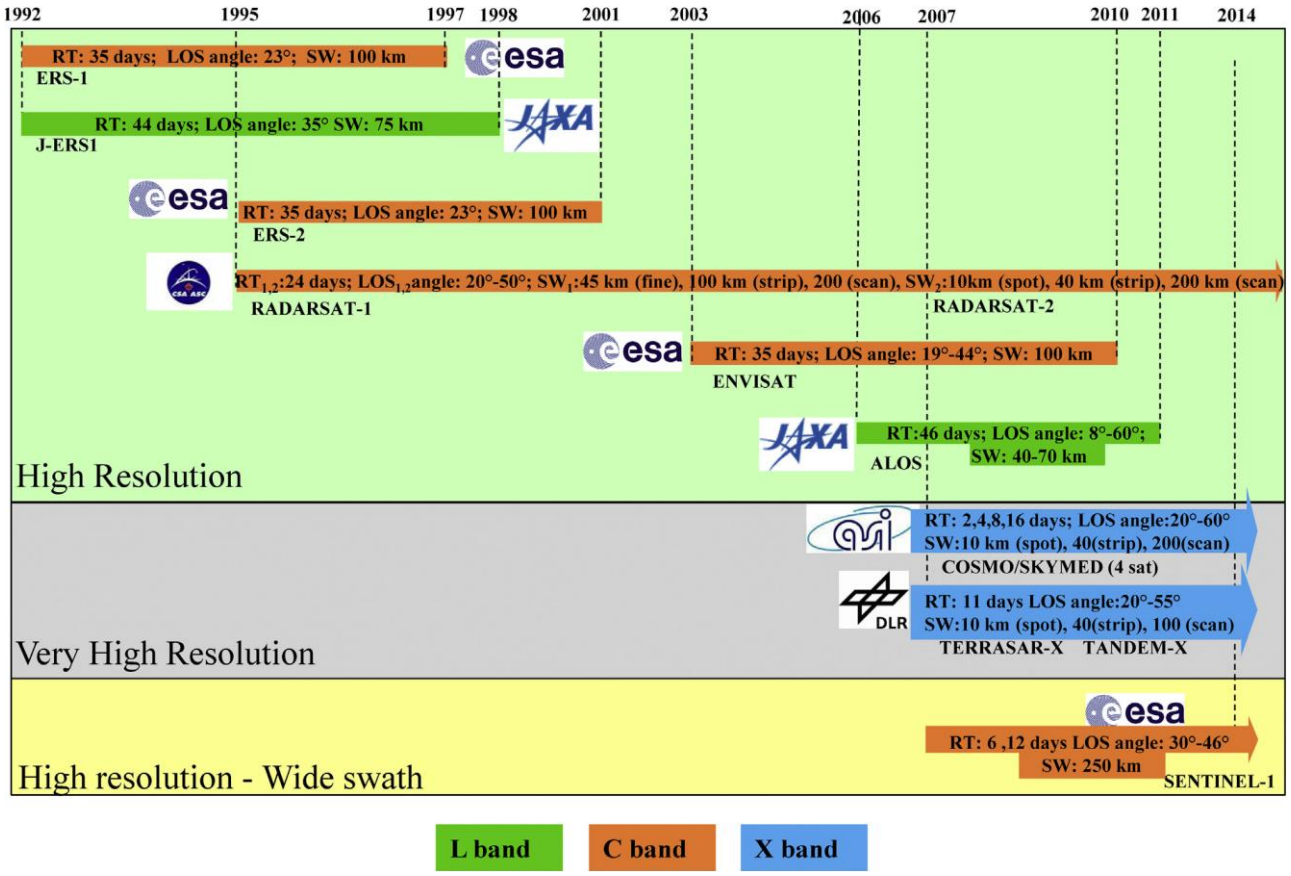

Figure 11. SAR sensors and radar missions (Peduto *et al.*, 2015)

Following, the detailed information about each satellite platform are presented (Table 3), including the information about the lifetime, the wavelength, the revisit time, the ground resolution and the incidence angle.

Table 3. Summary of the satellite platforms details.

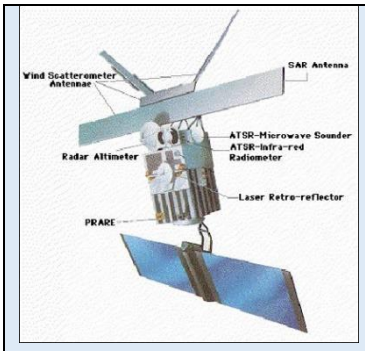	***ERS 1/2***: European Remote Sensing (ERS) satellites, ERS-1 and –2, are the first two satellites of the European Space Agency (ESA) that were launched into the same orbit in 1991 and 1995 respectively, for Earth observation missions. The ERS-1 mission finished on 10 March 2000 and ERS-2 was retired on 05 September 2011. **Wavelength:** 5.6 cm (C-band) **Revisit time:** 35 days **Ground resolution:** 25 m **Incidence angle:** 23°
	***RADARSAT-1/2:*** RADARSAT are the Earth observation satellites that belong to the Canadian Space Agency (CSA). The Radarsat-1 and -2 were launched on November 4th, 1995 and December 14th, 2007, respectively. They are instrumented with C-band Synthetic Aperture Radar (SAR). **Wavelength:** 5.6 cm (C-band) **Revisit time:** 24 days **Ground resolution:** 10-100 m **Incidence angle:** 10°-60°
	***ENVISAT:*** Envisat was ESA's successor to ERS. Envisat was launched in 2002 and ended on 8th April 2012. **Wavelength:** 5.6 cm (C-band) **Revisit time:** 35 days **Ground resolution:** 15-100 m **Incidence angle:** 23°
	***ALOS PALSAR:*** The Advanced Land Observing Satellite (ALOS) is a satellite of the Japan Aerospace Exploration Agency (JAXA) used for cartography, regional observation, disaster monitoring, and resource surveying. was launched on January 24th 2006 and ended on May 12th 2011. **Wavelength:** 24.1 cm (L-band) **Revisit time:** 46 days **Ground resolution:** 7-100 m **Incidence angle:** 8°-60°
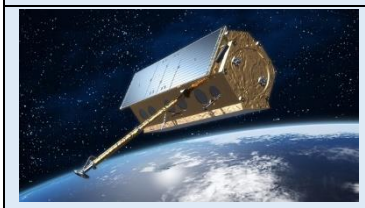	***TerraSAR-X:*** TerraSAR-X was launched on June 15th, 2007 and has been in operational service since January 2008. Following the launch of a second sister satellite, TanDEM-X in early 2010, the two satellites act as a pair. **Wavelength:** 3.1 cm (X-band) **Revisit time:** 11 days **Ground resolution:** 1-16 m **Incidence angle:** 20°-55°
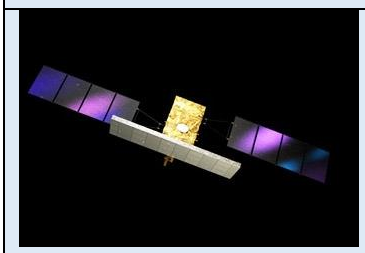	***Cosmo-SkyMed:*** the satellite was launched in 2007 and it is a Space-Earth Observation that consists of 4 satellites, each one equipped with a microwave high-resolution synthetic aperture radar (SAR). **Wavelength:** 3.1 cm (X-band) **Revisit time:** 1-8 days **Ground resolution:** 1-100 m **Incidence angle:** 20°-60°
	***Sentinel-1:*** the twin Sentinel-1 satellites was launched in 2013 and they represent the first operational system for Europe's Copernicus programme to detect small deformation of the Earth's surface. **Wavelength:** 5.6 cm (C-band) **Revisit time:** 6 days **Ground resolution:** 5-100 m **Incidence angle:** 18°-47°

3.3. SAR limitations

In this Section, the main SAR limitations are described. In particular, radiometric and geometric distortions are mentioned.

3.3.1 Geometric distortions

In the radar images the variations in scale can cause geometric distortions as function of the incident angle with respect to the surface morphology. There are three effects that can be observed in the radar images (Figure 12):

- **Foreshortening;** the radar measures distance in slant range and the slope area is compressed in the image. The effect of shortening is function of the angle that the slope forms with the incidence angle. The maximum distortion is reached if the radar beam is perpendicular to the slope.
- **Layover;** the radar beam reaches the top of the slope earlier than the bottom. The layover is an extreme case of foreshortening.
- **Shadowing;** the radar beam is not able to illuminate the ground surface. It is typical of the far range areas and since the radar beam does not illuminate the surface, shadowed regions will appear dark on an image as no energy can be backscattered.

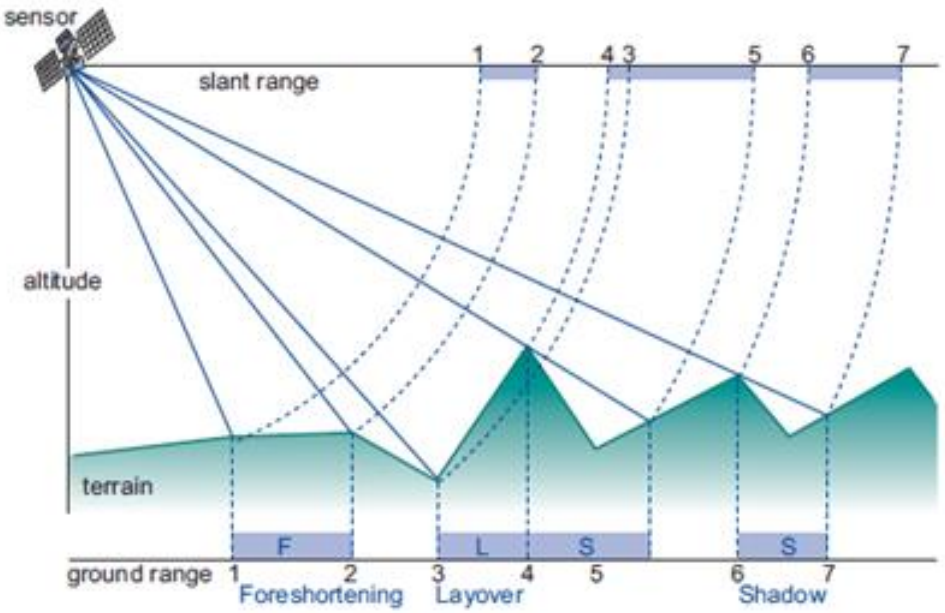

Figure 12. Geometric distortion in radar imagery (from Kerle et al., 2004).

3.3.2. Radiometric distortions

The backscattered signal depends on different parameters. Figure 13 shows the penetration capacity of the electromagnetic waves in vegetated areas, dry alluvium and dry snow ice, using different frequencies. I addition, the mentioned geometric distortions also have an influence on the received energy. An important property of the radar images is the *speckle* caused by the interference of backscattered signals coming from an area. The interference is due to the wave interaction; where the return signals can be smoothed or amplified, resulting in dark and bright pixels in the image. This effect makes more difficult the interpretation of the radar imagery. However, the speckle effects can be reduced using a multi-look processing or spatial filtering.

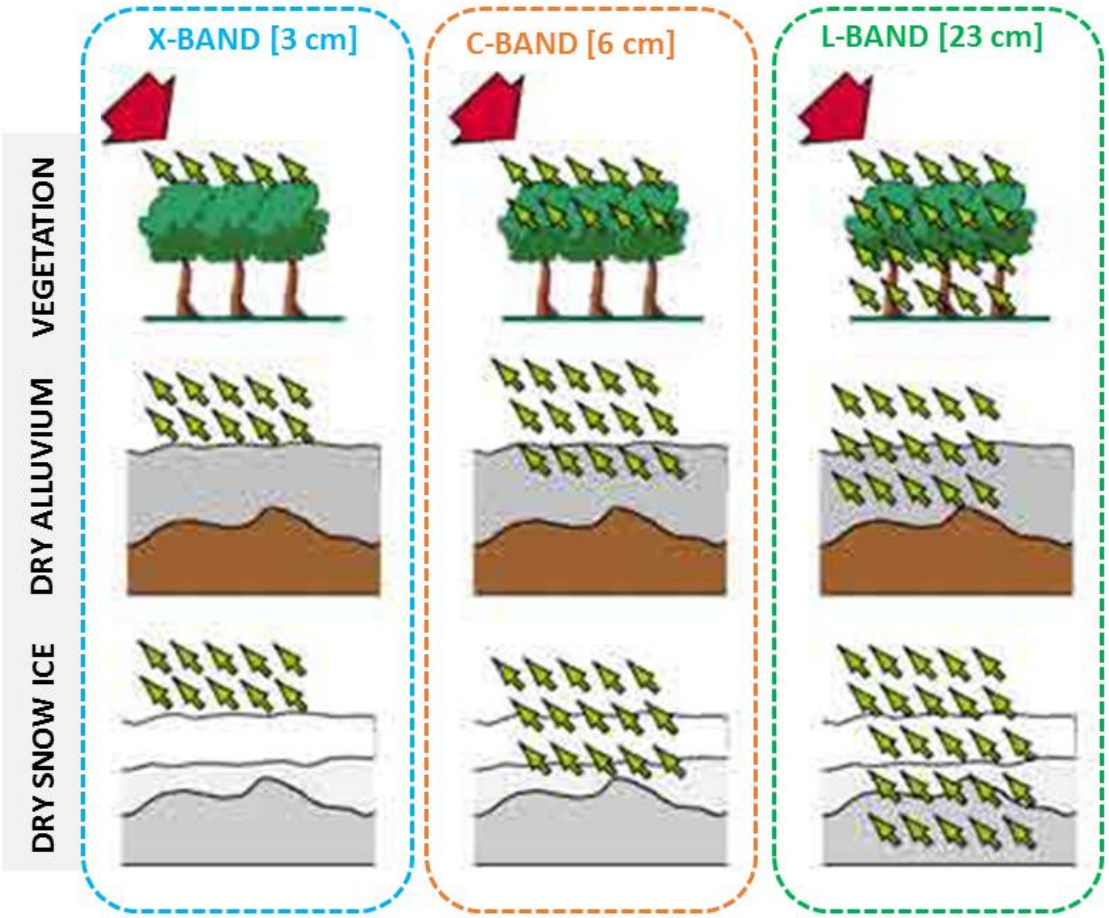

Figure 13. Penetration capacity for electromagnetic waves for X, C, and L-Band

(Modified from https://earth.esa.int).

3.4. InSAR, DInSAR and A-DInSAR techniques

Interferometric Synthetic Aperture Radar (InSAR), or SAR Interferometry, represents the measurement of signal phase change between two images acquired over the same area, at different time. The change in signal phase (Δφ) depends on several signals can be expressed by the following equation (Ferretti *et al.*, 2001):

$$\Delta\varphi = \Delta\varphi_{def} + \Delta\varphi_{topo} + \Delta\varphi_{orb} + \Delta\varphi_{ip} + \Delta\varphi_{atm} + \Delta\varphi_{n} \quad (3.1)$$ (Ferretti *et al.*, 2001)

is the phase change due to the deformation of the ground surface, is the phase change due to topography, is the phase change due to orbital errors, is the phase change due to integer phase ambiguities, is the phase change due to atmospheric phase effects and is the phase change due to random phase noise. The different components can be interpreted signal or noise in different applications. In this case, the phase change considered are due to the deformation of the ground surface. can be expressed as:

$$\Delta\varphi_{def} = \frac{2\pi}{\lambda}(2\Delta d) = \frac{4\pi}{\lambda}(\Delta d) \quad (3.2)$$ (Ferretti *et al.*, 2001)

Δd is the range displacement of the radar target and λ is the wavelength of the radar system. The phase difference represents the *Interferograms*. The phase in the interferograms can only be measured in 2π (values ranges from -π to +π) and each cycle in phase from –π to +π is defined a "fringe".

If an area appears to have the same surface characterization in all images under analysis, then the images are defined as coherent, conversely, if the land surface is disturbed between two acquisitions (i.e. an agricultural field has been ploughed, etc.), those subareas will decorrelate in an InSAR analysis, resulting in noise and no information can be obtained. The *coherence* is a parameter which ranges from 0 (lower coherence) to 1 (higher coherence).

The coherence of an interferogram (difference of the phase) depends on:

- Topographic orientation and slope angle (i.e. steep slopes induce low coherence)
- Terrain properties
- The time between image acquisitions (i.e. longer time intervals induce lower coherence)
- The distance between the satellite tracks during the first and second acquisitions, also referred to as the baseline (i.e. larger baselines induces lower coherence).

Various sources of decorrelation were observed such as:

- Vegetation; the change in the vegetation coverage (i.e. due to their growth and death) from two successive image acquisitions change the appearance of the surface characterization. Therefore, decorrelation problem can be observed using X-band and C-band sensors. L-band sensors can overcome this limitation, because their longer wavelength is able to penetrate the foliage.
- Construction; at a construction site, the appearance of the land surface is changing constantly. This is a problem that is common to X-band, C-band, and L-band sensors.
- Erosion; surface erosion will change the surface characterization of land and, for this reason can decorrelate those areas where erosion occurs.
- Rapid Movement; often, the rapid motion (i.e. landslides and earthquakes) causes destruction and, a total change in the land surface's characterization and, in those situations, interferometry can be successful. When the total movement between successive image acquisitions exceed one-half of the signal's wavelength, decorrelation can be observed.

Differential InSAR (DInSAR) refers to the subtraction of the topographic phase contribution based on a digital elevation model (DEM). These techniques referred to a single interferogram generated from a pair of SAR images (Rosen *et al.,* 2000). However, improved results have been obtained in the last years, implementing ***Advanced DInSAR techniques (A-DInSAR),*** which are based on the processing of multiple interferograms derived from a large set (at least 20 images) of SAR images (Ferretti *et al.,* 2001; Berardino *et al.,* 2002; Mora *et al.,* 2003; Arnaud *et al.*, 2003; Werner *et al.*, 2003; Hooper *et al.,* 2004).

3.5. Interferometric processing algorithms

Several algorithms were developed to process SAR images. These processing approaches used in the thesis can be grouped into three main categories (Crosetto *et al.,* 2015):

- Persistent Scatterers (PS) methods that work on localized targets (Ferretti *et al.*, 2001; Arnaud *et al.,* 2003; Werner *et al.,* 2003; Hooper *et al.*, 2004; Duro *et al.,* 2005; Costantini *et al.*, 2008)
- Small Baseline (SB) methods that utilize spatially distributed targets (Berardino *et al.,* 2002; Mora *et al.* 2003; Lanari *et al.,* 2004; Crosetto *et al.*, 2008; Prati *et al.*, 2010).
- Hybrid processing that incorporates both the PS and SBAS approaches (Hooper, 2008; Ferretti *et al.*, 2011).

The algorithm details of the approaches used in this thesis are summarized in table 4.

Table 4. Characteristics of the main processing approaches (modified from Crosetto *et al.*, 2016).

Algorithm	Reference	Baseline configuration	Pixel selection criterion	Deformation model
PSInSAR™	Ferretti *et al.* (2001)	Single master	Amplitude dispersion	Linear deformation in time
Small Baseline Subset (SBAS)	Berardino *et al.* (2002)	Small baselines	Coherence	Spatial smoothness
Coherence Pixel Technique (CPT)	Mora *et al.* (2003)	Small baselines	Coherence	Linear deformation in time
Interferometric Point Target Analysis (IPTA)	Werner *et al.* (2003)	Single master	Amplitude dispersion & Spectral phase diversity	Linear deformation in time
Stable Point Network (SPN)	Crosetto *et al.* (2008)	Small baselines	Amplitude dispersion, coherence, spectral coherence	Linear deformation in time
Stanford Method for Persistent Scatterers (StaMPS)	Hooper *et al.* (2004)	Single master	Amplitude and phase criterion	Spatial smoothness
Persistent scatterer pairs (PSP) method	Costantini *et al.* (2008)	Single master	Amplitude dispersion	Linear deformation in time
SqueeSAR™	Ferretti *et al.* (2011)	Single master after triangulation	Statistical homogeneity test	Deformation model in time

Chapter IV. Study areas

The research was performed in six study areas: Oltrepo Pavese, the valley bottom of the Oglio river, Ravenna, and Piemonte Region in Italy, Alto Guadalentín Basin in Spain, and London Basin in United Kingdom (Figure 14).

The criteria for selection the areas of interest are:

i. Characterized by ground deformations from high to moderate rates;

ii. Affected by ground deformation with unique or multiple causes;

iii. Representativeness of lowland areas and slopes instabilities;

iv. Availability of A-DInSAR and ancillary data.

Figure 14. Location of the study areas

Table 5. Study areas characteristics and available A-DInSAR data.

Study areas	SAR data	Processing	Elaborated by:	Sensor	Time span	Significance	Ground motion	Area
The Oltrepo Pavese (Italy)	ERS-1/2	SqueeSAR™	TRE	C-band	1992-2000	Representative lowland area of the Po Plain	Natural and anthropic causes	440 km^2
	RADARSAT	SqueeSAR™	TRE	C-band	2003-2010			
The valley bottom of the Oglio river (Italy)	ERS-1/2	PSInSAR™	TRE	C-band	1992-2000	Pre-Alpine and Alpine valley bottom land subsidence	Natural and anthropic causes	50 km^2
	RADARSAT	PSInSAR™	TRE	C-band	2003-2007			
	ENVISAT	PSInSAR™	TRE	C-band	2004-2010			
Ravenna (Italy)	ERS-1/2	SBAS	University of Padua	C-band	1992-2000	High-moderate ground motion in coastal area	Natural and anthropic causes	391 km^2
	ENVISAT	SBAS	University of Padua	C-band	2003-2010			
	TERRASAR-X	SBAS, CPT	University of Padua, University of Napoli	X-band	2012-2014			
	Sentinel-1	SBAS	University of Padua	C-band	2014-2016			
Piemonte Region (Italy)	ERS-1/2	PSInSAR™, SqueeSAR™	TRE	C-band	1992-2001	Regional scale analysis	Slope instabilities and land subsidence	25,000 km^2
	RADARSAT	SqueeSAR™	TRE	C-band	2003-2009			
	ENVISAT	PSInSAR™, SqueeSAR™	TRE	C-band	2003-2010			
	COSMO-SkyMed	PSP-IFSAR, SqueeSAR™	e-GEOS, TRE	X-band	2011-2014			
Alto Guadalentín Basin (Spain)[*1]	ERS-1/2	StaMPS	Altamira information	C-band	1992-2000	The higher subsidence of Europe for groundwater withdrawal	Anthropogenic subsidence for ground water extraction	277 km^2
	ENVISAT	StaMPS	Altamira information	C-band	2003-2007			
	ALOS-PALSAR	SPN	Altamira information	L-band	2007-2010			
	COSMO-SkyMed	SPN	Altamira information	X-band	2011-2012			
London Basin (Italy)	ERS-1/2	IPTA	CGG NPA	C-and	1992-2000	Ground motion due to groundwater level change	Natural and anthropic causes	1,360 km^2
	ENVISAT	IPTA	CGG NPA	C-and	2002-2010			

Regarding the identification of the ground motion areas, a novel methodology was implemented in the plain area of the Oltrepo Pavese (Italy) in order to distinguish different components of motion and to analyse the mechanisms of ground motion in order to respond to Questions 1 and 2 posed in the Introduction (Section 1.2.). A preliminary development of the methodology was tested in the area of the valley bottom of the Oglio river (Italy). Then, the systematic procedure was tested in Ravenna (Italy) in order to verify the reproducibility of the approach using multi-sensors A-DInSAR processed using another processing technique (Question 3, in Section 1.2.). Afterwards, we performed the same methodology in Piemonte Region to assess the applicability for detecting movements due to slope instabilities over large areas (Question 4 and in Section 1.2.).
In addition, the investigation of the mechanisms of ground motion were analysed in detail in the Alto Guadalentín Basin in Spain, where the highest subsidence rates measured in Europe (>10 cm/yr) were recognized as a direct consequence of long-term aquifer exploitation.
Finally, the London Basin was chosen as study area to use the A-DInSAR data to characterize the hydrological and geotechnical properties of the deposits of the basin and to integrate the A-DInSAR data in the modelling of ground deformation (Question 5 and 6 in Section 1.2.). The prediction of the ground motion expected in response to the groundwater level variations was performed in the London Basin since the availability of detailed time-series data from the observation borehole network provided by the Environment Agency (around ~200 piezometers), to reconstruct the historical groundwater level changes across the basin for the 1990s and 2000s.

4.1. Oltrepo Pavese (Po Plain, Italy)

The Oltrepo Pavese (Italy) is the plain sector of the Po river (Figure 15a), covering an area of about 440 km^2. The Oltrepo Pavese is a representative site of similar geological contexts in the Po Plain, where geohazards, due to natural and anthropic factors, were previously recognized. Volume changes of clayey soils; shrinkage during drying periods, and swelling during wet ones, resulted in severe damage to overlying structures. It is worth noting that the plain of the Oltrepo Pavese is characterized by discontinuous urban fabric, and 68% of the monitored area is covered by non-irrigated arable land.

Geological setting **-** The plain of the Oltrepo Pavese is constituted by alluvial quaternary deposits, originating from the combined action of Apennine streams that form coalescent fans and of the Po River (Brambilla, 1990; Pellegrini *et al.* 1995). These deposits overly the Miocene-Pliocene marine substratum, constituted by sandy-marls, sandstones, conglomerates, gypsy-marls, and calcareous-

marls. Three main geomorphological units composed of quaternary deposits were previously distinguished (Cavanna *et al.*, 1998, Pilla *et al.*, 2007):

- Post-würmian alluvial deposits,
- Würmian-holocenic alluvial deposits,
- Pre-würmian alluvial deposits.

Post-würmian alluvial deposits were sedimented by the most recent depositional activity of the Po River, and by the recent and present deposition from flooding events of the main Apennine streams. These deposits are localized in proximity to the Po River, and they are composed of sand, sandy silt, and silt. The deposits from the Apennine streams are characterized by gravel and sand.

Würmian-holocenic alluvial deposits are made up of alternating sand and gravel, with interbedded clays or argillaceous silt.

Pre-würmian alluvial deposits, located in the southern part of the study area, consist of older fluvial terraces, and is constituted by gravel and sand with a silty matrix. These deposits are strongly weathered and covered with clay soils and locally, loess deposits overlap this unit.

In the study area, quaternary sediment thickness decreases from west to east, with the minimum thickness and the outcrop of the marine substratum in correspondence with the Stradella thrust, evidence of the neotectonic activity that affects the area (Boni *et al.,* 1980).

Recent investigations have been performed to investigate the geotechnical properties of the quaternary deposits in the first 15 m of depth of the Oltrepo Pavese plain. On the basis of the analyses of penetrometer results (176 Dynamic Cone Penetration Test, 20 Standard Penetration Test and 266 Cone Penetration Test), calibrated against soil profile logs, six geotechnical classes of non-cohesive soils (from I1 to I6) and four geotechnical classes of cohesive soils (from C1 to C4), have been previously distinguished by Meisina (2006). Taking into account the geotechnical classification of these soils, eight engineering geological units were introduced in order to reduce the lithologic variability and to map the geotechnical behavior of representative and homogeneous geotechnical profiles (Figure 15b, c). Unit 1 represents the post-würmian alluvial deposit of the Po River, and is mainly constituted of non-cohesive soils (I3). Conversely, units 2, 3, 4 and 7 are würmian-holocenic alluvial deposits, characterized by cohesive soils. Unit 5 is composed of the alluvial fan of the Scuropasso River, and units 6 and 8 by the pre-würmian terraced deposits.

Hydrogeological setting **-** In general, post-würmian alluvial deposits contain a shallow phreatic aquifer with a water level near ground surface. In the Würmian-holocenic alluvial deposits, a shallow phreatic aquifer and deeper aquifers, of both phreatic and confined types, were distinguished. Deeply buried structures, consisting of a series of folds and fold-faults, shaped in the tertiary marine basement, have a direct control over aquifer geometry. These alluvial deposits show the constant

presence of a tabular clayey-silty cover, which acts as a seal, and limits water infiltration (Pilla *et. al.*, 2007). Groundwater exploitation of the Oltrepo Pavese is mainly derived from the aquifer contained in this unit.

In the pre-würmian unit, the depth of the water level in this unit reaches values up to 20 m in depth.

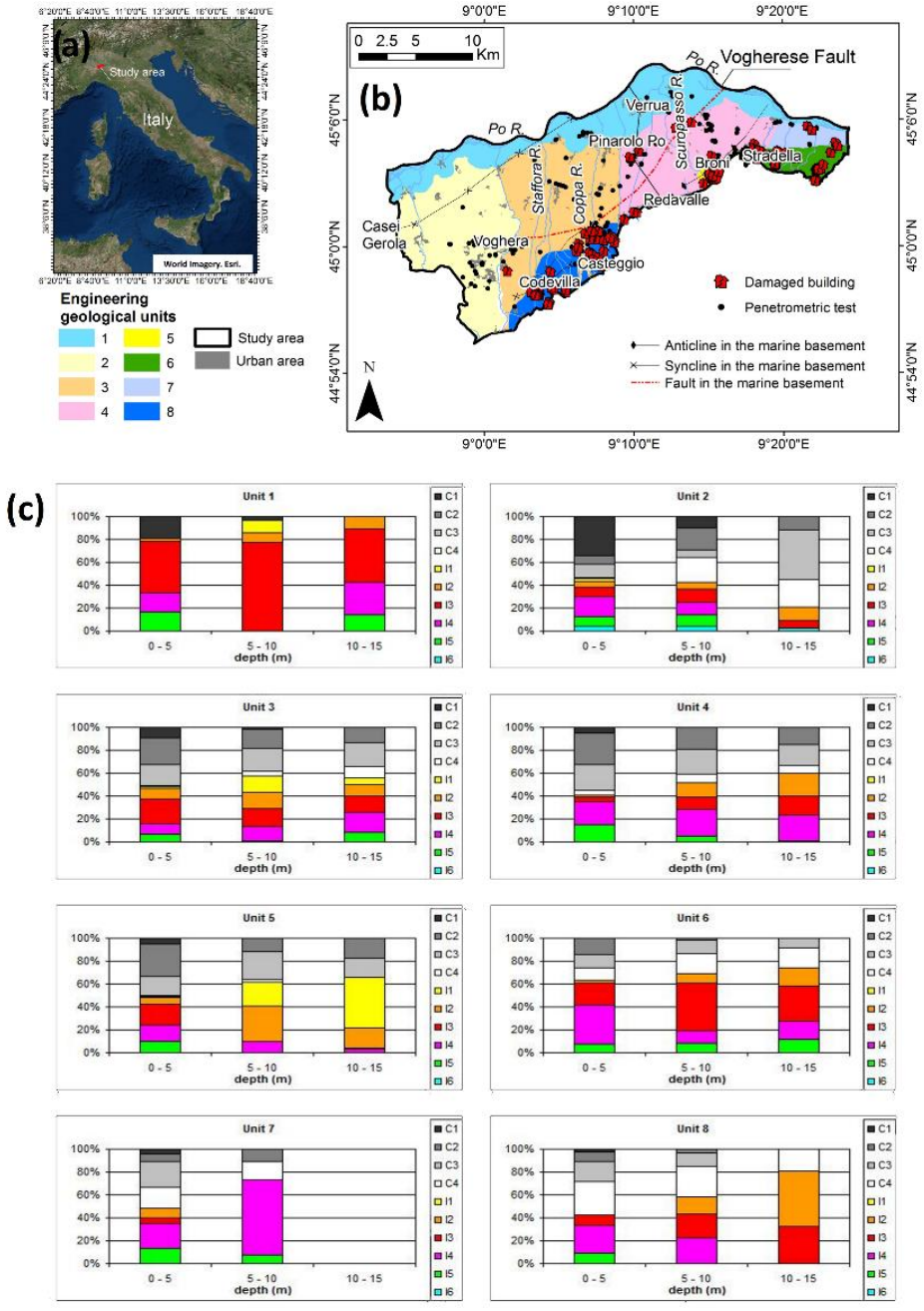

Figure 15. (**a**) Location of the study area. Sources: Esri, DigitalGlobe, Earthstar Geographics, CNES/Airbus DS, GeoEye, USDA FSA, USGS, Getmapping, Aerogrid, IGN, IGP, and the GIS User Community. (**b**) Distribution of the engineering geological units in the plain area of the Oltrepo Pavese. Damaged buildings, detected by Meisina et al. (2006) [31], are also reported. (**c**) Thickness percentage of the geotechnical classes in different depth intervals for each engineering geological unit.

4.2. The valley bottom of the Oglio river (Italy)

The valley bottom of the Oglio river (Italy) is a Pre-Alpine valley located upstream the Iseo Lake, and covering an area of about 50 km^2 (Figure 16a). It has been chosen as exemplificative case of pre-Alpine and Alpine valley bottom subsidence with both natural and anthropic components. The particular geological and geomorphological context deserves special attention, because it insists on densely populated area, in proximity of an alpine lake, susceptible to instability motion and flooding risk. Since the 1980, it is a high-urbanized area over unconsolidated alluvial materials.

Geological setting **–** The valley bottom of the Oglio River shows an approximate NE-SW trend. This area is characterized by the complex stacking of south-verging tectonic slices of the crystalline basement and its sedimentary cover succession of the Southalpine domain, upper Permian to Cretaceous in age (Bini *et al.*, 2007). The bedrock where the lake develops is mainly constituted by Mesozoic carbonate rocks (Figure 16b). The formations within the bottom of the valley are recent (Holocene at ground surface, Upper Pleistocene at some depth) alluvial deposits that are mainly constituted by successions of silt-sands, clay and sands-gravels layer with the presence in some sites of intercalation of peat associated to organic clay deposits. These sediments are the results of different morphologic actions: the Camuno glacier, the Iseo Lake and the Oglio river. The first morphologic factor has produced the detrital layer of the valley bottom, the second one in the past was found on the northern sector and it has limited the detrital contribution. The last one has produced the heterogeneous superficial succession of fine and gravels layers.

Hydrogeological setting **–** The shallow aquifer-system is located in the alluvial deposits of the valley, and the water level reaches values up to 4 m in depth.

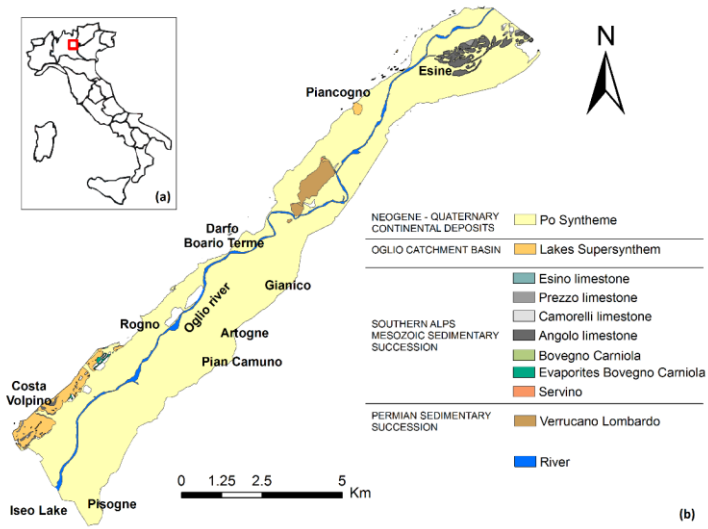

Figure 16. (**a**) Location of the study area. (**b**) Geological setting of the study area.

4.3. Ravenna (Italy)

The study area of Ravenna is located on the south-eastern portion of the Po River plain (Italy) covering an area of about 391 km^2 (Figure 17a). Ravenna is located along the Adriatic coast, where land subsidence of natural and anthropogenic origin occurs since the last century. Since its occurrence, subsidence has resulted in high economic losses and due to its magnitude, duration and extension, has been intensively studied in the last decades. The site is located in a densely populated area that is also characterized by natural landscapes such as wetlands, pinewoods, sandy beaches and sand dunes.

Geological setting – It is bounded by two mountain ranges, the Alps to the North and the Apennines to the South. These mountains range are related to two subduction zones: the Alps results from the subduction of the European plate beneath the Adriatic plate, and the Apennines from the subduction of the Adriatic plate under the Tyrrhenian lithosphere. The buried tectonic structures underlain around 2000 m of Quaternary sediments of Alpine and Apennines origin deposited under different environments, from continental to marine (Carminati *et al.,* 2003).
The pre-Quaternary basement is characterized by a complex structure of folds and faults which develop parallel to the main Apennine tectonic lines forming natural traps for the methane gas. Several Pliocene and Pleistocene gas fields are located in thrusted anticlines, with depths ranging between 1000 m and 4500 m, simple drape structures and stratigraphic traps (Gambolati *et al.,* 1991). A typical feature of this basin is that gas accumulation occurs in multiple zone reservoirs with thickness ranging from centimetres to a few tens of meters. The Quaternary sequence is made of normally consolidated layers of alternating silty-clay, sand and sandy silt (Figure 17b).

Hydrogeological setting – In the first 500 m of sediments accumulated since the Pleistocene, developed a multi-layer aquifer system that in the study area is characterized by an upper hydro-stratigraphic unit, named A, and a lower unit, named B (Figure 17c). The upper A unit belongs to the Sintema Emiliano-Romagnolo Superiore (AES) and is made of four main aquifer complexes, from A1 to A4. The deeper hydro-stratigraphic unit (B), also made of four different complexes (from B1 to B4), belongs to the Sintema Emiliano-Romagnolo Inferiore (AEI), the oldest part of the Supersynthem. This multi-layer aquifer system is characterized by sediments deposited during transgressive and regressive stages: the aquifers are mainly constituted by sandy layers, while the aquitard by silty-clayey layers. The recharge area is located in the thick coarse Apennine foothills as well as in the beds of the major rivers crossing the plain (Farina *et al.,* 2014).

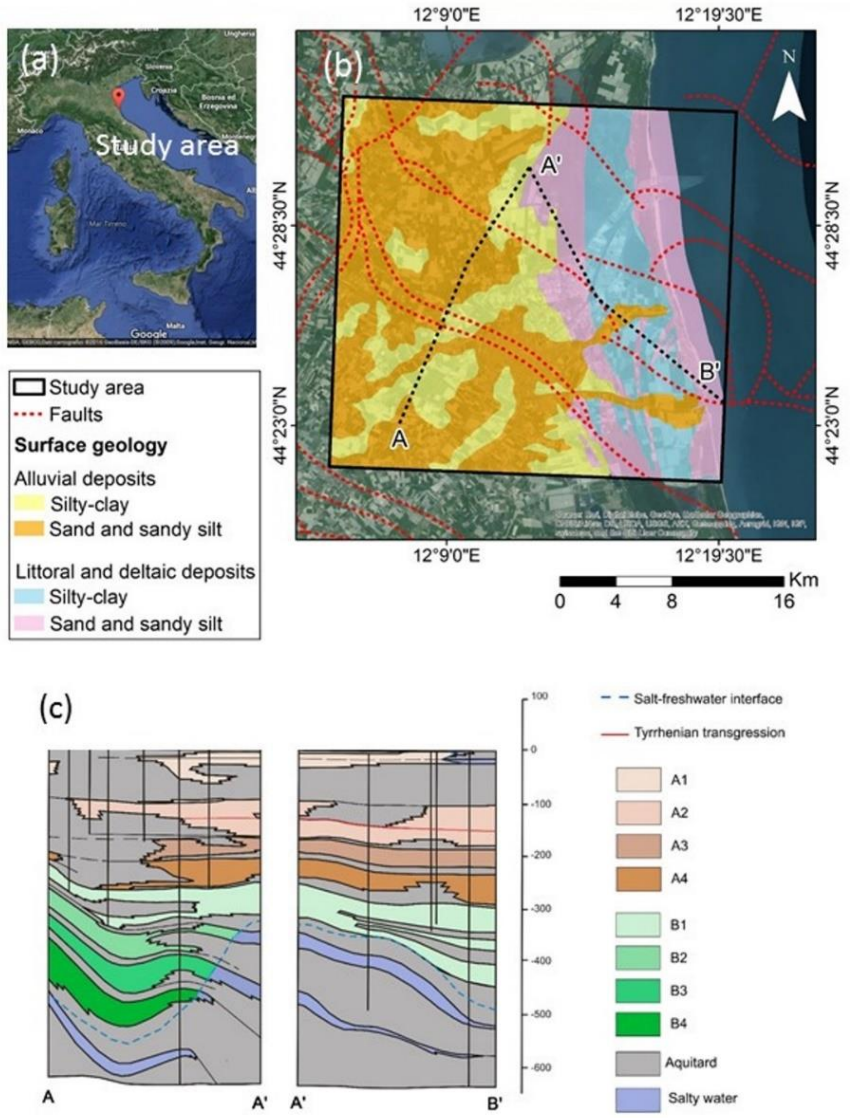

Figure 17. (**a**) Location of the study area. (**b**) Geological setting of the study area (CARG from Emilia Romagna). (**c**) Hydro-geological sections; their location is reported in Figure 1.c. (redrawn from AGIP, Regione Emilia Romagna, 1998).

4.4. Piemonte Region (Italy)

The Piemonte Region, located in northwest Italy, has an extension of 25,000 km^2. The wide area of the Piemonte Region has been chosen to assess the applicability of the methodology to detect ground motion areas at large scale.

Geological setting **–** It is characterized by different geological contexts such as Alps, Apennines, Langhe and Monferrato and Plain. In particular, the study area is located in the Alps domain and in

the Torino hill context. The Alps are characterized by high slope gradients and the presence of foliated and massive rocks, meanwhile in the Torin hill, the slopes in the argillaceous and marly successions are mantled with 1 to 6 m thick clayey-silty colluvial deposits. More than 30.000 slope instabilities were previously identified in the framework of the SIFraP project (Landslides information system in Piemonte). The alpine environment is mainly characterized by the presence of rock-falls/topples, large complex landslides and deep seated gravitational deformations. The Torino hill is mainly affected by rotational/translational slides, shallow rapid flows, slow flows and complex landslides.

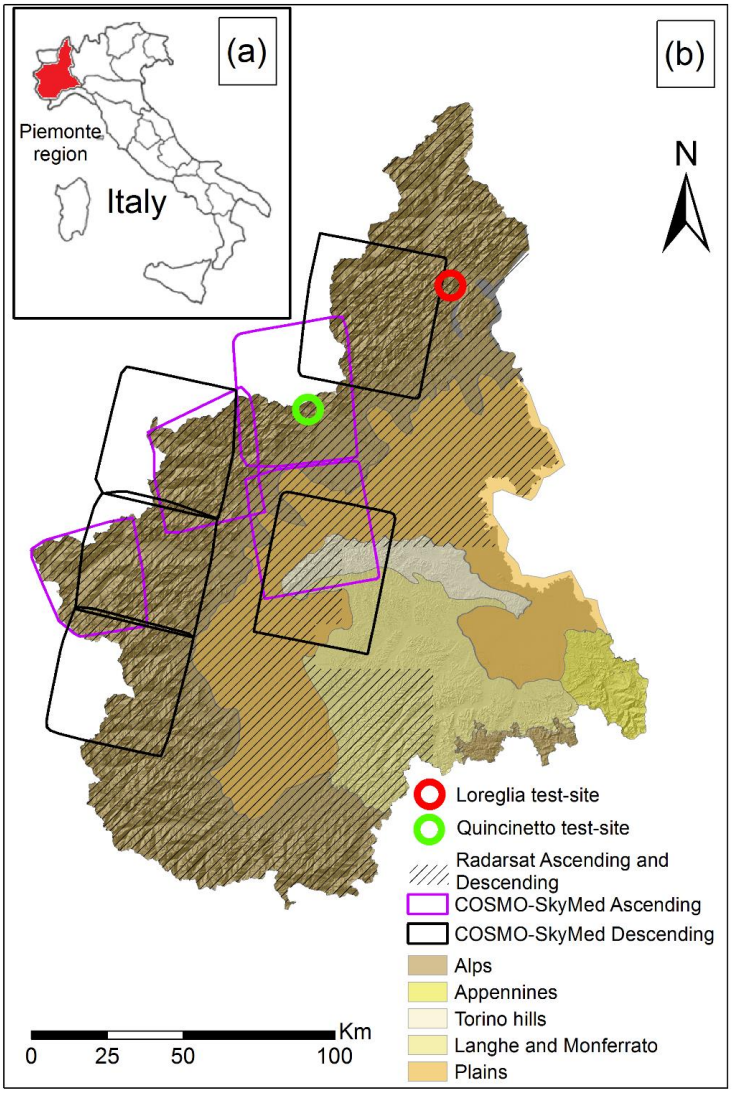

Figure 18. (**a**) Location of the study area. (**b**) Geological contexts in the studied area and location of the available SAR images acquired by RADARSAT and COSMO-SkyMed sensors that will be described in Section 6.3.

4.5. Alto Guadalentín Basin (Spain)

The Guadalentín Basin is located in the Murcia Province, southeast Spain and it has an extension of 277 km^2 (Figure 19). The area was chosen since that it recordered the highest subsidence rates measured in Europe (>10 cm/yr) in 2011, as a direct consequence of long-term aquifer exploitation. In the area, urban sites are located, but the agricultural lands are the land use prevalent.

Geological setting – It is filled by Neogene-Quaternary sediments transported by the Guadalentín River along an intramontane depression located in the eastern part of the Baetic Cordillera, which is an ENE-WSW-oriented alpine orogenic belt resulting from the ongoing convergence of the African and Iberian plates (Bourgois *et al.,* 1992). The Guadalentín is a tributary river of the Segura River and forms the Alto and Bajo Guadalentín sub-basins, where Lorca City developed (with approximately 100,000 inhabitants). The basin is mainly filled by Quaternary alluvial fan systems that overlap with Tertiary deposits that are mainly composed of conglomerate and calcarenite sediments that outcrop at the border of the basin. The prevailing NE-SW-oriented Alhama de Murcia Fault (AMF) crossing along these deposits (Figure 1a) represents the main active fault system of the study area (Martínez-Díaz et al., 2012). Underneath this sequence of materials, preorogenic deposits are present, which are composed of Paleozoic metamorphic complexes (IGME, 1981).

Hydrogeological setting – The Alto Guadalentín aquifer system is composed of Plio-Quaternary detrital and alluvial material, including clays, sands and conglomerates with clay and/or silt matrices; Miocene detritical with conglomerate and sand deposits; and local Triassic carbonate rocks. The Mesozoic marl and marl with intercalated sand and conglomerates represent the lower impermeable limit. The metamorphic substratum exhibits a horst and graben arrangement (Cerón and Pulido-Bosch, 1996); therefore, the depth of the impermeable limit varies within the region. In proximity of the East and West Basin borders, Tertiary deposits reach 400 m deep.

In the N-E sector, the Alto Guadalentín aquifer is laterally linked to the multi-layer aquifer system of the Bajo Guadalentín aquifer. The transition zone between the two aquifers is characterized by thick clay layers that lose lateral continuity towards the Alto Guadalentín; therefore, locally semi-confined aquifers can be found in this zone.

Since 1960, agricultural development has led to the exploitation of the aquifer system, which resulted in the aquifer being declared temporarily overexploited in 1987 (CHS, 2006). Although in the past, the piezometric level was close to the surface and artesian wells were exploited, groundwater drawdown became apparent in 1972 (Cerón and Pulido-Bosch, 1996).

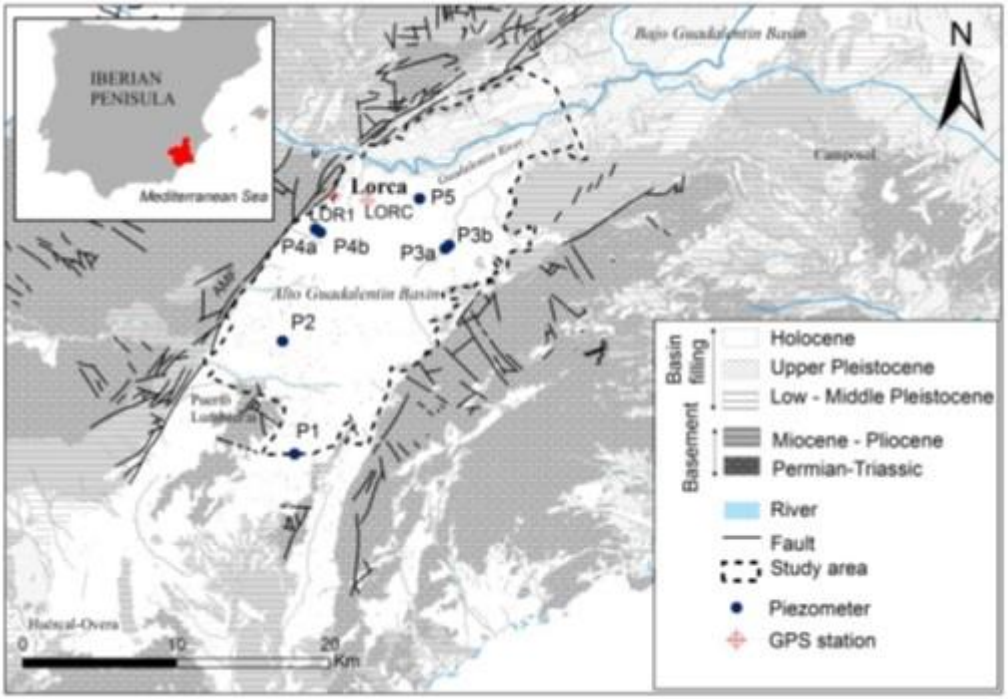

Figure 19. Geological setting of the Guadalentín Basin (redrawn from Martín *et al.,* 1973); piezometers and GPS sites used in this study area are also reported.

4.6. London Basin (United Kingdom)

The London Basin covers an area of ~2,500 km^2 in southern England (Figure 20). Ground motion induced by groundwater level change were previously recognized London Basin was chosen to model ground motion due to groundwater level change; by applying 1D model, since the large availability of geological, hydrogeological and geotechnical data and being an area of relevant interest. The London Basin is an a densely urbanized area, where, London, the capital and largest city in United Kingdom, is located.

Geological setting – The basin overlies the London platform formed of Palaeozoic basement which is bounded to the south by the Variscan Front (Royse *et al.* 2012). The Chalk Group, which reaches thicknesses of over 200 m in central London forms a rim around younger Palaeogene deposits which infill the London Basin (Ford *et al.* 2010; Mathers *et al.* 2014). The Palaeogene strata which overlie and confine the chalk have a variable lithology and form a broad flat valley through which the River Thames flows. The Palaeogene deposits comprise, the Thanet Formation, a fine-sand unit; the Lambeth Group consisting of vertically and laterally variable sequences mainly of clay with

silty and sandy horizons; the Harwich Formation a silty, sandy clay with gravel beds, and; the London Clay Formation, a dense fissured clay (Sumbler *et al.* 1996; Ellison *et al.* 2004). Quaternary deposits, primarily river terrace deposits associated with the River Thames and artificially modified ground, such as embankments or landfill and engineered cuttings and quarries provide a discontinuous cover at surface. The central London lies within a graben bounded by the Northern Boundary fault to the north and the Wimbledon-Streatham fault and the Greenwich fault to the south, where the chalk is downthrown by some 50 m.

Hydrogeological setting **–** The Chalk Group forms a principal aquifer in the London Basin supporting public water supply (Jones *et al.* 2012), industrial groundwater use such as ground source heating systems (Fry 2009) and significant baseflow to the River Thames (BFI 0.63). In the central area of the Basin, the chalk aquifer is confined by the overlying Palaeogene formations. The chalk aquifer is recharged on the interfluves - in the Chiltern Hills to the north and North Downs to the south, where the Chalk is present at surface and the aquifer is unconfined. The unconfined aquifer exhibits larger seasonal water table variations, with associated stream-head migration up dry periglacial valleys and where fracture sets exert strong linear river drainage patterns (Bloomfield *et al.* 2011).

The effects of faulting on the chalk aquifer and groundwater flow in the central London Basin has been highlighted in recent investigations (De Freitas 2009; Royse *et al.* 2012) whereby compartmentalisation of the chalk by faults and differential fault permeability leads to irregular groundwater flows and difficulties during dewatering. Both lithological variations and structural features exert significant control on aquifer properties in the Thames Basin (Bloomfield *et al.* 2011) and on the chalk in particular.

Historic overexploitation of the Chalk aquifer for industry and manufacturing up to the 1950s led to widespread lowering of groundwater levels, reaching a depth of up to 90 m below sea-level in the central London Basin (Jones *et al.* 2012). As a result, the Chalk aquifer became unconfined, leading to under-drainage and desaturation of the London Clay (Jones *et al.* 2012; Royse *et al.* 2012). In the 1950s a combination of aquifer depletion, improvements in surface water quality and water storage led to a decline in groundwater abstraction and a recovery of groundwater levels at a rate of up to 3 m/year (Jones *et al.* 2012). As groundwater recovery and re-saturation of the London Clay could potentially have negative impacts on the foundations of structures and infrastructure in the Basin, an action plan was developed by London Underground, Thames Water and the Environment Agency (EA), i.e. the GARDIT (General Aquifer Research Development and Investigation Team) strategy. As a result, an observation borehole network within the Basin was established by the EA to monitor and manage changes in groundwater levels. As a by-product of London's rising groundwater levels

an artificial recharge scheme was licensed in North London, NLARS (North London Artificial Recharge Scheme; Jones *et al.* 2012) to help control groundwater levels and maximise the available groundwater storage in the north part of the basin where groundwater levels were depleted (O'Shea *et al.* 1995, 1999).

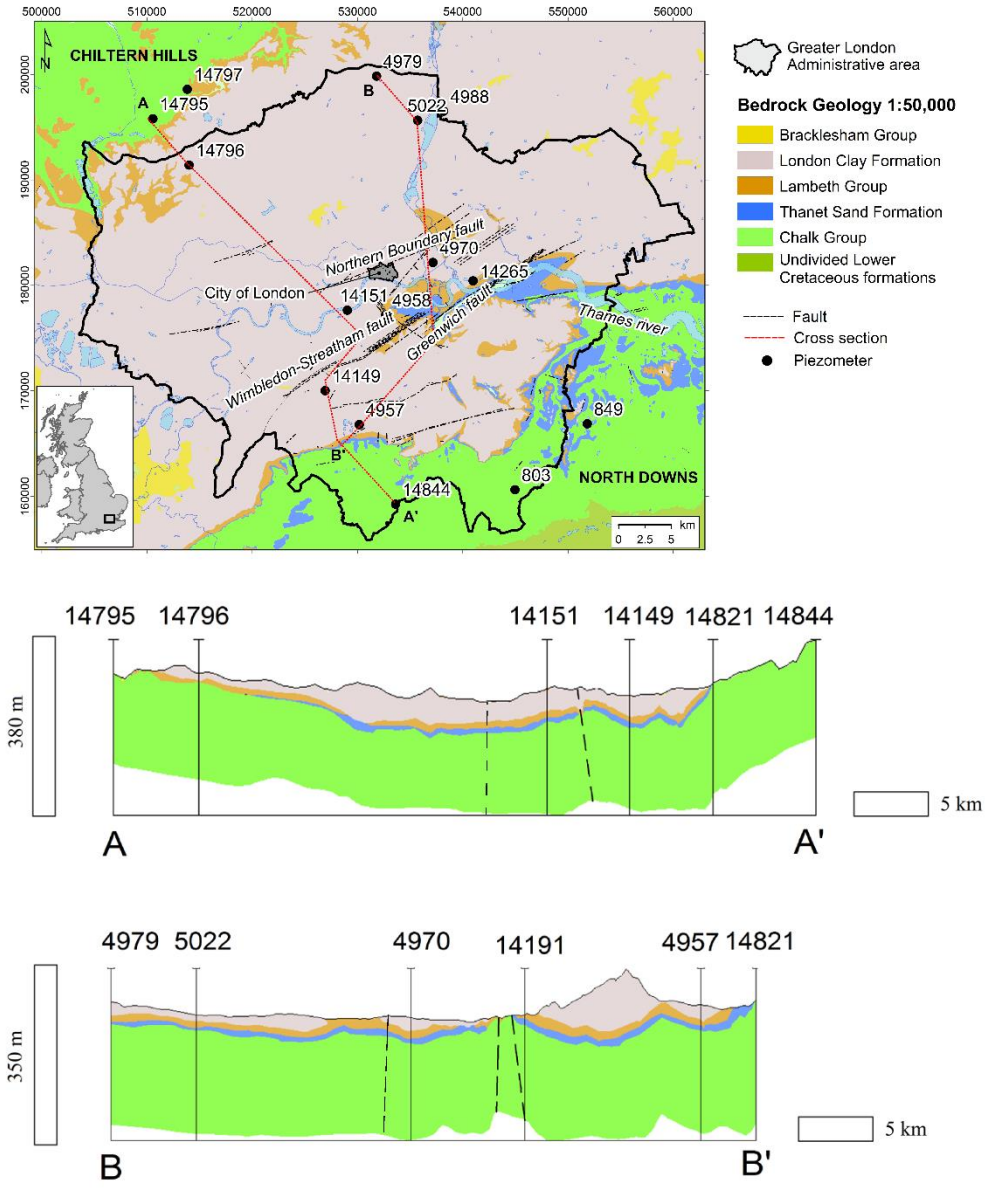

Figure 20. Geological setting of the study area with indication of water bodies and river network from the European Urban Atlas (EEA 2010). Geological materials © NERC. All rights reserved. Urban Atlas © Directorate-General Enterprise and Industry. British National Grid. Projection: Transverse Mercator. Datum: OSGB 1936.

Chapter V. Methodological approach

This Chapter is organized in three subsections that deal with the main objectives of the research: (i) the identification of ground motion areas, (ii) the identification of the driving mechanisms and (iii) the prediction of the development of the surface movements.

5.1. Ground motion areas identification

The first topic that has to be addressed in order to support decision making on policy, adaptation strategies and operational measures related to ground motion, is the collection of information on where the ground motion are located. Indeed, the identification of the ground motion areas learning from spatial and temporal patterns is fundamental to improve the knowledge about processes.

In this thesis, a novel methodology to analyse multi-sensors and multi-temporal A-DInSAR data for the geological interpretation of areas affected by ground motion is developed. Ground motion areas mapping represents a crucial aspect to identify areas where the attention of scientists has to be focused. In this context, the ambition of the work is to exploit the great potential contained A-DInSAR time series. The use of the entire time series to map the processes on the basis of their kinematical model fits with the last generation A-DInSAR time series acquired by COSMO-SkyMed and Sentinel-1 missions acting at very high spatio-temporal resolution and designed to investigate processes associated with rather fast dynamics.

The procedure consists of three main phases that has been implemented with open-source software. In the first phase, the vertical and E-W components of motion are disentangled, and a displacements time series (TS) accuracy assessment is performed. In the second phase, different statistic tests are applied in order to find the spatio-temporal pattern of the principal components of movement, and the kinematic model of the targets. The result of this step is the identification of areas with significant movement, so-called “ground motion areas”. Ground motion areas correspond to a cluster of a minimum 3 of PS, with a maximum distance of 50 meters, characterized by the same trends (linear, non-linear, seasonal). Ground motion areas do not have a geological significance, but the systematic procedure represents a useful and fast approach to detect sectors where A-DInSAR analysis detects spatio-temporal ground deformation, and where the attention of scientists has to be focused. Finally, the third step consists of a data fusion of the A-DInSAR data and the geological data to determine the

causes of ground motion processes. Multidisciplinary data, such as geotechnical, hydrogeological, and land use data, are fundamental to recognize ground motion mechanisms.

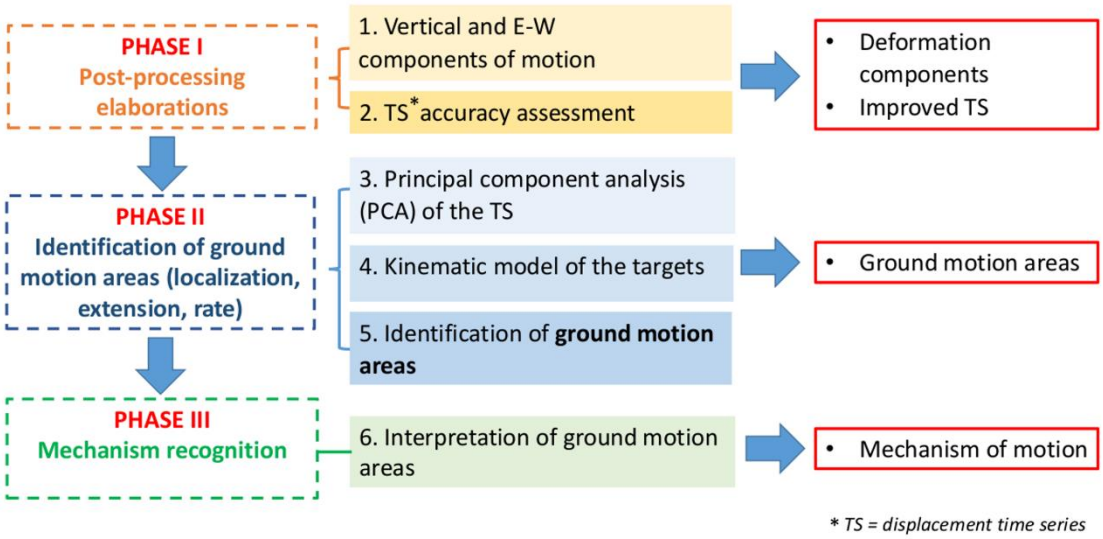

Figure 21. Flowchart of the methodological approach to detect ground motion areas

Figure 21 illustrates the proposed methodological approach, which consists of the following steps:

Step 1. Decomposition of the vertical and horizontal components of motion (Phase I). A-DInSAR techniques allow the obtaining of the average LOS velocities of targets. Smaller values of the satellite incidence angle (usually 23°–35°) make the measurements more susceptible to the vertical component of motion with respect to the horizontal; however, ignoring the horizontal components may implicate an over/under estimation of the deformation, leading to misinterpretation of the results. By the use of the datasets acquired in the ascending and descending modes, the vertical and horizontal components of target motion can be extracted using the following equations:

$$V_{EW} = \frac{(V_{desc}/h_{desc}) - (V_{asc}/h_{asc})}{(e_{desc}/h_{desc}) - (e_{asc}/h_{asc})} \quad (5.1)$$

$$V_{VERT} = \frac{(V_{desc}/e_{desc}) - (V_{asc}/e_{asc})}{(h_{desc}/e_{desc}) - (h_{asc}/e_{asc})} \quad (5.2)$$

V_{asc} is the average LOS velocity acquired in the ascending mode, V_{desc} is the average LOS velocity acquired in the descending mode, V_{VERT} is the vertical component of motion, and V_{EW} is the E-W component of motion. The e_{asc}, h_{asc} and e_{desc}, h_{desc} are the LOS directional cosines, respectively, for ascending and descending orbits. First, the average LOS velocity of each dataset was interpolated by an inverse distance weighted (IDW) approach, and, then, the component of motion was decomposed

using these interpolated maps. The method was previously used by several authors. If the horizontal component of motion is absent, the vertical component of motion can be extracted using the incidence angle (θ) of the dataset acquired in one mode (ascending or descending) using the following equation:

$$V_{VERT} = \frac{V_{asc,desc}}{\cos\theta} \quad (5.3)$$

Step 2. A-DInSAR displacement time series accuracy assessment (Phase I). The displacements time series detected by each target may be affected by local error or regional trends, which can be observed in the whole dataset. Therefore, post-processing analyses of the A-DInSAR data are fundamental in order to avoid misinterpretation of unreal ground movements. The check of the displacements time series is performed by selecting the most coherent (>0.9) targets with an average LOS velocity in the range ±0.5 mm/yr., where no significant movements are expected. More precisely, the approach proposed by Notti *et al.* (2015) was applied in order to correct problems due to phase unwrapping, regional unreal trends, and anomalous displacement detected on certain dates (i.e., unreal movements at the same time as meteorological events, such as snowfall).

Step 3. Principal component analysis (PCA) of the A-DInSAR displacement time series (Phase II). A-DInSAR measurements represent the cumulative ground movements (natural versus anthropic, superficial versus deep displacements, multi-year, and seasonal components); the overlapping of several ground motion components may make the accurate interpretation of ground deformation processes difficult. Recent studies have applied PCA to satellite-based time series analysis to detect spatio-temporal deformation patterns.

Here, principal component analysis (PCA), implementing a matrix organization of location versus time (T-mode), was performed in order to decompose the long-term (multi-year) and the seasonal components of ground motion. A matrix, in which each column contains the LOS displacements for each SAR image, and where each row contains the displacement time series of the targets (PS-DS), was formed. The main outcomes are the correlation and covariance matrices, the eigenvalues and eigenvectors, the percent variance that each eigenvalue captures, and the principal component (PC) score maps. In interpreting the principal components, PC scores related to each observation (PS-DS) are useful for knowing the correlations with the principal components in the whole dataset; the higher values correspond to higher correlations with the analysed PC. To detect the displacement time series of the PC, the displacement time series can be multiplied for the PC eigenvectors of each SAR image date.

Step 4. Identification of the kinematic model of the targets (Phase II). A-DInSAR data proves to be efficient for the estimation of linear and non-linear ground motion movements. Hence, automated

classification of displacement time series (TS) in large datasets are needed for TS interpretation at a regional scale. Here, an automatic sequential procedure, based on statistical tests, the PS-time program implemented by Berti *et al.* (2013), was used to classify the TS into one of three predefined target trends that are: uncorrelated, linear, and non-linear. The program permits the detection of the date (break) where abrupt changes in slope in the non-linear TS are recorded. This tool also assigns an additional parameter to the non-linear TS, called index "BICW", related to the bi-linearity of the TS (i.e., TS that records BICW higher than 1.2 indicates a strong bi-linearity)

Step 5. Identification of "ground motion areas" (Phase III). This task aims at detecting ground motion areas in order to focus the interpretation on significant sectors. Physical processes can be characterized as linear, non-linear, and seasonal ground movements. While the average velocity of targets with a linear trend is useful to separate movement and non-movement areas, the same parameter is not efficient for recognizing ground motion areas affected by non-linear and seasonal movements. Even targets with an average LOS velocity in the stable range (±1.5 mm/yr.) can be affected by significant seasonal and/or non-linear movements. Taking into account that non-linear and seasonal movements may cause considerable damage to buildings and infrastructure, PCA results were exploited to identify ground motion areas with linear, non-linear, and seasonal trends. The ground motion areas were identified using a spatial cluster of significant PC scores. First, we define the threshold of the PC scores by applying a statistical inspection of the PC score frequency distributions. If the histogram of the PC scores shows a normal distribution (skewness = 0), we consider the threshold equal to twice the standard deviation, while, if the PC scores shows asymmetrical distribution (skewness ≠ 0), the threshold is defined as being equal to the interquartile range (IQR). Then, PS-DS with PC scores higher than the threshold are selected, and a buffer zone of 50 m around the detected measuring points can be derived.

Therefore, ground motion areas consist of clusters of a minimum of 3 PS-DS with a maximum distance of 50 meters. The approach to extracting ground motion areas is based on the procedure proposed by Meisina *et al.* (2008), but, herein, the delineated areas are derived from the PCA analysis (Figure 22). The ground motion areas are not found on the basis of unstable velocity; hence, even seasonal and non-linear processes can be identified and taken into account for the interpretation of displacement time series. Following this, the kinematic model of the targets is combined with the ground motion areas in order to distinguish linear and non-linear processes. More precisely, the TS with BICW higher than 1.2 are selected to distinguish non-linear TS from the linear ground motion areas.

Step 6. Interpretation of "ground motion areas" (Phase III). Once the ground motion areas have been identified, the processes are interpreted by integrating them into a Geographical Information System (GIS) with ancillary data (such as geological, geotechnical hydrogeological, compressible thickness map, digital orthophoto, damaged buildings distribution). Mechanism recognition is based on cross-comparison of the representative subsoil geological profiles, and the relative displacement time series with multidisciplinary information. Analysis of the breaks and the detection of the deceleration and acceleration periods are crucial to correlate the processes with the triggering mechanisms. The final outcome is the attribution of driving-force systems and triggering mechanisms to ground motion areas.

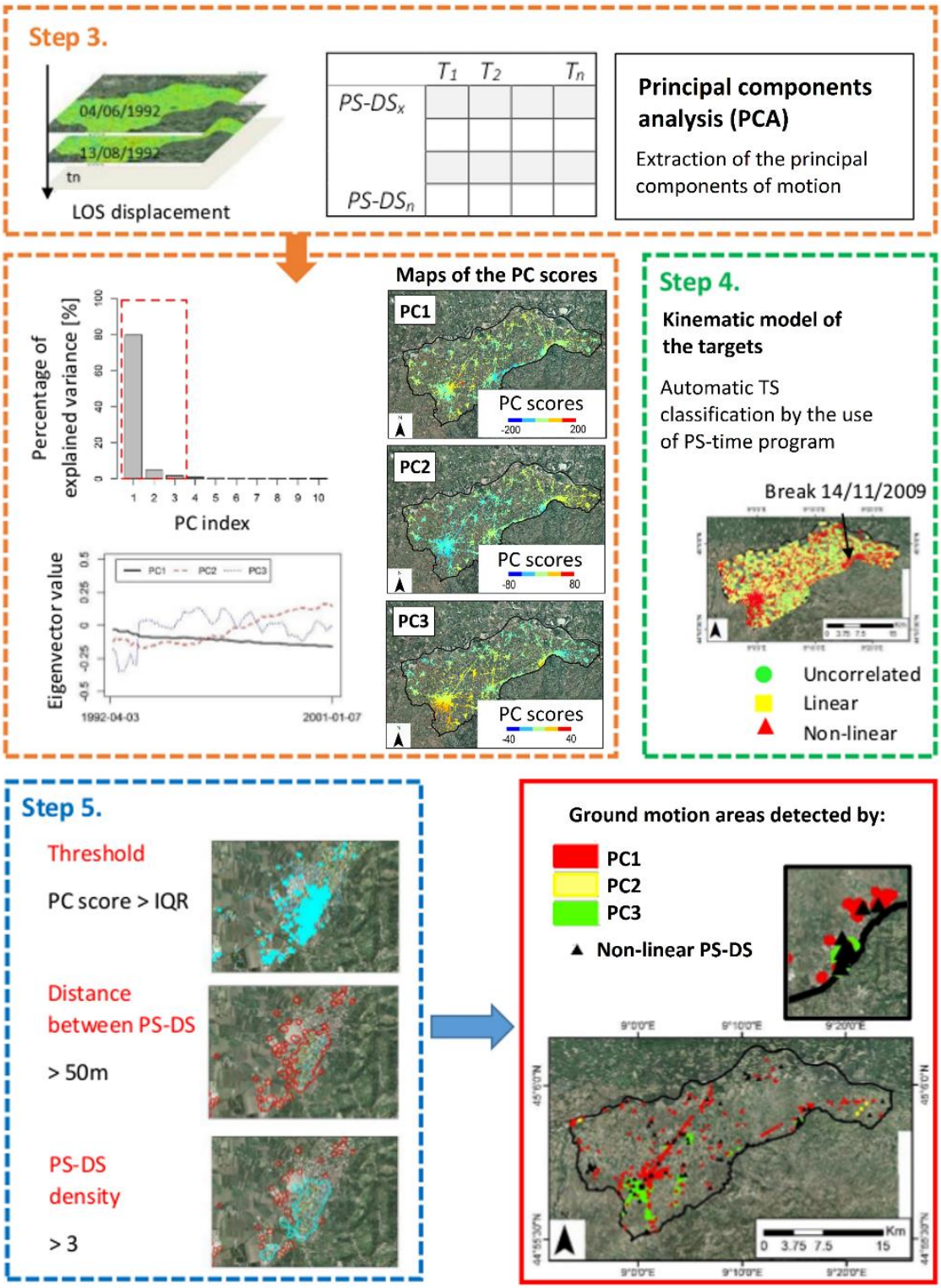

Figure 22. Flowchart of the phase II in the methodological approach, to identify ground motion areas.

5.2. Mechanism of ground motion

The ground motion can be induced by a wide variety of natural and anthropic drivers. In many cases, the ground motion evidences are the result of superimposed processes that acts at different spatio-temporal scale that makes it difficult to discern the contribution of the different processes and to evaluate the associated triggering factors. The complexity of the mechanism recognition requires a multidisciplinary approach including the experience of geotechnical engineers, hydrogeologists, geotechnical.

In this chapter, the analysis of the mechanisms is structured in three main phases, described in the following sections:

1. Data collection;
2. Geostatistical analysis;
3. Cross-comparisons.

5.2.1. Data Collection

The first step consists in the collection of ancillary data about the geological, hydrogeological and geotechnical setting. All the input datasets are imported and referred to a common reference system and projection by using a Geographic Information System (GIS) environment, which allows the overlap of the data. The available information of the geological model, the hydrogeological and geotechnical data are listed for each study area, in table 6. It worth noting that in some cases, the restricted availability of ancillary data (i.e. continuous monitoring of the piezometric level variations) limited the number of the possible factors to analyse and the interpretation of the ground motion.

Table 6. List of the available data for each study area.

Oltrepo Pavese (Italy)
Geological model: ▪ Geodatabase that includes 700 water wells drilled until a maximum depth of 216 m; 178 drilling boreholes until 55 m in depth; and 20 trenches until 5 m in depth. ▪ Thickness map of the upper clayey-silty deposits elaborated by Pilla *et al.* (2007) by interpolating the thickness data available from around 490 water wells, performed in the Oltrepo Pavese. *Hydrogeological data:* ▪ Thickness of the unsaturated zone in October 2005 (Pilla *et al.*, 2007) *Geotechnical data:* ▪ Engineering geological units' map implemented by Meisina *et al.* 2006 that summarize the geotechnical properties of the first 15 m of depth. The map was implemented by the analyses of penetrometer results (176 Dynamic Cone Penetration Test, 20 Standard Penetration Test and 266 Cone Penetration Test), calibrated against soil profile logs.
The valley bottom of the Oglio river
Geological model: ▪ Geodatabase building by the use of drilling boreholes for geological survey. *Hydrogeological data:* ▪ Scarcity of data. *Geotechnical data:* ▪ Scarcity of data.
Ravenna
Geological model: ▪ Geodatabase provided by Emilia Romagna Region. *Hydrogeological data:* ▪ Groundwater levels provided by ARPA Emilia Romagna. *Geotechnical data:* ▪ Geodatabase provided by Emilia Romagna Region.
Piemonte region
Geological model: ▪ Geodatabase provided by ARPA Piemonte. *Hydrogeological data:* ▪ Geodatabase provided by ARPA Piemonte. *Geotechnical data:* ▪ Geodatabase provided by ARPA Piemonte.
Alto Guadalentín Basin
Geological model: ▪ Collection of stratigraphic columns information from water wells and geodatabase building. ▪ Computation of soft soil thickness map. *Hydrogeological data:* ▪ Groundwater levels provided by the Geological Survey of Spain (IGME). *Geotechnical data:* ▪ Scarcity of data.
London Basin
Geological model: ▪ 3D geological model provided by the British Geological Survey (BGS). *Hydrogeological data:* ▪ Groundwater levels acquired by more than 200 piezometers during the period from 1990 to 2000, and provided by the Environment Agency. *Geotechnical data:* ▪ BGS GeoSure dataset that provides information about potential natural ground movement resulting from collapsible deposits, compressible ground, landslides, running sand, shrink-swell and soluble rocks, by using A (lowest) to E (highest) ratings for each of these six geohazards (BGS 2014). ▪ The Volume Change Potential (VCP) and plasticity index (I_p) of the London Clay as estimated by Jones & Terrington (2011) based on the BGS National Geotechnical Properties Database and index test data for the London Clay outcrop.

Recent studies have focused on the investigation of relationships between the ground motion and the thickness of the compressible sediments (Tomas *et al.*, 2010; Bozzano *et al.*, 2015). In many cases, the thickness of the compressible sediments plays a key role for the magnitude and distributions of the movements due to groundwater level change. For this reason, after the collection of available lithological data from boreholes drilled in the study area, a GIS geo-database is built in order to include all the sampled lithological information. Then, for each borehole the total thickness of the silt and clay-type layers located over the main exploited aquifer. This value represents the thickness of sediments more susceptible to compaction (Figure 23).

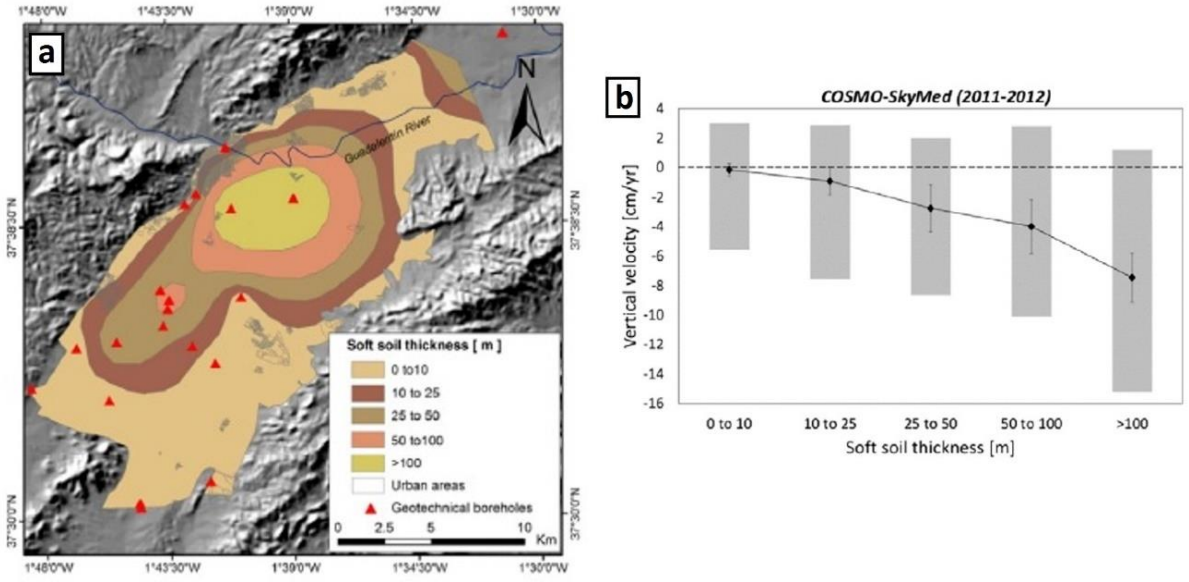

Figure 23. (**a**) Compressible thickness map and geotechnical borehole location. The thickness of the compressible deposits has been calculated by means of geotechnical borehole data. Urban areas are also reported. (b) Relationship between the soft soil thickness and the vertical deformation rates detected by the COSMO-SkyMed data.

In the Oltrepo Pavese, three additional data were considered to interpret the mechanisms of ground motion such as the land use change, the climatic overview and the database of damaged buildings. The effects due to the land use change were investigated by the use of the land Corine Land Cover changes (CLC) from 1990–2000 and 2000–2006, implemented by the Institute for Environmental Protection and Research (ISPRA) that match the available satellite data.

From the climatic point of view, the analyses of the drought periods were performed by extending the approach introduced by Meisina *et al.* (2003), using available measurements from 1960 and to match satellite observation time intervals.

Furthermore, the geodatabase of the damaged buildings was exploited. The geodatabase includes information (i.e. the date of the lesions, the adopted remediation, etc.) collected by Meisina *et al.* 2006, mainly referred to damages due to swelling/shrinkage of clayey soils.

Geostatistical analysis

It should be noted that the analysis the mechanisms depends on the availability of geological, geotechnical and hydrogeological data. Therefore, the estimation of unknown values at unsampled locations and the exploratory analysis of the dataset, it is fundamental to reach the spatial continuity of different parameters such as the thickness of compressible sediments and the groundwater level change. Geostatistics is the application of statistical methods to geo-referenced variables that provides accurate and reliable estimations of variables at locations where no measurements are available (Matheron, 1963). It allows the description of spatial patterns, the spatial interpolation and the modelling local of spatial uncertainty (Goovaerts, 1997).
Hence, an exploratory data analysis is performed and then the appropriate interpolation method is chosen to obtain the spatial continuity of the variable. Two interpolation method has been exploited in this thesis:

1.Ordinary Kriging; to create the thickness of compressible sediments map.

2. Inverse Distance Weighted (IDW); to create the map of the groundwater level.

The first one approach accounts for direction dependent variability (anisotropic spatial pattern) and for this reason was chosen for the interpolation of the soft soil thickness. Conversely, the second one is based on the principle that observations that are close to each other on the ground tend to be more alike than those further apart, hence observations closer to the sampling points should receive a larger weight. In this case, the interpolation model is not based on the direction dependent variability. The IDW approach was chosen for the interpolation of the groundwater level, since this variable did not highlight a clear direction dependent variability.

5.2.2. Cross-comparison

The spatial relationship between the ground motion and ancillary data have to be investigated in order to detect the reason for the movements. The initial analysis is performed by cross-comparisons between the average velocity detected by A-DInSAR data and the ancillary data. Then, the

examination of the time series information can give a better understanding of the timing of the movements and help the identification of correlations with the ancillary datasets.

Taking into account that the ground motion areas detected by means of the A-DInSAR analysis, described in Section 5.1, include temporal information about the movements, the cross-comparisons between these and the ancillary data can directly provide spatio-temporal information about the mechanisms. As shown in figure 24, the ground motion distribution of the seasonal movements detected by PC3 of Radarsat data acquired in Oltrepo Pavese is well correlated with areas characterized by phreatic condition of the aquifer.

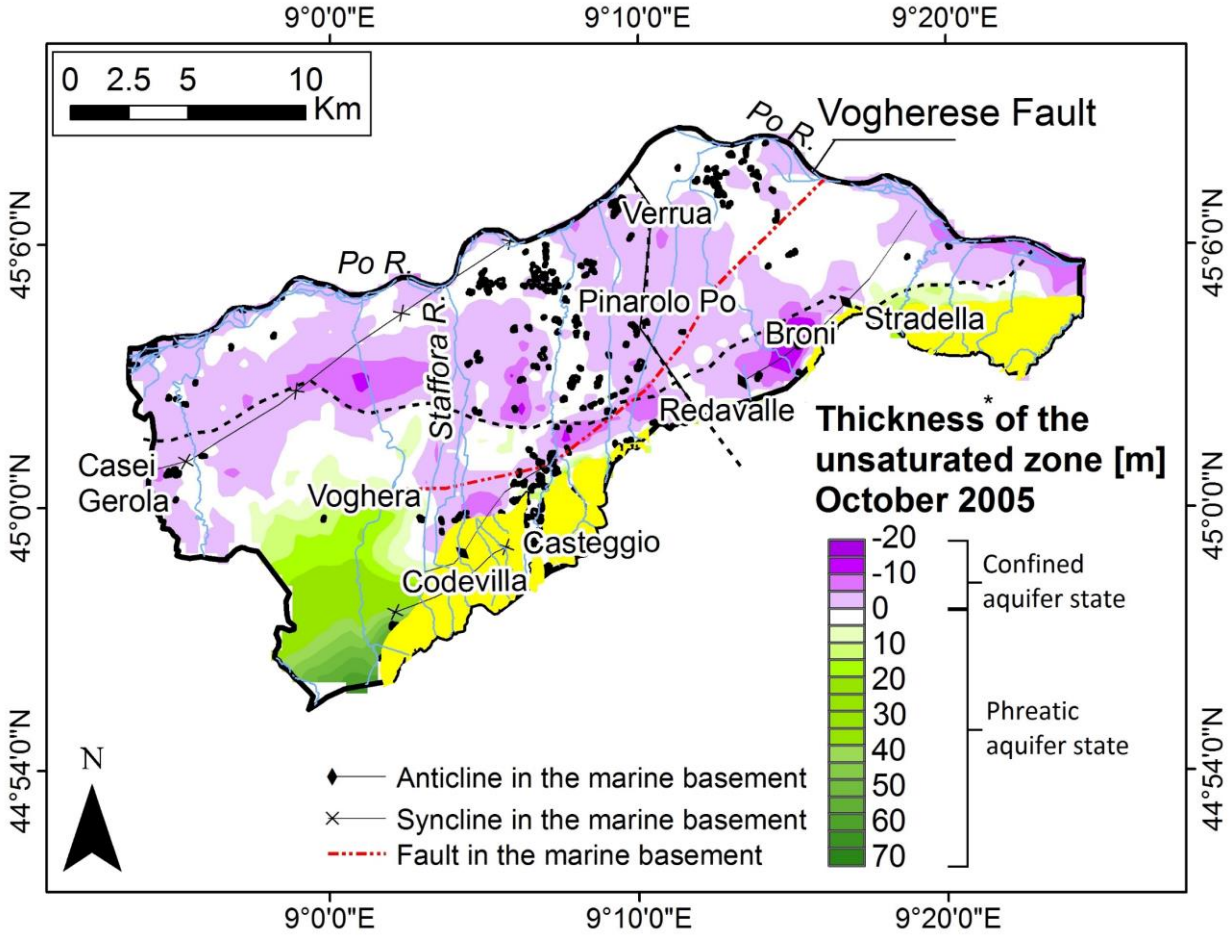

Figure 24. Example of cross-comparisons between the ancillary data, such as, the thickness of the unsaturated zone in October 2005 (modified from Pilla et al., 2007), and superimposed ground motion areas detected via PC3 of the Radarsat data (black box) in the Oltrepo Pavese. The pre-Würmian deposits are represented in yellow.

The information obtained by the ground motion detection can be analysed to recognize the mechanisms of ground motion. Furthermore, the procedure includes cross-comparisons with different factors as performed by Tomas *et al.* (2010b) and described in Section 1.1.2. In particular, the A-

DInSAR measurements have been compared with three independent both spatially and temporally factors:

- Geological factors (i.e. geological age and lithologies, soft soil thickness);
- Hydrogeological factors (i.e. piezometric levels of different aquifer layers);
- Geotechnical factors (i.e. engineering geological unit map).

5.3. Modelling ground motion caused by groundwater level change

The third objective of the work is the integration of the A-DInSAR data with numerical models. Several studies were previously performed on the modelling of ground motion using A-DInSAR data, as described in Section 1.1.3. Here, the ground motion changes due to groundwater level variations are simulated with the 1D model as applied by Tomás et *al.* 2010a and Ezquerro *et al.* 2014.

The ground motion response to hydraulic head changes were simulated at nine piezometers located in the London Basin (United Kingdom). The model was used to characterise the relationship between groundwater level and ground motion time-series data to assess the contrast in ground motion across different geological units and in different aquifer conditions.

The 1D model assumes that the aquifer pore pressure instantaneously equilibrates with piezometric level changes in the aquifer and any time-lag between the piezometer level variations and the compaction of the geological layers is not accounted for. Therefore, firstly a visual inspection of the relationship between the ground motion and groundwater records for boreholes is necessary to assess that the assumption can be made. The inspection is focused on the stress-strain analysis as described in Section 2.3. Then, it is fundament to compute the storage coefficient *S.* More precisely, the storage coefficient *S* or storativity represents the amount of water stored or released per unit of area of the aquifer and per unit head change. In the saturated zone, the pressure head, acts on the aquifer skeleton and on the density of the water in the pores. When the pressure increases, the aquifer skeleton expands, whilst if it decreases, the aquifer skeleton compacts (Sneed & Galloway 2000). If the water pressure is reduced, water is released from storage in response to expansion of the water in the pores and compaction of the aquifer-system. Therefore, the aquifer-system storage coefficient *S* is defined as (Galloway *et al.* 1998):

$$S = S'_k + S_k + S_w = S_k^* + S_w \quad (5.4.)$$ (Galloway *et al.* 1998)

Where S'_k and S_k are the skeletal storage of the aquitard and the aquifer, respectively, while S_w is the water storativity. S_k^* is the aquifer-system skeletal storage. Two aquifer-system skeletal storages, S_{ke} and S_{kv}, can be defined for the elastic and inelastic ranges of stress, respectively. The coarse-grained sediments in aquifer-systems deform elastically while the fined-grained sediments that consist on the confining aquitards may deform both elastically and inelastically.

In confined aquifers, even if the head drops and water is released from storage, the aquifer remains saturated. In this case, the storage coefficient can be defined as:

$$S=S_s \times b=(\rho_w \times g)(\alpha+n\beta)b \qquad (5.5.)$$ (Jacob 1940; Cooper 1966)

where S_s is the specific storage, b the thickness of the saturated aquifer, ρ_w the water density, g the acceleration of gravity, α the aquifer skeleton compressibility, n the porosity and β the fluid compressibility (approximately of 4.9×10^{-10} Pa^{-1}).
Note that, in compacting aquifer systems $S_k^* >> S_w$ and, assuming that S_w is negligible (Poland 1984) the storage coefficient is approximatively equal to the skeletal storage coefficient: $S \approx S_k^*$

Similarly to the methodology that other authors have implemented for different aquifer-systems (Hoffmann *et al.* 2003; Bell *et al.* 2008, Tomás *et al.* 2010, Chaussard *et al.* 2014), the relationship between the hydraulic heads changes and the vertical ground motion changes can be applied to compute the storage coefficient:

$$S=S_k^*=\Delta d/\Delta h \qquad (5.6.)$$ (Hoffmann *et al.* 2001)

Where Δd is the vertical displacement as estimated by the satellite data, and Δh is the hydraulic head change. Note that this equation assumes that ground deformation is only vertical, hence the approach can be applied in areas where the horizontal displacements are not significant.
Therefore, in this thesis, the ground motion changes due to groundwater level variations were simulated with the inversion of the of Equation (5.6.) introduced by Hoffmann *et al.* (2001) and the simulated displacements were quantified by the Equation (5.7.):

$$\Delta d=S\times\Delta h \qquad (5.7.)$$ (Tomás et al. 2010).

Furthermore, the aquifer state and geological interval over which the change in piezometric head occurred was determined for each piezometer. In doing so the spatial correlation between storage coefficient and aquifer condition is further assessed.

Chapter VI. Results

6.1. Methodology for detection and interpretation of Ground Motion Areas with the A-DInSAR time series analysis

Roberta Bonì[1*], Giorgio Pilla[1] and Claudia Meisina[1],

[1]Department of Earth and Environmental Sciences, University of Pavia, Via Ferrata 1, 27100 Pavia, Italy;

roberta.boni01@universitadipavia.it; giorgio.pilla@unipv.it; claudia.meisina@unipv.it.

[*]Correspondence: roberta.boni01@universitadipavia.it; Tel.: +39 0382985842

The paper has been published in the Special Issue "Earth Observations for Geohazards" of the Remote Sensing journal, 2016.

doi: 10.3390/rs8080686

Abstract: Recent improvement to Advanced Differential Interferometric SAR (A-DInSAR) time series quality enhances the knowledge of various geohazards. Ground motion studies need an appropriate methodology to exploit the great potential contained in the A-DInSAR time series. Here, we propose a methodology to analyze multi-sensors and multi-temporal A-DInSAR data for the geological interpretation of areas affected by land subsidence/uplift and seasonal movements. The methodology was applied in the plain area of the Oltrepo Pavese (Po Plain, Italy) using ERS-1/2 and Radarsat data, processed using the SqueeSAR™ algorithm, and covering time spans, respectively, from 1992 to 2000 and from 2003 to 2010. The test area is a representative site of the Po Plain, affected by various geohazards and characterized by moderate rates of motion, ranging from –10 to 4 mm/yr. Different components of motion were recognized: Linear, non-linear, and seasonal deformational behaviors. Natural and man-induced processes were identified such as swelling-shrinkage of clayey soils, land subsidence due to load of new buildings, moderate tectonic uplift and seasonal ground motion due to seasonal groundwater level variations.

Keywords: A-DInSAR; land subsidence; expansive soils; time-series analysis; principal component analysis; Oltrepo Pavese; Po Plain.

1. Introduction

Land surface dynamics can be the evidence of different processes (i.e., swelling/shrinkage of expansive soils, aquifer-system compaction, tectonic movements, consolidation due to the load of new buildings) of natural and anthropic origins. In many cases, the movements are due to the complex interactions of multi-driving forces, which act at various spatial and temporal scales [1-3]. The interference and/or overlap makes the effective decomposition of the components of motion difficult. For this reason, only a few authors have performed the decomposition of multi-driving force processes that trigger surface movements [4,5].

The areas affected by displacements need effective identification methods, semi-continuous spatio-temporal surface deformation monitoring and mechanism recognition analysis, in order to adopt the appropriate risk mitigation strategies, and to develop a sustainable management of natural resources.

Advanced Differential Interferometric SAR (A-DInSAR) is a powerful remote sensing tool, capable of mapping displacements over wide areas at very high spatial resolutions. The technique is based on the processing of multiple interferograms derived from a large set of SAR images in order to obtain a displacement time series, along the line of sight (LOS) of the satellite, of radar targets on the Earth's surface [6-8]. To date, several studies have documented the application of A-DInSAR data to monitor and to improve knowledge regarding different types of land surface dynamics [9-11].

Up to now, geohazard-mapping methodologies are mainly based on the visual inspection of average LOS velocity, such in the case of the ground stability areas in the framework of the PanGeo project [12], or in hotspot analysis and hotspot and cluster analysis of average LOS velocity to detect slow-moving landslides [13,14].

Most of the studies aimed at identifying the areas affected by ground motion, at regional scale and local scale, were focused on the average rates of displacement detected by the A-DInSAR technique [15-17]. Meisina et al. (2008) [16] implemented a systematic methodology to identify anomalous areas selected on the basis of the average LOS velocity, and Peduto et al. (2015) [17] introduced the average LOS velocity by weighting the radar target values on their coherence value. Both methodologies were mainly based on the average LOS velocity analysis, constrained by the fact that previous A-DInSAR data allowed the obtaining of noisy time series that difficult to interpret, showing some limitations in the distinguishing of ground deformation due to different processes, or to detect shallow deformations caused by seasonal processes.

Taking in to account the recent improvements of A-DInSAR data acquired by the COSMO-SkyMed satellites, and the current ESA Sentinel missions, which act at higher spatial and temporal resolution, it is necessary to develop an appropriate methodology to analyse extremely large datasets that consist of an enormous amount of measuring points.

The goal of this study is to present a novel methodology to analyse multi-sensors and multi-temporal A-DInSAR data for the geological interpretation of areas affected by land subsidence/uplift and seasonal movements. The approach is aimed at (i) improving the detection of ground motion areas; (ii) understanding the spatio-temporal evolution of ground motion areas; and (iii) supporting the interpretation of driving-force mechanisms. The proposed methodology is addressed to overcome limitations, such as the analysis of large data sets, by allowing exploitation of the great potential contained in A-DInSAR time series. In this paper, for the first time, ground motion areas are identified on the basis of their peculiar ground deformation behaviors.

The procedure was applied in the Oltrepo Pavese (Po Plain, Italy) by use of ERS-1/2 and Radarsat data processed using the SqueeSAR™ algorithm, and covering the time spans from 1992 to 2000 and from 2003 to 2010, respectively. The test area is a representative site of the Po Plain, characterized by various geohazards with moderate rates of motion. The obtained results are helpful for scientists and authorities in charge of land use planning in order to improve public safety and to assess the management of groundwater resources.

2. Study Area

The study area is located in the central area of the Po Plain, within the Oltrepo Pavese (Italy), covering an area of about 440 km^2 (Figure 1a). The plain of the Oltrepo Pavese is constituted by alluvial quaternary deposits, originating from the combined action of Apennine streams that form coalescent fans and of the Po River. These deposits overly the Miocene-Pliocene marine substratum, constituted by sandy-marls, sandstones, conglomerates, gypsy-marls, and calcareous-marls [18,19].

Three main geomorphological units composed of quaternary deposits were previously distinguished: Post-würmian alluvial deposits, würmian-holocenic alluvial deposits, and pre-würmian alluvial deposits [20,21].

The post-würmian alluvial deposits were sedimented by the most recent depositional activity of the Po River, and by the recent and present deposition from flooding events of the main Apennine streams. These deposits are localized in proximity to the Po River, and they are composed of sand, sandy silt, and silt. The deposits from the Apennine streams are characterized by gravel and sand. In general, post-würmian alluvial deposits contain a shallow phreatic aquifer with a water level near ground surface.

The würmian-holocenic alluvial unit is the most prevalent geomorphologic unit of the study area. These deposits are made up of alternating sand and gravel, with interbedded clays or argillaceous silt. A shallow phreatic aquifer and deeper aquifers, of both phreatic and confined types, were

distinguished in this unit. Deeply buried structures, consisting of a series of folds and fold-faults, shaped in the tertiary marine basement, have a direct control over aquifer geometry [22]. These alluvial deposits show the constant presence of a tabular clayey-silty cover, which acts as a seal, and limits water infiltration [21]. Groundwater exploitation of the Oltrepo Pavese is mainly derived from the aquifer contained in this unit.

Conversely, the pre-würmian unit, located in the southern part of the study area, consists of older fluvial terraces, and is constituted by gravel and sand with a silty matrix, characterized by lower permeability [19]. These deposits are strongly weathered and covered with clay soils. Locally, loess deposits overlap this unit. The depth of the water level in this unit reaches values up to 20 m in depth.

In the study area, quaternary sediment thickness decreases from west to east, with the minimum thickness and the outcrop of the marine substratum in correspondence with the Stradella thrust, evidence of the neotectonic activity that affects the area [23]. The distensive regime of the neotectonic activity supported higher alluvial sediments accumulation in the north-western sector of the plain with respect to the south-eastern sector [24]. The structural setting of the Oltrepo Pavese plain is conditioned by the presence of an important NE–SW tectonic discontinuity, known in the literature as the Vogherese Fault (Figure 1b) [25]. This tectonic lineament is a portion of the composite seismogenetic source called Rivanazzano-Stradella belonging to the Northern Apennines outer thrust front [26], which triggered an earthquake of Mw 3.94 ± 0.34 in 1971 [27].

From the climatic point of view, the plain area of the Oltrepo Pavese is characterized by a humid continental climate; with records of an average annual rainfall of around 700 mm. Two rainy seasons, with maxima in May and in October–November, have been detected by previous authors [28]. In the last two decades, the region has experienced many drought periods, such as from March 1989 to August 1993, and from May 1998 to September 2000 [28].

Here, the analyses of the droughts periods, performed by Meisina et al. (2003) [28] were extended from 1960 to 2010, using available measurements from 1960 and to match satellite observation time intervals. Therefore, climatic measurements acquired at the Voghera weather station were exploited, and the annual rainfall deficit was computed as the difference between the monthly water balance (difference between precipitation and potential evapotranspiration) and the average monthly water balance obtained for the period from 1960 to 2010. A significant drought period was identified from 2003 to 2007.

It is worth noting that the plain of the Oltrepo Pavese is characterized by discontinuous urban fabric, and 68% of the monitored area is covered by non-irrigated arable land [29]. The study area is a representative site of similar geological contexts in the Po Plain, where geohazards, due to natural and

anthropic factors, were previously recognized. Volume changes of clayey soils; shrinkage during drying periods, and swelling during wet ones, resulted in severe damage to overlying structures [30].

2.1. Engineering Geological Units

Recent investigations have been performed to investigate the geotechnical properties of the quaternary deposits in the first 15 m of depth of the Oltrepo Pavese plain. On the basis of the analyses of penetrometer results (176 Dynamic Cone Penetration Test, 20 Standard Penetration Test and 266 Cone Penetration Test), calibrated against soil profile logs, six geotechnical classes of non-cohesive soils (from I1 to I6) and four geotechnical classes of cohesive soils (from C1 to C4), have been previously distinguished [31].

Taking into account the geotechnical classification of these soils, eight engineering geological units were introduced in order to reduce the lithologic variability and to map the geotechnical behavior of representative and homogeneous geotechnical profiles (Figure 1b, c). Unit 1 represents the post-würmian alluvial deposit of the Po River, and is mainly constituted of non-cohesive soils (I3). Conversely, units 2, 3, 4 and 7 are würmian-holocenic alluvial deposits, characterized by cohesive soils. Unit 5 is composed of the alluvial fan of the Scuropasso River, and units 6 and 8 by the pre-würmian terraced deposits.

Figure 1b highlights the prevalent reported occurrence of damaged buildings [31], located over units 8 (34%) and 6 (29%), which correspond with pre-würmian deposits, and over units 5 (20%) and 4 (9%), which correspond, respectively, with the alluvial fan of the Scuropasso River and würmian-holocenic deposits, which are characterized by a high content of clay deposits that are susceptible to swelling–shrinkage processes due to the moisture changes in the dry–wet periods [31].

The majority of problems are experienced with single storey family residences, founded on conventional shallow strip, concrete footings, which generally extend to a depth of between 1 m and 2 m, below ground level [30]. In most of the cases, the remedial measures adopted were pile underpinnings, which had an economical incidence of 20% on the value of the house [30].

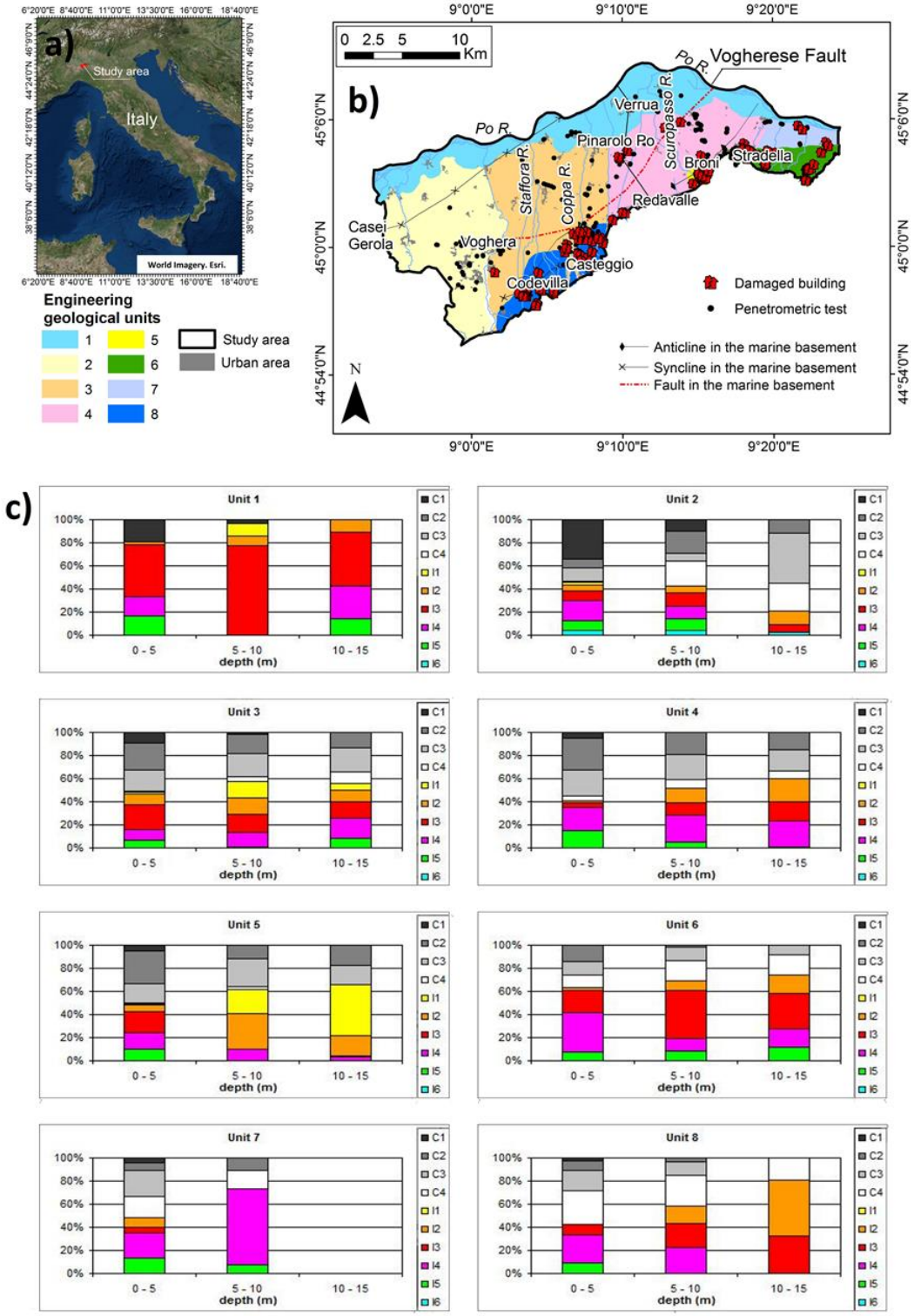

Figure 1. (**a**) Location of the study area. Sources: Esri, DigitalGlobe, Earthstar Geographics, CNES/Airbus DS, GeoEye, USDA FSA, USGS, Getmapping, Aerogrid, IGN, IGP, and the GIS User Community. (**b**) Distribution of the engineering geological units in the plain area of the Oltrepo Pavese. Damaged buildings, detected by Meisina et al. (2006) [31], are also reported. (**c**) Thickness percentage of the geotechnical classes in different depth intervals for each engineering geological unit.

3. Advanced DInSAR data

The Persistent Scatterer Interferometry (PSI) technique represents a class of the A-DInSAR techniques that uses radar targets on the Earth's surface to produce, starting from a set of images, the displacement time series along the line of sight of the satellite (LOS) of individual persistent scatterers (PS) [6]. The technique allows the obtaining of data regarding land deformation over wide areas with millimeter precision [6]. However, it has some limitations in rural areas due to low density of PS and phase ambiguities. A new algorithm, named "SqueeSAR™", has been developed in order to overcome this problem and to extract the deformation of distributed scatterers (DS), increasing the density of measuring points; and, for this reason, it was exploited to process the SAR scenes used in this work [32].

The input satellite data for this analysis consist of SAR images acquired by sensors operating in the C-band (wavelength, 5.6 cm; frequency, 5.3 GHz) onboard the ERS-1 and ERS-2 and Radarsat (RSAT) satellites. The scenes were acquired in the ascending mode, covering the time intervals from 9 July, 1992, to 2 August, 2000, and from 24 March, 2003, to 5 May, 2010. The dataset acquired in the descending mode covers the time intervals from 3 April, 1992, to 7 January, 2001, and from 28 April, 2003, to 5 January, 2009. The ERS-1/2 images were acquired with a nominal repeat cycle of 35 days, while the Radarsat images were acquired with a nominal repeat cycle of 24 days. These scenes were processed with the SqueeSAR™ technique by Tele-Rilevamento Europa (TRE). The algorithm allows the extraction of movement measurements, not only from traditional persistent scatterers (PS), such as anthropic structures or rocks, but also from distributed scatterers (DS), such as sparse vegetated areas [32]. This permitted to have a high density of A-DInSAR data over non-urban areas. The algorithm improved the quality of the displacement time-series; atmospheric effects can be better estimated and removed, and so the resulting time series are characterized by less noise. Available SAR images were processed with the SqueeSAR™ technique to identify acceleration and slowing of scatterers, in order to better observe the kinematic evolution of seasonal and non-linear processes.

The processing results have precision along the LOS, usually better than 1 mm/year, depending on the amount of available data, the local PS density (a key element in the estimation of spurious atmospheric phase components), and the distance from the reference point.

The geocoding accuracy of the PS locations is around +7 m in the eastern direction, and +2 m in the north–south direction, while the estimated accuracy of the elevation values was better than 1 m.

Additional details of the SAR datasets are summarized in Table 1. It has been possible detect more than 20,000 PS-DS over an area of around 430 km^2. It worth noting that, as explained in Section 2, the area is mainly characterized by non-irrigated arable land, which was classified by Plank et al. (2009) [33] as being not at all suitable for the A-DInSAR technique using the C-, X-, and L-band sensors. To

provide a quantitative assessment of the PS-DS density for this area, given the land use, the Corine Land Cover (CLC), which was implemented by the Lombardia region using colour and infrared orthophotos from IT2007 (made by Blom CGR - pixels 50 cm), and named "DUSAF 2007" [29] was exploited. More precisely, such analysis was carried out by selecting, respectively, PS and DS in the non-irrigable arable land (CLC code 211). The results reveal that the ascending scenes shows the PS density of 3.29 and 18.69 PS/km^2, respectively, for ERS-1/2 and Radarsat sensors. Conversely, the PS-DS densities for the same dataset are 20.74 and 39.42 PS-DS/km^2. In the case of the descending scenes, PS densities are 8.83 and 13.56 PS/km^2, respectively, for ERS-1/2 and Radarsat sensors, and the PS-DS densities for the same dataset are 37.63 and 29.10 PS-DS/km^2. By applying the SqueeSAR™ technique, an improvement of measuring-point density was obtained for the non-irrigable land. However, the PS-DS density for this land use coverage still shows low densities, which are comparable with values obtained using the PSI technique over the non-irrigable arable land in Britain [34]. Higher PS-DS density was detected in the continuous and discontinuous urban fabric (CLC code 11), and the road and rail networks and associated land (CLC code 122), which reach an average of 334.27 ± 43.57 and 137.35 ± 31.96 PS-DS/km^2, respectively.

Table 1. Details on the SAR datasets, their processing and results.

Satellite	**Orbit**	**Incidence angle**	**N° of scenes**	**N° of PS-DS**	**PS-DS density in study area [PS-DS/km^2]**	**PS-DS density for CLC code 11 [PS-DS/km^2]**	**PS-DS density for CLC code 122 [PS-DS/km^2]**	**PS-DS density for CLC code 211 [PS-DS/km^2]**	**Average LOS velocity [mm/yr]**
ERS-1/2	Asc.	22.1°	27	21,308	49	227.46	96.66	20.74	–0.2
ERS-1/2	Desc.	21.2°	79	32,917	76	367.77	149.40	37.63	–0.4
RSAT	Asc.	35.3°	89	34,503	79	369.09	172.32	39.42	–0.3
RSAT	Desc.	35°	84	27,273	63	322.76	131.03	29.10	–0.2

Asc.: ascending orbit, Desc.: descending orbit. CLC code 11: continuous and discontinuous urban fabric, CLC code 122: road and rail networks and associated land, CLC code 211: non-irrigated arable land.

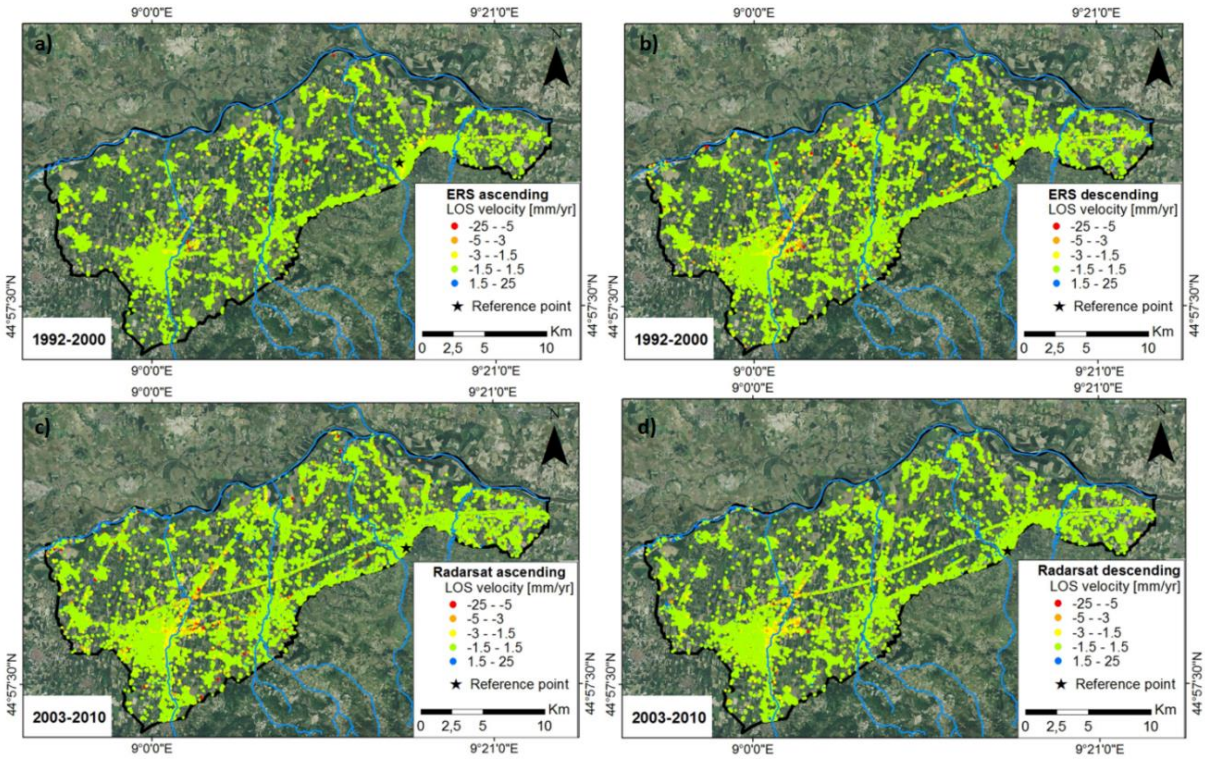

Figure 2. Average line of sight (LOS) velocity measured by the use of ERS-1/2 ascending (**a**) and descending (**b**) data (time interval from 1992 to 2000), and Radarsat ascending (**c**) and descending (**d**) data (time interval from 2003 to 2010). The reference point for each dataset is also reported.

4. Methodology

Taking into account the quality improvement of the A-DInSAR time series, it is necessary to develop an appropriate methodology to exploit the great potential contained in the A-DInSAR data for the geological interpretation of ground-motion areas. A systematic methodology to analyze the temporal evolution of ground motion areas is proposed here (Figure 3).

The procedure consists of three main phases. In the first phase, the vertical and E-W components of motion are disentangled, and a displacements time series (TS) accuracy assessment is performed. In the second phase, different statistic tests are applied in order to find the spatio-temporal pattern of the principal components of movement, and the kinematic model of the targets. The result of this step is the identification of areas with significant movement, so-called "ground motion areas". Ground motion areas correspond to a cluster of a minimum 3 of PS, with a maximum distance of 50 meters, characterized by the same trends (linear, non-linear, seasonal). Ground motion areas do not have a geological significance, but the systematic procedure represents a useful and fast approach to detect sectors where A-DInSAR analysis detects spatio-temporal ground deformation, and where the

attention of scientists has to be focused. Finally, the third step consists of a data fusion of the A-DInSAR data and the geological data to determine the causes of ground motion processes. Multidisciplinary data, such as geotechnical, hydrogeological, and land use data, are fundamental to recognize ground motion mechanisms

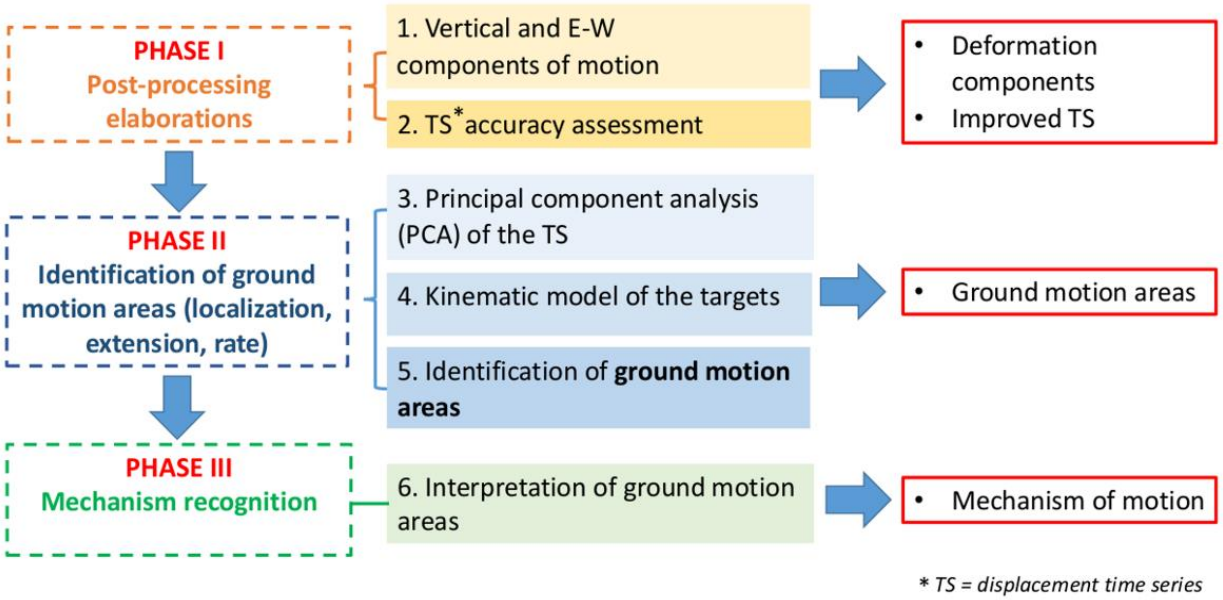

Figure 3. Flowchart of the methodological approach to detect ground motion areas and to recognize the triggering mechanisms.

Figure 3 illustrates the proposed methodological approach, which consists of the following steps:

Step 1. Decomposition of the vertical and horizontal components of motion (Phase I). A-DInSAR techniques allow the obtaining of the average LOS velocities of targets. Smaller values of the satellite incidence angle (usually 23°–35°) make the measurements more susceptible to the vertical component of motion with respect to the horizontal; however, ignoring the horizontal components may implicate an over/under estimation of the deformation, leading to misinterpretation of the results [35]. By the use of the datasets acquired in the ascending and descending modes, the vertical and horizontal components of target motion can be extracted using the following equations:

$$V_{EW} = \frac{(V_{desc}/h_{desc}) - (V_{asc}/h_{asc})}{(e_{desc}/h_{desc}) - (e_{asc}/h_{asc})} \quad (1)$$

$$V_{VERT} = \frac{(V_{desc}/e_{desc}) - (V_{asc}/e_{asc})}{(h_{desc}/e_{desc}) - (h_{asc}/e_{asc})} \quad (2)$$

V_{asc} is the average LOS velocity acquired in the ascending mode, V_{desc} is the average LOS velocity acquired in the descending mode, V_{VERT} is the vertical component of motion, and V_{EW} is the E-W component of motion. The easc, hasc and edesc, hdesc are the LOS directional cosines, respectively, for ascending and descending orbits. First, the average LOS velocity of each dataset was interpolated by an inverse distance weighted (IDW) approach, and, then, the component of motion was decomposed using these interpolated maps. The method was previously used by several authors [36,37]. If the horizontal component of motion is absent, the vertical component of motion can be extracted using the incidence angle (θ) of the dataset acquired in one mode (ascending or descending) using the following equation:

$$V_{VERT} = \frac{V_{asc,desc}}{\cos\theta} \quad (3)$$

Step 2. A-DInSAR displacement time series accuracy assessment (Phase I). The displacements time series detected by each target may be affected by local error or regional trends, which can be observed in the whole dataset. Therefore, post-processing analyses of the A-DInSAR data are fundamental in order to avoid misinterpretation of unreal ground movements. The check of the displacements time series is performed by selecting the most coherent (>0.9) targets with an average LOS velocity in the range ±0.5 mm/yr., where no significant movements are expected. More precisely, the approach proposed by Notti *et al.* (2015) [38] was applied in order to correct problems due to phase unwrapping, regional unreal trends, and anomalous displacement detected on certain dates (i.e., unreal movements at the same time as meteorological events, such as snowfall).

Step 3. Principal component analysis (PCA) of the A-DInSAR displacement time series (Phase II). A-DInSAR measurements represent the cumulative ground movements (natural versus anthropic, superficial versus deep displacements, multi-year, and seasonal components); the overlapping of several ground motion components may make the accurate interpretation of ground deformation processes difficult. Recent studies have applied PCA to satellite-based time series analysis [39,40] to detect spatio-temporal deformation patterns.

Here, principal component analysis (PCA), implementing a matrix organization of location versus time (T-mode), was performed in order to decompose the long-term (multi-year) and the seasonal components of ground motion. A matrix, in which each column contains the LOS displacements for each SAR image, and where each row contains the displacement time series of the targets (PS-DS), was formed. The main outcomes are the correlation and covariance matrices, the eigenvalues and

eigenvectors, the percent variance that each eigenvalue captures, and the principal component (PC) score maps. In interpreting the principal components, PC scores related to each observation (PS-DS) are useful for knowing the correlations with the principal components in the whole dataset; the higher values correspond to higher correlations with the analyzed PC. To detect the displacement time series of the PC, the displacement time series can be multiplied for the PC eigenvectors of each SAR image date.

Step 4. Identification of the kinematic model of the targets (Phase II). A-DInSAR data proves to be efficient for the estimation of linear and non-linear ground motion movements [8]. Hence, automated classification of displacement time series (TS) in large datasets are needed for TS interpretation at a regional scale. Here, an automatic sequential procedure, based on statistical tests, the PS-time program implemented by Berti et al. (2013) [41], was used to classify the TS into one of three predefined target trends that are: Uncorrelated, linear, and non-linear. The program permits the detection of the date (break) where abrupt changes in slope in the non-linear TS are recorded. This tool also assigns an additional parameter to the non-linear TS, called index "BICW", related to the bi-linearity of the TS (i.e., TS that records BICW higher than 1.2 indicates a strong bi-linearity [38])

Step 5. Identification of "ground motion areas" (Phase III). This task aims at detecting ground motion areas in order to focus the interpretation on significant sectors. Physical processes can be characterized as linear, non-linear, and seasonal ground movements. While the average velocity of targets with a linear trend is useful to separate movement and non-movement areas, the same parameter is not efficient for recognizing ground motion areas affected by non-linear and seasonal movements. Even targets with an average LOS velocity in the stable range (±1.5 mm/yr.) can be affected by significant seasonal and/or non-linear movements. Taking into account that non-linear and seasonal movements may cause considerable damage to buildings and infrastructure [42], PCA results were exploited to identify ground motion areas with linear, non-linear, and seasonal trends. The ground motion areas were identified using a spatial cluster of significant PC scores. First, we define the threshold of the PC scores by applying a statistical inspection of the PC score frequency distributions. If the histogram of the PC scores shows a normal distribution (skewness = 0), we consider the threshold equal to twice the standard deviation, while, if the PC scores shows asymmetrical distribution (skewness ≠ 0), the threshold is defined as being equal to the interquartile range (IQR). Then, PS-DS with PC scores higher than the threshold are selected, and a buffer zone of 50 m around the detected measuring points can be derived.

Therefore, ground motion areas consist of clusters of a minimum of 3 PS-DS with a maximum distance of 50 meters. The approach to extracting ground motion areas is based on the procedure

proposed by Meisina et al. (2008) [16], but, herein, the delineated areas are derived from the PCA analysis (Figure 4). The ground motion areas are not found on the basis of unstable velocity; hence, even seasonal and non-linear processes can be identified and taken into account for the interpretation of displacement time series. Following this, the kinematic model of the targets is combined with the ground motion areas in order to distinguish linear and non-linear processes. More precisely, the TS with BICW higher than 1.2 are selected to distinguish non-linear TS from the linear ground motion areas.

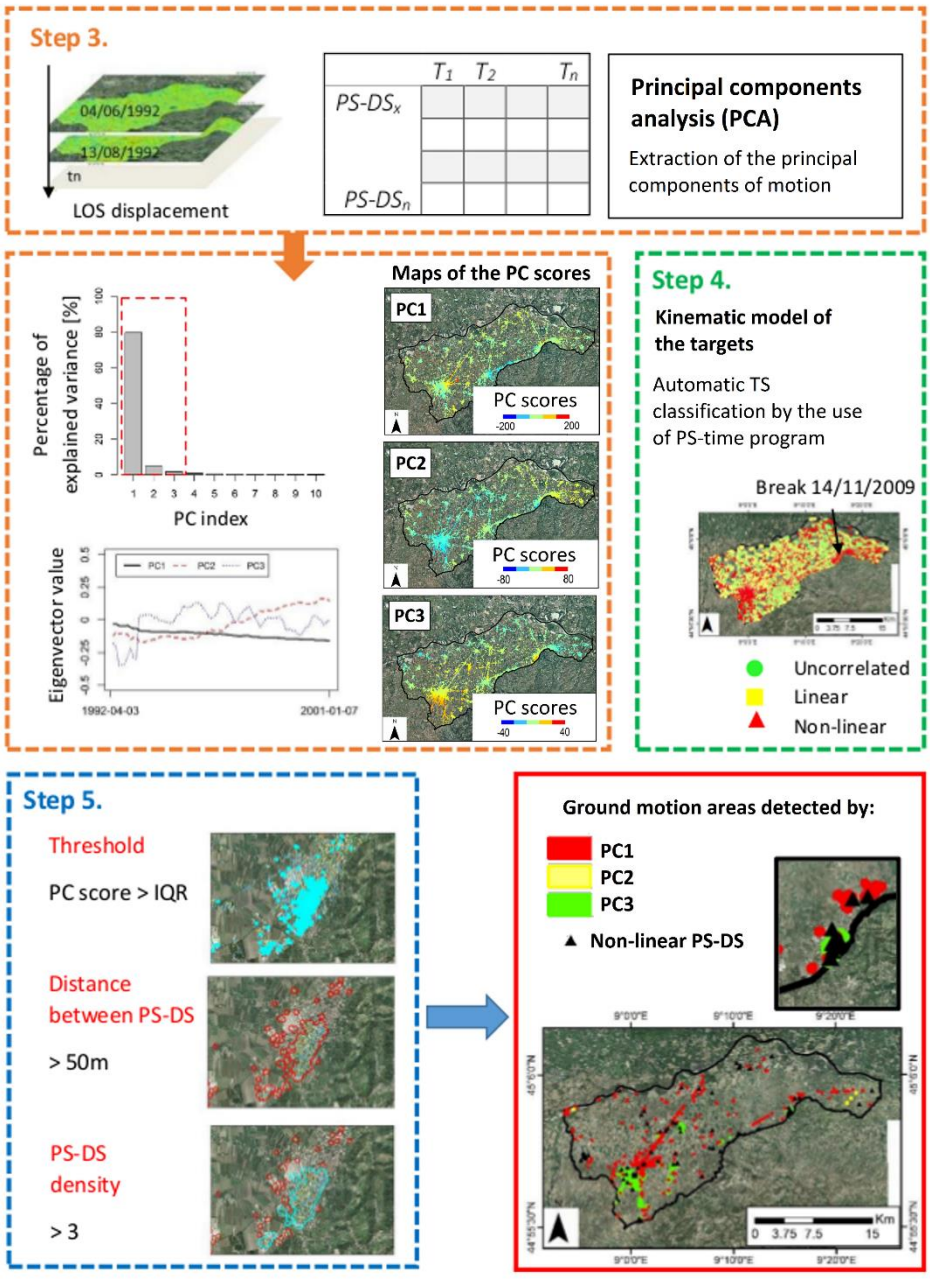

Figure 4. Flowchart of the phase II in the methodological approach, to identify ground motion areas.

Step 6. Interpretation of "ground motion areas" (Phase III). Once the ground motion areas have been identified, the processes are interpreted by integrating them into a Geographical Information System (GIS) with ancillary data (such as geological, geotechnical hydrogeological, compressible thickness map, digital orthophoto, damaged buildings distribution). Mechanism recognition is based on cross-comparison of the representative subsoil geological profiles, and the relative displacement time series with multidisciplinary information. Analysis of the breaks and the detection of the deceleration and acceleration periods are crucial to correlate the processes with the triggering mechanisms. The final outcome is the attribution of driving-force systems and triggering mechanisms to ground motion areas.

5. Results

5.1. Post-Processing Elaborations (Phase I)

The decomposition of the horizontal and vertical components of motion highlights that the motion is mainly vertical, both in the period of 1992–2000 and 2003–2010 in the Oltrepo Pavese. The results are consistent with literature data over the study area [43]. Therefore, the east–west component of motion was considered to be negligible. Following this, the procedure was implemented on the datasets that shows the higher PS-DS density and a higher number of scenes (Table 1) in order to analyze the datasets with higher spatial and temporal resolutions. Hence, the ERS-1/2 descending and Radarsat ascending data were exploited to monitor the time intervals, from 1992 to 2000, and from 2003 to 2010.

A-DInSAR displacement time series accuracy assessment has provided the detection of anomalous displacements recorded on 9 March, 1997, and 16 July, 2000, by the ERS-1/2 descending datasets, and on 10 December, 2008, for the Radarsat ascending dataset. The anomalous displacement identified in the Radarsat dataset might be related to the snowfall occurred on the day of SAR acquisition. Consequently, these scenes were not included in the following analyses.

5.2. Identification of the Ground Motion Areas (Phase II)

Once the post-processing elaborations have been performed on the A-DInSAR data, the improved displacement time series have been exploited in order to delineate ground motion areas.

In order to achieve the spatio-temporal extraction of the principal components of motion, a matrix of the ERS-1/2 desc. and Radarsat asc. dataset was formed.

The results show that the PC1 explains 79% of the variance, and PC2 and PC3 explain, respectively, 4.7% and 1.8% of the variance in the ERS-1/2 dataset. In the Radarsat, 69% of the variance is explained by PC1, while 5.7% and 1.7 % are explained by PC2 and PC3.

Figure 5a, b shows the spatial distribution of the principal components score units. The spatial pattern of the PC of the deformation highlights that the first and the third principal components of motion mainly affect the southwestern sector of the study area, while the second component is mainly localized in the northeastern zone. It worth noting that the distribution of the components of motion is heterogeneous across the Oltrepo Pavese, and that the comparison between the ERS-1/2 and Radarsat data reveals that the spatial distribution of the components of motion detected during the period of 1992–2000 is correlated with that of the period of 2003–2010 (Figure 5a, b).

A visual inspection of the principal components eigenvectors (Figure 5c, d) highlights that in the ERS-1/2 and Radarsat datasets, the first component (PC1) corresponds to the long-term lowering of the Earth's surface. The second corresponds to the long-term uplift ground motion, and the third PC highlights seasonal deformations.

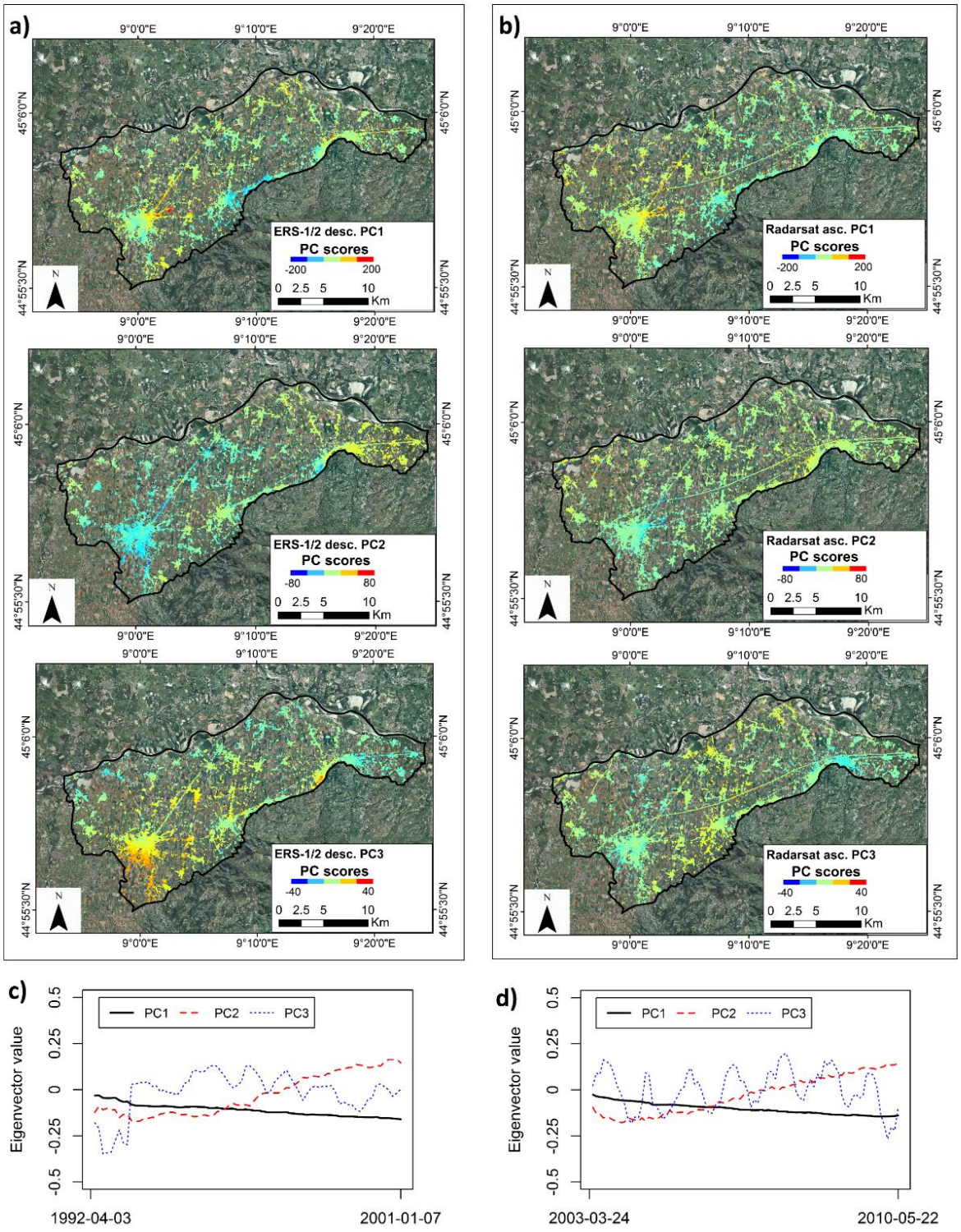

Figure 5. Principal component score maps for the period of 1992–2000 (**a**) and 2003–2010 (**b**). Eigenvectors of the principal components (PC) of the ERS-1/2 desc. (**c**) and Radarsat asc. (**d**) datasets.

Ground motion areas were delineated using the PC scores, applying the procedure described in Section 4, in order to focus the interpretation of the processes on significant sectors. The results reveal that 30%–40% of the ground motion areas, delineated using the PC1 of the ERS-1/2 and Radarsat measurements, is located in proximity of the town of Voghera and along the railway of Voghera–Pavia (Figure 6), and it records an average LOS velocity in the range from –2 to –3.7 mm/yr, in the period of 1992–2000, and in the range of –2 to –4.8 mm/yr, in the period of 2003–2010. A distinct concentration of ground motion detected by PC1 is visible only in the time span of 1992–2000, along Emilia Road, from the town of Broni to the town of Redavalle, and along the railway from Broni to the town of Arena Po. The average LOS velocity ranges from –6.4 to 2 mm/yr.

Ground motion areas mapped via PC2, of both ERS-1/2 and Radarsat data are centred in the area between the town of Stradella and the town of Monteacuto (Figure 6). The average LOS velocity records an uplift maximum of 3.40 mm/yr, in the period of 1992–2000, and 2.58 mm/yr, in the period of 2003–2010.

Ground motion areas observed using PC3 are mainly located in the southern sector of Voghera and in proximity to Lungavilla, Codevilla, Casei Gerola, and Broni (Figure 6). In the second period, ground motion areas via PC3 are not present in the southern sector of Voghera, and the movements are mainly localized along the Coppa River (see location in Figure 1) and in proximity to Verrua Po. Seventy-four percent and 97% of the ground motion areas detected using PC3, respectively, for the ERS-1/2 and Radarsat data show an average LOS velocity in the range of ±1.5 mm/yr.

As was previously explained, an automated time series classification tool was used to distinguish uncorrelated, linear, and non-linear trends. The outcome of this step reveals that around 40% of the targets are classified as uncorrelated, both in the periods of 1992–2000 and 2003–2010. Thirty-five percent and 22% of the targets are classified, respectively, as non-linear and linear during the time interval of 1992–2000. In the following period (2003–2010), 28% and 27% of the targets are classified as linear and non-linear, respectively.

Furthermore, the results of the kinematic model analysis were combined with the ground motion areas detected using the PCA approach. Figure 6 shows the results of the overlapping of the ground motion areas, detected using PC1, PC2, and PC3, and the non-linear PS-DS characterized by a strong non-linearity (BICW > 1.2). Mainly, changes in trends in displacement time series were identified at the end of 1999 and 2008 in the areas of Broni, Voghera, Lungavilla, and Casei Gerola, and, in most of the cases, the non-linear targets are superimposed on seasonal ground motion areas detected via PC3, which represent the seasonal components of motion.

Overall, the ground motion area detected at Voghera records a linear displacement time series that is active during both periods, while, in Broni, the ground motion occurs only in the period from 1992 to 2000.

The ground motion area centered in the north sectors of Voghera could be related to the presence of over 6–7 m of shallow thick clay deposits in the subsoil, and to groundwater exploitation for industrial supply. Unfortunately, the lack of historical data regarding the piezometric level variations did not allow us to analyze the effects of its variations on the land subsidence recognized in this area. The phenomenon is characterized by a linear trend for both the periods of 1992–2000 and 2003–2010, and no evident acceleration has been recognized (Figure 6).

The ground motion areas along the railway Voghera–Pavia and along the railway from Broni to Arena Po show a linear trend and rates of average LOS velocities in the range of –5 to 1 mm/yr, for both periods. Given the close association with the local transport network, these ground motion areas could be due to the consolidation of the railroad embankment, and anthropogenic activity could have an influence on the surface settlement of these areas.

Areas of moderate uplift were observed via PC2 of the ERS-1/2 and Radarsat data, in the sector from Stradella to Monteacuto, where geomorphic evidence of an active emergent thrust was previously observed [43]. The terraced surfaces derived from topographic profiles, combined with inferences on the ages of the terraces of the exanimated area, were used to carry out estimations about the late quaternary uplift rates across the escarpment. The agreement between the distribution and trend of deformation with the uplift trend, found by previous authors in the same area, suggests that the deformation could be due to deep-ground motion related to tectonic movements.

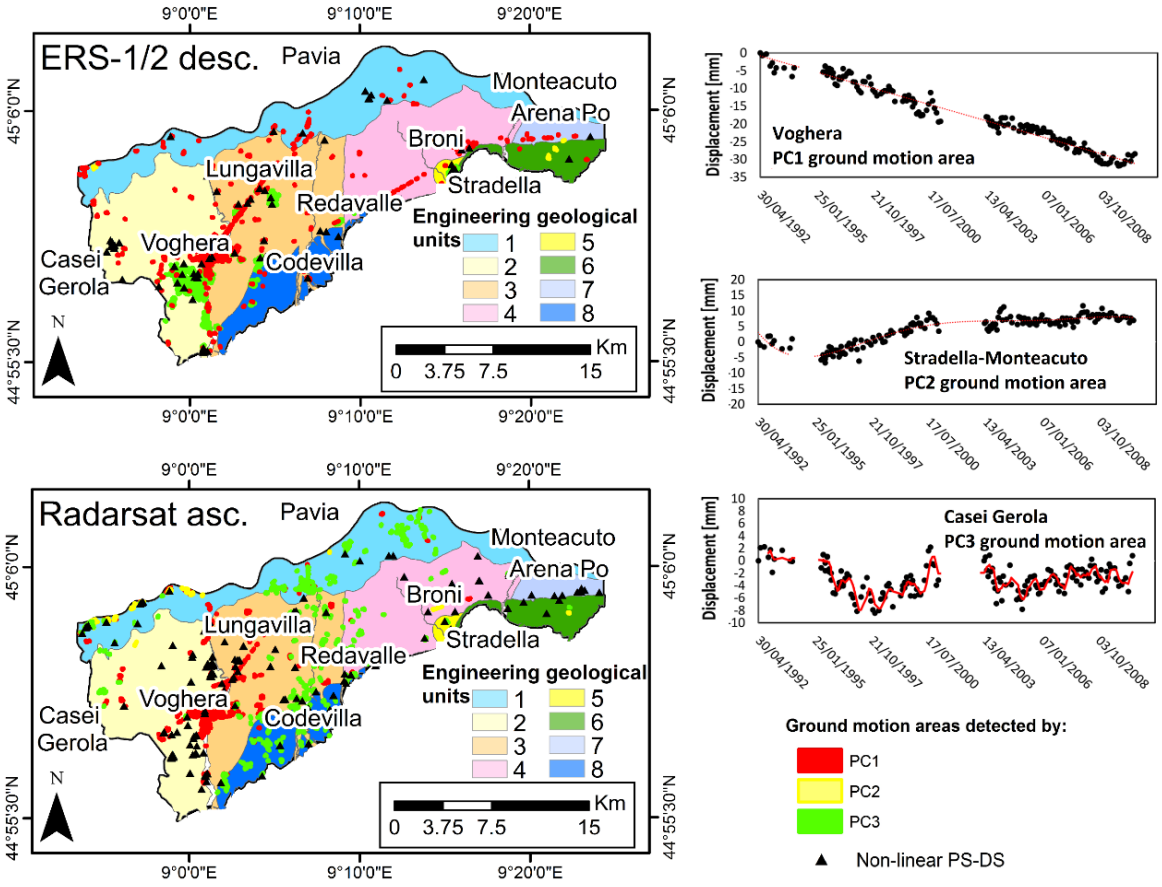

Figure 6. Ground motion areas detected using PC1, PC2, and PC3, and non-linear PS-DS of the ERS-1/2 desc. and Radarsat asc. data overlapped on the engineering geological units. TS of the deformational behavior detected at Voghera, Stradella–Monteacuto, and Casei Gerola are also reported. In the case of Voghera, it is represented by the TS linear regression line (dotted red line). Conversely, for Stradella–Monteacuto a 5° order polynomial regression line (dotted red line) is reported. For the TS detected at Casei Gerola, the red line is the moving average over a period of four months.

5.3. Mechanism Recognition (Phase III)

A spatio-temporal analysis for mechanism recognition was performed, considering some factors and evidence, which might have relevance in explaining the patterns of ground motion, as observed in others ground motion areas by previous authors [44-46]: (i) the geotechnical properties of the deposits; (ii) the thickness of the superficial clayey soils and the hydrogeological setting; (iii) the distribution of damaged buildings; and (iv) land use change effects.

Different natural and man-induced processes were recognized such as swelling–shrinkage of clayey soils located over engineering geological unit 8, and seasonal ground motions due to seasonal groundwater level variations, which are located over engineering geological units 3 and 4.

Land subsidence due to the load of new buildings was observed over engineering geological units 1, 2 and 3, and moderate tectonic uplift was recognized in the sector from Stradella to Monteacuto, where geomorphic evidence of an active emergent thrust was previously observed [43].
The main conditioning and triggering factors on ground motion were examined in detail in section 6.

6. Discussions

The approach of this work was to identify areas with significant movements where the attention of scientists has to be focused by the use of A-DInSAR time series analysis. Ground motion areas were mapped on the basis of their peculiar ground deformation behaviors using a systematic and reproducible procedure.

Although various methodologies were implemented to map the ground motion areas using the average velocity detected by A-DInSAR data [12-17], examples of ground motion areas mapping on the basis of A-DInSAR time series still not a common practice for the scientific community.

While the average velocity may be useful to investigate physical processes characterized by linear trend, the same parameter is not efficient to detect and to interpret ground motion areas affected by non-linear and seasonal movements. In these cases, the use of the average velocity may be resulting in misleading interpretations of the processes.

Our intent is to propose a novel approach to take into account of different deformational behaviors. Hence, the reliability of the results obviously depends on the quality of the dataset. However, the first phase of the procedure is focused on the time series check in order to correct problems due to phase unwrapping, regional unreal trends, and anomalous displacement detected on certain dates. In addition, if whole dataset is affected by a relevant error, it can be easily detected applying the PCA, being clearly visible as principal component of motion and could be subtracted from the entire dataset.

The approach allowed to detect ground motion areas due to different processes, proving the capabilities to identify ground motion areas that record low average LOS velocities, in the range of ±1.5 mm/yr affected by geohazards that may impact public safety.

In this section, main conditioning and triggering factors on ground motion were discussed.

6.1. Comparison between Ground Motion and Engineering Geological Units

As regards geotechnical interpretation, the relationship between the engineering geological units and the ground motion was analyzed by computing the maximum and minimum of the displacement measured for each unit (Figure 7). Furthermore, the PS-DS density for each unit was extracted in order to take in to account the distribution of measures. Figure 7a, b shows the results of the spatial analysis for the periods of 1992–2000 and 2003–2010. It worth noting that the extreme values of

cumulated displacement observed in the first period are higher than those of the second one. A decrease of deformation was observed, and, in general, the cumulated displacement decreases from unit 1 to 8. The PS-DS density reaches an average for the engineering geological units of 108 and 113 PS-DS/km^2, respectively, for the ERS-1/2 and Radarsat data.

Engineering geological unit 1, which is composed of recent and actual alluvial deposits of the Po River, shows the lower PS-DS density (~40 PS-DS/km^2), and, for this reason, the maximum cumulated land subsidence may be due to local movements.

Units 2, 3, and 4 are characterized by cohesive soils (50%–60% of the thickness) in first five meters, and show an average PS-DS density of ~100 PS-DS/km^2. These units record a maximum cumulated land subsidence that varies from 100 mm to 200 mm in the first period, and an average value of 150 mm in the second one.

Unit 5 is composed of the alluvial fan of the Scuropasso River, with heterogeneous soils in the first 15 m of depth. As shown in Figure 7, this unit show the higher PS-DS density (~300 PS-DS/km^2) and the maximum cumulated land subsidence reaches ~51 mm for both periods.

Units 6, 7, and 8 are characterized by cohesive soils, predominant only in the first five meters of depth, and gravel and sand in the sub-soil. The PS-DS detected over these units is around 100 PS-DS/km^2 and the maximum cumulated land subsidence reaches values in the ranges of 100–180 mm and 50–100 mm, respectively, for the periods of 1992–2000 and 2003–2010. Note that the maximum cumulated uplift of 159 mm was detected for unit 6, in the period of 1992–2000.

In addition, comparisons between the engineering geological units and the areas of ground motion detected using the principal component analyses were carried out for the monitored periods (Figure 7c, d). The results of the analyses show that the area of ground motion reaches around 23 and 17 km^2, respectively, in the periods of 1992–2000 and 2003–2010. Therefore, the ground motion area decreases from the first period to the second one. It worth noting that the study area is mainly characterized by PC3, which corresponds to seasonal deformation. Seasonal deformations may be due to seasonal aquifer compaction and/or swelling-shrinkage of clayey soils.

The PC1 ground motion that corresponds to the long-term lowering trend is mainly localized on units 2 and 3 for both periods; while, PC2 ground motion that corresponds to the uplift long-term trend is mainly localized on units 1 and 6 for the entire monitored period.

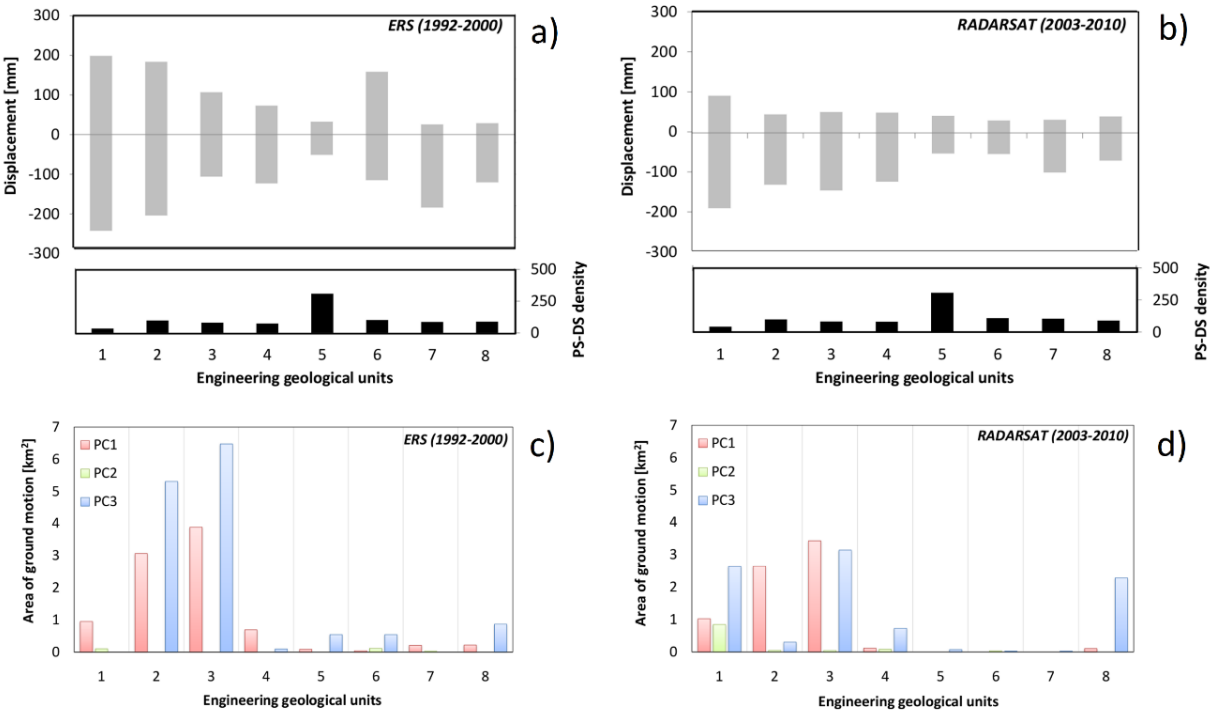

Figure 7. Cumulated displacement (mm) and PS-DS density (PS-DS/km^2) for the periods of 1992–2000 (**a**) and 2003–2010 (**b**) for each engineering geological unit, which describes the geotechnical properties of the first 15 m of depth. See Figure 1 for the engineering geological unit map. Areas (km^2) of ground motion detected by PC1, PC2, and PC3 for each engineering geological unit, for the time intervals of 1992–2000 (**c**) and 2003–2010 (**d**).

6.2. Comparison between Ground Motion and Hydrogeological Settings

Another important factor that controls ground motion is the presence, and the thickness, of clayey soils, which may be susceptible to the consolidation process. A thickness map of the upper clayey-silty deposits was elaborated by Pilla *et al.* (2007) [21] by interpolating the thickness data available from around 490 water wells, performed in the Oltrepo Pavese (Figure 8a). This map allows to analyze the relationship between the average LOS velocity and the thickness of the upper compressible deposits. The Oltrepo Pavese is characterized by the presence of a tabular clayey-silty cover, which increases from the northeast to the southwest. The thickness of the clayey-silty deposits ranges from 0 to 40 m, and the maximum thickness is observed in the southeastern sector of Voghera, and in proximity of the towns of Broni and Stradella (Figure 8b, c). Figure 8d, e shows the comparison between the average LOS velocity, detected by ERS-1/2 and Radarsat data, and the thickness of the upper clayey-silty deposits along N-S and E-W sections (Figure 8a). The results reveal that the peaks of average LOS velocity are consistent with the maximum thickness of clayey-

silty deposits. As a consequence, the thickness of the upper clayey-silty deposits seems to be a controlling factor of the rate of ground motion as observed in others case histories, such as in Murcia, Vega Media of the Segura River Basin and Alto Guadalentín Basin, in Spain [46-48], and along the Venice coast and Sibari plain, in Italy [49,50].

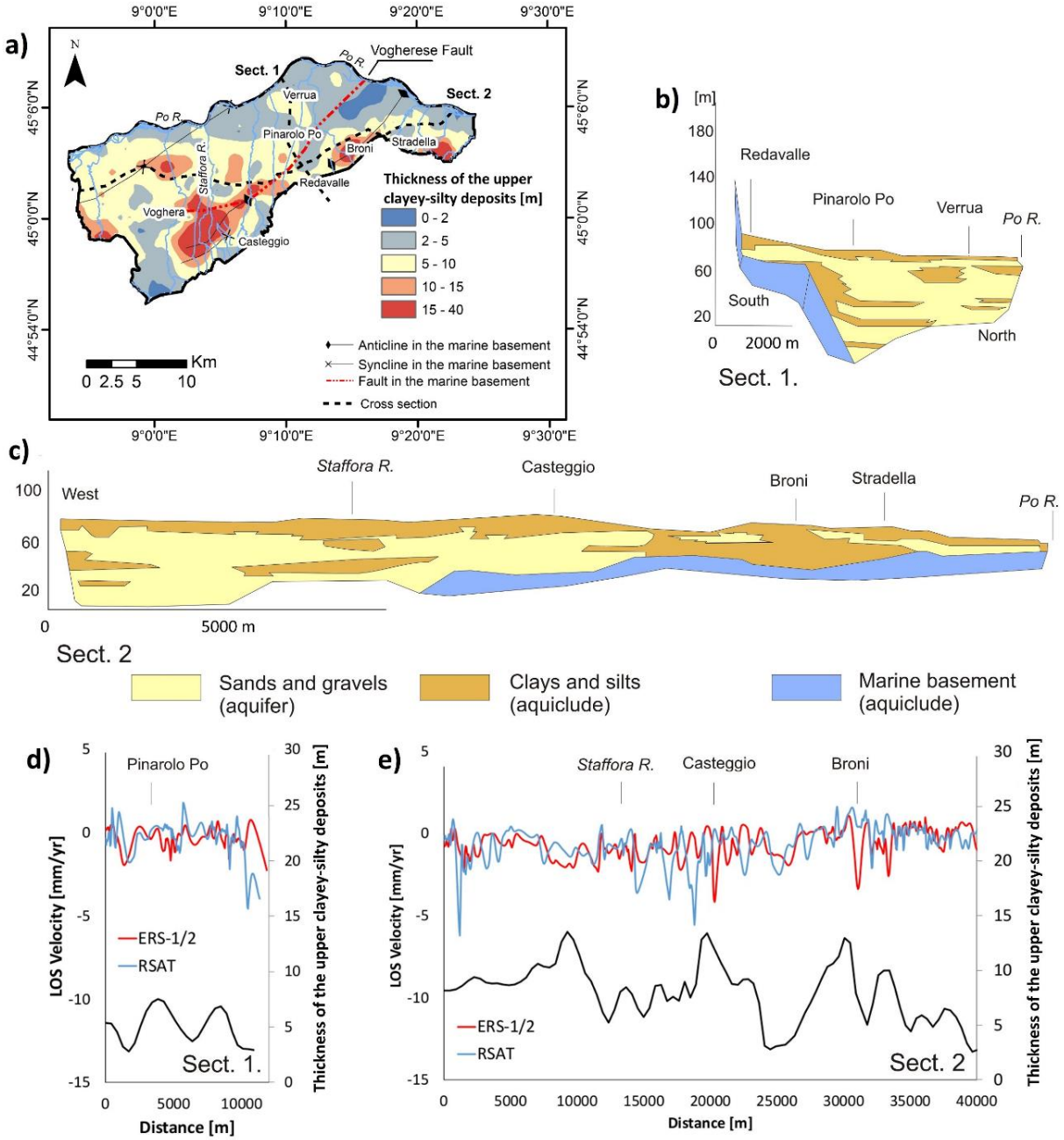

Figure 8. (**a**) Thickness of the upper clayey-silty deposits (modified from Pilla *et al.*, 2007 [21]). Hydrogeological sections 1 (**b**) and 2 (**c**), simplified from Cavanna *et al.* (1998) [17]. Relationship between the average LOS velocity detected by ERS-1/2 asc. and Radarsat (RSAT) desc. sensors, and the thickness of the upper clayey-silty deposits along sections 1 (**d**) and 2 (**e**).

Furthermore, the constant presence of a tabular clayey-silty coverage, which acts as a seal, is a crucial factor in determining the hydraulic condition of aquifer state. Indeed, the clayey-silty cover limits infiltration, and influences aquifer recharge, which occurs in correspondence with the coalescent fans originating from the deposition of the Apennine streams [21]. Analysis of the hydraulic condition role on ground motion was performed using the unsaturated zone thickness, measured in October, 2005 (Figure 9). The unsaturated zone thickness detected in October, 2005, was established by Pilla *et al.* (2007) [21] using a piezometric level obtained from around 60 water wells across the study area. For the computation of the unsaturated zone, the piezometric levels were subtracted to the base of the clayey-silty cover. When the values are negative, the aquifer is confined and the flow is mainly horizontal. Conversely, when the values are positive, the aquifer is phreatic. Figure 9 shows the overlapping of the ground motion areas mapped using PC3 of the Radarsat data with the hydraulic condition of the aquifer in October, 2005. The results reveal that the seasonal ground motions (PC3), which are located over engineering geological units 3 and 4, occur where phreatic condition of the aquifer was observed. The role of the seasonal fluctuations of the groundwater level on the ground motion areas is clear. Seasonal ground motions related to fluctuations in the groundwater level were previously recognized by others authors in Santa Clara Valley and Los Angeles Basin in the United States [51,52]. Meanwhile, the ground motion areas located over engineering geological unit 8 are due to others processes, which are explained in Section 6.3.

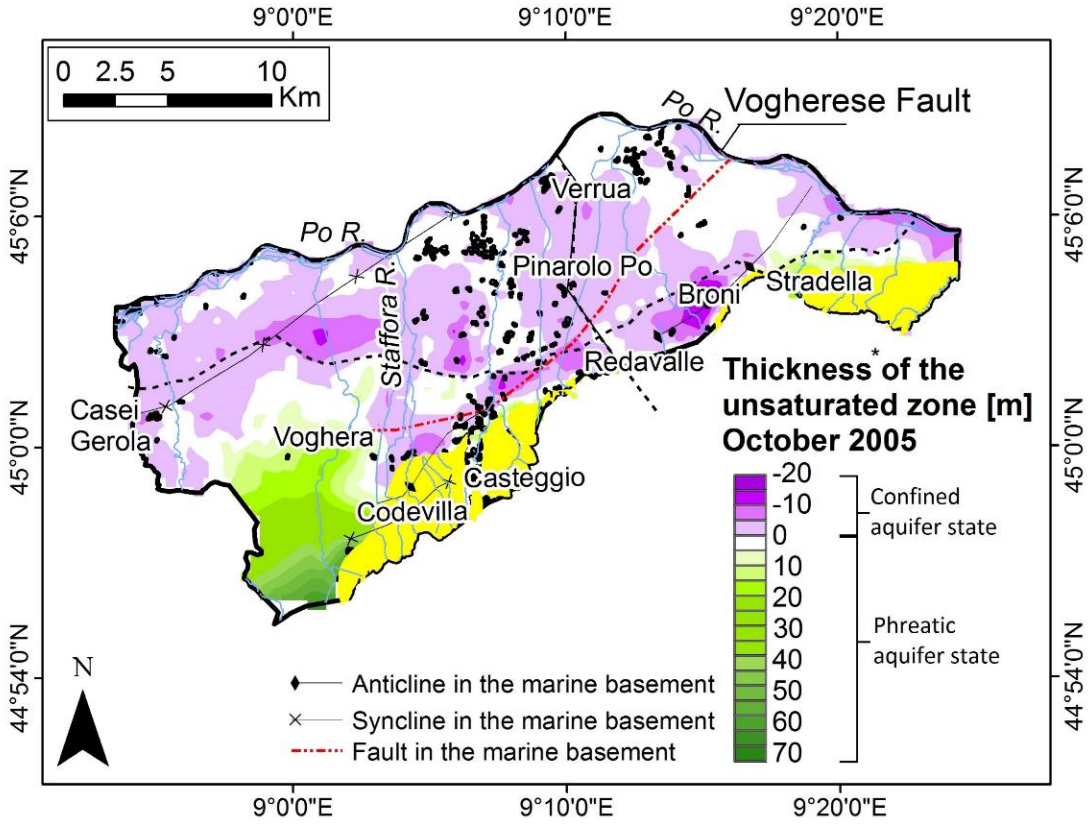

Figure 9. Thickness of the unsaturated zone in October, 2005 (modified from Pilla *et al.*, 2007), and superimposed ground motion areas detected via PC3 of the Radarsat data (black box). The pre-würmian deposits are represented in yellow.

6.3. Comparison between Ground Motion Areas and Damaged Buildings

Most locations in the Oltrepo Pavese experienced damage to buildings due to swelling and shrinkage of clayey soils, respectively, during wet and dry periods. In most cases, the damaged buildings are single storey family residences, built on conventional shallow strip concrete footings. The damage was mainly detected over engineering geological unit 8, where clayey soils susceptible to swelling/shrinkage were previously identified [28]. Meisina et al. (2006) [30] implemented a damaged building database.

Here, comparisons between the damaged building distribution and ground motion areas were performed. The results of the analyses highlight that the occurrence of damaged buildings is mainly localized over the ground motion areas detected using PC3. Therefore, this is consistent with the hypothesis that the seasonal deformational behavior detected by the third component of ground motion in engineering geological unit 8 may be explained by the swelling-shrinkage of clayey soils.

In Codevilla (see location in Figure 6), located over engineering geological unit 8, the higher density of damaged buildings (12 damaged buildings in an area of around 0.6 km^2) corresponds to ground motion areas delineated using the PC3 of ERS-1/2 and Radarsat data (Figure 10a). In this area, the shallow alluvial deposits of the first 8 m of depth exhibit swelling potentials from medium to very high [30].

The swelling potential appears to be in good agreement with the displacements time series. Average LOS displacement time series was computed in the buffer zone of 100 m from the damaged building with code 425 in order to consider a significant number of measurements (around twenty PS-DS). The results reveal that the seasonal component of motion detected in the TS is directly correlated with the effective rainfall detected at the nearest pluviometric station, located in Voghera (Figure 10a, b). In particular, significant damage, which consists of cracks, appeared in this building in August, 1999 (crack width 5–10 mm). The pre-damage period from 1998 to 1999 was recognized as a drought period [30], and the average effective rainfall from May to November of 49.45 mm corresponds to around –6.14 mm of ground motion. In February and March, 2001, partial pile underpinning was carried out as a remedial measure for this building. In the following drought period, 2003–2007, the variability of the effective rainfall corresponds to there being no clear cyclic displacements time series. However, the average effective rainfall from May to November, of 62.95 mm, corresponds to around –1.27 mm of ground motion.

The results confirm that the ground motion areas detected at Codevilla via PC3 are due to swelling–shrinkage phenomena triggered by the variation of water content in these soils.

Overall, Codevilla seems to be characterized by an average LOS velocity range that is commonly defined as stable (±1.5 mm/yr.) during the periods of 1992–2000 and 2003–2010; however, in this case, the seasonal deformation is significant, and it provides evidence of damage, suchs as cracks in buildings, dislocations, and the breaking of walls, which were recognized by Meisina et al. (2006) [30, 53]. In particular, the damaged buildings, required the installation of micropile construction, up to 8 m in depth, in order to reinforce structures.

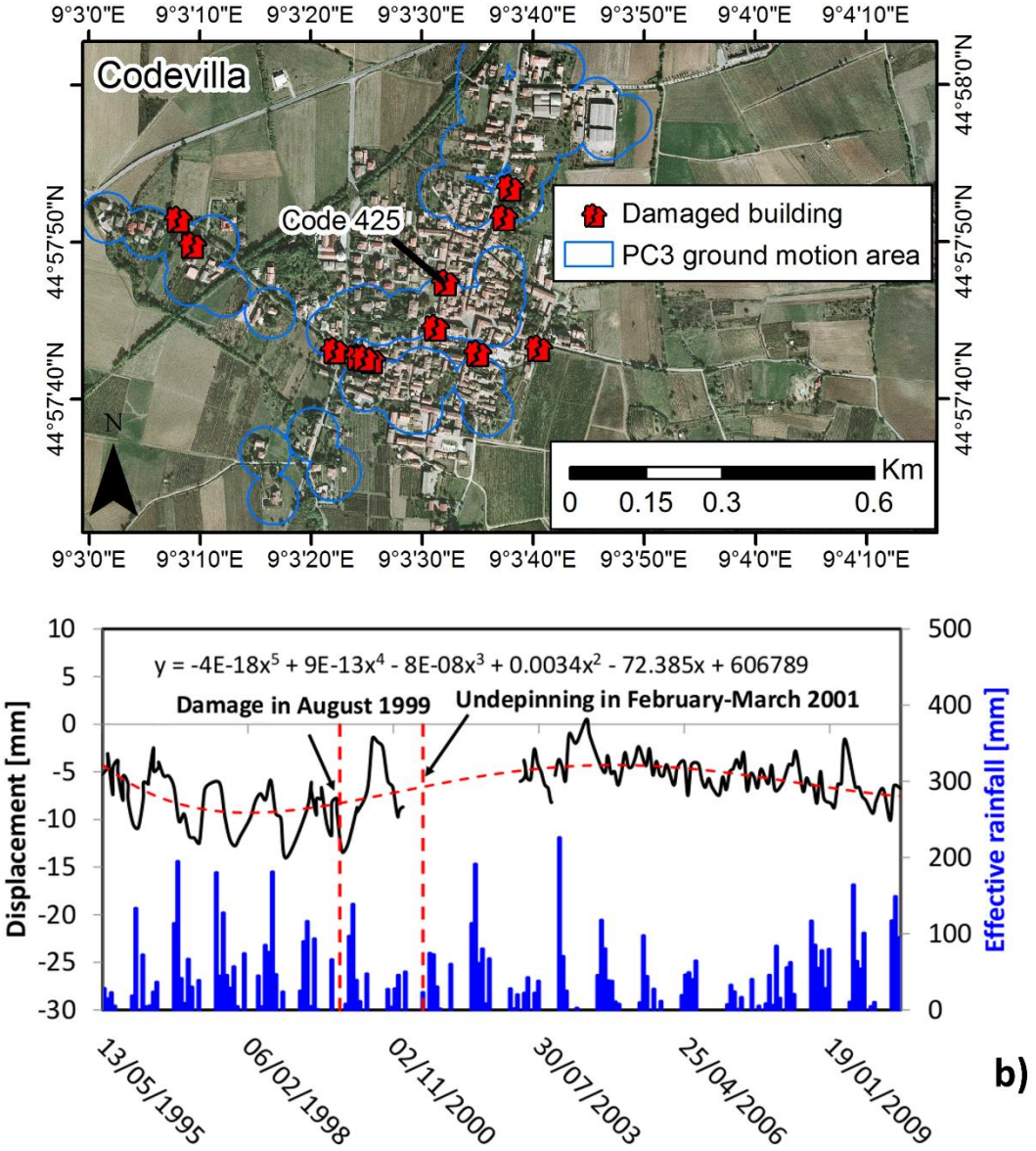

Figure 10. (**a**) Ground motion areas in Codevilla, detected by the ERS-1/2 and Radarsat PC3, and the distribution of damaged buildings detected by Meisina et al. (2006) [30]. (**b**) Average LOS displacement time series in the buffer zone of 100 m from the damaged building (code 425) versus effective rainfall measured at the Voghera weather station. The dotted red line is the polynomial regression trend (5° order) of the displacement time series. The equation for polynomial regression has been also indicated.

6.4. Comparison between Ground Motion and Land Use Change Effects

In order to define the influence of land use change on ground motion, a visual inspection was performed by comparing orthophoto 1988 [54] and 2000 [55] and orthophoto 2003 and 2007 provided by the Lombardia Region, with PC1 ground motion areas. In addition, Corine Land Cover changes (CLC) from 1990–2000 and 2000–2006, implemented by the Institute for Environmental Protection and Research (ISPRA) [56,57] that match our satellite data, were exploited. These layers were created by using a working scale of 100,000; therefore, the land cover cannot be mapped in all its complexity, and the definitions of the units were established by the combination of surfaces, which are a greater or lesser homogeneous, whatever the scale used. From the total of the ground motion areas delineated by PC1 of the ERS-1/2 and Radarsat data, only two and three areas seem to be influenced by land use changes, respectively. More precisely, in the period of 1992–2000, land use change from non-irrigated arable land to discontinuous urban fabric, which occurred over engineering geological units 1 and 2, matches with PC1 ground motion areas detected by ERS-1/2 data. In the period of 2000–2006, land use change from non-irrigated arable land to construction sites occurred over engineering geological unit 3, which matches PC1 ground motion area detected using Radarsat data.

It worth noting that these ground motion areas, detected during the period of 1992–2000, are not present in the period of 2003–2010. Therefore, the stress increment produced by a building's load seems to have dissipated in the first period. Figure 11 shows ground motion detected by the PC1 of ERS-1/2 data in Voghera. The average displacement time series of the PS-DS in the ground motion areas highlight the decrease of the average LOS velocity from –3.15 mm/yr. during 1992–2000 to –0.80 for 2003–2010 (Figure 11c).

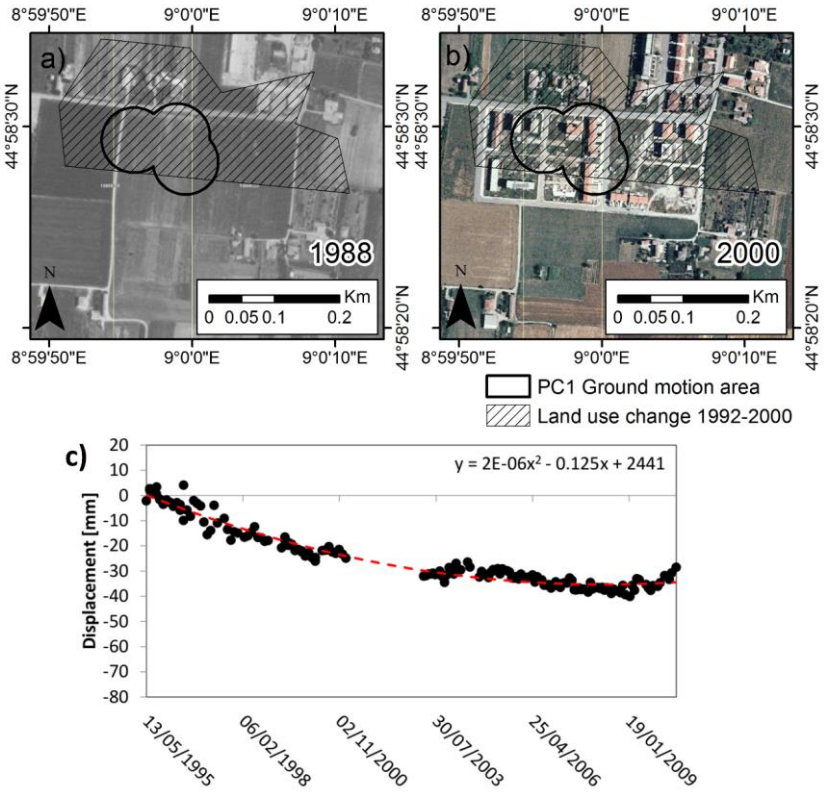

Figure 11. Location of the representative ground motion area detected using PC1 of the ERS-1/2 sensors in Voghera, superimposed on the land use change from 1990–2000, and on the Ortophotos acquired from 1988 (**a**) and 2000 (**b**). (**c**) Average displacement time series detected in the ground motion area. The dotted red line is the polynomial regression trend (2° order) of the displacement time series. The equation for polynomial regression has been also indicated.

7. Conclusions

A challenge to ground motion studies is the disentanglement of different phenomena and to assess their relative contributions. Indeed, specific causes of deformation phenomena in lowlands are, presently unknown due to the interaction of causes, either by deep ("geological" causes) or superficial causes (withdrawal of water and gas, soil consolidation, load-induced compaction), which take place at different spatio-temporal scales and of which the mixed-effects must be decorrelated. This paper demonstrated the ability of a novel methodology to detect and to disentangle the contributions of different geohazards, by analyzing multi-sensors and multi-temporal A-DInSAR data. The principal novelty of the proposed approach is the exploitation of full time series, which enables the detection of ground motion areas affected by linear, non-linear, and seasonal movements. The proposed methodology consists of three phases:

1. Post processing elaborations; disentanglement of the vertical and horizontal components of motion and displacements time series accuracy assessments, performed by selecting the most coherent (>0.9) targets with an average LOS velocity in the range ±0.5 mm/yr., where no significant movements are expected.
2. Identification of ground motion areas; application of two approaches for automatic A-DInSAR time series analyses. First, principal components analysis of the time series is performed, implementing a matrix organization of location versus time (T-mode). Then, PS-time software is used to find the kinematic behavior of the time series (i.e., uncorrelated, linear and non-linear trend). Finally, ground-motion areas were identified using a spatial cluster with a buffer zone of 50 m around the targets, characterized by a significant correlation with the principal components of motion. The results of both approaches are overlapped to distinguish linear and non-linear ground motion areas.
3. Mechanism recognition: comparison between ground motion areas and ancillary data (i.e., geological, geotechnical, hydrogeological, and land use information) in order to interpret the driving forces of the subsidence mechanisms.

The methodology was tested in Oltrepo Pavese (Italy), which is a representative site of moderate subsidence of the Po Plain, using ERS-1/2 and Radarsat data covering a time span of around twenty years. Results confirm its high capability for the detection of the temporal evolution of deformation patterns due to different geohazards, not recognizable by conventional analyses of the average LOS velocity alone (i.e., seasonal components of motion). Three deformational behaviors were detected: linear, non-linear (accelerations and decelerations of the movements), and seasonal components of motion. The comparison between a kinematic model of the ground motion areas and hydrogeological and engineering geological data allow understanding of the causes of motions that are often superimposed. The main natural and man-induced processes are swelling–shrinkage of clayey soils, land subsidence due to the load of new buildings, moderate tectonic uplift, and seasonal ground motion due to seasonal groundwater level variations. Overall, the cumulated displacements observed in the 1992–2000 period are higher than those detected in the period of 2003–2010 and a decrease of deformation was observed. The findings in this work confirmed that the combination of A-DInSAR time series analysis and hydrogeological data is capable of supporting the knowledge of the relationship between groundwater level fluctuations and deformations, and to provide fundamental information about the aquifer state conditions.

The proposed methodology can be easily applied to others geological contexts, using different A-DInSAR data. The reliability of the results depends on the quality of the dataset. New opportunities

will be provided by the improvement of the time series acquired by new sensors of the COSMO-SkyMed and Sentinel missions.

The procedure will also allow specifying the priority area of where to address prevention activities, in order to optimize the costs and benefits and to draw a management plan of land use and groundwater resources, at national and regional scales. The procedure may also be used in land subsidence studies to discern the contributions of the seasonal components of motion from others processes, such as soil consolidation and solid and fluid extraction or injection. The approach will be tested, in the future, in geological contexts characterized by others geohazards, such as landslides.

Acknowledgments: The A-DInSAR data we used were provided by Lombardia Region (Italy) in the framework of the project Report IRER n° 2010B009: "Interpretazione geologica e idrogeologica dei dati radar derivanti dal Piano Straordinario di Telerilevamento nazionale (PST) e da dati Radarsat con particolare riferimento alle province di Lecco e Pavia". The data were processed by Tele-Rilevamento (TRE). The authors would like to thank the reviewers for their valuable comments and suggestions to improve the quality of the paper.

Author Contributions: Roberta Bonì analyzed the A-DInSAR data and prepared the manuscript. Giorgio Pilla provided hydrogeological data and supported their interpretation. Claudia Meisina provided the engineering geological data and provided guidance and support throughout the research process. All authors co-wrote and reviewed the manuscript.

Conflicts of Interest: The authors declare no conflict of interest.

References

1. Galloway, D.L.; Jones, D.R.; Ingebritsen, S.E. *Land Subsidence in the United States: U.S.* Geological Survey. Circular 1182; U.S. Geological Survey: Reston, Virginia, USA, 1999; p. 177.
2. Cigna, F.; Jordan, H.; Bateson, L.; McCormack, H.; Roberts, C. Natural and anthropogenic geohazards in greater London observed from geological and ERS-1/2 and ENVISAT persistent scatterers ground motion data: results from the EC FP7-SPACE PanGeo Project. Pure and Applied Geophysics. 2014, 1-31, doi:10.1007/s00024-014-0927-3.
3. Tosi, L.; Teatini, P.; Strozzi, T. Natural versus anthropogenic subsidence of Venice. Nat. Sci. Rep. 2013, doi:10.1038/srep02710.
4. Kroon, I.C.; Nguyen, B.L.; Fokker, P.A.; Muntendam-Bos. A.G.; de Lange, G. Disentangling shallow and deep processes causing surface movement. Mathematical Geosciences. 2009, 41(5). 571-584, doi:10.1007/s11004-008-9197-x.

5. Tomas, R.; Li, Z.; Lopez-Sanchez, J.M.; Liu, P.; Singleton, A. Using wavelet tools to analyse seasonal variations from InSAR time-series data: a case study of the Huangtupo landslide. Landslides. 2016, 13: 437-450, doi:10.1007/s10346-015-0589-y.
6. Ferretti, A.; Prati, C.; Rocca, F. Permanent scatterers in SAR interferometry. IEEE Trans. Geosci. and Remote Sens. 2001, 39(1). 8-20, doi:10.1109/36.898661.
7. Strozzi, T.; Wegmüller, U.; Tosi, L., Bitelli, G.; Spreckels, V. Land Subsidence Monitoring with Differential SAR Interferometry. Photogrammetric Engineering and Remote Sensing. 2001, 67(11). 1261–1270.
8. Mora, O.; Mallorqui, J.J.; Broquetas, A. Linear and nonlinear terrain deformation maps from a reduced set of interferometric SAR images. IEEE Trans. Geosci. Remote Sens. 2003, 41, 2243–2253, doi:10.1109/TGRS.2003.814657.
9. Galloway, D.L.; Hoffmann, J. The application of satellite differential SAR interferometry-derived ground displacements in hydrogeology. Hydrogeology Journal. 2007, 15(1), 133-154, doi:10.1007/s10040-006-0121-5.
10. Tomás, R.; Romero, R.; Mulas, J.; Marturià, J.J.; Mallorquí, J.J.; Lopez-Sanchez, J.M.; Herrera, G.; Gutiérrez, F.; González, P.J.; Fernández, J.; Duque, S.; Concha-Dimas, A.; Cocksley, G.; Castañeda C.; Carrasco, D.; Blanco, P. Radar interferometry techniques for the study of ground subsidence phenomena: A review of practical issues through cases in Spain. Environ. Earth Sci. 2014, 71, 163–181, doi:10.1007%2Fs12665-013-2422-z.
11. Zhao, C. Y.; Zhang, Q.; Ding, X. L.; Lu, Z.; Yang, C. S.; Qi, X. M. Monitoring of land subsidence and ground fissures in Xian, China 2005–2006: mapped by SAR interferometry. Environmental geology. 2009, 58(7), 1533-1540, doi:10.1007/s00254-008-1654-9.
12. Bateson, L.; Cuevas, M.; Crosetto, M.; Cigna, F.; Schijf, M.; Evans, H. PANGEO: enabling access to geological information in support of GMES: deliverable 3.5 production manual. 2012, Version 1. Available at: http://www.pngeoproject.eu/sites/default/files/pangeo_other/D3.5-PanGeo-Production-Manual-v1.3.pdf, Accessed on: 26/06/2016.
13. Lu, P.; Catani, F.; Casagli, N.; Tofani, V. Hotspot analysis of Permanent Scatterers (PS) for slow-moving landslides detection. In Proceedings of Landslide Processes: from geomorphological mapping to dynamic modelling, Strasbourg, France. 2009, pp57-62.
14. Lu, P.; Casagli, N.; Catani, F.; Tofani, V. Persistent Scatterers Interferometry Hotspot and Cluster Analysis (PSI-HCA) for detection of extremely slow-moving landslides. International Journal of Remote Sensing. 2012, 33(2), 466-489, doi:10.1080/01431161.2010.536185.

15. Di Martire, D.; Novellino, A.; Ramondini, M.; Calcaterra, D. A-Differential Synthetic Aperture Radar Interferometry analysis of a Deep Seated Gravitational Slope Deformation occurring at Bisaccia (Italy). Science of the Total Environment. 2016, 550, 556-573.
16. Meisina, C.; Zucca, F.; Notti, D.; Colombo, A.; Cucchi, A.; Savio, G.; Giannico, C.; Bianchi, M. Geological interpretation of PSInSAR data at regional scale. Sensors. 2008, 8(11):7469–7492, doi:10.3390/s8117469.
17. Peduto, D.; Cascini, L.; Arena, L.; Ferlisi, S.; Fornaro, G.; Reale, D. A general framework and related procedures for multiscale analyses of DInSAR data in subsiding urban areas. ISPRS Journal of Photogrammetry and Remote Sensing. 2015, 105, 186-210, doi:10.1016/j.isprsjprs.2015.04.001.
18. Brambilla G. Prime considerazioni cronologico-ambientali sulle filliti del Miocene superiore di Portalbera (Pavia-Italia settentrionale). Nuove ricerche archeologiche in provincia di Pavia. Civico Museo Archeologico di Casteggio e dell'Oltrepò Pavese, Atti del Convegno di Casteggio (PV),Casteggio, Italy. 1992, 109-113.
19. Pellegrini, L.; Vercesi, P.L. Considerazioni morfotettoniche sulla zona a sud del Po tra Voghera (PV) e Sarmato (PC). Atti Ticinensi di Scienze della Terra, Pavia, Italy. 1995, 38, 95-118.
20. Cavanna, F.; Marchetti, G.; Vercesi, P.L. Idrogeomorfologia e insediamenti a rischio ambientale. Il caso della pianura dell'Oltrepò Pavese e del relativo margine collinare. Universita degli studi di Pavia, Fondazione Lombardia Ambiente, Isabel Litografia, Gessate, Italy. 1998, pp. 14-72.
21. Pilla, G.; Sacchi, E.; Ciancetti G. Studio idrogeologico, idrochimico ed isotopico delle acque sotterranee del settore di pianura dell'Oltrepò Pavese (Pianura lombarda meridionale). Giornale di Geologia Applicata. 2007, 5, 59-74.
22. Braga, G.; Cerro, A. Le strutture sepolte della pianura pavese e le relative influenze sulle risorse idriche sotterranee. Atti Ticinensi di Scienze della Terra, Pavia, Italy. 1988, 31, 421–433.
23. Boni, A.; Boni, P.; Peloso, G.F.; Gervasoni, S. Dati sulla Neotettonica del Foglio di Pavia (59) e di parte dei fogli Voghera (71) ed Alessandria (70). C.N.R.P.F. Geodinamica. pubbl. n° 356. "Contributo alla realizzazione della Carta Neotettonica D'Italia. 1980, parte III", 1199-1223.
24. Assereto, E. Ricerche geologiche e geofisiche per la definizione di strutture sepolte nel settore pianeggiante sud-orientale della provincia di Pavia. Master Thesis. unpubblished. Unipv. 1980/1981.
25. Boni. Note illustrative della Carta Geologica d'Italia, F. 59 Pavia, Servizio geologico, Pavia, Italy. 1967, 68 pp.
26. Burrato, P.; Ciucci, F.; Valensise, G. An inventory of river anomalies in the Po Plain, Northern Italy: evidence for active blind thrust faulting. Ann. Geophys, Italy. 2003, 46, 5, 865-882.

27. Guidoboni, E.; Ferrari, G.; Mariotti, D.; Comastri, A.; Tarabusi, G.; Valensise, G. CFTI4Med, catalogue of strong earthquakes in Italy (461 BC-1997) and Mediterranean Area (760 BC-1500), INGV-SGA. 2007.
28. Meisina, C.; Zucca, F.; Fossati, D.; Ceriani, M.; Allievi, J. Ground deformation monitoring by using the permanent scatterers technique: the example of the Oltrepo Pavese (Lombardia, Italy). Engineering Geology. 2006, 88(3), 240-259, doi:10.1016/j.enggeo.2006.09.010.
29. DUSAF 2007. Available at: http://www.geoportale.regione.lombardia.it, Accessed on: 26/06/2016.
30. Meisina, C. Light buildings on swelling/shrinking soils: case histories from Oltrepo Pavese (north-western Italy). Int. Conf. on Problematic Soils, Nottingham, United Kingdom. July 2003, 28–30, vol. 2, pp. 365–374.
31. Meisina. C. Engineering geological mapping for urban areas of the Oltrepo Pavese plain (Northern Italy) IAEG2006, Nottingham, United Kingdom. 6-10 September 2006.
32. Ferretti, A.; Fumagalli, A.; Novali, F.; Prati, C.; Rocca, F.; Rucci, A. A new algorithm for processing interferometric datastacks: SqueeSAR™. IEEE Trans. Geosci. Remote Sens. 2011, 49, 3460–3470, doi:10.1109/TGRS.2011.2124465.
33. Plank, S.; Singer, J.; Minet, C.; Thuro, K. GIS based suitability evaluation of the differential radar interferometry method (D-InSAR) for detection and deformation monitoring of landslides. FRINGE 2009, ESA, Frascati, Italy, 30 Nov.–4 Dec. 2009. 2010, pp. 1–8.
34. Cigna, F.; Bateson, L. B.; Jordan, C. J.; Dashwood, C. Simulating SAR geometric distortions and predicting Persistent Scatterer densities for ERS-1/2 and ENVISAT C-band SAR and InSAR applications: Nationwide feasibility assessment to monitor the landmass of Great Britain with SAR imagery. Remote Sensing of Environment. 2014, 152, 441-466, doi:10.1016/j.rse.2014.06.025.
35. Samieie-Esfahany, S.; Hanssen, R.; van Thienen-Visser, K.; Muntendam-Bos, A. (2009. November). On the effect of horizontal deformation on InSAR subsidence estimates. FRINGE 2009, ESA, Frascati, Italy. 30 Nov.–4 Dec. 2009, (Vol. 30).
36. Raspini, F.; Cigna, F.; Moretti, S. Multi-temporal mapping of land subsidence at basin scale exploiting Persistent Scatterer Interferometry: case study of Gioia Tauro plain (Italy). Journal of Maps. 2012, 8(4). 514-524, doi:10.1080/17445647.2012.743440.
37. Notti, D.; Herrera, G.; Bianchini, S.; Meisina, C.; García-Davalillo, J. C.; Zucca, F. A methodology for improving landslide PSI data analysis. International Journal of Remote Sensing. 2014, 35(6). 2186-2214, doi:10.1080/01431161.2014.889864.

38. Notti, D.; Calò, F.; Cigna, F.; Manunta, M.; Herrera, G.; Berti, M.; Meisina, C.; Tapete, D.; Zucca, F. A User-Oriented Methodology for DInSAR Time Series Analysis and Interpretation: Landslides and Subsidence Case Studies. Pure and Applied Geophysics. 2015, 172(11), 3081-3105, doi:10.1007/s00024-015-1071-4.
39. Lin, Y. N. N.; Kositsky, A. P.; Avouac, J. P. PCAIM joint inversion of InSAR and ground-based geodetic time series: Application to monitoring magmatic inflation beneath the Long Valley Caldera. Geophysical Research Letters. 2010, 37(23).
40. Chaussard, E.; Bürgmann, R.; Shirzaei, M.; Fielding, E.J.; Baker, B. Predictability of hydraulic head changes and characterization of aquifer-system and fault properties from InSAR-derived ground deformation. Journal of Geophysical Research: Solid Earth. 2014, 119(8). 6572-6590, doi:10.1002/2014JB011266.
41. Berti, M.; Corsini, A.; Franceschini, S.; Iannacone, J.P. Automated classification of Persistent Scatterers Interferometry time series. Natural Hazards and Earth System Science. 2013, 13(8), 1945-1958, doi:10.5194/nhess-13-1945-2013.
42. Corti, T.; Muccione, V.; Köllner-Heck, P.; Bresch, D.; Seneviratne, S.I. Simulating past droughts and associated building damages in France. Hydrology and Earth System Sciences. 2009, 13(9). 1739-1747, doi:10.5194/hess-13-1739-2009.
43. Benedetti, L. C.; Tapponnier, P.; Gaudemer, Y.; Manighetti, I.; Van der Woerd, J. Geomorphic evidence for an emergent active thrust along the edge of the Po Plain: The Broni-Stradella fault. Journal of Geophysical Research: Solid Earth. 2003, 108(B5), doi:10.1029/2001JB001546.
44. Bozzano, F.; Esposito, C.; Franchi, S.; Mazzanti, P.; Perissin, D.; Rocca, A.; Romano, E. Understanding the subsidence process of a quaternary plain by combining geological and hydrogeological modelling with satellite InSAR data: The Acque Albule Plain case study. Remote Sensing of Environment. 2015, 168, 219-238, doi:10.1016/j.rse.2015.07.010.
45. Chaussard, E.; Amelung, F.; Abidin, H.; Hong, S. H. Sinking cities in Indonesia: ALOS PALSAR detects rapid subsidence due to groundwater and gas extraction. Remote Sensing of Environment. 2013, 128, 150-161, doi:10.1016/j.rse.2012.10.015.
46. Herrera, G.; Fernández, J. A.; Tomás, R.; Cooksley, G.; Mulas, J. Advanced interpretation of subsidence in Murcia (SE Spain) using A-DInSAR data-modelling and validation. Nat. Hazards Earth Syst. Sci. 2009, 9(3), 647-661, doi:10.5194/nhess-9-647-2009.
47. Tomás, R.; Herrera, G.; Cooksley, G.; Mulas, J. Persistent Scatterer Interferometry subsidence data exploitation using spatial tools: The Vega Media of the Segura River Basin case study. Journal of Hydrology. 2011, 400(3), 411-428, doi:10.1016/j.jhydrol.2011.01.057.

48. Bonì, R.; Herrera, G.; Meisina, C.; Notti, D.; Béjar-Pizarro, M.; Zucca, F.; González, P.J.; Palano, M.; Tomás, R.; Fernández, J.; Fernández-Merodo, J.A.; Mulas, J.; Aragón, R.; Guardiola-Albert, C.; Mora, O. Twenty-year advanced DInSAR analysis of severe land subsidence: The Alto Guadalentín Basin (Spain) case study. Engineering Geology. 2015, 198, 40-52, doi:10.1016/j.enggeo.2015.08.014.
49. Tosi, L.; Teatini, P.; Carbognin, L.; Brancolini, G. Using high resolution data to reveal depth-dependent mechanisms that drive land subsidence: the Venice coast, Italy. Tectonophysics. 2009, 474(1), 271-284, doi:10.1016/j.tecto.2009.02.026.
50. Cianflone, G.; Tolomei, C.; Brunori, C. A.; Dominici, R. InSAR Time Series Analysis of Natural and Anthropogenic Coastal Plain Subsidence: The Case of Sibari (Southern Italy). Remote Sensing. 2015, 7(12), 16004-16023, doi:10.3390/rs71215812.
51. Colesanti, C.; Ferretti, A.; Novali, F.; Prati, C.; Rocca, F. SAR monitoring of progressive and seasonal ground deformation using the permanent scatterers technique. Geoscience and Remote Sensing. IEEE Transactions. 2003, 41(7), 1685-1701, doi:10.1109/TGRS.2003.813278.
52. Watson, K. M.; Bock, Y. & Sandwell, D.T. Satellite interferometric observations of displacements associated with seasonal groundwater in the Los Angeles basin. Journal of Geophysical Research: Solid Earth. 2002, 107(B4), doi:10.1029/2001JB000470.
53. Meisina, C.; Zucca, F.; Fossati, D.; Ceriani, M.; Allievi, J. PS InSAR integrated with geotechnical GIS: some examples from southern Lombardia. Geodetic deformation monitoring: from geophysical to engineering roles. Springer Berlin Heidelberg. 2006, pp. 65-72, doi:10.1007/978-3-540-38596-7_8.
54. Geoportale Nazionale Ministero dell'ambiente e della tutela del territorio e del mare. Available at: http://wms.pcn.minambiente.it/ogc?map=/ms_ogc/WMS_v1.3/raster/ortofoto_bn_88.map, Accessed on: 26/06/2016.
55. Geoportale Nazionale Ministero dell'ambiente e della tutela del territorio e del mare. Available at: http://wms.pcn.minambiente.it/ogc?map=/ms_ogc/WMS_v1.3/raster/ortofoto_colore_00.map, Accessed on: 26/06/2016.
56. Corine Land Cover, SINAnet, Ispra. Available at: http://www.sinanet.isprambiente.it/it/sia-ispra/download-mais/corine-land-cover/corine-land-cover-cambiamenti-1990-2000/view, Accessed on: 26/06/2016.
57. Corine Land Cover, SINAnet, Ispra. Available at: http://www.sinanet.isprambiente.it/it/sia-ispra/download-mais/corine-land-cover/corine-land-cover-cambiamenti-2000rev-2006/view, Accessed on: 26/06/2016.

6.2. PSI-based methodology to land subsidence mechanism recognition

R. Bonì[1]*, C. Meisina[1], C. Perotti[1], F. Fenaroli[2]

[1]Department of Earth and Environmental Sciences, University of Pavia, Via Ferrata 1, 27100 Pavia, Italy;

[2]STUDIO TECNICO FENAROLI FABIO V. Mandalossa 3 - 25055 Pisogne (BS), Italy

*Correspondence to: R. Bonì (roberta.boni01@univesitadipavia.it).

The paper has been published in the Proceedings of the International Association of Hydrological Sciences, 2015. 372: 357-360.

doi:10.5194/piahs-372-357-2015

Abstract: A methodology based on Persistent Scatterer Interferometry (PSI) is proposed in order to disentangle the contribution of different processes that act at different spatio-temporal scales in land subsidence (i.e. vadose zone processes as swelling/shrinkage of clay soils, soil consolidation and fluid extraction). The methodology was applied in different Italian geological contexts characterized by natural and anthropic processes (i.e. a Prealpine valley and the Po Plain in northern Italy).

1. Introduction

Persistent Scatterer Interferometry (PSI) technique has significantly upgraded our ability to detect and quantify the land subsidence over wide areas. However the PSI technique shows two main limitations: 1) the PSI measurements represent the cumulative ground movements (natural plus anthropic and superficial plus deep displacements); therefore, the overlapping of several causes may make difficult the interpretation of ground deformation processes; 2) most of the geological processes are non-linear with seasonal and multiyear components, which are difficult to identify only through the use of the average rate of displacements VLOS (velocity along the Line of Sight). This work presents a methodology to analyse the ground deformations in order to disentangle the contribution of different processes that act at different spatio-temporal scales (i.e. swelling/shrinkage of clay soils, soil consolidation and fluid extraction), by the integration of PSI data and ground-based measurements.

2. Study areas

Two different geological contexts located in northern Italy and characterized by natural and anthropic processes were analysed: A Prealpine valley and a sector of the Po Plain (Figs.1 and 2).
The Valley bottom of the Oglio River (50 km^2) is located upstream the Iseo Lake and it is constituted by alluvial deposits (silt-sand, clay and sand-gravel layers) on Southalpine basement. This area is susceptible to subsidence processes, being, since the 1980, a high-urbanized area over unconsolidated alluvial materials.
The plain sector of the Oltrepo Pavese corresponds to the Southern and Central sector of the Po River Plain, with an extension of about 443 km^2. The Quaternary cover consists in the succession of impermeable sediments (silt and clay) and more permeable horizons (gravels and sandy). The area is particularly vulnerable to swelling/shrinkage of the clayey soils, subsidence due to ground water pumping and to natural consolidation of soft soils.

3. PSI datasets

PSI data elaborated by Tele-Rilevamento Europa (T.R.E.) using images acquired by ERS 1-2 (1992-2000) and RADARSAT (2003-2010) satellites were used. The datasets of the Valley bottom of the Oglio River were processed with PSInSAR™ technique and the Po Plain datasets with the SqueeSAR™ technique. The PSInSAR™ technique allows to obtain high resolution displacement measurements from individual radar reflectors or Persistent Scatterers (PS) like anthropic structure or rocks, the SqueeSAR™ technique permits to obtain measures also from distributed scatterers (DS) like sparse vegetated areas (Ferretti et al. 2011).

4. Methodology

The procedure is divided into three steps: 1) post-processing elaborations 2) characterization of ground motion areas 3) mechanism recognition.
Deformation accuracy assessment was carried out during the first step; the stable velocity range, the vertical and horizontal components of the motion were identified. The quality of Times Series was improved and possible errors (anomalous estimates not related to real ground motion) were corrected adopting the methodology of Notti *et al.* (2015). Thus, in a second step, the identification of the ground motion areas was performed using spatial clustering based of the unstable V_{LOS} (anomalous areas). Trends (i.e. uncorrelated, linear, non-linear) of deformation time series (TS) were recognized by the application of the Automated Classification of Persistent Scatterers Interferometry time-series (Berti *et al.* 2013). Selecting the unstable linear time series, the frequency distribution of the LOS

velocity was analysed and normal populations were separated through the expectation–maximization algorithm for mixtures of univariate normal function (Benaglia *et al.*, 2009) in order to distinguish linear processes triggered by different causes (i.e. natural and anthropic).
At the third step, the PSI data were compared to predisposing (i.e. soft soil thickness geological and geotechnical model) and triggering factors (i.e. piezometric level variations etc.). Moreover, seasonal component of motion was analyzed at detailed scale; considering detrended deformation time series.

4.1. Post-processing elaborations

The velocity threshold was assessed considering the twice of the standard deviation of the PS/DS with the higher coherence (>0.8-0.9) and a common stability threshold was set to ±2 mm/year for the PSI datasets over the Prealpine valley and ±1.5 mm/year for the plain area of Oltrepo Pavese. The movements are mainly vertical in both the study areas. Only in the Po Plain datasets, anomalous displacements were detected on the 09/03/1997 and 16/07/2000 (ERS dataset), and on 10/12/2008 scene (RADARSAT dataset). The last RADARSAT (RSAT) anomalous values might be related to snowfall occurred on the day of the Synthetic Aperture Radar (SAR) acquisition.

4.2. Characterization of the subsidence areas

Spatial clustering analysis based on the unstable VLOS allows to detect in the Prealpine valley 17 and 31 anomalous areas (around 1-1.5 km^2) in the time span 1992-2000 and 2003-2010, respectively (Fig. 1 panels *a* and *b*). In the Po Plain, 117 and 122 anomalous areas (around 7 km^2) were identified in the time span 1992-2001 and 2003-2010 (Fig. 2 panels *a* and *b*).
Most of unstable TS of the Prealpine valley have linear trends (Fig. 1. panels c and d). The VLOS ranges from -2 to -8 mm/yr in the period 1992-2000 and from -2 to -10 mm/yr in the period 2003-2010.
In the Po Plain the 51% (ERS) and 50% (RSAT) of unstable TS show non-linear trends within the range from -6.6 to -1.5 mm/yr in the time interval 1992-2001, and from -7 to -1.5 mm/yr in the period 2003-2010. The unstable linear TS show values within the range from -8 to -1.5 mm/yr (ERS) and from -7 to -1.5 mm/yr (RSAT) in the monitored periods (Figs. 2 panels c and d).
Local ground motions triggered by anthropic processes (i.e. external load due to new buildings with VLOS between -3 and -13 mm/yr) were recognized. In addition, the spatial distribution of the nonlinear TS in the Po Plain displays break dates in the ERS dataset (after 03/05/1998) and in the RSAT dataset (31/08/2009) related to wet and dry periods.

4.3. Mechanism recognition

The spatio-temporal analysis at large scale allowed to identify main ground motion areas located at Costa Volpino and Pisogne towns in the first test site and Voghera and Broni towns at the second one, where we carried out detailed analysis.

Different natural control mechanisms (i.e. water level fluctuation of the Iseo Lake, thickness of unconsolidated alluvial sediments) were analyzed to understand the displacements of the valley bottom of the Oglio River. The analysis highlights the geomorphologic control of the subsidence pattern; the stronger subsidence rate occurs in correspondence to a slope change (Fig. 1 panels e and f). Subsidence due to dissolution of evaporitic rocks will also be investigated.

The comparison of the TS with the geological model of the Po Plain shows that the time series characterized by stable velocity detains seasonal component of motion (seasonal amplitude is about 10 mm) where clay deposits are found (Figure 2.e). Subsidence areas due to groundwater exploitation were identified in the 1992 – 2001 period, (maximum V_{LOS} = -5 mm/yr); after 2003 (RSAT dataset) the decrease of groundwater pumping results in a decreasing trend of motion. (Figure 2.f).

5. Conclusions

A new methodology based on PSI data was developed and validated in various geological contexts. The procedure allowed to identify multiyear (groundwater pumping, construction of new buildings, consolidation of soft soils, geomorphological processes) and seasonal (volume change of clay soils, groundwater oscillations) ground movements and proved to be an efficient tool for distinguish different anthropic and natural processes. The methodology can be used for land use planning and civil protection purposes.

References

Benaglia, T., Chauveau, D., Hunter, D. R. and Young, D. (2009). “mixtools”: an R package for analyzing finite mixture models. J. Statist. Software, 32, 1–29.

Berti, M., Corsini, A., Franceschini, S. and Iannacone, J. P. (2013). Automated classification of Persistent Scatterers Interferometry time series. Natural Hazards and Earth System Science, 13(8), 1945-1958.

Ferretti, A., Fumagalli, A., Novali, F., Prati, C., Rocca, F., & Rucci, A. (2011). A new algorithm for processing interferometric data-stacks: SqueeSAR. Geoscience and Remote Sensing, IEEE Transactions on, 49(9), 3460-3470.

Notti, D., Calò, F., Cigna, F., Manunta, M., Herrera, G., Berti, M., Meisina, C., Tapete, D. and Zucca, F. (2015). A User-Oriented Methodology for DInSAR Time Series Analysis and

Interpretation: Landslides and Subsidence Case Studies. Pure and Applied Geophysics, DOI 10.1007/s00024-015-1071-4.

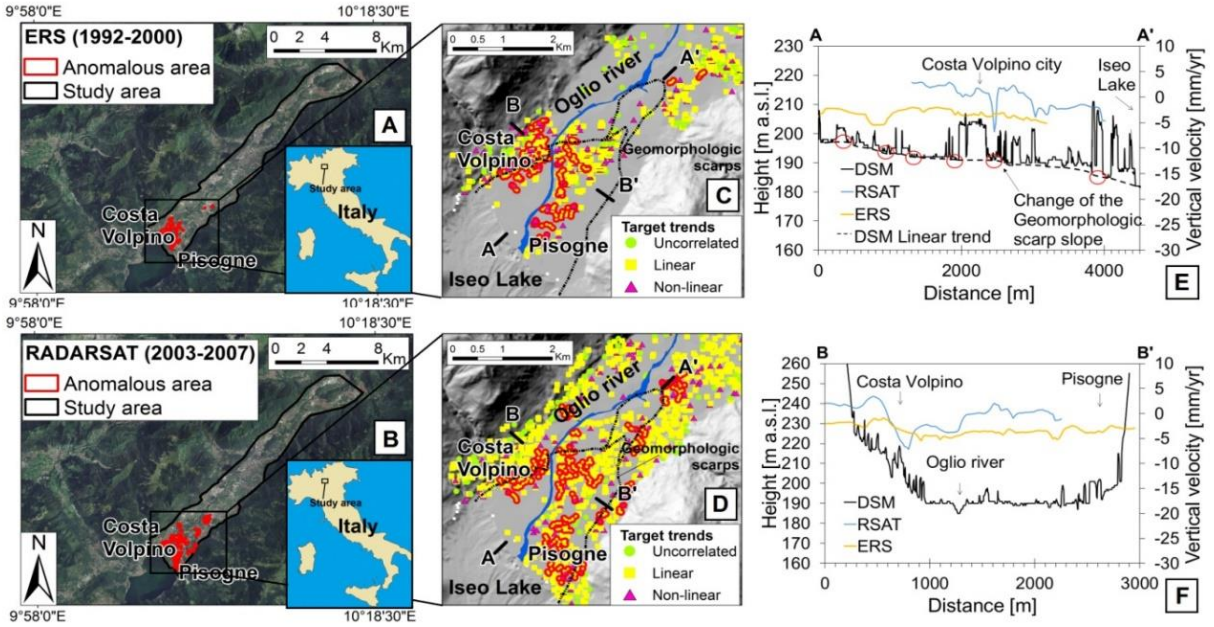

Figure 1. Anomalous areas detected by ERS descending (A) and RADARSAT descending (B). Target trends of ERS (C) and RADARSAT (D) dataset, and Digital surface model (DSM) of the Valley bottom of the Oglio river. Cross sections along the A-A' (E) and B-B'(F) sections of the ERS and RADARSAT (RSAT) datasets.

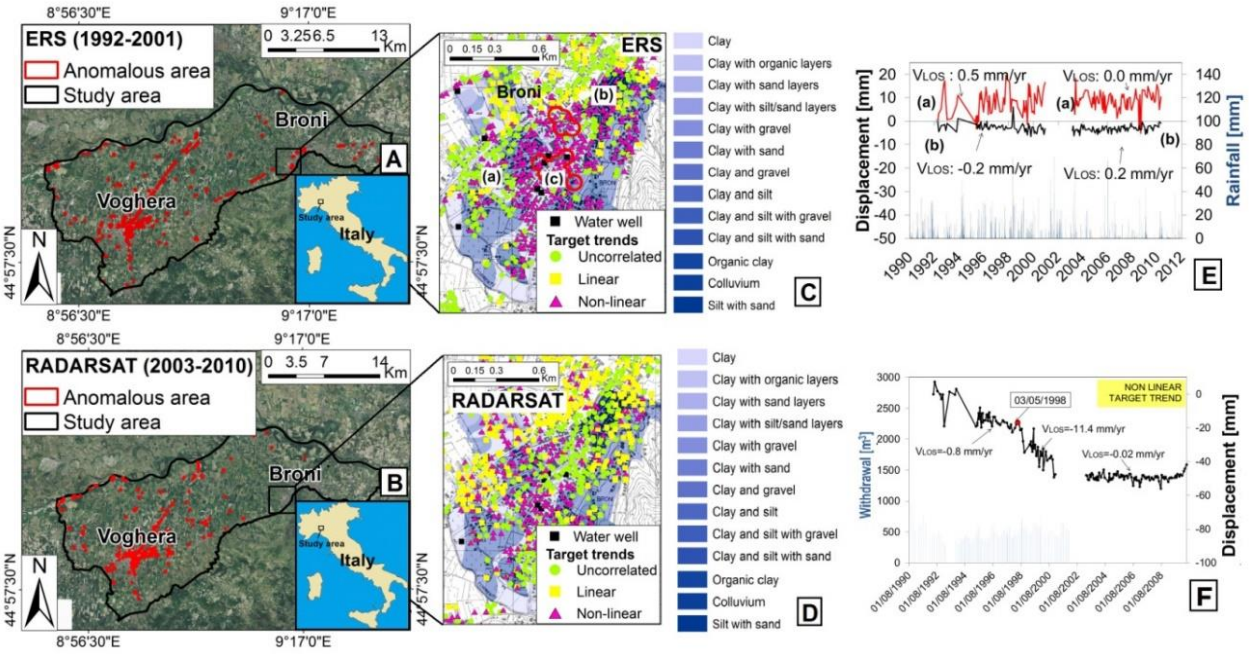

Figure 2. Anomalous areas detected by ERS descending (A) and RADARSAT ascending (B). Target trends of ERS (C) and RADARSAT (D) dataset, and lithological map of Broni town. TS of ERS and RADARSAT datasets at the location a, b compared with daily rainfall (E). Comparison of TS at location *c* and the groundwater exploitation (F).

6.3. Integration of multi-sensor A-DInSAR data for landslide inventory update

Roberta Bonì[1*], Massimilano Bordoni[1], Claudia Meisina[1], Alessio Colombo[2] and Luca Lanteri[2]

[1]Department of Earth and Environmental Sciences, University of Pavia, Via Ferrata 1, 27100 Pavia, Italy;

[2]ARPA Piemonte - Agenzia Regionale per la Protezione Ambientale, Dipartimento Tematico Geologia e Dissesto Struttura Semplice Monitoraggi e Studi Geologici, Via Pio VII, 9, Torino 10135, Italy.

The paper has been submitted for the 4th World Landslide Forum "LANDSLIDE RESEARCH AND RISK REDUCTION FOR ADVANCING CULTURE OF LIVING WITH NATURAL HAZARDS" Ljubljana, Slovenia, May 29 – June 2, 2017.

Abstract: A systematic and reproducible methodology to analyze multi-sensors advanced satellite radar differential interferometry (A-DInSAR) data for identifying ground motion areas and for updating landsides inventories is proposed. We apply the methodology in a wide area of north-western Italy, corresponding to Piedmont region that is affected by different landslides. We use satellites images acquired, in ascending and descending acquisition geometry, by C-band (ERS ½ and ENVISAT, RADARSAT) and X-band (COSMO-SkyMed) sensors and processed using SqueeSARTM, PSInSARTM and PSP-IfSAR techniques. Landslides characterized by linear and non-linear behavior were recognized.

Keywords: A-DInSAR, Landslides, Piedmont

1. Introduction

In the last decade, advanced satellite radar differential interferometry (A-DInSAR) has become a powerful tool for updating landslides inventories. The technique contributes (i.) to monitor the deformation pattern over large areas (ii.) to verify or modify the landslide boundaries and (iii.) to define the state of activity of the phenomenon (Meisina et al., 2008; Cascini et al., 2010; Herrera et al., 2013; Cigna et al., 2013; Bianchini et al., 2013; Di Martire et al., 2016; Dai et al. 2016). The recent improvements to A-DInSAR data acquired by the COSMO-SkyMed satellites and the future new ESA Sentinel missions, that act at higher spatio-temporal resolution, need an appropriate

methodology to analyze extremely large datasets that consist on enormous amount of measuring points.

To address these problems, a guiding procedure was proposed to analyze multi-sensors A-DInSAR data for update the landslides inventories. The methodology was applied in a wide area of north-western Italy, corresponding to Piedmont region that is affected by a large amount of different landslides. Satellites images were acquired, in ascending and descending acquisition geometry, by C-band (ERS ½ and ENVISAT, RADARSAT) and X-band (COSMO-SkyMed) sensors and processed using SqueeSARTM, PSInSARTM and PSP-IFSAR techniques.

2. Study Area

The Piedmont region, located in northwest Italy, has an extension of 25,000 km2 and it is characterized by different geological contexts such as Alps, Apennines, Langhe and Monferrato and Plain (Figure 1b). In particular, the study area is located in the Alps domain and in the Torino hill context. The Alps are characterized by high slope gradients and the presence of foliated and massive rocks, meanwhile in the Torin hill, the slopes in the argillaceous and marly successions are mantled with 1 to 6 m thick clayey-silty colluvial deposits.

The SIFraP project (Landslides information system in Piedmont) identified more than 30.000 slope instabilities for the Piedmont region. The alpine environment is mainly characterized by the presence of rock-falls/topples, large complex landslides and deep seated gravitational deformations. The Torino hill is mainly affected by rotational/translational slides, shallow rapid flows, slow flows and complex landslides.

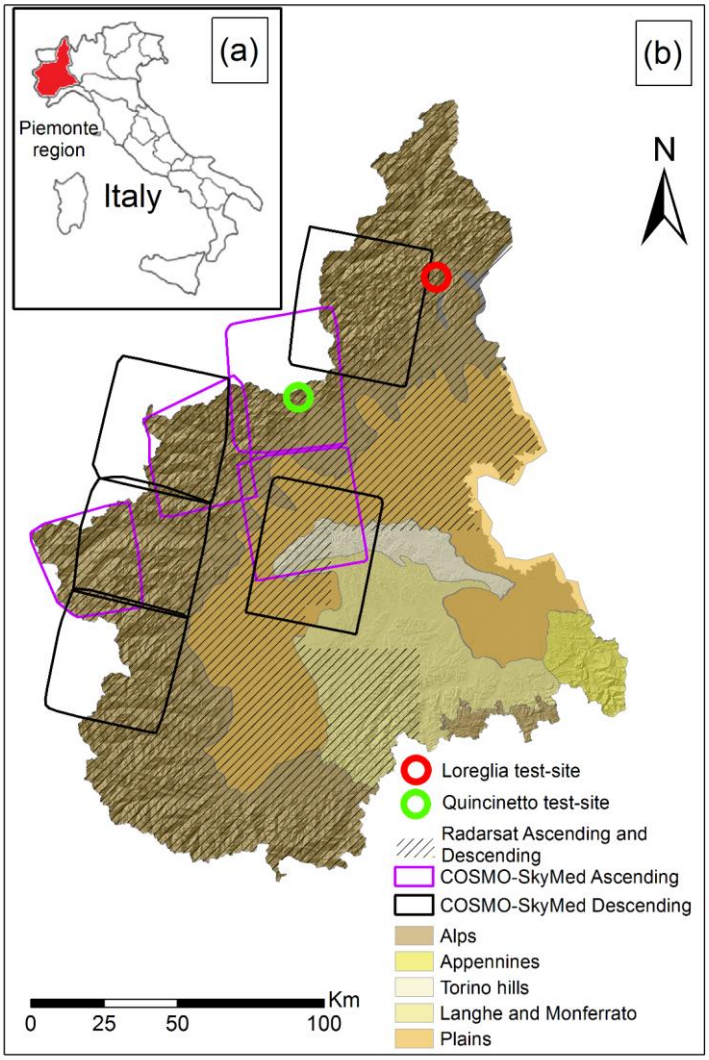

Figure 1(**a**) Location of the study area. (**b**) Geological contexts in the studied area and location of the available SAR images acquired by RADARSAT and COSMO-SkyMed sensors.

3. A-DInSAR data

The input satellite data for this study consists of ERS-1/2, Envisat, RADARSAT and COSMO-SkyMed SAR scenes acquired in ascending and descending mode (Table 1).

The ERS-1/2 and Envisat datasets are characterized by nominal repeat cycle of 35 days and a total coverage over the Piedmont Region.

The available scenes acquired by the RADARSAT and COSMO-SkyMed sensors are represented in Fig. 1b and are characterized by nominal repeat cycle respectively of 24 and 11 days.

Satellites images acquired by C-band (ERS ½ and ENVISAT and RADARSAT) and X-band (and COSMO-SkyMed) sensors and processed using PSInSARTM (Ferretti et al., 2001) SqueeSARTM (Ferretti et al., 2011) and PSP-IfSAR techniques (Costantini et al., 2011), were exploited. The project was carried out in collaboration with ARPA Piemonte (Regional environmental agency) and a part of the interferometric data were provided by the Italian Ministry of Environment in the frame of the "Extraordinary Plan of Environmental Remote Sensing" (PST-A).

Table 1. Details on the SAR datasets and their processing.

Dataset	Satellite	Orbit	Time span	Processing technique
PST-A Piemonte	ERS-1/2	Asc. Desc.	1992-2001	PSInSAR™
ERS Piemonte	ERS-1/2	Desc.	1992-2001	PSInSAR™
Bardonecchia	ERS-1/2	Asc. Desc.	1992-2001	SqueeSAR™
Piemonte Nord	RADARSAT	Asc. Desc.	2003-2009	SqueeSAR™
Piemonte Sud	RADARSAT	Asc. Desc.	2003-2009	SqueeSAR™
Torino	RADARSAT	Asc. Desc.	2003-2009	SqueeSAR™
PST-A Piemonte	Envisat	Asc. Desc.	2003-2010	PSInSAR™
Cosmo PST-A	COSMO-SkyMed	Asc. Desc.	2011-2014	PSP-IFSAR
Alta Val Susa	COSMO-SkyMed	Asc. Desc.	2011-2014	PSP-IFSAR
Orco-Lanzo	COSMO-SkyMed	Asc.	2008-2015	SqueeSAR™

4. Method

To date, various methodology has been proposed to employ A-DInSAR data to identify ground motion areas and to update landsides inventories (Meisina et al., 2008, Cascini et al., 2010; Cigna et al., 2013; Di Martire et al., 2016). However, the previous approaches were mainly based on the average rates of displacement, constrained by the fact that the previous A-DInSAR data allowed to obtain noisy time series difficult to interpret, showing some limitations to distinguish non-linear processes. A novel methodology is proposed, to identify the areas of ground motion in order to

update the landslide inventories, on the basis of the temporal patterns in the displacement time series. The methodology consists of three main phases (Fig.2):

1) post-processing elaborations of the A-DInSAR data (to remove possible errors that affect the whole dataset);

2) identification of the ground motion areas characterized by different deformation style mode (i.e. lowering, uplift and non-linear trend) by the use of automatic and semi-automatic statistical analysis on the displacement time series (TS);

3) interpretation of the ground motion areas providing analysis between the ground motion areas and the landslides distribution (The Piedmont Landslide inventory – SIFraP) at large scale, and then at local scale with a detailed in situ analysis for the most interesting sites.

Following, step by step the procedure is described.

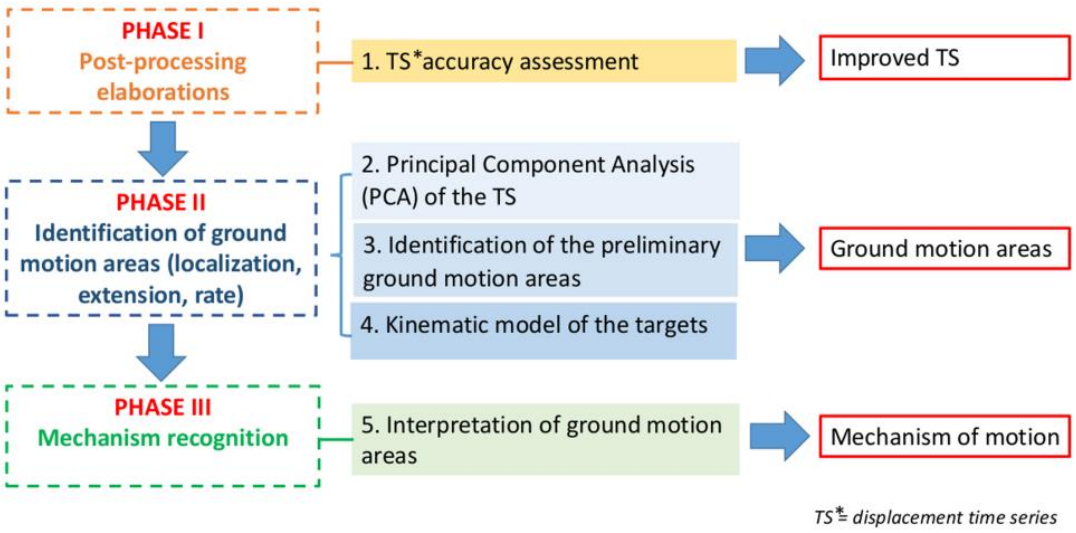

Figure 2. Flowchart of the methodological approach to detect the ground motion areas.

4.1. Time series accuracy assessment (Phase I)

The displacements time series (TS) detected by each target (PS or DS) may be affected by local error or regional trends that can be observed in the whole dataset. Therefore, post-processing analysis on the A-DInSAR data are necessary to avoid misinterpretation of unreal ground movements. The check of the displacements time series is performed selecting the most coherent (>0.9) targets with average line of sight (LOS) velocities in the range ±0.5 mm/yr; where no significant movements are expected. More precisely, the approach proposed by Notti et al. (2015)

was applied, in order to correct problems due to regional unreal trends and anomalous displacement detected at certain date (i.e. unreal movements at the same time of meteorological events as snowfall).

4.2. Principal Component analysis (PCA) of the TS (Phase II)

Principal Component Analysis (PCA) was previously applied on SAR scenes to extract the spatiotemporal variability of deformation (Chaussard et al., 2014). Here, the same approach is applied on SAR scenes acquired by C-band and X-band sensors to detect the Principal Component of motion for each dataset. It is worth noting that each dataset has been previously divided, distinguishing slope and flat areas in order to better detect the Principal Component of the different geomorphological contexts.

Then, Principal Component Analysis (PCA) is implemented using a matrix organization location versus time (T-mode). A matrix, in which each column contains the LOS displacements for each SAR scene and where each row contains the displacement time series of the targets (PS-DS), was formed. The main outcomes are: the eigenvectors, the percent of variance that each eigenvalue captures, and the Principal Components (PC) score maps. The Principal Components, PC scores related to each observation (PS-DS) are fundamental for knowing the correlations with the Principal Components in the whole dataset; the higher values correspond to higher correlation with the analyzed PC.

4.3. Identification of the preliminary ground motion areas (Phase II)

Landslides can be characterized by linear (e.g. Constant displacement rates) and non-linear ground movements (e.g. acceleration, deceleration, seasonal movements). While the average LOS velocity of targets is useful to separate movement and non-movement areas, the same parameters is not efficient to recognize ground motion areas affected by non-linear processes. Even targets with an average LOS velocity in the stable range can be affected by significant non-linear movements.

Therefore, PCA results can be exploited to identify ground motion areas with linear and non-linear trends over wide areas.

The ground motion areas are identified using spatial cluster of significant PC scores. First, the threshold of the PC scores was defined by applying a statistical inspection of the PC score frequency distributions.

If the histogram of the PC scores shows a normal distribution (skewness=0), the twice of the standard deviation was considered as threshold, whereas, if the PC scores shows asymmetrical distribution (skewness≠0) the threshold is defined as being equal to the interquartile range (IQR). Then, PS-DS with PC scores higher than the threshold are selected and a buffer zone of 50 m around the detected measuring points can be derived.

Therefore, ground motion areas consist of clusters of a minimum of 3 PS-DS with a maximum distance of 50 meters. In the case of the COSMO-SkyMed data, it was implemented a maximum distance of 25 meters in order to taking into account of the higher targets density.

The approach to extracting ground motion areas is based on the procedure proposed by Meisina et al. (2008), but, herein, the delineated areas are derived from the PCA analysis.

4.4. Kinematic model of the targets (Phase II)

Following, an automatic sequential procedure based on statistical tests, thought PS-time program implemented by Berti et al. (2013), was exploited to classify the TS into one of three predefined target trends that are: uncorrelated, linear and non-linear.

Then, the preliminary ground motion areas are filtered using an index of correlation (Ic) that is the ratio between correlated (i.e. linear and non-linear) and total number of PS-DS. The index is computed using the following equation (1):

$$Ic = \frac{PS - DS_{lin,non-lin}}{PS - DS_{tot}} \quad [1]$$

The ground motion areas that are taking into account in the next steps are distinguished by Ic higher than 40%. This filter permits to focus the attention on ground motion areas characterized by significant trends (i.e. linear and non-linear).

4.5. Interpretation of the ground motion areas (Phase III)

Once, the ground motion areas have been detected, the processes are interpreted by integrating these into a Geographical Information System (GIS) with ancillary data (such as topographic maps, aerial orthophotos, Digital Elevation Model, landslide inventory, geological and geotechnical data) in order to update the landslide inventories.

Taking into account that the different geometry acquisitions and the LOS measurements did not permit to detect the real movements (Plank et al., 2012)., the percentage of the real movement is computed in the area where there is the coverage by data acquired by the four sensors (ERS-1/2, Envisat, RADARSAT and COSMO-SkyMed).

In addition, if both geometry acquisitions are available, vertical and horizontal components of motion were computed (Notti et al., 2014).

5. Results and discussion

In order to analyse the percentage of landslides suitable for the different sensors (ERS-1/2, Envisat, RADARSAT and COSMO-SkyMed) and to evaluate their effectiveness in slope movements identification, a simple statistical analysis of the number of landslide with PS-DS information was firstly performed (Fig.3).

For this purpose, the Persistent Scatterers (PS)-Distributed Scatterers (DS) were overlaid upon the SIFrAP landslide inventory. The results highlight the improvement of the landslides detection using the COSMO-SkyMed data, where the percentage of landslides with at least 1 PS-DS, increase from around 20% with the ERS-1/2 data to 60% with the COSMO-SkyMed data. It is worth noting that about the 80%-90% of the DSGSD are detected by the COSMO-SkyMed data (Fig.3).

By the use of the available A-DInSAR data, ground motion areas were detected following the methodology described in the section 4.

The results of the PCA application for each dataset show that, in most of the cases, two Principal Components were recognized. The first Component of motion (PC1) explains a percentage of variance in the range from 65 to 95% of the movement and corresponds to a linear movement away from the satellite sensor. Conversely, the second Component of motion (PC2) explains a percentage of variance in the range from 1 to 20% and it is a movement towards the satellite sensor. Only two datasets acquired by RADARSAT and COSMO-SkyMed sensors show a third Component of motion (PC3) that explains percentage of variance in the range from 2 to 5% and corresponds to a non-linear trend with acceleration in the movement of lowering associated to determined break in the time series.

The methodology has the strength to immediately differentiate ground motion areas with different pattern in the deformation, also at regional scale. Thanks to the application of PCA analysis, an enormous amount of measuring points can be easily processed, detecting the principal components

which describe the deformation over wide areas. The full time series exploitation allow to recognize the processes which are characterized by linear or non-linear trends, identifying also different portions of the same landslide characterized by different typologies of movement.

Supplementary information about the kind of kinematic behavior were added to the landslides inventory in order to support the understanding of the mechanisms of the landslide movements.

The reliability of the results obviously depends on the quality of the dataset.

Additional statistical analysis was carried out to assess the percentage of the landslides mapped via SIFrAP (update until 2014), distinguishing the typologies, that includes ground motion areas. The 40%-80% of the landslides detected using PC1, PC2 and PC3 of the RADARSAT and COSMO-SkyMed data, are rockfalls (Table 2). This is consistent with the fact that this type of landslide in mainly covered by debris which are targets at high coherence. The 10%-20% of the landslides detected by PC1, PC2 and PC3 are complex landslides and DSGSD.

Following, local scale analysis was carried out in two test areas, selected on the basis of their representativeness from the geological-geomorphological point of view, that are located over Loreglia and Quincinetto villages. In particular, Loreglia represents a case study where the methodologies allowed to identify different kinematic trends in the same phenomena. Instead, Quincinetto is an example of very hazardous phenomenon, with clues of a possible dramatic collapse.

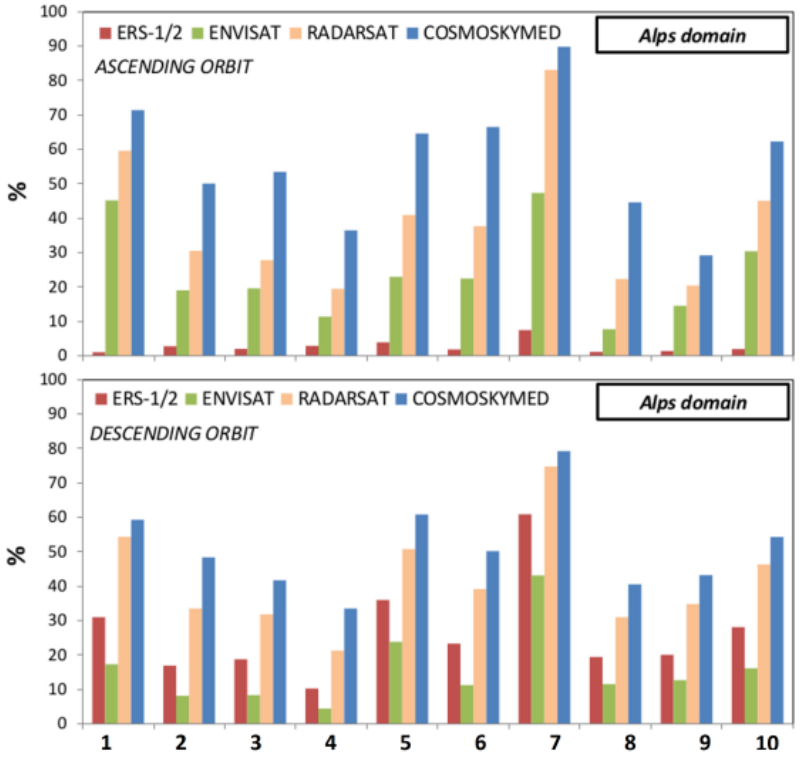

Fig. 4 Percentage of landslides with at least 1 PS-DS in the Alps domain using all available A-DInSAR data acquired in ascending and descending geometries. 1 Areas affected by rockfalls. 2 Areas affected by shallow landslides. 3 Slow flow. 4 Shallow rapid flow. 5 Complex landslides. 6 Rockfalls/topples. 7 DSGSD. 8 Rotational/translational slides. 9 Non classified. 10 Total number of landslides.

Table 2. Percentage of landslides with ground motion areas detected by Radarsat and COSMO-SkyMed data.

SIFrAP Landslides typology	Landslides with ground motion areas detected by RADARSAT			Landslides with ground motion areas detected by COSMO-SkyMed		
	PC1	PC2	PC3	PC1	PC2	PC3
Rockfalls	36%	54%	26%	40%	47%	78%
Shallow landslides	3%	5%	3%	3%	3%	-
Slow flow	4%	3%	-	4%	4%	-
Shallow rapid flow	4%	4%	23%	4%	4%	-
Complex landslides	16%	8%	14%	16%	15%	-
Rockfalls/ topples	9%	7%	20%	8%	5%	-
DSGSD	13%	7%	11%	11%	9%	2%
Rotational/ translational slides	10%	7%	3%	12%	11%	-
Non classified	3%	2%	-	3%	2%	-

5.1. Loreglia landslide case study

Loreglia landslide is a complex phenomenon located in Strona valley, starting with a rotational geometry that evolves into a debris slide and flow. This landslide affected entirely the village of Loreglia. It is still active, as testified by several cracks and fissures that affect buildings and roads in the historical part of the village. The landslide is not monitored by in situ instruments, therefore in this case the A-DInSAR technique is the unique tool to monitor the movements.

The landslide occupies an area of 402500 m2. It is located along a west-facing hillslope with an altitude ranging between 1100 and 60o m a.s.l. Slope gradient reaches an average value of 40°. Bedrock geology is composed of dioritic-kinzigitic rocks (Fig.4a). Landslide affects glacial deposits and colluvial deposits. The thickness of the glacial deposits is in the order of 20-25 m. Due to aspect of the slope (west-facing), this landslide can be better investigated using A-DInSAR data acquired in descending geometry. This landslide has been detected by ERS-1/2 and ENVISAT and RADARSAT data. ERS-data, acquired in the period 1992-2000, showed VLOS in the order of -5 mm/y in correspondence of the landslide, with peaks of -10 mm/y. Displacement series of this time period were steady and linear. With reference to RADARSAT data acquired in descending geometry (period March 2003-January 2010), ground motion areas were detected.

90% of RADARSAT targets showed a significant Los displacement. In the covered period, VLOS had average values of -5/-4 mm/y, with peaks in the order of 10 mm/y (Fig. 4d). Lowering displacement characterized particularly the historical centre of the village.

The application of the developed methodology allowed to identify two ground motion areas (Fig. 4b): i) an area characterized by a linear lowering displacement, during the period of acquisition of RADARSAT data; ii) an area, located in correspondence of Loreglia village, characterized by a non-linear displacement time series, that highlights an increase in displacement rate exactly in correspondence of the break of August 2008 (Fig. 4d). The first ground motion area belonged to the PC1 identified by the application of the PCA to the used dataset, while the second one belonged to the PC3. It is important to highlight that the two ground motion areas are divided, in field, by a morphological break of the slope continuity.

A-DInSAR data time series classification confirms that most of the targets were characterized by non-linear trends, with a limited percentage (10-15%) of targets with linear trend (Fig. 4c). Evidence ratio of the breakpoint of the non-linear time series (BICW, Berti et al., 2013) allowed to verify real presence of a break in the time series which determined its non-linearity. Non-linear targets in the historical part of Loreglia village had BICW values higher than 1.2, demonstrating further the strong non-linearity of these time series. Instead, in the slope area located under the village, non-linear targets had BICW values always lower than 1.0. ENVISAT data were contemporary to RADARSAT

dataset and showed similar values of VLOS along the landslide (-10/-3 mm/y). August 2008 break was also identified in ENVISAT data time series only in correspondence of PC3 ground motion area.

A-DInSAR time series was correlated with rainfall data taken by the rain gauge of Omegna station (10 km east from the test site), belonging to the Piedmont region network of meteorological stations.

The break event, which caused the increase in the rate of displacement of a portion of Loreglia landslide, was linked to an intense rainy period, affected the study site in spring and summer 2008. A strong correlation appeared between the cumulated rainfall amount of 90 days and the break of August 2008. The acceleration in displacement rate occurred in correspondence of a period of exceptional rainfalls, with a peak of 1000 mm in 90 days at the beginning of August 2008 (Fig. 4e). Similar rainfall amount was not measured before or after this break.

The identified ground motion areas followed well the results of the classification of targets time series, allowing, thus, to identify two parts of the landslide with different movement behaviors. A further demonstration of the existence of these different parts of the phenomenon was given by the analysis of the rate of displacement along the LOS before and after the identified break. In the sector of the landslide characterized by a linear trend of displacement, VLOS was around -5/-4 mm/y (Fig. 4d). Instead, in the other ground motion area, VLOS increased significantly after August 2008 break, passing from -4 to -10 mm/y (Fig. 4d).

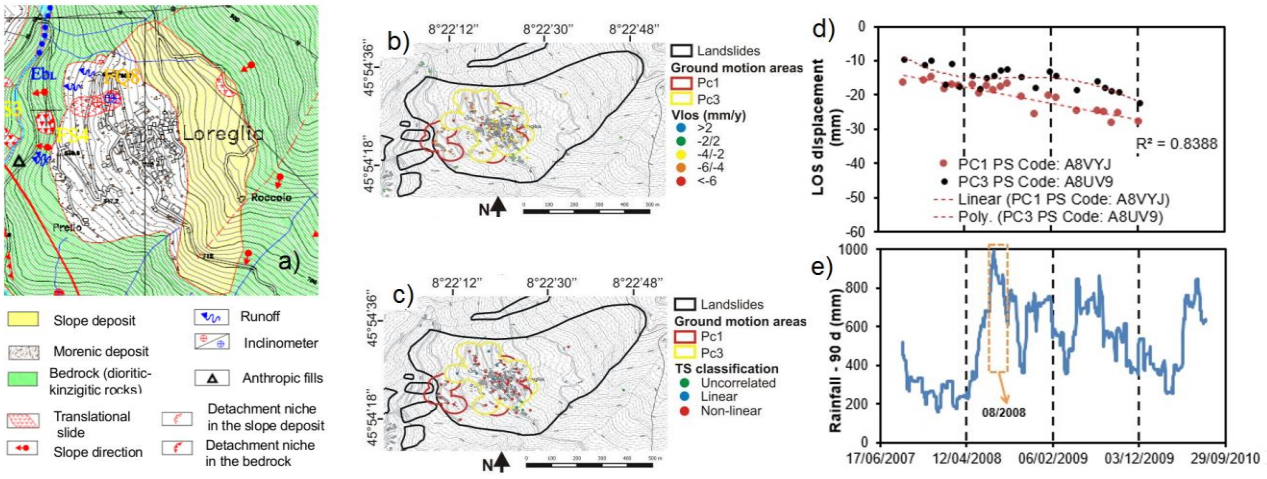

Figure 4. Loreglia case study: a) Geological setting of Loreglia landslide; b) displacement rate along the LOS (VLOS) for RADARSAT data acquired in descending geometry; c) time series (TS) classification of the same RADARSAT data; d) typical trend of LOS displacement in the two identified ground-motion areas; e) cumulated rainfall amount of 90 days.

5.2. *Quincinetto landslide case study*

Quincinetto landslide is a complex phenomenon in Dora Baltea river valley, starting as a debris slide and evolving in a rock fall (Fig. 5a). This landslide is still active, threatening the buildings close to the phenomenon and a highway located at the end of the affected slope. The hazard of this landslide is also confirmed by several rockfalls started from the landslide detachment zone, happened in the last years.

The most important one occurred in 2 May 2012, when, after a particularly intense thunderstorm, 45m3 of rocks and debris moved along the slope damaging the highway in the bottom of the valley. The landslide occupies an area of 36200 m2, with a length of 840 m and a width of 50 m. It is located along a north east-facing hillslope and it affects a part of this slope between altitudes of 870 and 280 m a.s.l. Slope gradient reaches an average value of 32°. Landslide deposits is formed of debris and boulders of different dimensions, composed of metamorphic rocks, especially, micaschists and gneiss.

Due to aspect of the slope (north east-facing), this landslide can be better investigated using A-DInSAR data acquired in ascending geometry. This landslide was investigated through ERS-1/2, ENVISAT, RADARSAT and COSMO-SkyMed data. Last sensor data were also used to detect ground motion areas.

The first three types of sensors showed that for the covered time span (1992-2010) the landslide was active in its upper part, with steady VLOS generally in the range -27/-10 mm/y. Considering COSMO-SkyMed dataset, in the upper part of Quincinetto landslide, all the targets showed VLOS higher than -2 mm/y, for the acquisition period of this satellite (May 2011-April 2014). In particular, most of the targets of this sector had VLOS in the order of -15/-10 mm/y, testifying a strong rate of displacement similar to that one measured by previous sensors (Fig. 5b). In the remnant parts of the phenomenon, the rate of displacement, registered in the period of COSMO-SkyMed dataset acquisition, is lower, with most of the targets with a VLOS between -2 and 2 mm/y (Fig. 5b). In the most active sector of the landslide, A-DInSAR data time series classification highlighted that 92% of the targets were characterized by linear trends, with a constant rate of measured displacement (Fig. 5c). The application of the developed methodology allowed to identify an extended ground motion area in the upper part of the landslide (Fig. 5c). Another littler area was identified at the edge of the landslide crown (Fig. 5c). Both these ground motion areas belonged to the PC1 identified by the application of the PCA to the used dataset. They testified a significant lowering displacement, characterized by a constant in time linear displacement trend. The identified ground motion areas followed well the results of the classification of targets time series, allowing thus to identify the most active sectors of the landslide body.

Furthermore, the COSMO-SkyMed data were compared with the measurements acquired by five GPS stations (see the location in Figure 5c), installed since October 2012. It must be taken into account that satellite-registered velocities are referred to the LOS. Therefore, in order to compare ground (GPS) and interferometric measures, it was necessary to estimate the percentage of real movement that the satellite is able to identify in relation to the acquisition geometry and to the topographic characteristics of the site (Plank et al., 2012). Displacement along the LOS was then divided for this percentage, obtained the displacement along the slope that is directly comparable with GPS measures. For the time period covered by COSMO-SkyMed data, GPS and DInSAR time series are quite in agreement, with slowly higher displacements measured by satellite data (Fig. 5d, e). The error between the A-DinSAR and the GPS measurements reaches values of 3.67 mm/yr and 5.83 mm/yr, respectively at G6QUIA2 and G6QUIA4.

Hence, large instable area can be considered as a predisposing factor for the activation of phenomena as the one occurred at the beginning of May 2012.

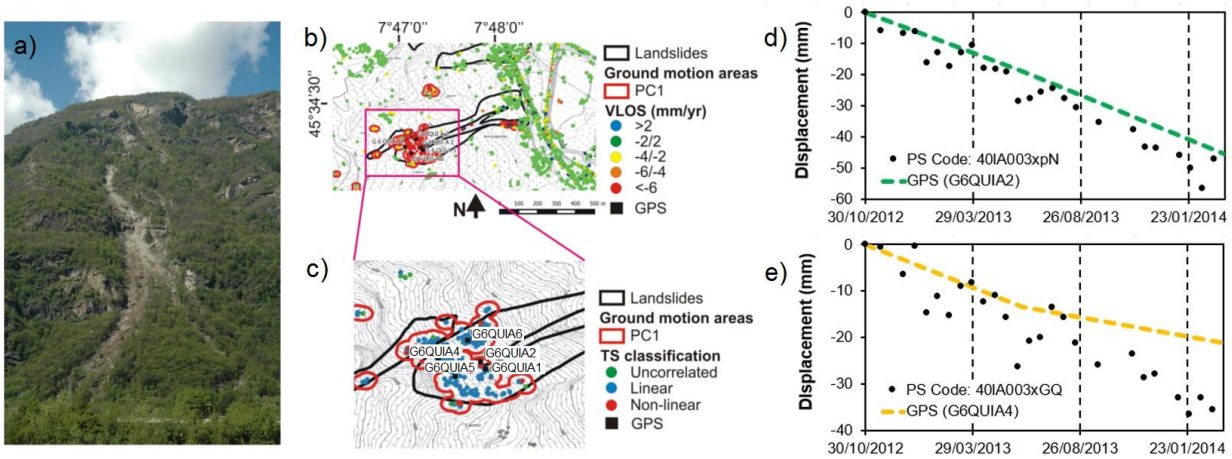

Figure 5. Quincinetto case study: a) Picture of Quincinetto landslide; b) displacement rate along the LOS (VLOS) for COSMO-SkyMed data acquired in ascending geometry; c) time series (TS) classification of the same COSMO-SkyMed data.; d) comparison between displacement measured by G6QUIA2 GPS and the closest COSMO-SkyMed target; e) comparison between displacement measured by G6QUIA4 GPS and the closest COSMO-SkyMed target.

6. Conclusions

The ability of a novel methodology to detect different landslides over wide area, by analysing multi-sensors and multi-temporal A-DInSAR data is described. The proposed methodology is addressed to overcoming limitations such as the analysis of large datasets by exploiting the great potential contained in the A-DInSAR time series. The principal novelty of the proposed approach is the exploitation of full time series, which enables to the detection of ground motion areas affected by

linear and non-linear trend. The 80%-90% of the DSGSD can be detected by the use of the COSMO-SkyMed data. The methodology allows to identify different portion of the landslide characterized by different behaviors. For example, non-linear process was identified in the village of Loreglia and the break event, which caused the increase in the rate of displacement of a portion of Loreglia landslide, was linked to an intense rainy period, affected the study site in spring and summer 2008. In this case, the A-DInSAR data represents the unique technique to monitor the landslide's movements. Furthermore, the methodology shows the capability to identify large unstable area that can be considered as a predisposing factor for the activation of phenomena as the one occurred at the beginning of May 2012 in Quincinetto landslide.

The proposed methodology can be easily applied to others geological contexts, using different A-DInSAR data. Future investigations will be performed to assess areas affected by new landslides and to update the state of activities of the landslide inventory in the Piemonte region.

Acknowledgments

The work was developed in the framework of the Project "Servizio di aggiornamento del SifraP, 2016 (Sistema Informativo Frane in Piemonte) finalizzato alla definizione della pericolosità da frana mediante analisi di dati d'archivio, fotointerpretazione ed analisi di dati di interferometria satellitare". The authors would like to thank the anonymous reviewers for their valuable comments and suggestions to improve the quality of the paper.

References

Berti M, Corsini A, Franceschini S, Iannacone J P (2013) Automated classification of Persistent Scatterers Interferometry time series. Natural Hazards and Earth System Science. 13(8), 1945-1958, doi:10.5194/nhess-13-1945-2013.

Bianchini S, Herrera G, Mateos R M, Notti D, Garcia I, Mora O, Moretti S (2013). Landslide activity maps generation by means of persistent scatterer interferometry. Remote Sensing, 5(12), 6198-6222.

Cascini L, Fornaro G, Peduto D (2010) Advanced low- and full-resolution DInSAR map generation for slow-moving landslide analysis at different scales. Eng. Geol. 112, 29–42.

Chaussard E, Bürgmann R, Shirzaei M, Fielding E J, Baker B (2014) Predictability of hydraulic head changes and characterization of aquifer-system and fault properties from InSAR-derived ground deformation. Journal of Geophysical Research: Solid Earth. 119(8). 6572-6590.

Cigna, F., Bianchini, S., and Casagli, N. (2013). How to assess landslide activity and intensity with Persistent Scatterer Interferometry (PSI): the PSI-based matrix approach. Landslides, 10(3), 267-283.

Costantini M, Chen T, Xu Y, Trillo F, Vecchioli F, Kong L, Jiang D, Hu Q (2011) High resolution ground deformations monitoring by COSMO-SkyMed PSP SAR interferometry: accuracy analysis and validation. ESA FRINGE Proceedings, 19–23 September 2011. Frascati, Italy.

Dai, K., Li, Z., Tomás, R., Liu, G., Yu, B., Wang, X., Chenge H, Chenb J, Stockamp J (2016). Monitoring activity at the Daguangbao mega-landslide (China) using Sentinel-1 TOPS time series interferometry. Remote Sensing of Environment, 186, 501-513.

Di Martire, D., Tessitore, S., Brancato, D., Ciminelli, M.G., Costabile, S., Costantini, M., Graziano, G.V., Minati, F., Ramondini, M., Calcaterra, M., 2016. Landslide detection integrated system (LaDIS) based on in-situ and satellite SAR interferometry measurements. Catena 137, 406–421.

Ferretti A, Fumagalli A, Novali F, Prati C, Rocca F, Rucci A (2011) A new algorithm for processing interferometric data-stacks: SqueeSAR. IEEE Transactions on Geoscience and Remote Sensing, 49(9), 3460-3470.

Ferretti A, Prati C, Rocca F (2001) Permanent scatterers in SAR interferometry. IEEE Trans. Geosci. and Remote Sens. 39(1). 8-20, doi:10.1109/36.898661.

Herrera G, Gutiérrez F, García-Davalillo J C, Guerrero J, Notti D, Galve J P, Fernández-Merodoa J, Cooksley, G. (2013). Multi-sensor advanced DInSAR monitoring of very slow landslides: The Tena Valley case study (Central Spanish Pyrenees). Remote Sensing of Environment, 128, 31-43.

Meisina C, Zucca F, Notti D, Colombo A, Cucchi A, Savio G, Giannico C, Bianchi M (2008) Geological interpretation of PSInSAR data at regional scale. Sensors. 8(11):7469–7492.

Notti D, Calò F, Cigna F, Manunta M, Herrera G, Berti M, Meisina C, Tapete D, Zucca F (2015) A User-Oriented Methodology for DInSAR Time Series Analysis and Interpretation: Landslides and Subsidence Case Studies. Pure and Applied Geophysics. 172(11), 3081-3105.

Notti D, Herrera G, Bianchini S, Meisina C, García-Davalillo J C, Zucca F (2014) A methodology for improving landslide PSI data analysis. International Journal of Remote Sensing. 35(6). 2186-2214, doi:10.1080/01431161.2014.889864.

Plank S, Singer J, Minet C, Thuro K (2012) Pre-survey suitability evaluation of the differential synthetic aperture radar interferometry method for landslide monitoring. Int. J. Remote Sens. 33 (20), 6623–6637.

6.4. Twenty-year Advanced DInSAR analysis of severe land subsidence: the Alto Guadalentín Basin (Spain) case study

Roberta Bonì[1,*], Gerardo Herrera[2,3,4], Claudia Meisina[1], Davide Notti[1,10], Marta Béjar-Pizarro[2,3] , Francesco Zucca[1], Pablo J. González[5], Mimmo Palano[6], Roberto Tomás[2,7,3], José Fernández[8], José Antonio Fernández-Merodo[2,3], Joaquín Mulas[2,3], Ramón Aragón[2,3], Carolina Guardiola-Albert[2] and Oscar Mora[9]

[1] Department of Earth and Environmental Sciences, University of Pavia, Via Ferrata 1, 27100 Pavia, Italy ; E-Mails: roberta.boni01@universitadipavia.it; claudia.meisina@unipv.it; davidenotti@gmail.com; francesco.zucca@unipv.it.

[2] Geohazards InSAR laboratory and modelling group. Instituto Geológico y Minero de España (IGME), C/. Alenza 1, 28003 Madrid, Spain; E-Mails: g.herrera@igme.es; m.bejar@igme.es; jose.fernandez@igme.es; j.mulas@igme.es; r.aragon@igme.es; c.guardiola@igme.es.

[3] Unidad Asociada de investigación IGME-UA de movimientos del terreno mediante interferometría radar (UNIRAD),Universidad de Alicante, P.O. Box 99, 03080 Alicante, Spain.

[4] Earth Observation and Geohazards Expert Group (EOEG), EuroGeoSurveys, the Geological Surveys of Europe, 36-38, Rue Joseph II, 1000 Brussels, Belgium.

[5] Institute of Geophysics and Tectonics. School of Earth and Environment. University of Leeds, Leeds, LS2 9JT, United Kingdom; E-Mail: p.j.gonzalez@leeds.ac.uk.

[6] Istituto Nazionale di Geofisica e Vulcanologia, Osservatorio Etneo - Sezione di Catania, Piazza Roma 2, 95123 Catania, Italy; E-Mail: mimmo.palano@ingv.it.

[7] Universidad de Alicante, Dpto. de Ingeniería Civil. Escuela Politécnica Superior de Alicante. P.O. Box 99. 03080 Alicante Spain; E-Mail: roberto.tomas@ua.es.

[8] Instituto de Geociencias (CSIC, UCM), Plaza de Ciencias 3, Ciudad Universitaria, 28040 Madrid, Spain; E-Mail: jft@mat.ucm.es

[9] Altamira Information, C/. Còrsega 381-387, 08037 Barcelona, Spain; E-Mail: oscar.mora@altamira-information.com.

[10] Departamento de Geodinámica, Universidad de Granada, Avenida Fontenueva, Granada, Spain

[*] Author to whom correspondence; E-Mail: roberta.boni01@universitadipavia.it.

Tel.: +39 382985831

The paper has been published in Engineering Geology, Volume 198, 23 November 2015, Pages 40–52

doi:10.1016/j.enggeo.2015.08.014

Abstract: A twenty-year period of severe land subsidence evolution in the Alto Guadalentín Basin (southeast Spain) is monitored using multi sensor SAR images, processed by advanced differential interferometric synthetic aperture radar (DInSAR) techniques. The SAR images used in this study consist of four data sets acquired by ERS-1/2, ENVISAT, ALOS and COSMO-SkyMed satellites between 1992 and 2012. The integration of ground surface displacement maps retrieved for different time periods allows us to quantify up to 2.50 m of cumulated displacements that occurred between 1992 and 2012 in the Alto Guadalentín Basin. DInSAR results were locally compared with global positioning system (GPS) data available for two continuous stations located in the study area, demonstrating the high consistency of local vertical motion measurements between the two different surveying techniques. An average absolute error of 4.6±4 mm for the ALOS data and of 4.8±3.5 mm for the COSMO-SkyMed data confirmed the reliability of the analysis. The spatial analysis of DInSAR ground surface displacement reveals a direct correlation with the thickness of the compressible alluvial deposits. Detected ground subsidence in the past 20 years is most likely a consequence of a 100-200 m ground water level drop that has persisted since the 1970s due to the overexploitation of the Alto Guadalentín aquifer system. The negative gradient of the pore pressure is responsible for the extremely slow consolidation of a very thick (>100 m) layer of fine-grained silt and clay layers with low vertical hydraulic permeability (approximately 50 mm/h) wherein the maximum settlement has still not been reached.

Keywords: Land subsidence; Persistent Scatterer Interferometry (PSI); Spatio-temporal analysis; Lorca; groundwater level; GPS

7. Introduction

Land subsidence triggered by the overexploitation of aquifers represents a common hazard impacting extensive areas worldwide. For instance, well-known examples of pumping-induced subsidence affected the Antelope valley in California (Galloway *et al.,* 1998), the North China Plain (Changming *et al.,* 2001), Bangkok in Thailand (Phien-Wej *et al.,* 2006) and the city of Bologna in Italy (Stramondo *et al.,* 2007). This type of land subsidence causes permanent inundation of land, aggravates flooding, changes topographic gradients and thus causes infrastructure damage, ruptures the land surface, and reduces the capacity of aquifers to store water, posing a risk for the society that can have a sound economic impact (Holzer and Galloway, 2005). For these reasons, mapping and monitoring the areal extent and temporal evolution of this phenomenon are critical. Differential SAR interferometry represents an advanced remote sensing tool capable of mapping displacements over wide areas at a very high spatial resolution and with a lower annual cost per measurement point and per square kilometre than other conventional techniques such as GPS, topographic

measure and extensometers (Tomás *et al.,* 2014). According to Sansosti *et al.* (2010), advanced DInSAR techniques can be grouped into two main categories: persistent scatterer (PS) methods that work on localized targets (Ferretti *et al.,* 2001; Arnaud *et al.,* 2003; Werner *et al.* 2003; Hooper 2008), and small baseline (SB) methods that use spatially distributed targets (Lundgren *et al.,* 2001; Berardino *et al.,* 2002; Mora *et al.,* 2003; Schmidt and Burgmann 2003; Prati *et al.,* 2010). In the past decade, several works have focused on the application of these methods to monitor pumping-induced subsidence and to understand the relationship between changes in pore-fluid pressure and aquifer system compaction (e.g., Hoffmann *et al.,* 2001; Declercq *et al.,* 2005; Herrera *et al.,* 2009). Therefore, more case histories are necessary to improve the characterization of the spatio-temporal responses of aquifer systems to hydro-mechanical stresses and to learn to manage the effects, which can be triggered in geologically similar areas.

A recent study (González and Fernández, 2011a) revealed that the Alto Guadalentín Basin, located in southern Spain, is affected by the highest subsidence rates measured in Europe (>10 cm/yr) as a direct consequence of long-term aquifer exploitation. In particular, the authors used ERS and ENVISAT data from 1992 to 2007 to identify a delayed transient nonlinear compaction of the Alto Guadalentín aquifer due to the 1990-1995 drought period. Land subsidence due to groundwater exploitation in this region was also detected by Rigo *et al.* (2013) through the analysis of ENVISAT data, reaching a maximum velocity value of 7.3±0.9 cm/yr during the period 2004-2005. Recently, González *et al.* (2012) evaluated the relationship between crust unloading due to groundwater overexploitation and stress change on regional active tectonic faults.

This paper presents several novelties with respect to previous works. Previously published displacement measurements obtained from ERS and ENVISAT satellite SAR images for the period 1992-2007 (González and Fernández, 2011a; Rigo *et al.,* 2013) are extended using advanced DInSAR techniques (Duro *et al.,* 2005) to process ALOS PALSAR (2007-2010) and COSMO-SkyMed (2011-2012) SAR images. The combination of multi-sensor SAR images with different resolutions allows for a wider monitoring time span of 20 years (1992-2012) over the Alto Guadalentín basin. Additionally, the satellite measurements provide locally comparable results with measurements acquired by two permanent GPS stations located in the study area. Furthermore, new geological and hydrogeological data were collected and analysed in order to assess aquifer system compressibility and ground water level changes in the past 50 years. The comparison of these data with advanced DInSAR displacement measurements allows for better spatial and temporal understanding of the governing mechanisms of subsidence due to overexploitation of the Alto Guadalentín aquifer system.

8. Study area

The Guadalentín Basin is located in the Murcia Province, southeast Spain. It is filled by Neogene-Quaternary sediments transported by the Guadalentín River along an intramontane depression located in the eastern part of the Baetic Cordillera, which is an ENE-WSW-oriented alpine orogenic belt resulting from the ongoing convergence of the African and Iberian plates (Bourgois *et al.*, 1992; Martínez-Díaz, 2002; Masana *et al.*, 2004; Gràcia *et al.*, 2006; Palano *et al.*, 2013). The Guadalentín is a tributary river of the Segura River and forms the Alto and Bajo Guadalentín sub-basins, where Lorca City developed (with approximately 100,000 inhabitants). The basin is mainly filled by Quaternary alluvial fan systems that overlap with Tertiary deposits that are mainly composed of conglomerate and calcarenite sediments that outcrop at the border of the basin. The prevailing NE-SW-oriented Alhama de Murcia Fault (AMF) crossing along these deposits (Figure 1a) represents the main active fault system of the study area (Martínez-Díaz *et al.*, 2012). Underneath this sequence of materials, preorogenic deposits are present, which are composed of Paleozoic metamorphic complexes (IGME, 1981).

The Alto Guadalentín aquifer system covers an area of approximately 277 km^2 (Figure 1a), and it is composed of Plio-Quaternary detrital and alluvial material, including clays, sands and conglomerates with clay and/or silt matrices; Miocene detritical with conglomerate and sand deposits; and local Triassic carbonate rocks. The Mesozoic marl and marl with intercalated sand and conglomerates represent the lower impermeable limit. The metamorphic substratum exhibits a horst and graben arrangement (Cerón and Pulido-Bosch, 1996); therefore, the depth of the impermeable limit varies within the region. In proximity of the East and West Basin borders, Tertiary deposits reach 400 m deep. In the N-E sector, the Alto Guadalentín aquifer is laterally linked to the multi-layer aquifer system of the Bajo Guadalentín aquifer (CHS, 2014). The transition zone between the two aquifers is characterized by thick clay layers that lose lateral continuity towards the Alto Guadalentín; therefore, locally semi-confined aquifers can be found in this zone. The spatial variability of the clayey material's thickness is evident from analysis of the available lithological columns (explained in subsection 4.1).

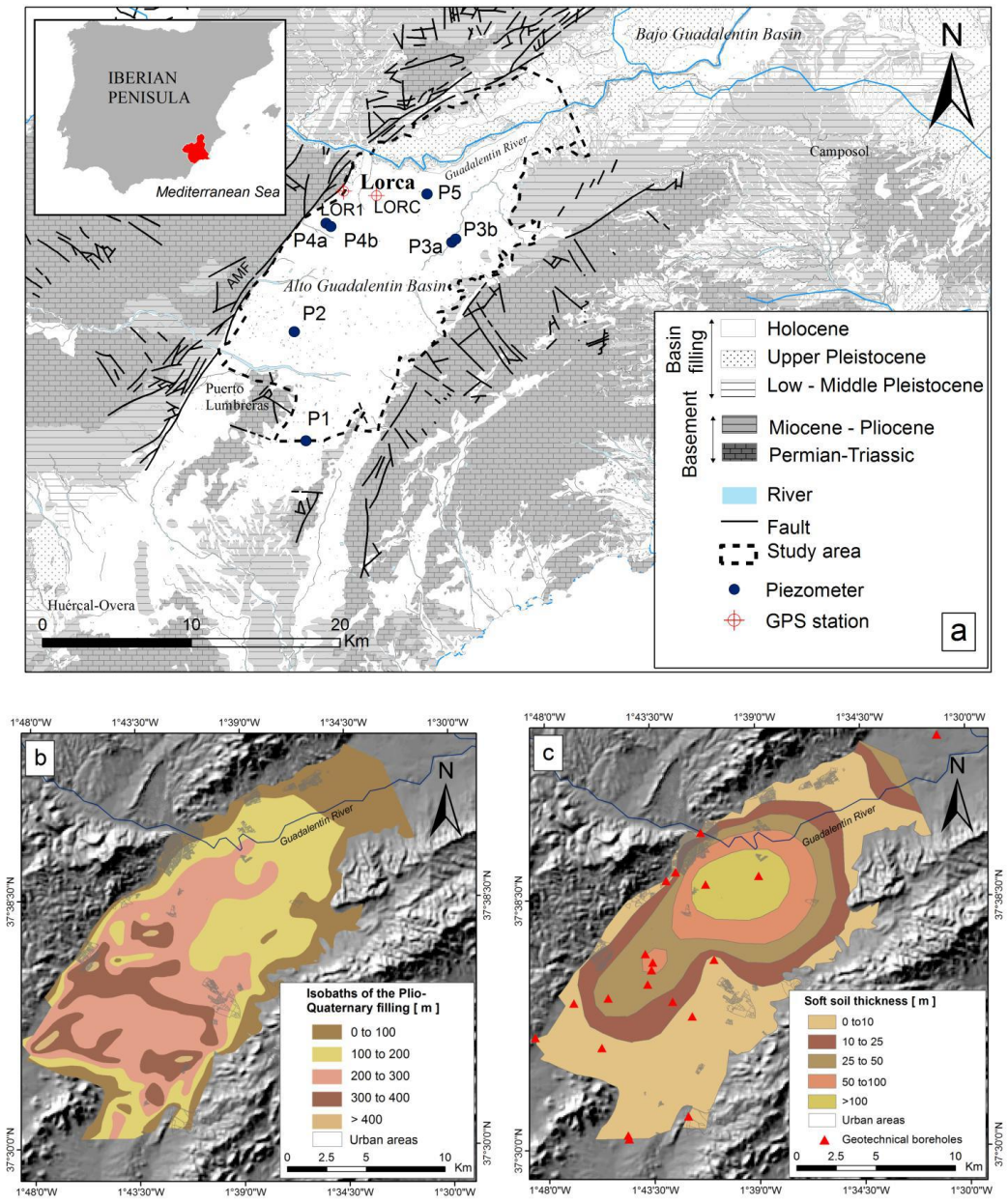

Figure 1. (a) Geological setting of the Guadalentín Basin (redrawn from Martín *et al.*, 1972); piezometers and GPS sites used in this study area are also reported. **(b)** Plio-quaternary filling (based on Cerón and Pulido-Bosch, 1996). **(c)** Compressible thickness map and geotechnical boreholes location. The thickness of the compressible deposits has been calculated by means of geotechnical boreholes data. (For the interpretation of the compressible thickness map, the reader is referred to the paragraph 4.1 in the maintext). Urban areas are also reported in panels b and c.

Since 1960, agricultural development has led to the exploitation of the aquifer system, which resulted in the aquifer being declared temporarily overexploited in 1987 (CHS, 2006). Although in the past, the piezometric level was close to the surface and artesian wells were exploited, groundwater drawdown became apparent in 1972 (Cerón and Pulido-Bosch, 1996). In 1988, the

amount of extraction reached a maximum historical value of 77.6 hm^3/year (IGME 1994). After 1988, a general reduction of pumping and/or abandonment of wells were recorded due to CO_2 pollution of groundwater resources and to new sources of water transferred from the Tajo River to the Segura River (Cerón and Pulido-Bosch, 1996).

In 2004, the last recorded extraction volume value was 43.3 hm^3/year, with a reserve of 10 hm^3/year. A deficit in the groundwater reserve was recorded from 1965 to 2009, corresponding to an annual rate of decline of 33 hm^3/year (Alonso and Aróstegui, 2014).

In addition, the occurrence of drought periods, from 1990 to 1995 and from 2005 to 2007, increased the resource deficit (CHS, 2014). In particular, the first drought period triggered a nonlinear aquifer compaction episode due to the decrease of pore-pressure within the aquifer system (González and Fernández, 2011a).

The groundwater balance (Table 1) determined using available data from IGME (1994) and CHS (2005), illustrates the precarious situation of the aquifer due to the high deficit between the input and the output.

Table 1. Groundwater balance components for Alto Guadalentín aquifer, based on data from IGME 1994, and CHS 2005 (Values in hm^3/yr). I_{ES}: runoff infiltration; I_D: direct infiltration from rain; R_R: irrigation return; S_{BN}: net output by pumping.

Budget item		**Dry year (2003-2004) CHS 2005**	**Average year (1976-1988) IGME 1994**	**Wet year (1989) IGME 1994**
Input	I_{ES}	3.1	5.3	12.4
	I_D	1.2	8.0	32.8
	R_R	7.2	8.8	6.9
	Total	11.5	22.1	52.1
Output	S_{BN}	43.3	50	60
Storage variation		-31.8	-27.9	-7.9

We have examined the historical evolution of the piezometric level from 1975 to 2012. Sources include data on the piezometric levels in 1975 and 1992 derived from Cerón (1995, 1999) (Figures 2a and 2b) and piezometric maps from 2008 (Figure 2c) and 2012 (Figure 2d) drawn by the *Confederación Hidrográfica del Segura*, the area's groundwater administration body (CHS, 2014).

Cerón's piezometric maps for 1975 and 1992 were prepared by interpolating data from 28 and 57 piezometers, respectively. The *Confederación Hidrográfica del Segura* prepared piezometric maps by incorporating the means of the data from nine piezometers. The differences between these piezometric maps provide a qualitative estimate of piezometric drawdown between 1975 and 1992 (Figure 2e), 1992 and 2008 (Figure 2f), 2008 and 2012 (Figure 2g), and over the entire monitored period spanning 1975-2012 (Figure 2h). Overall, it can be observed that the highest and most extended water drawdown occurred in the first period (215 m maximum). In the second period, there was an extended recovery of the water level (65 m maximum), except for the western sector of the basin where the drawdown reaches a maximum value of 132 m. The period from 2008 to 2012 highlights a recovery of the piezometric level (10 m maximum), except for the southern area of the basin where the drawdown reaches up to 31 m.

Based on these maps, most of the drawdown from 1975 to 2012 was due to water depletion that occurred in the first period (1975-1992). After 1992, water depletion mainly occurred in the western and southern areas of the basin. Widespread piezometric recuperation began in 1992 towards the eastern and northern areas followed by an overall stabilization in 2012, except for in the southern area. This spatial trend coincides with groundwater level variations of the piezometers located in the northern part of the basin (P3a, P3b, P4a, P4b and P5 in Figure 2i; see Figure 1a for their exact locations).

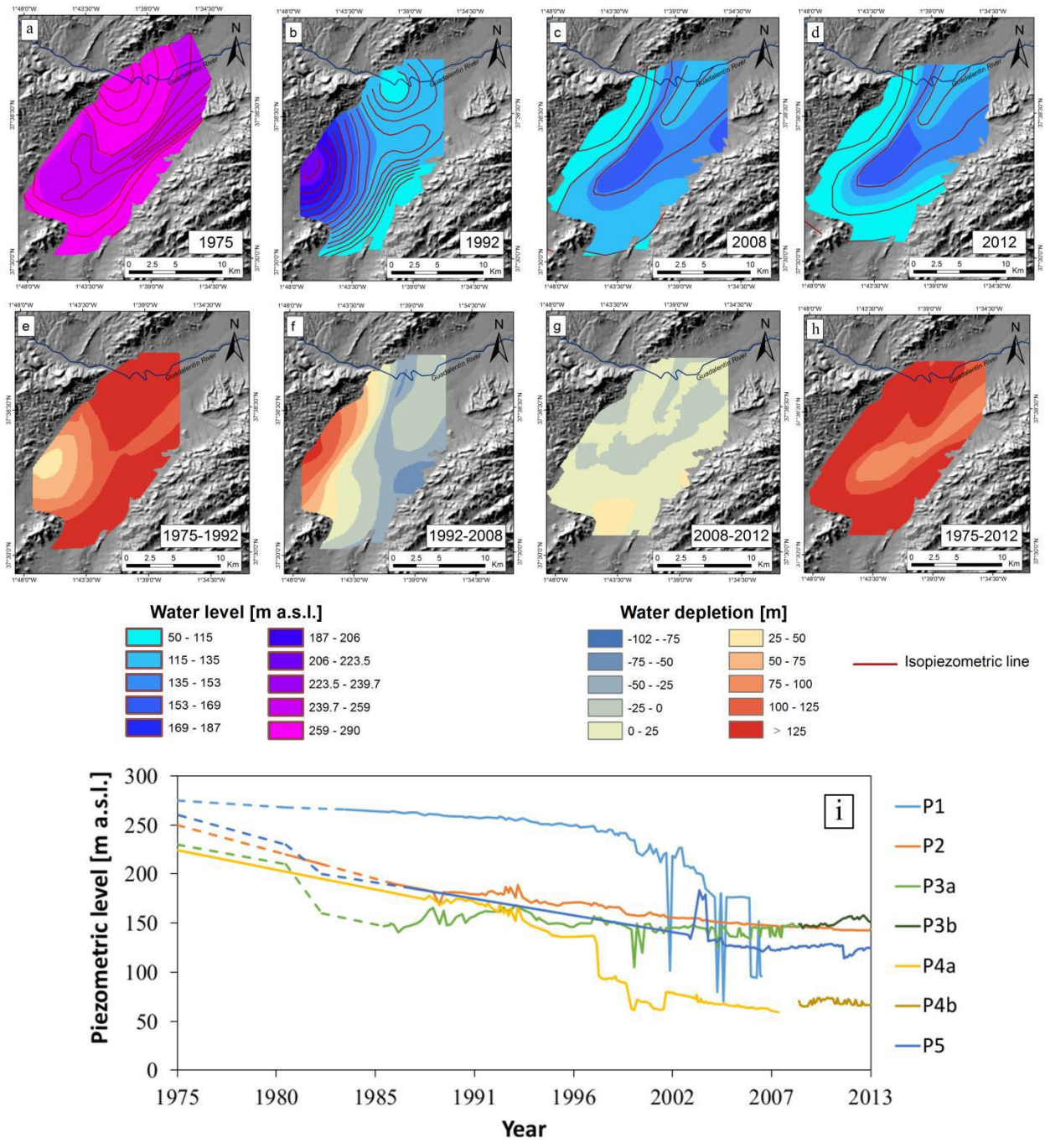

Figure 2. Maps of the water level [m a.s.l.] in 1975 **(a)** and 1992 **(b)**, derived from Cerón (1995, 1999); in 2008 **(c)** and 2012 **(d)** from Confederación Hidrográfica del Segura (CHS, 2014). Piezometric drawdown from 1975 to 1992 **(e)**, from 1992 to 2008 **(f)**, from 2008 to 2012 **(g)** and from 1975 to 2012 **(h)**. Note that positive values represent drawdown of the water level and the negative values are recovery of the water level. **(i)** Time series of seven piezometers from 1975 to 2013. The dotted lines represent measures obtained from Cerón (1995). See the location of the piezometers in Figure 1a.

9. Advanced DInSAR processing and results

3.1. SAR data and processing

To study the temporal evolution of ground surface displacement in the Alto Guadalentín Basin, we collected and processed a large amount of C-band SAR data (ERS-1, ERS-2 and ENVISAT), L-band SAR data (ALOS PALSAR), and X-band SAR data (COSMO-SkyMed).

Both ERS and ENVISAT-ASAR datasets, covering periods from 1992 to 2001 and from 2003 to 2007, were processed independently using DORIS interferometric software (Kampes *et al.*, 2003) to handle all SAR data, including co-registration and interferogram generation. By adopting the small baseline approach (Berardino *et al.,* 2002; González and Fernández, 2011b), we generated a line of sight (LOS) displacement time series using StaMPS software (Hooper, 2008). To determine the temporal evolution of the displacement, we merged the two results. Considering that ENVISAT-ASAR results were spatially denser (45% more than the ERS, see Table 2), we used nearest-neighbour interpolation to transfer the ENVISAT-ASAR time series results to the ERS master grid. The two-time series products were subsequently combined by minimizing the linear velocity change between the two separated time series (González and Fernández, 2011b). From this, we obtained a continuous time series of displacements for all pixels selected in the ERS dataset (7747 PS, see Table 2) from 1992 to 2007.

The ALOS PALSAR dataset from 2007 to 2010 and the COSMO-SkyMed dataset from 2011 to 2012 were processed independently using DIAPASON interferometric software for all SAR data handling. Additionally, SPN software (Arnaud *et al.*, 2003, Duro *et al.*, 2005) using the persistent scatterer approach was used to obtain three main products from a set of Single Look Complex (SLC) SAR images: (a) the average displacement velocity along the LOS of every pixel (PS), (b) a map of precise reflector heights (being the difference between the height given by the digital elevation model and the true height of each reflector), and (c) the LOS displacement time series of individual PS. In both cases, a 25-m photogrammetrically derived digital elevation model was used to remove the topographic interferometric phase and to perform the final geocoding of results. Note that because the different sensors measure displacement using different incidence angles, the capacity to measure the vertical component of the displacement differs. For instance, ERS-1/2 and ENVISAT have a 23° incidence angle, which permits the detection of 92% of vertical displacements, whereas ALOS and COSMO-SkyMed satellites only measure 83% and 75% of vertical displacements, respectively.

Table 2. Details on the SAR data sets, their processing and results.

Satellite	**ERS-1/2**	**ENVISAT**	**ALOS PALSAR**	**COSMO_SkyMed**
λ (cm)	5.6 (C-band)	5.6 (C-band)	22.9 (L-band)	3.1 (X-band)
Orbit	Desc.	Desc.	Asc.	Asc.
Look angle (º)	23	23	34	42
Time span	22/06/1992 - 21/12/2000	15/03/2003 - 15/03/2007	19/01/2007 - 14/06/2010	17/05/2011 - 14/10/2012
Number of scenes	32	19	14	83
Processing technique	StaMPS	StaMPS	SPN	SPN
Georeference accuracy	25	25	10	5
Nº. PS	7747	11120	28196	761339
PS density (PS/km^2)	33	48	120	3254
Vel. (cm/yr)	-2.0±3.2		-2.5±2.9	-1.3±,1.8
Vel. Range (Max; Min)	0.5; -11.9		2.1; -12.8	2.3; -11.4

3.2. Advanced DInSAR results

The persistent scatterer density retrieved from the combined ERS and ENVISAT dataset is approximately 4 to 99 times smaller than that obtained using the ALOS PALSAR and the COSMOSkyMed datasets, respectively (see Table 2). This variability is related to the spatial resolution of every sensor, the capacity to penetrate vegetation (which depends on the wavelength), temporal sampling and the type of processing.

In this case, we considered a threshold of 1 cm/year to indicate an area affected by significant subsidence. As a consequence, annual velocities in the range of ±1 cm/yr are considered stable (Figure 3) and are color-coded green, whereas yellow to red pixels indicate movement away from the satellite (subsidence). Less than 1% of all PS show uplift; these are depicted in blue.

To homogenize the geometrical distortions introduced by the different acquisition angles of the various sensors, both the average velocity and the cumulative surface displacements in the LOS obtained for each dataset have been projected along the vertical direction. The total subsidence from 1992 to 2012 has been determined by taking into account the vertical cumulative surface

displacements of the different datasets. The results show that cumulative displacement reached up to 250 cm, with an average subsidence of 180 cm over an extension of 14.8 km^2, located in the central sector of the Alto Guadalentín Basin (Figure 3d). The areal extent of the subsidence exhibits a SW-NE elliptical shape parallel to the valley direction, showing an apparent deceleration trend over time (Figs. 3a to 3c). Note that the spatial extent of severe subsiding areas (faster than -10 cm/yr) has been reduced from 14.4 km^2 in 1992-2007, to 11.7 km^2 in 2007-2010 and 7.4 km^2 in 2011-2012.

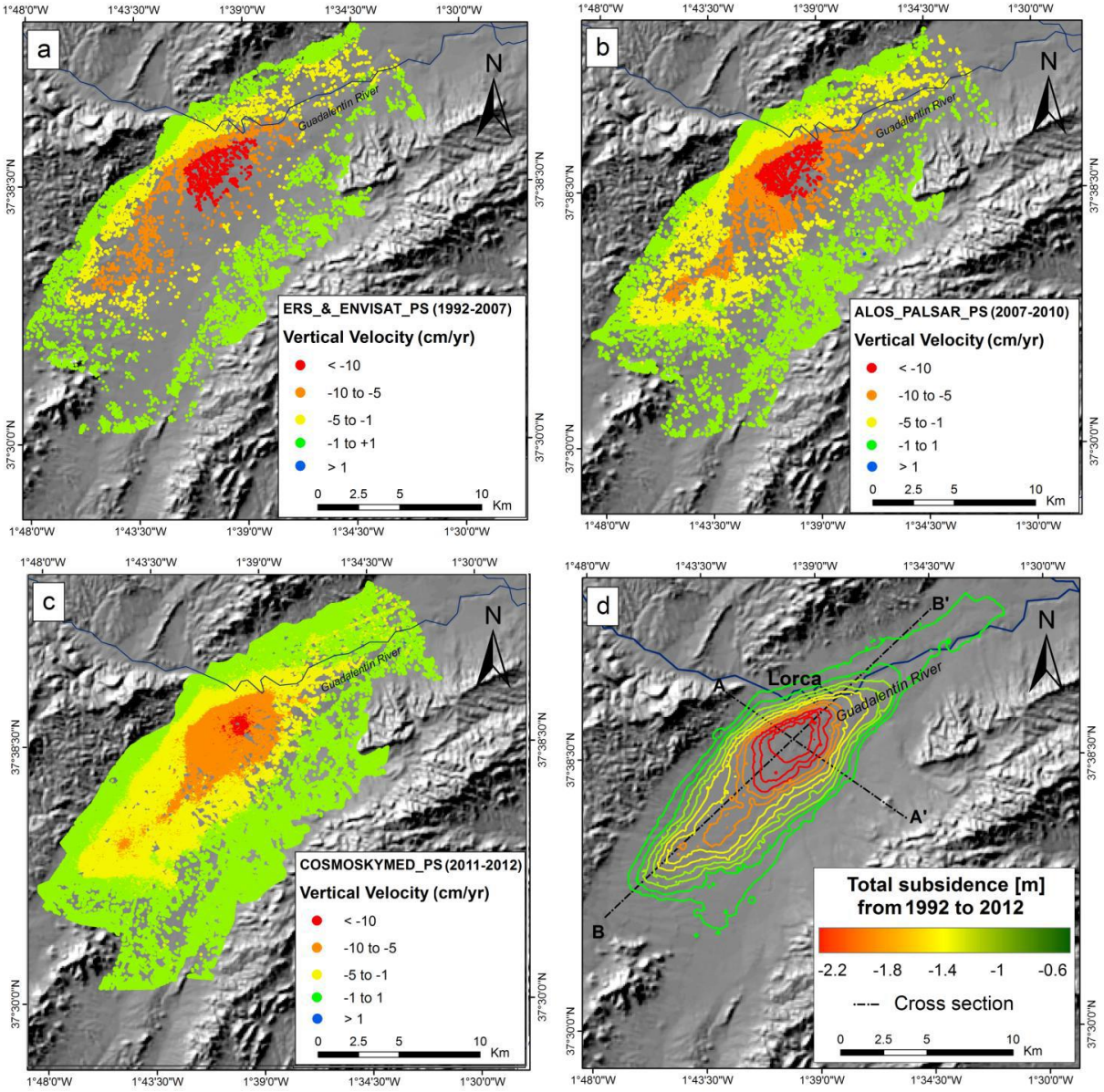

Figure 3. Vertical velocity maps for the 1992-2007 period (obtained using data from ERS and ENVISAT satellites) **(a)**, for the 2007-2010 period (ALOS PALSAR satellite) **(b)** and for the 2011-2012 period (COSMO-SkyMed satellites) **(c)**. Cumulated displacements (m) of the Alto Guadalentín Basin from 1992 to 2012. Locations of the cross sections A-A´ and B-B´, plotted in Figure 7, are marked in panel **(d)**.

3.3. Comparison with GPS time series

DInSAR displacements were compared with vertical displacements measured by two continuous GPS stations (LOR1 and LORC; Figure 1a). The GPS stations are located in the north-western sector of the Alto Guadalentín Basin and belong to different networks (REGAM and MERISTEMUM) that developed by local institutions mainly for mapping, engineering and cadastral purposes. The LOR1 station is located in a relatively stable zone, while LORC is located in an area affected by higher subsidence rates. Raw GPS observations were processed using GAMIT/GLOBK software packages (Herring *et al.*, 2010) by following the approach described by Palano (2015). To improve the overall configuration of the network and to tie regional measurements to an external global reference frame, data from ~15 continuously operating global tracking stations, largely from the EUREF (Beutler *et al.*, 2008) permanent network, were introduced during processing. Daily time series were obtained by aligning our loosely constrained solutions with the ITRF2008 global reference frame (Altamimi *et al.*, 2012).

The LOR1 dataset covers the period 4th September 2008-15th June 2013, while LORC spans the period 26th August 2007-22nd May 2013. For each of these, we superimposed the deformation time series considering the nearest PS from the GPS station, in a range less than 60 m. DInSAR displacements have been converted into vertical movements assuming that ground deformation is purely vertical and considering that the ALOS PALSAR and the COSMO-SkyMed sensors identify 83% and 75% of the vertical deformations, respectively. The simple visual inspection of GPS and DInSAR time series (Figure 4) reveals good agreement between the different surveying techniques. To obtain a quantitative appraisal of DInSAR quality, first we computed the average (μ) and standard deviation (σ) of the absolute differences between the two-time series and then computed the average and standard deviation of the two series difference. The average and the standard deviation of the absolute difference are 4.7±4.0 and 4.6±4.1 mm for the ALOS data at LOR1 and LORC stations, respectively. The difference between the two-time series shows average values of 0.6±6.4 mm and -3.6±5.2 mm for the LOR1 and LORC stations, respectively. Regarding the COSMO-SkyMed data, the absolute differences are 5.8±4.0 mm for LOR1 and 3.9±2.8 mm for LORC. The results of the difference between the two-time series shows average values of -4.8±5.2 mm for LOR1 and 3.4±3.2 mm for LORC.

Recent validations of DInSAR performance with truth measurements (Strozzi *et al.*, 2001; Hanssen 2003; Casu *et al.*, 2006; Crosetto *et al.*, 2008; Herrera *et al.*, 2009; Tomás *et al.*, 2010a) report error values within the range of ±6.9 mm. The measurements confirm the high reliability of the analysed DInSAR data. The vertical motion (subsidence in our case) estimated at the LORC station from 2008 to 2013, in averaged time intervals of 6 months, shows a decreasing rate beginning with an

initial velocity of ~10 cm/yr and ending at ~8 cm/yr (see LORC time series in Figure 4). This feature is also visible in the COSMO-SkyMed displacement results (Figure 4).

We are aware that the use of only two GPS stations to sample a limited sector of the study area cannot adequately validate the DInSAR displacements over the entire investigated area. Unfortunately, the lack of additional measures of the vertical ground deformation field (e.g., levelling measurements and episodic GPS measurements) prevents us from validating the DInSAR displacements with independent measurements at the scale of the basin.

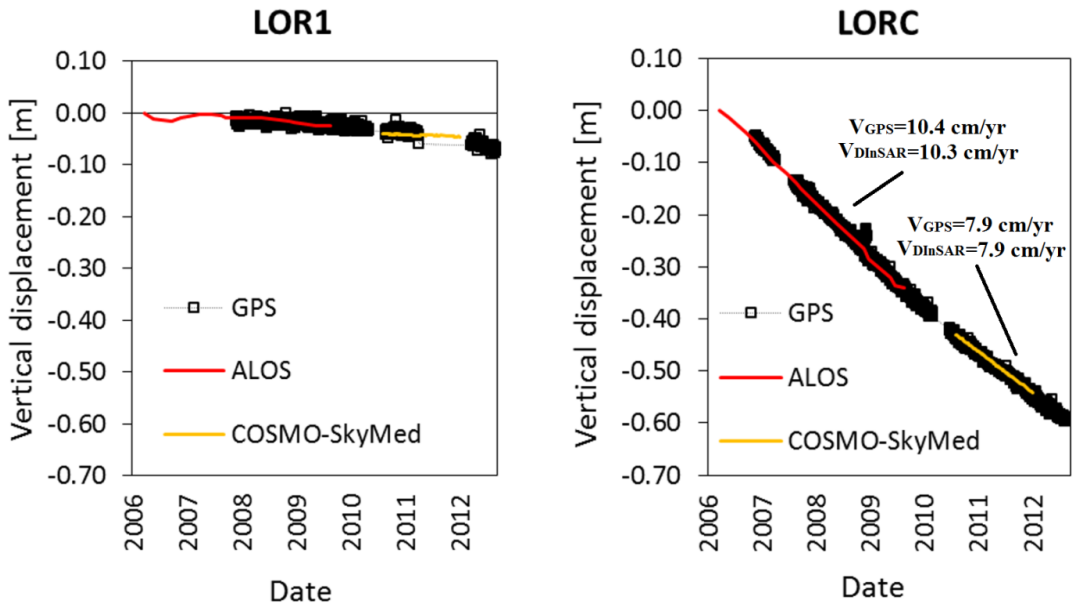

Figure 4. Comparison between the DInSAR and GPS vertical displacements time series. See Figure 1a for the GPS stations location. At the LORC time series has been reported the vertical velocity rate [cm/yr] detected in the period 2007-2010 and 2011-2012 by the GPS and DInSAR measurements.

10. Results analysis

In this section, the InSAR data derived from three independent processes are spatially and temporally cross-compared with triggering factors (piezometric level variations) and conditioning factors of subsidence (the type and thickness of the different lithologies). Note that the analysis of the relationship between the groundwater overdraft, aquifer compaction and ground subsidence suffers from the low spatial resolution of geological and hydrogeological data.

4.1. Comparison with lithology

As previously mentioned, the Alto Guadalentín Basin is mainly filled by Holocene sediments. Towards the northwest area, older and less deformable sedimentary Pleistocene formations (alluvial

fan, colluviums, piedmonts, etc.) are outcropping (Figure 1). By computing the average cumulated subsidence for each geological unit, we detected that the greatest cumulative subsidence value (-0.5 m) in the period 1992-2012, affects the Holocene sediments. For this time interval, Pleistocene sedimentary units account for a cumulative subsidence of -0.2 m, whereas Permian-Triassic and Miocene-Pliocene rock outcrops bordering the basin are the most stable, exhibiting no deformation.

Therefore, as expected, the most recent units are affected by land subsidence, whereas older materials are less affected or are unaffected by this process. Taking into account the Plio-Quaternary isobaths map elaborated by Cerón and Pulido-Bosch (1996) (Figure 1b), we examined the relationship between the thickness of Plio-Quaternary filling and the subsidence rate estimated from the different available satellites (Figure 5, panels a, b and c). The results of this comparison suggest that maximum subsidence does not coincide with the thickest Plio-Quaternary filling. This could be explained by considering the different thickness of compressible materials such as silts, sands and clays within the Plio-Quaternary formations.

To solve this mismatch, we developed a soft soil thickness map (Figure 1c) based on the stratigraphic information available from 23 boreholes drilled for water pumping and hydrological research in the 1960s. The soft soil thickness for each borehole was calculated as the total thickness of the silt and clay-type layers located over the upper layer of gravels above the substratum. An ordinary Kriging interpolation method was used to predict the soft soil thickness where borehole data were lacking. It can be observed that soft soils thicker than 100 m are located in the central part of the basin towards the northeast (Figure 1c), whereas towards the southwest and bordering areas of the basin, thinner soft soils are found. In this case, the relationship between soft soil thickness and subsidence rates estimated from the different satellites is straightforward; i.e., maximum subsidence rates are found on the thickest soft soils (Figures 5, panels d, e and f), and contrarily, the average subsidence values estimated for the thinnest soft soils are within the stable range.

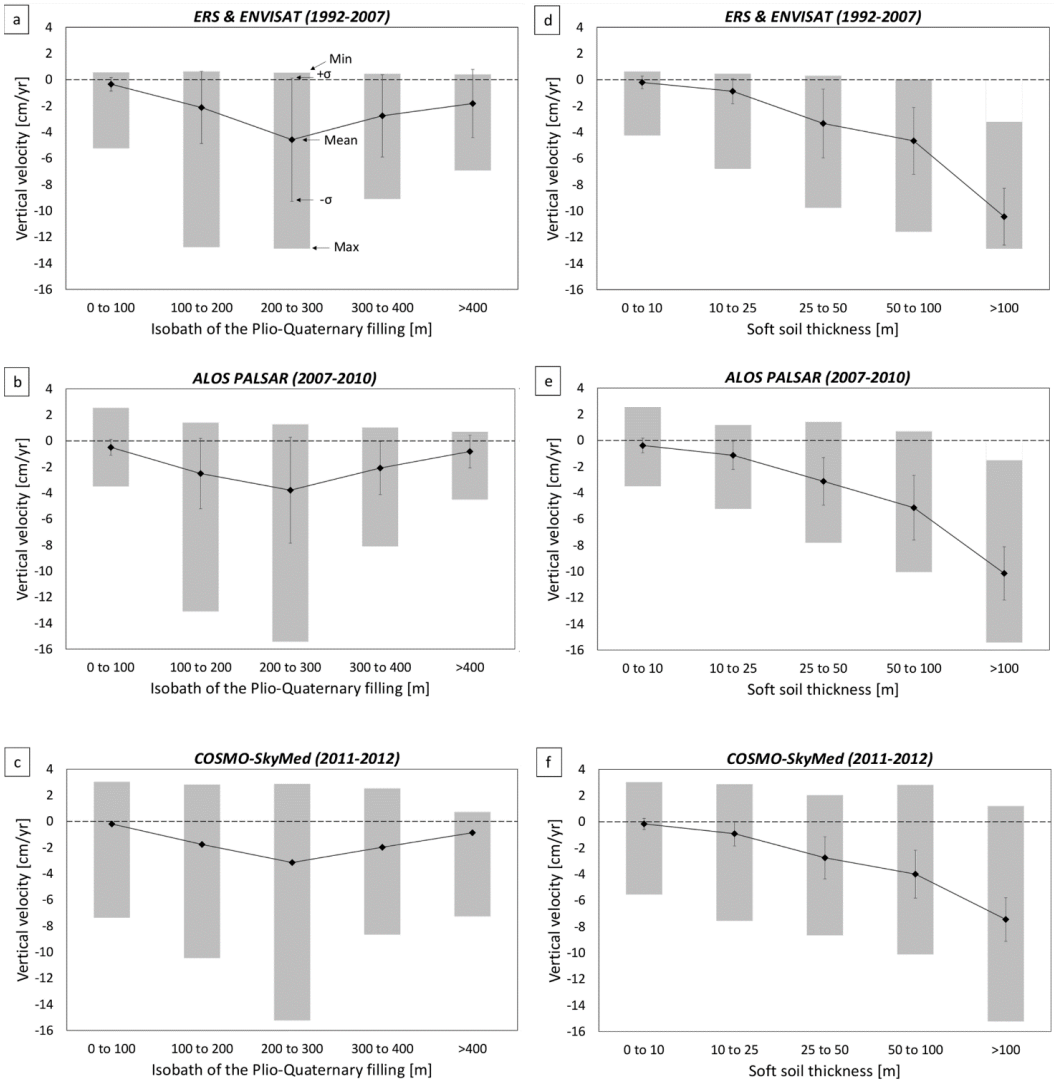

Figure 5. (a) Relationship between the isobaths of the Plio-Quaternary filling (Cerón and Pulido-Bosch, 1996) and the vertical velocity [cm/yr] valued for the ERS & ENVISAT dataset. The same for **(b)** the ALOS dataset and **(c)** for the COSMO-SkyMed dataset. See the Plio-Quaternary filling map in Figure 1b. Relationship between the soft soil thickness and the vertical deformation rates for the three dataset are shown in panels **(d)**, (**e)** and **(f)** respectively. See compressible thickness map in Figure 1c. The maximum, minimum, mean (black dots) and the standard deviation of the average values of deformation rates are represented.

4.2. Comparison with piezometry

Ground surface displacements estimated using advanced DInSAR were compared with groundwater variations observed spatially for the different time intervals (Figures 6 and 7), as well as with local data recorded by piezometers (Figure 8).

Ground water drawdown estimated from 1975 to 2012 was compared with cumulative displacements from 1992 to 2012, which were obtained by adding the displacements estimated by

ERS and ENVISAT, ALOS satellites and COSMO-SkyMed. The results from this comparison show no clear correlation between these measures (Figure 6). Indeed, in the period 1992-2008, the highest water drawdown (>125 m) corresponds to an average subsidence of 0.02 cm, whereas the maximum recovery of the piezometric level (up to 75 m) coincides with an average subsidence of 12.4 cm (Figure 6a). Similarly, no clear correlation is apparent when comparing groundwater drawdown with cumulative displacements measured from 2008 to 2012 (Figure 6b). Thus, the highest subsidence (52.2 cm) occurs where water recovery is recorded (up to 25 m). Finally, the comparison between groundwater drawdown from 1975 to 1992 and the cumulative displacements from 1992 to 2012 reveals a clear correlation. Hence, a greater groundwater drawdown corresponds to a greater cumulative subsidence (Fig. 6c).

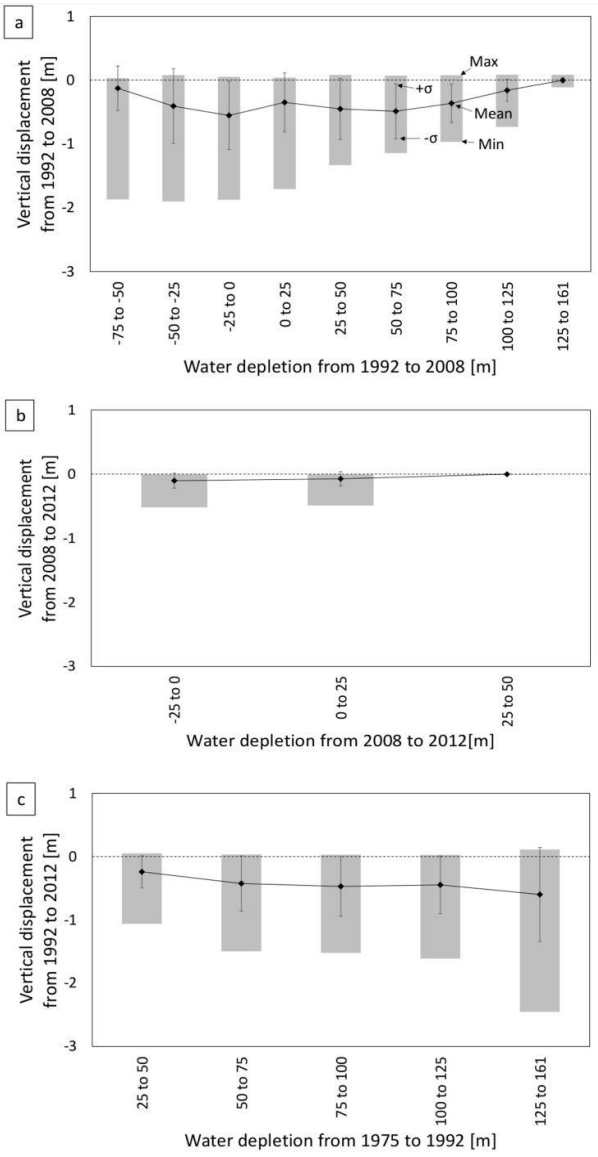

Figure 6. (a) Comparison of the vertical displacements [m] with the water depletion [m] detected in the period 1992-2008, **(b)** and 2008-2012. **(c)** Comparison of the total displacements from 1992 to 2012, with the water depletion from 1975 to 1992.

Therefore, it is reasonable to consider that the displacements observed from 1992 to 2012 could be due to the piezometric drawdown beginning in the 1970s, which corresponds to a longer delayed compaction process than that suggested by González and Fernández (2011a) for the 1990-1995 drought period.

The comparison of variables, subsidence and groundwater drawdown along two transects, A-A´ and BB´ (Figures 7a to 7f), shows their relationship to the thickness of the compressible deposits and the depth of the substratum (Cerón and Pulido-Bosch, 1996) (Figures 7c, 7f). As shown in Figures 7a and 7b, there seems to be a deceleration during the period 2011-2012 with respect to previous periods (1992-2007 and 2007-2010). No clear relationship is observed between measured cumulative displacement in the periods 1992-2008 and 2008-2012 and groundwater evolution (Figures 7b and 7e) in either transect. Note that the stabilization of the piezometric level in the period 2008-2012 does not coincide with the measured subsidence pattern. Contrarily, good agreement is observed if we consider groundwater depletion measured since 1975 and cumulative displacements.

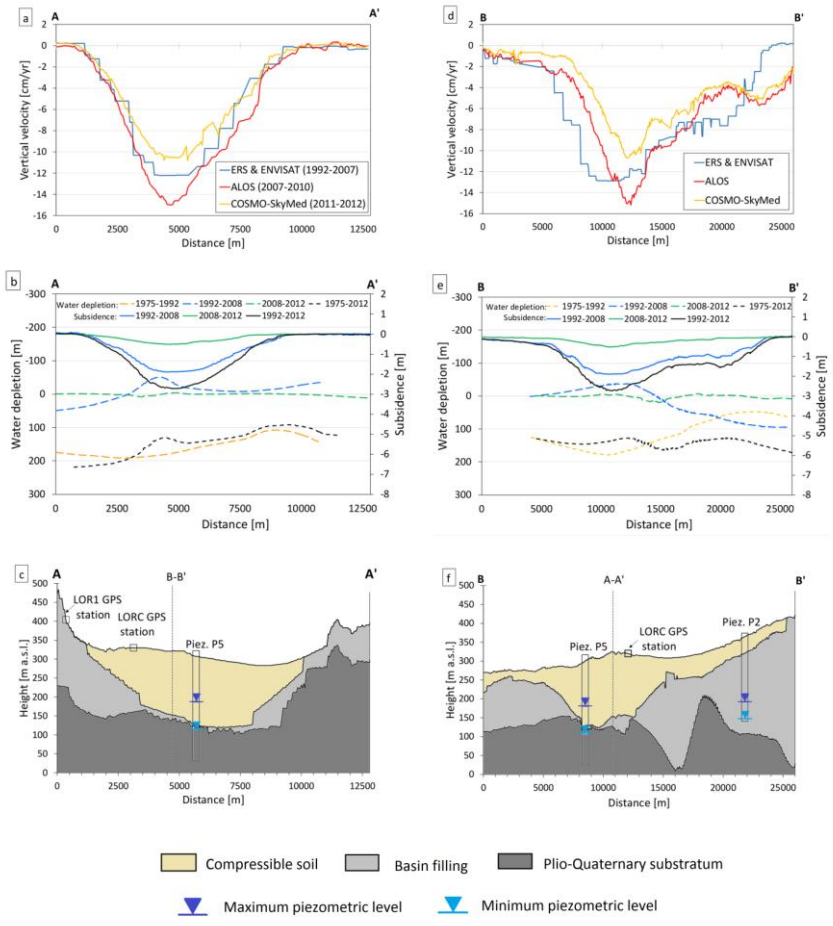

Figure 7. Profile of the deformation rates of multi sensor data **(a)**, **(d)**; and comparison of the vertical displacements with the water depletion (dotted lines) along the A-A′ **(b)** and B-B′ **(e)** profiles. The geological cross sections are shown in panels **(c)** and **(f)** respectively. See the location of the cross sections in Figure 3d. The maximum and minimum piezometric level stand for the maximum and minimum water level recorded at the piezometer. GPS stations locations are also reported (square symbols).

A detailed time series analysis of subsidence and ground water evolution is presented for the seven available piezometers (Figure 8).

The water table level ranges from 200 to 275 m a.s.l in 1975 and between 70 and 160 m a.s.l in 2013 (Figure 2i). No correlation is observed at piezometer P1, located in the southern zone, where the highest groundwater drawdown (162 m) from 1992 to 2007 corresponds to 13 cm of cumulated subsidence in the period 1992-2012 (Figure 8a and Table 3). This is likely due to the absence of soft soils in the southern border of the basin, where conglomerates with a sand-clay matrix from the alluvial fans are dominant (Figure 1c).

Certain correlation is observed in the western part of the basin (piezometers P2, P4a and P4b) where the soft soil thickness is moderate (from 18 to 21 m). In this sector, groundwater drawdowns between 31 and 107 m in the period 1992-2007 correspond to cumulative subsidence in the range of 38 to 48 cm during the period 1992-2012 (Table 3). Piezometer P2 displays a steady lowering of the piezometric level from 1989 to 2013 (Figure 8b) that correlates well with a more or less steady subsidence rate. Contrarily, piezometers P4a-b, which are jointly analysed due to their proximity and characteristics (Figure 1a), exhibit a high ground water level variability that is not in agreement with the estimated subsidence linear rate (Figure 8d).

In the eastern part of the basin, piezometers P3a-b display a water level evolution that is in agreement with subsidence accelerations and decelerations. The piezometric 1owering observed in the period 1992-2007 (Figure 8c) coincides with the transient compaction of the aquifer previously reported by González and Fernández (2011a), which was followed by piezometric recovery until 2012 when the subsidence progressively decelerated (Table 3).

In the central part of the basin where the thickest soft soils are found (approximately 190 m), the time series of piezometer P5 reveals a groundwater level recovery from 2007 to 2013 that does not correspond with measured subsidence steady rates (Figure 8e). This indicates an inelastic, unrecoverable and permanent deformation of this aquifer, as previously reported by Rigo *et al.* (2013), which was triggered by the groundwater exploitation beginning in the early 1970s.

Overall, a clear correlation between groundwater level drawdown and subsidence accelerations/decelerations is not observed (Table 3, Figure 8). This uncorrelation is related to the presence of very thick (>100 m) unconsolidated sediments (clay and silts) that are responsible for an apparent time delay between water level depletion and ground surface displacement. Indeed, most of these fine-grained silt and clay layers with low vertical hydraulic conductivity (approximately 50 mm/h) and slow deformability have been drained since the 1970s due to the negative gradient of the pore pressure as a result of aquifer overexploitation (Figure 2h).

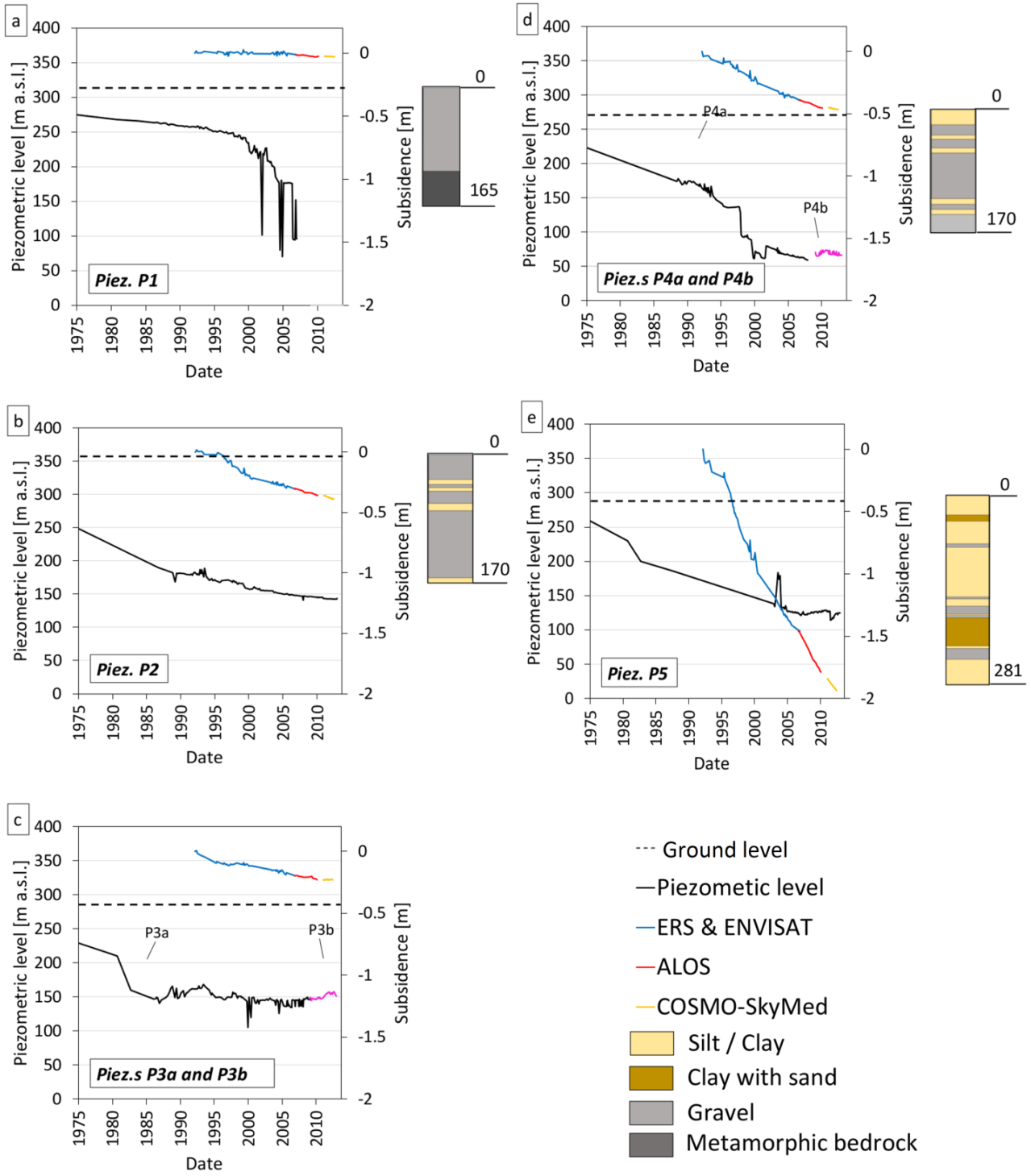

Figure 8. Comparison of the water level variations from 1975 to 2012 (black and pink line) at the different piezometers (P1, P2, P3a, P3b, P4a, P4b, and P5) located on Figure1a, and the vertical displacements detected by the satellite sensors (blue, red and yellow lines). In addition, for some piezometers it is represented the lithological column. The dotted line is the ground level. Piez. stands for piezometer.

Table 3. Piezometers dataset. The water level variations, the subsidence and the rate of the displacements considering three time intervals (1992-2007, 2007-2010, 2011-2012) and for the whole monitored period (1992-2012) are specified for each piezometer. The rate indicates the vertical velocity measured at the PS closest respect to the piezometer. CSK stands for the COSMO-SkyMed data.

Piez.	Monitored period	Ground surface [m a.s.l.]	Quat. depht [m]	Softsoil thikness [m]	Parameters	1992-2007 **ERS-ENV**	2007-2010 **ALOS**	2011-2012 **CSK**	1992-2012
P1	1984-2007	317.75	200-300	0.97	Water Level variation [m]	-162	-	-	-
					Subsidence [m]	0	0	0.13	0.13
					Rate [cm/yr]	0	-0.5	-0.3	-
P2	1989-2013	359.08	200-300	20.53	Water Level variation [m]	-31	-2	-2	-35
					Subsidence [m]	-0.40	-0.06	-0.02	-0.48
					Rate [cm/yr]	-2.4	-1.6	-2.6	-
P3a	1986-2009	289.69	100-200	60.52	Water Level variation [m]	-25	4	11	-10
P3b	2009-2013	287.69			Subsidence [m]	-0.05	-0.01	0	-0.06
					Rate [cm/yr]	-0.3	-0.1	0.2	-
P4a	1972-2008	271.62	200-300	17.92	Water Level variation [m]	-107	11	-6	-102
P4b	2009-2013	318			Subsidence [m]	-0.30	-0.06	-0.02	-0.38
					Rate [cm/yr]	-3	-2	-1	-
P5	1987-2013	295	100-200	190.52	Water Level variation [m]	-15*	5	-6	16*
					Subsidence [m]	-1.6	-0.3	0	-1.9
					Rate [cm/yr]	-10.6	-9.9	-6.7	-

*Due to the lack of piezometric measures from 1987 to 2003, the reported water level variation values cover the 2003-2007 time interval and as a consequence the entire water level variation start from the same date.

4.3. Subsidence analysis

The calculation of subsidence-induced ground settlement (δ) triggered by groundwater abstraction is usually performed with consideration of three parameters: (a) the thickness of deformable soils (H), which is spatially correlated with the calculated settlements discussed in subsection 4.1; (b) the variation in the stress state due to groundwater drawdown (Δh) since the 1970s (subsection 4.2), which is responsible for the effective stress increase, causing the consolidation of deformable soils; and (c) the deformability of the soil, which mainly depends on the nature of the different layers that constitute the aquifer system and its geological history.

Under a certain effective stress increase, a larger deformation is expected in soil than in rock, and a normally consolidated soil is potentially more deformable than an overconsolidated soil (Tomás *et al.*, 2010b). This can be clearly observed in Figure 3, in which lower values of subsidence are found in the border area and the reliefs. In these areas, older rocky lithologies are generally present, in comparison with the younger Holocene sediments that fill the valley and exhibit the greatest subsidence values.

The settlement calculation derived from these three parameters corresponds to the deformation (δ) of the soft soil thickness (H) after the whole excess pore pressure (Δu) induced by a piezometric level change has been dissipated. Therefore, during transient situations of the soil consolidation process (i.e., those situations in which $\Delta u \neq 0$), settlement will be lower than δ. Consequently, the magnitude of the settlement measured at certain times during the consolidation process will also depend on time. Hence, the total deformation will only be reached when all of the excess pore pressure is drained from the soil.

This process can be very quick for permeable soils (at times, almost instantaneously) or quite slow (years to decades) for fine soils with very low permeability.

Pumping tests performed in the Alto Guadalentín basin differentiate four typologies of soils and hydrogeological behaviors (CHS, 1990): highly fine soil (interbed) with a permeability value lower than 50 mm/h, fine soil with a permeability value of 50-90 mm/h, medium soil with a permeability value of 90-120 mm/h, and coarse soil with a permeability value of up to 120 mm/h.

Therefore, due to the low vertical hydraulic permeability of fine-grained silts and clays (approximately 50 mm/h), the excess pore pressure in the interbed is dissipated with a delay with respect to the dissipation of the pore pressure in the aquifer system.

In this case study, a joint comparison of all of the available data suggests that the aquifer system is suffering a delayed compaction process, where the maximum settlement has still not been reached.

This interpretation is in agreement with the observed trend of the time-subsidence curves derived from InSAR and GPS data (Figures 4 and 8), which indicates that the aquifer system deformation is

suffering a deceleration that coincides with the theoretical consolidation curves obtained from laboratory tests for unconsolidated sediments. In the future, the execution of a deep geotechnical borehole will allow for laboratory tests to be conducted to clarify the role of soil deformability and to model the behavior of this aquifer system.

11. Discussion

In this paper, subsidence triggered by overexploitation of the Alto Guadalentín aquifer system is investigated through the collection and analysis of geological and hydrological information combined with displacement maps and time-series retrieved from multi-sensor and multi-temporal SAR images.

Advanced DInSAR techniques have been used to process ALOS PALSAR (2007-2010) and COSMOSkyMed (2011-2012) SAR images. Both low- and high-resolution images provide similar subsidence patterns for the entire study area. These results have been combined with previously published displacement measurements obtained from ERS and ENVISAT satellite SAR images for the period 1992-2007, which allow for the mapping and monitoring of subsidence phenomenon due to Alto Guadalentín aquifer overexploitation between 1992 and 2012.

Retrieved subsidence maps reveal a 13 km x 4 km SW-NE lengthened subsidence area parallel to the Guadalentín valley direction, which exhibits subsidence rates higher than 5 cm/yr and a 250-cm maximum cumulative displacement in the 20-year monitoring period.

Although the area affected by subsidence is similar among the different monitoring periods and sensor resolutions, there seems to be a slight deceleration during the period 2011-2012 with respect to the previous periods (1992-2007 and 2007-2010). These results obtained from multi-sensor and multitemporal SAR images have been compared with GPS measurements, showing errors of 4.6±4 mm for the ALOS data and 4.8±3.5 mm for the COSMO-SkyMed data.

The Alto Guadalentín aquifer system is formed by Plio-Quaternary and Miocene detrital materials that can reach 400 m deep with a lower impermeable limit formed by Mesozoic marls and conglomerates. Although the presence of Plio-Quaternary sediments coincides well with measured isplacements, there is not a direct relationship between their thickness and the magnitude of the displacement rate. This can be explained by the spatial variability of the grain size and the thickness of Plio-Quaternary sediment.

Stratigraphic information from 23 boreholes drilled for water pumping in the 1960s was analysed to determine the spatial variability of Plio-Quaternary sediments. An area of 22 km^2 where soft soils (i.e., clays and silts) are thicker than 100 m has been identified in the central part of the basin

towards the northeast (Figure 1c), where the transition zone between Alto and Bajo Guadalentín aquifers is found.

Contrarily, on the bordering areas of the basin and particularly towards the southwest, thinner compressible soils alternate with thick layers of gravels and conglomerates from alluvial fans, colluviums and piedmonts (Silva *et al.,* 2008). In this case, a clear correlation is observed between measured displacement rates and the soft soil thickness map.

Recompilation and analysis of the available piezometric information has provided a qualitative estimate of the spatial and temporal evolution of groundwater drawdown between 1975 and 2012 (Figure 2). This analysis reveals that the most intense groundwater drawdown occurred from 1975 to 1992 (215 m maximum), followed by a partial recovery and groundwater level stabilization until 2012.

Currently, most of the pumping wells are located in this southern and southwestern sector of the aquifer, which is responsible for the deficit of the groundwater reserve.

Comparison of the spatial and temporal evolution of the aquifer groundwater level to estimated displacements does not reveal a clear correlation between groundwater level variations and subsidence rate changes. As previously reported by Rigo *et al.* (2013), the aquifer system is affected by inelastic, unrecoverable and permanent deformation, indicating a delayed compaction process longer in time than that suggested by González and Fernández (2011a).

This hypothesis is supported by the presence of a very thick (>100 m) soft soil layer with a very low permeability (approximately 50 mm/h), which is responsible for the very slow consolidation process.

Indeed, most of the fine-grained silt and clay layers with low vertical hydraulic conductivity have been drained since the 1960s due to aquifer overexploitation and the negative gradient of the pore pressure has persisted since that time (Figure 2h). This negative gradient is responsible for a delayed consolidation process, wherein the maximum settlement has still not been reached.

This hypothesis is in agreement with the observed trend of time-subsidence curves derived from InSAR and GPS data, which indicate that the aquifer system deformation is suffering a deceleration coinciding with the theoretical consolidation curves obtained from laboratory tests for unconsolidated sediments. In the future, the execution of a deep geotechnical borehole allows for laboratory tests to be conducted to better understand the role of soil deformability and to model the behaviour of this aquifer-system.

12. Conclusions

In this paper, the combined analysis of geological and hydrological information with displacement maps and time-series retrieved from multi-sensor and multi-temporal SAR images generates several novel conclusions with respect to previous works:

1) A 20-year spatio-temporal evolution of subsidence was determined using DInSAR techniques where the accumulated subsidence due to overexploitation of the Alto Guadalentín aquifer-system reaches maximum values of 2.5 m. Additionally, the satellite measurements provide locally comparable results with measurements acquired by two permanent GPS stations located in the study area.

2) The spatial variability of the grain size and thickness of Plio-Quaternary sediments was determined, informing the development of a new soft soil thickness map, which correlates well with the magnitude of measured displacements.

3) The spatio-temporal evolution of groundwater between 1975 and 2012 revealed that the most intense drawdown occurred from 1975 to 1992 (215 m maximum), followed by partial recovery and groundwater level stabilization until 2012; this points to an unclear correlation with the displacement time series.

These findings suggest that the aquifer system is experiencing a very slow consolidation process where a very thick soft soil layer with low permeability has been drained since the 1960s due to aquifer overexploitation. As a result, a negative gradient is maintained in this layer, which creates a delayed consolidation process wherein the maximum settlement has yet to be reached.

Conflict of interest

The authors declare that there are no conflicts of interest.

Acknowledgments

This work was developed during Roberta Bonì's stay within the Geohazards InSAR Laboratory and Modelling Group of the Instituto Geológico y Minero de España in the framework of the DORIS project (Ground Deformation Risk Scenarios: an Advanced Assessment Service) funded by the EC-GMES-FP7 initiative (Grant Agreement 423 no. 242212). ALOS PALSAR images were provided by the project JAXA-1209. Part of this work is supported by the Spanish Government under project TEC2011-28201-C02 and by the project 15224/PI/10 from the Regional Agency of Science and Technology in Murcia. Additional funding was obtained from the Spanish Research Program through the projects AYA2010-17448, ESP2013-47780-C2-1-R and ESP2013-47780-C2-2-R and by the Ministry of Education, Culture and Sport through the project PRX14/00100.

References

Alonso, M., S., and Aróstegui, J., L., G. (2014) Sobreexplotación de acuíferos en la cuenca del Segura, ISBN: 978-84-92988-22-8.

Altamimi, Z., Métivier, L., Collilieux, X. (2012). ITRF2008 plate motion model. J. geophys. Res. 117, B07402, doi:10.1029/2011JB008930.

Arnaud A., Adam, N., Hanssen, R., Inglada, J., Duro, J., Closa, J. Eineder M. (2003). ASAR ERS interferometric phase continuity. International Geoscience and Remote Sensing Symposium, 21-25 July 2003, Toulouse (France).

Berardino, P., Fornaro, G., Lanari, R., Sansosti, E. (2002). A new algorithm for surface deformation monitoring based on small baseline differential SAR interferograms. Geoscience and Remote Sensing, IEEE Transactions on, 40 (11), 2375-2383.

Beutler, G., Moore, A.W., Mueller, I.I. (2008). The International Global Navigation Satellite Systems (GNSS) Service: developments and achievements. Journal of Geodesy, 83 (3-4), 297-307, doi:10.1007/s00190-008-0268-z.

Bourgois, J., Mauffret, A., Ammar, A., Demnati, A. (1992). Multichannel seismic data imaging of inversion tectonics of the Alboran Ridge (Western Mediterranean Sea). Geo-Marine Letters, 12 (2-3), 117-122.

Casu, F., Manzo, M., Lanari, R. (2006). A quantitative assessment of the SBAS algorithm performance for surface deformation retrieval from DInSAR data. Remote Sensing of Environment, 10 2(3), 195-210.

Cerón, J.C. (1995), Estudio hidrogeoquimico del acuifero del Alto Guadalentín (Murcia) [Ph.D. 229 thesis]: Granada, University of Granada, pp. 265.

Cerón, J.C., and Pulido-Bosch, A. (1996). Groundwater problems resulting from CO2 pollution and overexploitation in Alto Guadalentín aquifer (Murcia, Spain). Environmental Geology, 28 (4) 223–228, doi:10.1007/s002540050096.

Cerón, J. C., Pulido-Bosch, A., Bakalowicz, M. (1999). Application of Principal Components Analysis to the study of CO2-rich thermomineral waters in the aquifer system of Alto Guadalentín (Spain). Hydrological sciences journal, 44 (6), 929-942.

Changming, L., Jingjie, Y., Kendy, E. (2001). Groundwater exploitation and its impact on the environment in the North China Plain. Water International, 26 (2), 265-272.

CHS (1990), Estudio y redacción del Plan de ordenación del acuífero Alto Guadalentín, Tech. rep.

CHS (2005), Estudio de cuantificación del volumen anual de sobreexplotación de los acuíferos de la unidad hidrogeológica 07.28 Alto Guadalentín y 07.33 Águilas, Tech. rep.

(ftp://ftp.chsegura.es/oph/phcsegura/borrador/anejo12docs/FichaSub_070_057_AltoGuadalentin.pdf)

CHS (2006), Plan especial ante situaciones de alerta y eventual sequia en la cuenca del Segura: 238 Confederacion hidrografica del Segura, Tech. rep., 298 p., 239.

CHS (2014), Plan Hidrológico de la Cuenca del Segura 2015/2021. Análisis piezométrico histórico y de los ultimos 25 años (1990-2014) de las masas de Agua subterráneas de la demarcación Hidrográfica del Segura. 070.057 Alto Guadalentín. Tech. rep.

http://www.chsegura.es/chs/cuenca/sequias/pes/eeapes.html#doc_completa

Crosetto, M., Biescas, E., Duro, J., Closa, J., Arnaud A. (2008). Generation of Advanced ERS and Envisat Interferometric SAR Products Using the Stable Point Network Technique. Photogrammetric Engineering & Remote Sensing, 74 (4), 443-450.

Declercq, P.-Y., Devleeschouwer, X., Pouriel, F. (2005). Subsidence Revealed by PSInSAR Technique in the Ottignies-Wavre Area (Belgium) Related to Water Pumping in Urban Area. Fringe 2005 Workshop, Proceedings of the Conference held 28 November -- 2 December, 2005 in Frascati, Italy. Edited by H. Lacoste and L. Ouwehand. ESA SP-610. European Space Agency, 2006. Published on CDROM., p.66.1.

Duro J., Inglada, J., Closa, J., Adam, N. Arnaud A. (2003). High resolution differential interferometry using time series of ERS and ENVISAT SAR data. FRINGE 2003, 1-5 December 2003, Frascati (Italy).

Ferretti A., Prati C., Rocca F. (2001). Permanent scatterers in SAR interferometry. IEEE Trans Geosci Remote Sens 39(1), 8-20, doi:10.1109/36.898661.

Galloway, D. L., Hudnut, K. W., Ingebritsen, S. E., Phillips, S. P., Peltzer, G., Rogez, F., Rosen, P. A. (1998). Detection of aquifer system compaction and land subsidence using interferometric synthetic aperture radar, Antelope Valley, Mojave Desert, California. Water Resources Research, 34(10), 2573-2585.

González, P. J., Fernández, J. (2011a). Drought-driven transient aquifer compaction imaged using multitemporal satellite radar interferometry. Geology, 39 (6), 551-554, doi:10.1130/G31900.1.

González P.J., Fernández J. (2011b). Error estimation in multitemporal InSAR deformation time series, with application to Lanzarote, Canary Islands, Journal of Geophysical Research, 116, B10404, doi:10.1029/2011JB008412.

González, P. J., Tiampo, K. F., Palano, M., Cannavó, F., Fernández, J. (2012). The 2011 Lorca earthquake slip distribution controlled by groundwater crustal unloading. Nature Geoscience, 5 (11), 821-825, doi:10.1038/ngeo1610.

Gràcia, E., Pallàs, R., Soto, J. I., Comas, M., Moreno, X., Masana, E., Santanach, P., Diez, S., García, M., Dañobeitia, J.J. (2006). Active faulting offshore SE Spain (Alboran Sea): Implications for earthquake hazard assessment in the Southern Iberian Margin. Earth and Planetary Science Letters, 241(3), 734-749, doi:10.1016/j.epsl.2005.11.009.

Hanssen, R. F. (2003, May). Subsidence monitoring using contiguous and PS InSAR quality assessment based on Precision and Reliability. In The 11th FIG Symposium on DeformationMeasurements, Santorini, Greece.

Herrera, G., Fernández, J.A., Tomás, R., Cooksley, G., Mulas, J. (2009). Advanced interpretation of subsidence in Murcia (SE Spain) using A-DInSAR data – modelling and validation. Natural Hazards and Earth System Science 9, 647–661.

Hoffmann, J., Zebker, H.A., Galloway, D.L., Amelung, F. (2001). Seasonal subsidence and rebound in Las Vegas Valley, Nevada, observed by synthetic aperture radar interferometry. Water Resources Research 37, 1551–1566.

Holzer, T.L., Galloway, D.L. 2005. Impacts of land subsidence caused by withdrawal of underground fluids in the United States. Reviews in Engineering Geology, XVI, 87-99.

Hooper, A. (2008). A multi-temporal InSAR method incorporating both persistent scatterer and small baseline approaches. Geophys. Res. Lett. 35(16), L16302, doi:10.1029/2008GL034654.

IGME (1981). Mapa Geologico de España, 1:50.000, Sheet Lorca (953). Servicio de Publicaciones Ministerio de Industria, Madrid.

IGME (1994). Estudio para la regulación y apoyo a la gestión de los recursos hídricos subterráneos del Alto Guadalentín (Murcia). Modelo matemático de flujo subterráneo. IGME internal report ref. 33237.

Kampes, B. M., Hanssen, R. F., Perski, Z. (2003, December). Radar interferometry with public domain tools. In Proceedings of FRINGE (pp. 1-5).

Lundgren, P., Usai, S., Sansosti, E., Lanari, R., Tesauro, M., Fornaro, G., Berardino, P. (2001). Modelling surface deformation observed with synthetic aperture radar interferometry at Campi Flegrei caldera. J. Geophys. Res., 106 (B9), 19355-19366, doi:10.1029/2001jb000194.

Martín, V. J. M., Espinosa, G. J. S., Pérez, R. A. (1973). Mapa geológico de España: E. 1:50,000. Madrid: Servicio de Publicaciones, Ministerio de Industria y Energía. Instituto geológico y minero de España (IGME).

Martınez-Dıaz, J. J. (2002). Stress field variation related to fault interaction in a reverse oblique-slip fault: the Alhama de Murcia fault, Betic Cordillera, Spain. Tectonophysics 356 (4), 291-305.

Martínez-Díaz, J. J., Bejar-Pizarro, M., Álvarez-Gómez, J. A., Mancilla, F. D. L., Stich, D., Herrera, G., Morales, J. (2012). Tectonic and seismic implications of an intersegment rupture: The damaging May 11th 2011 Mw 5.2 Lorca, Spain, earthquake. Tectonophysics 546, 28-37.

Masana, E., Martínez-Díaz, J. J., Hernández-Enrile, J. L., Santanach, P. (2004). The Alhama de Murcia fault (SE Spain), a seismogenic fault in a diffuse plate boundary: Seismotectonic implications for the Ibero-Magrebian region. J. Geophys. Res. 109, B01301, doi:10.1029/2002JB002359.

Mora, O., Mallorqui, J.J., Broquetas, A. (2003). Linear and nonlinear terrain deformation maps from a reduced set of interferometric SAR images. IEEE Trans. Geosci. Remote Sens. 41(10), 2243-2253.

Palano, M., González, P., Fernández, J. (2013). Strain and stress fields along the Gibraltar Orogenic Arc: constraints on active geodynamics. Gondwana Res. 23, 1071-1088, doi:10.1016/j.gr.2012.05.021.

Palano, M. (2015). On the present-day crustal stress, strain-rate fields and mantle anisotropy pattern of Italy. Geophys. J. Int., 200 (2), 969-985, doi:10.1093/gji/ggu451.

Phien-Wej, N., Giao, P. H., Nutalaya, P. (2006). Land subsidence in Bangkok, Thailand. Eng. Geol.82 (4), 187-201.

Prati, C., Ferretti, A., Perissin, D. (2010). Recent advances on surface ground deformation measurement by means of repeated spaceborne SAR observations. J. Geodyn. 49 (3-4), 161-170, doi: 10.1016/j.jog.2009.10.011.

Rigo, A., Béjar-Pizarro, M., Martínez-Díaz, J. (2013). Monitoring of Guadalentín valley (southern Spain) through a fast SAR Interferometry method. J. Appl. Geophys. 91, 39-48.

Sansosti, E., Casu, F., Manzo, M., Lanari R. (2010). Space-borne radar interferometry techniques for the generation of deformation time series: an advanced tool for Earth's surface displacement analysis. Geophys. Res. Lett. 37(20), L20305, doi:10.1029/2010gl044379.

Schmidt, D.A., Bürgmann R. (2003). Time-dependent land uplift and subsidence in the Santa Clara valley, California, from a large interferometric synthetic aperture radar data set. J. Geophys. Res. 108, B92416, doi:10.1029/2002jb002267.

Silva, P. G., Bardají, T., Calmel-Avila, M., Goy J. L., Zazo, C. (2008). Transition from alluvial to fluvial systems in the Guadalentín Depression (SE Spain) during the Holocene: Lorca Fan versus Guadalentín River. Geomorphology, 100, 140-153.

Stramondo, S., Saroli, M., Tolomei, C., Moro, M., Doumaz, F., Pesci, A., Loddo, F., Baldi, P., Boschi, E. (2007). Surface movements in Bologna (Po Plain-Italy) detected by multitemporal DInSAR. Remote Sensing of Environment, 110 (3), 304-316.

Strozzi, T., Wegmuller, U., Tosi, L., Bitelli, G., Spreckels, V. (2001). Land subsidence monitoring with differential SAR interferometry. Photogrammetric engineering and remote sensing, 67 (11), 1261-1270.

Tomás, R., Herrera, G., Delgado, J., Lopez-Sanchez, J.M., Mallorquí, J.J., Mulas, J. (2010a). A ground subsidence study based on DInSAR data: calibration of soil parameters and subsidence prediction in Murcia City (Spain). Eng. Geol. 111, 19-30.

Tomás, R., Herrera, G., Lopez-Sanchez, J.M., Vicente, F., Cuenca, A. & Mallorquí, J.J. (2010b). Study of the land subsidence in Orihuela City (SE Spain) using PSI data: Distribution, evolution and correlation with conditioning and triggering factors. Engineering Geology, 115, 105-121.

Tomás, R., Romero, R., Mulas, J., Marturià, J.J., Mallorquí, J.J., Lopez-Sanchez, J.M., Herrera, G., Gutiérrez, F., González, P.J., Fernández, J., Duque, S., Concha-Dimas, A., Cocksley, G., Castañeda, C., Carrasco, D., Blanco, P. (2014). Radar interferometry techniques for the study of ground subsidence phenomena: a review of practical issues through cases in Spain. Environmental Earth Sciences 71, 163-181.

Werner, C., Wegmuller, U., Strozzi, T., Wiesmann, A. (2003). Interferometric point target analysis for deformation mapping. In: Geoscience and remote sensing symposium, IGARSS '03. Proceedings. 2003 IEEE International, 21–25 July 2003 pp 4362–4364 vol.4367. doi:10.1109/igarss.2003.1295516.

6.5. Characterisation of hydraulic head changes and aquifer properties in the London basin using Persistent Scatterer Interferometry ground motion data

Roberta Bonì[1,2],*, Francesca Cigna[1], Stephanie Bricker[1], Claudia Meisina[2], Harry McCormack[3]

[1]British Geological Survey, Natural Environment Research Council, Nicker Hill, Keyworth, Nottinghamshire, NG12 5GG, UK.

[2]Department of Earth and Environmental Sciences, University of Pavia, Via Ferrata 1, 27100 Pavia, Italy.

[3]CGG, NPA Satellite Mapping, Crockham Park, Edenbridge, Kent, TN8 6SR, UK.

* Corresponding author; Visiting student at (1); Present address: (2); email: roberta.boni01@universitadipavia.it

The paper has been published in the Journal of Hydrology, Volume 540, September 2016, Pages 835–849

doi:10.1016/j.jhydrol.2016.06.068

Abstract: In this paper, Persistent Scatterer Interferometry was applied to ERS-1/2 and ENVISAT satellite data covering 1992-2000 and 2002-2010 respectively, to analyse the relationship between ground motion and hydraulic head changes in the London Basin, United Kingdom. The integration of observed groundwater levels provided by the Environment Agency and satellite-derived displacement time series allowed the estimation of the spatio-temporal variations of the Chalk aquifer storage coefficient and compressibility over an area of ~1,360 km^2. The average storage coefficient of the aquifer reaches values of 1×10^{-3} and the estimated average aquifer compressibility is 7.7×10^{-10} Pa^{-1} and 1.2×10^{-9} Pa^{-1} for the periods 1992-2000 and 2002-2010, respectively. Derived storage coefficient values appear to be correlated with the hydrogeological setting, where confined by the London Clay the storage coefficient is typically an order of magnitude lower than where the chalk is overlain by the Lambeth Group. PSI-derived storage coefficient estimates agree with the values obtained from pumping tests in the same area. A simplified one-dimensional model is applied to simulate the ground motion response to hydraulic heads changes at nine piezometers. The comparison between simulated and satellite-observed ground motion changes reveals good agreement, with errors ranging between 1.4 and 6.9 mm, and being 3.2 mm on average.

Keywords: Persistent Scatterer Interferometry (PSI); London; groundwater level; Chalk aquifer; storage; compressibility

1. Introduction

Many cities rely on groundwater for water supply. In most parts of Europe over 40% of water supply comes from urban aquifers (Wolf *et al.* 2006). Monitoring and careful management of urban aquifers is needed to ensure that the aquifers are utilised in a sustainable manner and groundwater extracted for use is naturally replenished. One of the most obvious effects related to prolonged groundwater over-exploitation across city-regions is land subsidence related to falling groundwater levels and/or uplift caused by recovery of groundwater heads due to the reduction in abstraction (Morris *et al.* 2003; Bell *et al.* 2008).

Changes to the aquifers and the geological strata overlying aquifers need to be understood and quantified, such that i) changes in groundwater levels do not cause inundation of water into underground assets, ii) differential changes in ground saturation do not significantly affect ground engineering properties, and iii) ground level change does not cause damage to existing infrastructure. Aquifer consolidation is commonly calculated based on Terzaghi's consolidation theory (Terzaghi 1943). With the vertical total stress unchanged, a variation in pore-fluid pressure causes a proportional change in effective stress within the aquifer, resulting in a volume change. The latter is influenced by the compressibility of the aquifer. When the effective stress does not exceed the maximum effective stress that the system has experienced in the past (i.e. pre-consolidation stress), the fluctuations in the water level create small elastic deformation of the aquifer-system and small land surface displacement. On the contrary, if the effective stress exceeds the pre-consolidation stress, the pore structure of susceptible fine-grained aquitards in the system may undergo significant rearrangement and the deformation is mainly inelastic (Galloway *et al.* 1999). Vertical ground motion can therefore be the effect of the elastic and/or inelastic compaction which depends on the hydraulic head changes and the thickness of the unconsolidated deposits (Riley 1969; Helm 1975, 1976).

The amount of water released or stored per unit of area of the aquifer and per unit head change is defined as the storage coefficient or storativity (Fetter, 2001). This is a key property of the aquifer system that reflects the response of aquifers and aquitards to hydraulic head changes, and is important to estimate the available groundwater resource. The storage coefficient is usually obtained either *in situ* by measuring drawdown rates during pumping tests or from lab-based porosity values. Results from pumping tests are limited in that they are representative only of the permeable portion of the aquifer within proximity of the pumping well and several assumptions

about the hydraulic conditions and pumping well are made (Fetter, 2001). Validity of the results of the test is dependent on the duration of the test and the number of observation wells used to measure the aquifer response. In addition, pumping test sites are biased towards high-yielding aquifer conditions since most tests are conducted on prospective abstraction wells. Meanwhile, lab measurements have a small-sample volume, samples may be disturbed and therefore may not be representative of the *in situ* conditions (Riley 1998). These methods are also only able to estimate this parameter for a limited number of points due to their costs, and in some cases, the results are of questionable reliability (Balkhair 2002; Schad & Teutsch 1994; Kaczmaryk & Delay 2007).

During the last two decades, many studies have integrated satellite interferometric synthetic aperture radar (InSAR; Gabriel *et al.* 1989; Massonnet & Rabaute 1993) and groundwater level change data to estimate the aquifer-system storage coefficient (Hoffmann *et al.* 2001, 2003; Galloway & Hoffmann 2007; Bell *et al.* 2008; Tomás *et al.* 2006, 2011; Ezquerro *et al.* 2014; Revees *et al.* 2014; Chaussard *et al.* 2014). Persistent Scatterer Interferometry (PSI) is an InSAR processing method that exploits significant stacks of time-stamped SAR images to identify radar targets or Persistent Scatterers (PS) on the Earth's surface for which the displacement time series along the line of sight (LOS) of the satellite is reconstructed (e.g., Ferretti *et al.* 2001; Werner *et al.* 2003; Hooper *et al.* 2004). The technique has been successfully used to analyse land deformation due to groundwater level variations in a number of cities and regions world-wide, such as Mexico City (Osmanoğlu *et al.* 2011) and Morelia in central Mexico (Cigna *et al.* 2012), Vega Media, Madrid, Alto Guadalentín and Granada Basins in Spain (Herrera *et al.* 2009, Ezquerro *et al.* 2014, Bonì *et al.* 2015, Notti *et al.* 2016).

In the United Kingdom (UK) the most important aquifer is the Chalk which accounts for 60% of the groundwater used in England and Wales (UK Groundwater Forum 1998) and supports approximately 80% of public water supply in the River Thames Catchment and 20% in London (Thames Water, undated). Not only are public water supplies taken directly from groundwater, but also from surface water sources derived from rivers with a high groundwater baseflow index (BFI). The River Thames in London is one such river with a large groundwater baseflow component (BFI of 0.63 for the River Thames at Kingston gauging station 39001; NRFA 2016). The Chalk aquifer in London has been exploited for public and industrial supply since the 1850s and is one of the most monitored and managed aquifer-systems in the UK (Jones *et al.* 2012; Royse *et al.* 2012). The chalk aquifer continues to be an important source of water for London however, a reduction in abstraction since the 1950s has led to problems with rising groundwater levels and as a result artificial recharge schemes (O'Shea & Sage 1999; Jones *et al.* 2012) and open-loop ground source heating schemes (Fry 2009) have been encouraged as part of the aquifer management schemes. The chalk aquifer is

also host to increasing subsurface infrastructure such as transport tunnels, with dewatering schemes necessary to facilitate their installation (Royse *et al.* 2012). It is therefore essential to understand the variations of aquifer properties throughout the Chalk, in order to safeguard the groundwater resource and manage its multiple uses.

To date there have been few studies on the Chalk aquifer storage coefficient variations throughout the London Basin, although there has been a number of specific studies on the properties of the Chalk. Lewis *et al.* (1993) estimated the Chalk storage by using data derived from pumping tests across the whole of England. Allen *et al.* (1997) analysed the aquifer properties of the Chalk of England using 2,100 pumping tests collated by the British Geological Survey (BGS) and the Environment Agency. However, detailed field studies are necessary to determine the physical properties of the Chalk aquifer in the London Basin, in order to take into account the site specific matrix-fracture interaction.

A recent study by Cigna *et al*. (2015) revealed that an area of ~200 km^2 in the administrative area of Greater London (~1,580 km^2) has been affected by anthropogenic land subsidence due to groundwater abstraction. In particular, these authors made use of PSI ground motion information for 1992-2000 and 2002-2010 and geological data to delineate natural and anthropogenic geohazards within the framework of the European Commission FP7-SPACE project PanGeo. Another study by Bateson *et al.* (2009) used PSI data of the period 1997-2005 to validate the results of the modelled subsidence due to groundwater abstraction for the Merton area of south-west London.

To date, PSI ground motion data have not been used to estimate the storage coefficient in the London Basin and to understand the spatio-temporal variability of this parameter under different aquifer conditions. For the first time, in this paper, such an analysis is undertaken by exploiting ground motion data for the years 1992-2000 and 2002-2010, obtained by processing two stacks of ERS-1/2 and ENVISAT radar imagery by using the Interferometric Point Target Analysis (IPTA) technique (Werner *et al.* 2003). The analysis allows the characterisation of the aquifer properties over an area of ~1,360 km^2. The results obtained based on the satellite ground motion observations are compared with storage coefficient records obtained *in situ* via pumping tests. Furthermore, the ground motion response to hydraulic head changes are analysed at nine piezometers.

2. Study area

2.1 Geology

The London Basin covers an area of ~2,500 km^2 (Figure 1) in southern England. The basin overlies the London platform formed of Palaeozoic basement which is bounded to the south by the Variscan Front (Royse *et al.* 2012). The Chalk Group, which reaches thicknesses of over 200 m in central London forms a rim around younger Palaeogene deposits which infill the London Basin (Ford *et al.* 2010; Mathers *et al.* 2014). The Palaeogene strata which overlie and confine the chalk have a variable lithology and form a broad flat valley through which the River Thames flows. The Palaeogene deposits comprise, the Thanet Formation, a fine-sand unit; the Lambeth Group consisting of vertically and laterally variable sequences mainly of clay with silty and sandy horizons; the Harwich Formation a silty, sandy clay with gravel beds, and; the London Clay Formation, a dense fissured clay (Sumbler *et al.* 1996; Ellison *et al.* 2004). Quaternary deposits, primarily river terrace deposits associated with the River Thames and artificially modified ground, such as embankments or landfill and engineered cuttings and quarries provide a discontinuous cover at surface.

Figure 1 shows the bedrock geology of the London Basin and the location of the main faults. It is evident that much of central London lies within a graben bounded by the Northern Boundary fault to the north and the Wimbledon-Streatham fault and the Greenwich fault to the south, where the chalk is downthrown by some 50 m. However, recent investigations by the London Basin Forum (Mortimore *et al.* 2011; Royse *et al.* 2012) and ground conditions encountered during recent engineering projects, such as the Channel Tunnel Rail Link, Thames Water Ring Main (Newman 2009), Crossrail (Aldiss 2013) and the Docklands Light Railway, show that the geological structure of the London Basin is more complex than previously thought and faults are under-represented by current mapping (Aldiss, 2013). Reactivation of basement tectonic structures during the break-up of Pangea and the alpine orogeny (Jurassic – Tertiary) is likely to have resulted in the propagation of faults and fracture networks throughout the younger London Basin sequences, explaining significant faulting observed in the Chalk Group and overlying units during these more recent site investigations. A 3D geological model of the Thames Valley generated by the BGS in order to visualize the distribution of the geological units along the valley (Mathers *et al.* 2014) has been used to extract the cross sections A-A’ and B-B’ in Figure 1.

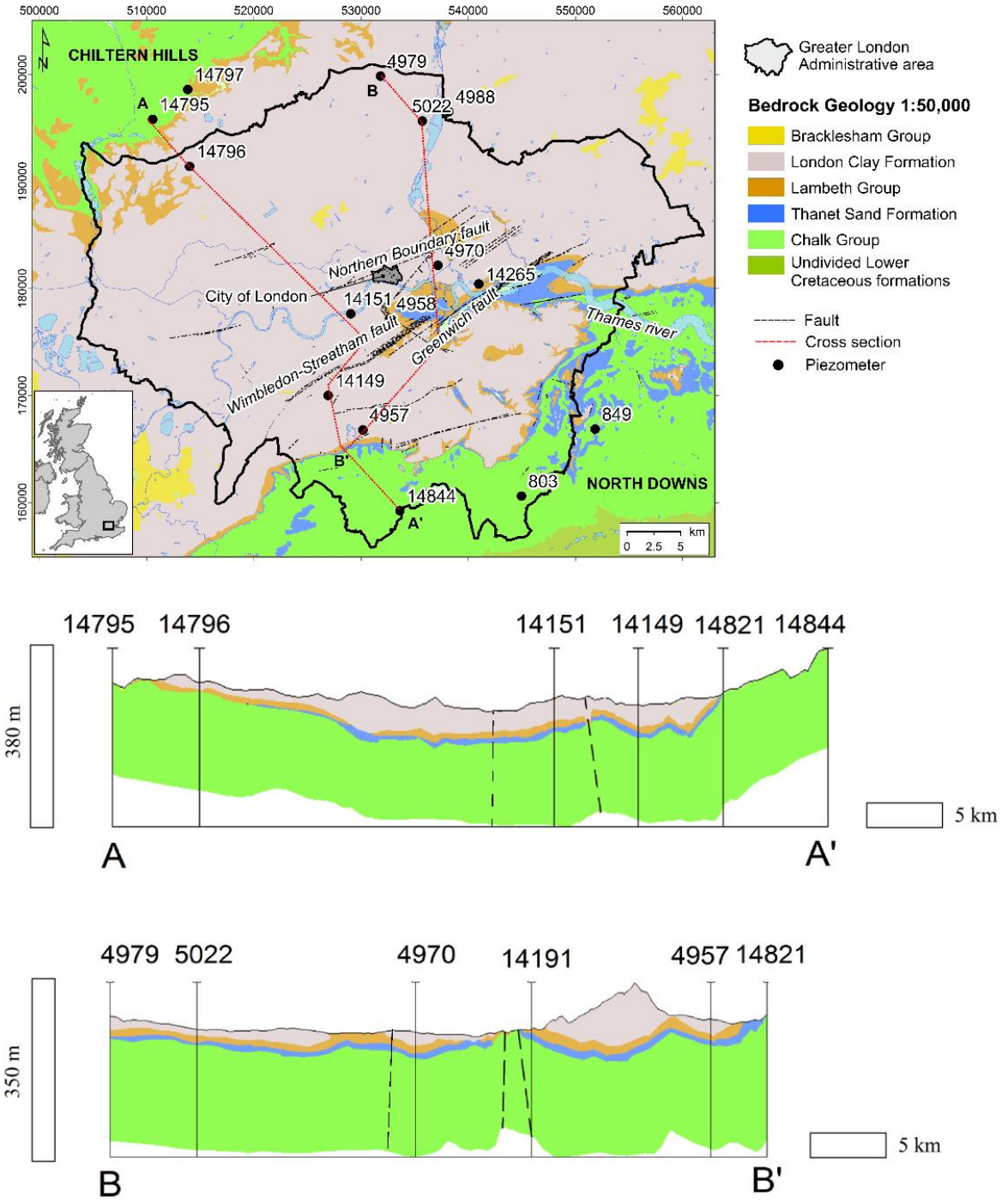

Figure 1. Geological setting of the study area with indication of water bodies and river network from the European Urban Atlas (EEA 2010). Geological materials © NERC. All rights reserved. Urban Atlas © Directorate-General Enterprise and Industry. British National Grid. Projection: Transverse Mercator. Datum: OSGB 1936.

2.2 Hydrogeology

The Chalk Group forms a principal aquifer in the London Basin supporting public water supply (Jones *et al.* 2012), industrial groundwater use such as ground source heating systems (Fry 2009) and significant baseflow to the River Thames (BFI 0.63). In the central area of the Basin, the chalk aquifer is confined by the overlying Palaeogene formations. Whilst the Palaeogene deposits do not form principle aquifers, the lithological variability within and across the units leads to hydrogeological heterogeneity and where present the sand-rich horizons can contain significant quantities of groundwater. The sand-rich Thanet Formation, for example, is highly permeable and often in hydraulic continuity with the underlying chalk aquifer. The chalk aquifer is recharged on the interfluves - in the Chiltern Hills to the north and North Downs to the south, where the Chalk is present at surface and the aquifer is unconfined. The unconfined aquifer exhibits larger seasonal water table variations, with associated stream-head migration up dry periglacial valleys and where fracture sets exert strong linear river drainage patterns (Bloomfield *et al.* 2011).

The effects of faulting on the chalk aquifer and groundwater flow in the central London Basin has been highlighted in recent investigations (De Freitas 2009; Royse *et al.* 2012; EA 2015) whereby compartmentalisation of the chalk by faults and differential fault permeability leads to irregular groundwater flows and difficulties during dewatering. Both lithological variations and structural features exert significant control on aquifer properties in the Thames Basin (Bloomfield *et al.* 2011) and on the chalk in particular. The Chalk is a dual porosity medium, with matrix and fracture porosity (Price 1987; Barker 1991; Price *et al.* 1993). The primary porosity of the Chalk (typically 0.25 to 0.40) is related to the presence of the *coccoliths* in the matrix, through which the aquifer does not drain readily due to the very small pore throats (Price *et al.* 1976, Bloomfield *et al.*1995). Instead, the groundwater storage of the aquifer is mainly derived from secondary porosity along faults, through the fractures, which are also widened by dissolution processes and long bedding planes such as marl bands and flint horizons (MacDonald & Allen 2001). In the London Basin, permeable horizons in the overlying Thanet Formation, Lambeth Group and Harwich Formation also provide some storage capability. The specific yield for the basal sands, comprising the Thanet sands and lower-most sand units of the Lambeth Group, was found to be in the range 1×10^{-2} to 3×10^{-2} in the Lee Valley in the north of the London Basin (O'Shea & Sage 1999).

Historic overexploitation of the Chalk aquifer for industry and manufacturing up to the 1950s led to widespread lowering of groundwater levels, reaching a depth of up to 90 m below sea-level in the central London Basin (Jones *et al.* 2012). As a result, the Chalk aquifer became unconfined, leading to under-drainage and desaturation of the London Clay (Jones *et al.* 2012; Royse *et al.* 2012). In the 1950s a combination of aquifer depletion, improvements in surface water quality and water storage

led to a decline in groundwater abstraction and a recovery of groundwater levels at a rate of up to 3 m/year (Jones *et al.* 2012). As groundwater recovery and re-saturation of the London Clay could potentially have negative impacts on the foundations of structures and infrastructure in the Basin, an action plan was developed by London Underground, Thames Water and the Environment Agency (EA), i.e. the GARDIT (General Aquifer Research Development and Investigation Team) strategy. As a result, an observation borehole network within the Basin was established by the EA to monitor and manage changes in groundwater levels. Since 1999 there has been an increase in the licensed volume of abstraction of at least 3×10^6 l/d in central London (EA 2007, EA 2015) which has been successful in stabilising the rise of groundwater levels. As a by-product of London's rising groundwater levels an artificial recharge scheme was licensed in North London, NLARS (North London Artificial Recharge Scheme; Jones *et al.* 2012) to help control groundwater levels and maximise the available groundwater storage in the north part of the basin where groundwater levels were depleted (O'Shea *et al.* 1995, 1999).

Records from the observation borehole network, provide detailed time-series data to reconstruct the historical groundwater level changes across the London Basin for the 1990s and 2000s (Figure 2) and evaluate the relationship with ground level change over the same period. In particular, 236, 166 and 214 piezometers were employed to evaluate the groundwater level changes respectively in the periods 1992-2000, 2002-2010 and 1992-2010, to match with the satellite observation periods (see section 3).

In 1992-2000, an average groundwater level rise of 2.5 m was recorded, with 26% of the observation boreholes revealing groundwater level rises of more than 5 m. The most notable groundwater level rise mainly affects the north-west and south-east of the London Basin (Figure 2. panel *a*). Conversely, over the second period (2002-2010), an average groundwater level fall of 0.5 m was recorded by the network, and 12% of the boreholes showed groundwater level falls exceeding 5 m, with peaks of 30-40 m. In the central area of the London Basin, an area of around 52 km^2 recorded 7 m of groundwater level lowering (Figure 2. panel *b*).

In the whole monitored period (1992-2010), a groundwater level rise of 5 m was recorded on average across the area of interest (Figure 2. panel *c*). The northern sector of the London Basin is characterized by a general rise of the groundwater level during the whole period from 1992 to 2010, whilst the central sector records a rise in the groundwater level from 1992 to 2000 and a subsequent fall in the period 2002-2010. The southern sector is mainly characterized by falling groundwater levels in the whole monitored period.

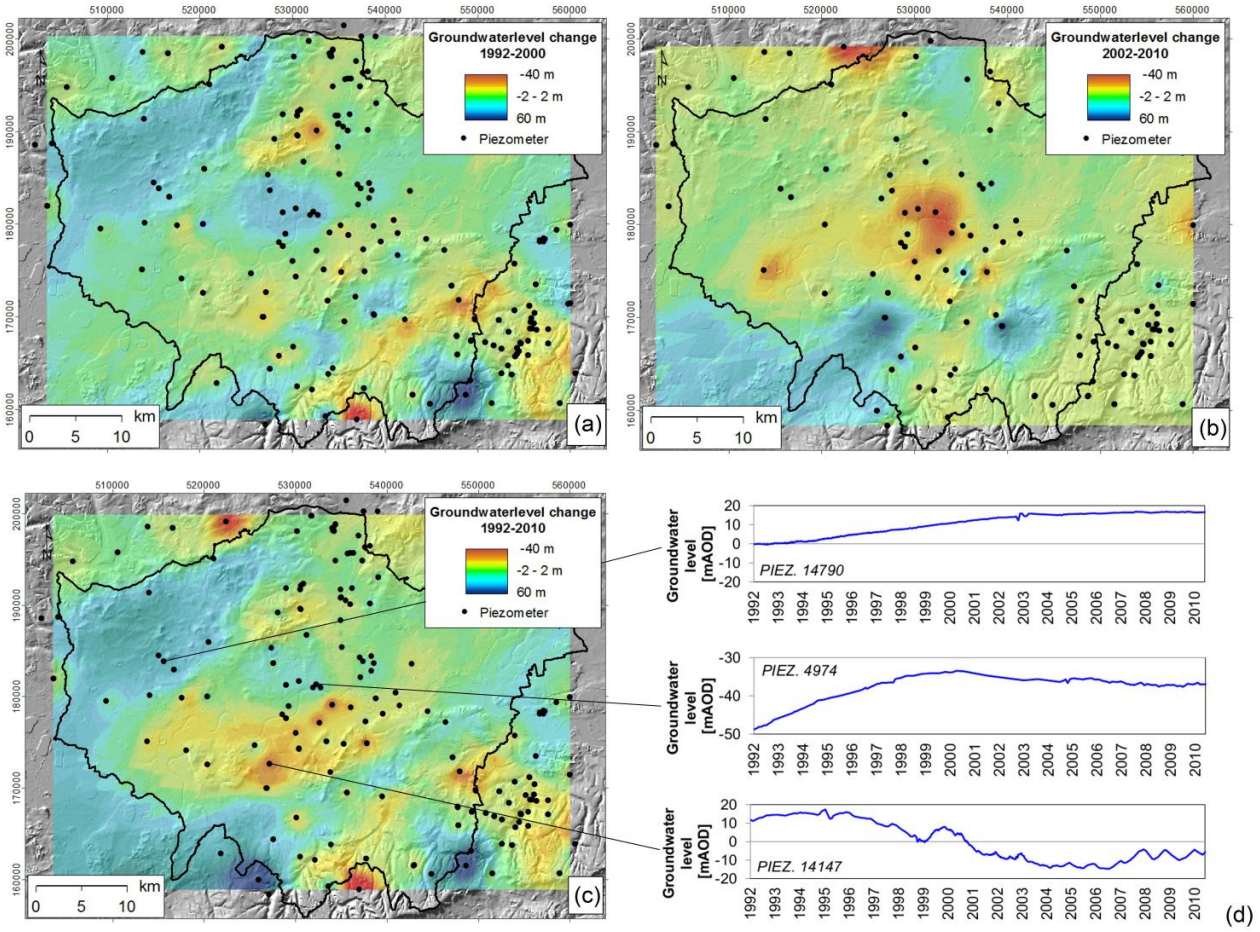

Figure 2. Groundwater level changes in the periods (a) 1992-2000, (b) 2002-2010 and (c) 1992-2010, overlapped onto shaded relief of NEXTMap® DTM at 50 m resolution. Positive and negative values indicate, respectively, rise and fall of the groundwater level. (d) Groundwater level time series are included to illustrate different temporal changes observed across the Basin. British National Grid. Projection: Transverse Mercator. Datum: OSGB 1936. NEXTMap® Britain © 2003, Intermap Technologies Inc., All rights reserved. Groundwater level data © Environment Agency copyright and/or database rights 2015. All rights reserved.

3. Input data and methodology

3.1. SAR data and PSI analysis

The input satellite data for this study consists of 27 ERS-1 and ERS-2 SAR scenes acquired in ascending mode along track 201, and 45 ENVISAT advanced SAR (ASAR) Image Mode IS2 scenes acquired in descending mode along track 51, both datasets characterised by nominal repeat cycle of 35 days. The first dataset covers the time interval from 19/06/1992 to 31/07/2000 and the second one from 13/12/2002 to 17/09/2010.

PSI ground motion data over the area of Greater London were obtained by using the GAMMA SAR and Interferometry software and, in particular, the IPTA algorithm (Werner *et al.* 2003). With the IPTA method, the temporal and spatial characteristics of interferometric signatures collected from point targets were exploited to obtain surface deformation histories, terrain heights, and relative atmospheric path delays. Following the conventional approach to PSI processing, the single-master method was used to form interferograms for each dataset (using the scenes acquired on 13/01/1997 and 11/05/2007 as masters for the ERS and ENVISAT processing, respectively), and interferometric pairs were formed with all the remaining slave scenes.

The incidence angle of the employed sensor modes for both datasets is 23° from the vertical direction, which permits the detection of 92% of vertical displacements. Assuming the occurrence of sole vertical ground motion across the Basin, LOS displacements and velocities for both datasets were projected along the vertical direction. This was done by dividing the LOS estimates by the cosine of the incidence angle, hence by 0.92, corresponding with an increase in the LOS values by 8.6% (Figure 3. panels *a* and *b*). This assumption is justified by the generally smaller magnitude of the horizontal than vertical component of the motion in areas affected by land motion due to groundwater exploitation (e.g. Samieie-Esfahany *et al.* 2009; Klemm *et al.* 2010). Moreover, no significant horizontal component of land motion has been previously detected in London based on InSAR data (Aldiss *et al.* 2014; Cigna *et al.* 2015; Bingley *et al.* 2007), in fact only small-scale, fault-controlled E-W lateral movements have been detected (Mason *et al.* 2015).

The processing results show a total of 730,254 ERS-1/2 persistent scatterers (PS), over a processing area of ~2,500 km^2, hence a target density that amounts to 292 PS/km^2. The total number of ENVISAT PS found across the 2,350 km^2 processing area (slightly smaller than the ERS-1/2 area due to the different footprints of the satellite frames) amounts to 838,939, hence 336 PS/km^2.

As observed by Cigna *et al.* (2015), who used the same input PSI data of this study, the larger number of scenes composing the ENVISAT stack – as opposed to the ERS one – resulted in PS datasets with denser networks of reflectors. The retrieved density of PS was also influenced by the

threshold that was used for the interferometric phase standard deviation during the processing, and the resulting minimum average coherence adopted to minimise the presence of lower quality targets in the results (i.e. 0.53 for ERS and 0.49 for ENVISAT), with the ERS dataset showing less PS than the ENVISAT one, due to the higher threshold employed.

The uncertainty in the estimated ground motion velocity was also calculated during the IPTA processing and the analysis of interferometric phase residuals derived based on the iterative regression analysis to separate phase components due to linear and nonlinear deformation, topographic errors and atmospheric delay. For over 95 % of the PS targets within the administrative area the uncertainty of the resulting velocities along the satellite LOS was found between 0.09 and 1.09 mm/year in the ERS-1/2 dataset, and between 0.17 and 1.13 mm/year in the ENVISAT dataset (Cigna *et al.* 2015).

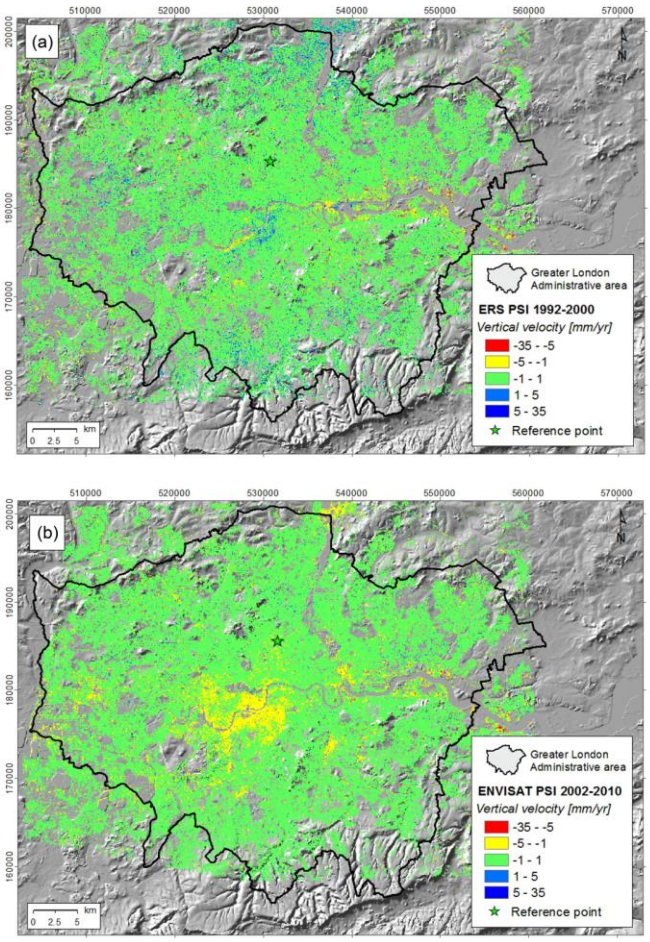

Figure 3. Vertical motion velocities estimated for the London Basin with PSI analysis in (a) 1992-2000 and (b) 2002-2010, overlapped onto shaded relief of NEXTMap® DTM at 50 m resolution. British National Grid. Projection: Transverse Mercator. Datum: OSGB 1936. ERS-1/2 and NVISAT PSI data © CGG NPA Satellite Mapping. NEXTMap® Britain © 2003, Intermap Technologies Inc., All rights reserved.

3.2. Estimation of the aquifer storage coefficient and compressibility

The storage coefficient *S* or storativity represents the amount of water stored or released per unit of area of the aquifer and per unit head change. In the saturated zone, the pressure head, acts on the aquifer skeleton and on the density of the water in the pores. When the pressure increases, the aquifer skeleton expands, whilst if it decreases, the aquifer skeleton compacts (Sneed & Galloway 2000). If the water pressure is reduced, water is released from storage in response to expansion of the water in the pores and compaction of the aquifer-system. Therefore, the aquifer-system storage coefficient *S* is defined as (Galloway *et al.* 1998):

$$S = S'_k + S_k + S_w = S_k^* + S_w \quad (1)$$ (Galloway *et al.* 1998)

Where S'_k and S_k are the skeletal storage of the aquitard and the aquifer, respectively, while S_w is the water storativity. S_k^* is the aquifer-system skeletal storage. Two aquifer-system skeletal storages, S_{ke} and S_{kv}, can be defined for the elastic and inelastic ranges of stress, respectively. The coarse-grained sediments in aquifer-systems deform elastically while the fined-grained sediments that consist on the confining aquitards may deform both elastically and inelastically.

In confined aquifers, even if the head drops and water is released from storage, the aquifer remains saturated. In this case, the storage coefficient can be defined as:

$$S=S_s \times b=(\rho_w \times g)(\alpha+n\beta)b \quad (2)$$ (Jacob 1940; Cooper 1966)

where S_s is the specific storage, b the thickness of the saturated aquifer, ρ_w the water density, g the acceleration of gravity, α the aquifer skeleton compressibility, n the porosity and β the fluid compressibility (approximately of 4.9×10^{-10} Pa^{-1}).

Note that, in compacting aquifer systems $S_k^* >> S_w$ and, assuming that S_w is negligible (Poland 1984) the storage coefficient is approximatively equal to the skeletal storage coefficient: $S \approx S_k^*$

To a first approximation, for this study, S_w is assumed as negligible in the Chalk aquifer, since that the water storage is generally more than one order of magnitude lower than the specific storage (Price 1987).

By inspecting groundwater level variations and ground displacement time series for nine boreholes across the network, stress-strain curves were derived by plotting the hydraulic head (that represents the applied stress) versus the vertical displacement (that represents the strain). Figure 4 shows the strain reaction to the most evident cycles of loading and unloading of the stress (hydraulic head) at

three piezometers where significant hydraulic head changes were observed. The results show a recovery of the strain corresponding with the stress dissipation. A direct temporal correlation between start and end dates for rising water level and ground uplift, and falling level and subsidence was found. As a consequence, taking into account the linear correlation observed between groundwater level changes and displacements, the deformational behaviour of the aquifer was considered as mainly elastic (hence well described by S_{ke}), which is consistent with previous investigations highlighting the importance of elastic storage for both the confined and unconfined chalk (MacDonald & Allen 2001). This suggested that the hydraulic head changes produced an instantaneous effect on the aquifer pore pressure.

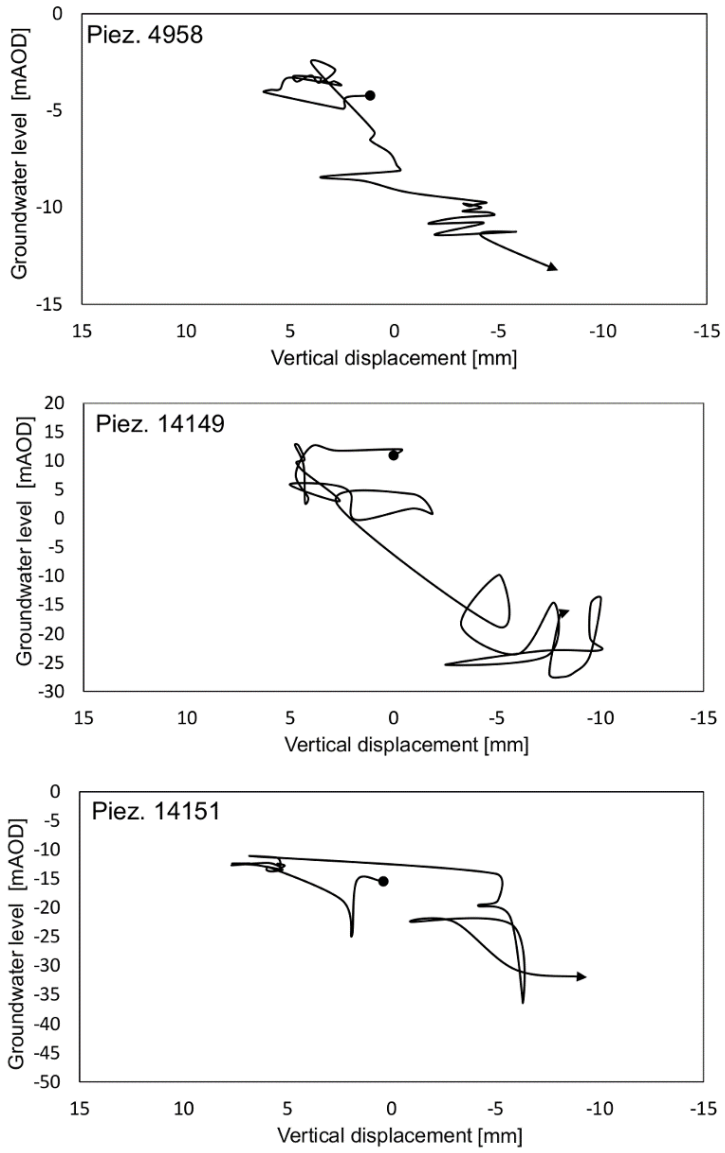

Figure 4. Stress-strain curve at three piezometers. See location in figure 1 and piezometers time series in figure 5.

In the London Basin, the aquifer exhibits semi-confined and confined conditions for ~1,360 km^2 of the study area. Similarly to the methodology that other authors have implemented for different aquifer-systems (Hoffmann *et al.* 2003; Bell *et al.* 2008, Tomás *et al.* 2006, Chaussard *et al.* 2014), for this area, the relationship between the hydraulic heads changes and the vertical ground motion changes was applied to compute the storage coefficient:

$S=S_k^*=\Delta d/\Delta h$ (4) (Hoffmann *et al.* 2001)

Where Δd is the vertical displacement as estimated by the satellite data, and Δh is the hydraulic head change. Note that this equation assumes that ground deformation is only vertical, a hypothesis that is justified by the fact that the horizontal displacements are believed to be not significant for this area.

The Chalk aquifer properties are mainly the result of the fracture network throughout its thickness, and the contribution from the matrix porosity is largely lower than that from the fractures (see section 2). Equation (2) can be therefore expanded to:

$Ss=\rho_w g(\alpha_f+\alpha_m+n_f\beta+n_m\beta)$ (5) (Price 1987)

Where α_f is the compressibility of the aquifer due to the presence of fractures, α_m is the compressibility of the aquifer skeleton unfractured, n_f represents the porosity resulting from the fractures, n_m is the matrix porosity, and $(n_f\beta+n_m\beta)$ indicates the specific storage of water S_{sw}.
As the latter is negligible, the total compressibility of the Chalk aquifer α can therefore be computed as:

$\alpha=\alpha_f+\alpha_m=Ss/\rho_w g$ (6)

4. Results and discussion

4.1. Modelling ground motion caused by groundwater level change

A simple 1D model based on the inversion of Equation (4) by Hoffmann *et al.* (2001) has been used to estimate the vertical displacement of the ground in response to changes in hydraulic head in the chalk aquifer. The model is used to characterise the relationship between groundwater level and ground motion time-series data to assess the contrast in ground motion across different geological units and in different aquifer conditions.

The 1D model assumes that the aquifer pore pressure instantaneously equilibrates with piezometric level changes in the aquifer and any time-lag between the piezometer level variations and the

compaction of the geological layers is not accounted for. This assumption is supported by our inspection of the ground motion and groundwater records for boreholes across the Basin (see section 3.2). As applied by other authors (Tomás *et al.* 2010; Ezquerro *et al.* 2014) to predict the ground motion changes due to groundwater level variations, in this study the simulated displacements were quantified by inverting Equation (4) as:

$$\Delta d = S \times \Delta h \qquad (7)$$

The relationship between hydraulic head changes that occurs from 1992 to 2010 and the vertical displacement detected by PSI data for nine piezometers (see the localisation in figure 1) was analysed. Note that whilst the simulated displacements are only referred to ground motion due to measured groundwater level changes, PS measurements indicate the total motion for any given point, which can be due to several processes (including anthropogenic factors, e.g. engineering works, or natural processes, e.g. compaction of soft sediments). If not accounted for, this could lead to an over-estimation of the storage. In order to minimise the influence of ground motion triggered by other factors on the estimation of the aquifer storage, in this study PS time series showing unrelated motion patterns and rates, for instance, high rates of uplift or land subsidence due to other processes as identified by the geohazard mapping carried out during the project PanGeo (Cigna *et al.* 2015) were first excluded from the analysis. Moreover, the average vertical displacement based on the remaining time series was estimated by using buffer areas with a radius of 500 m from each piezometer. For each piezometer at least 10 PS time series were used. Groundwater level data of ~200 piezometers were then compared with the average vertical displacement of the time series within each buffer area.

The aquifer storage coefficient *S* was calculated by using Equation (4) in the time interval where a good fit between piezometer data and average displacement time series was evident. The summary of storage coefficients computed for the nine boreholes are displayed in Table 1. In addition, the absolute average error between the simulated and PSI-derived displacements was estimated.

For each piezometer, the geological sequence was compared with the groundwater level variation to classify the aquifer state according to its confined condition (i.e. confined, semi-confined, unconfined) and the geological interval over which the piezometric head varied (Table 1). The same approach of storage coefficient computation that was applied in the confined aquifer condition was extended to estimate the storage coefficient in semi-confined conditions, in which storage within the confining unit is considered important (Burbey *et al.* 2003). Note that a transition between confined and unconfined conditions was detected at piezometer 14265 (Figure 5) and two different storage

coefficients were estimated for the different aquifer conditions in the periods 01/02/1996-12/12/1997 and 14/01/2004-13/12/2004 respectively for the confined and semi-confined conditions. Figure 5 shows the simulated displacements at six piezometers in order to represent the main ground motion responses to hydraulic head changes in the different states of the aquifer. These are obtained by using the groundwater level data and the estimated storage coefficients as inputs to equation (7).

In the North London Basin, the aquifer exhibits both confined and semi-confined conditions, varying spatially and occasionally temporally. When the piezometric level is within the Lambeth Group, a hydraulic head change of around 1.98 m corresponds to 2.93 mm of surface displacement (Figure 5; piezometer 4979). When the Chalk is confined by the London Clay, the hydraulic head change of 11.50 m produces approximately 5.85 mm of surface displacement (Figure 5; piezometer 4988).

In the Central London Basin, temporary transition of the water table across the units was detected (Figure 5; piezometer 14265). In this case, the simulated displacement was estimated using two storage coefficient values, taking into account the groundwater level variations in the lithological units.

In the South London Basin, the aquifer is confined by thicker deposits of the London Clay and lower values of storage coefficient were detected. Hydraulic head change of 13.16 m produces around 6.92 mm of surface displacement (Figure 5; piezometer 14149).

A correlation between the derived storage coefficient and the aquifer condition is also observed (table 1). Where the chalk is confined by the London Clay the storage coefficient is of the order of 1×10^{-4}, whilst where overlain by the Lambeth Group and semi-confined condition are expected to exist the storage is higher, typically 1×10^{-3} and indicative of additional storage provided by sand-rich horizons in the Lambeth Group. Also note that the absolute average difference error between the simulated and PSI-derived displacement shows higher values where the clay deposit is thicker (Table 1), and this fact could be due to swelling and shrinking of the London Clay deposits which have a high plasticity (e.g. Freeborough *et al.* 2006; Jones & Terrington 2011). To take into account the possible influence of shrink-swell clays on the observed errors, the BGS GeoSure dataset that provides information about potential natural ground movement resulting from collapsible deposits, compressible ground, landslides, running sand, shrink-swell and soluble rocks, by using A (lowest) to E (highest) ratings for each of these six geohazards (BGS 2014) was also analysed. This dataset is mapped at the 1:50,000 scale, and a 50 m buffer around the location or area of interest is generally recommended for its correct use. For this reason, GeoSure ratings for each piezometer (Table 1) were extracted as the predominant ratings observed within the 500 m buffer around each

piezometer location, not only to account for this recommendation but also to be consistent with the radius used around each piezometer for the time series analysis. The Volume Change Potential (VCP) and plasticity index (I_p) of the London Clay as estimated by Jones & Terrington (2011) based on the BGS National Geotechnical Properties Database and index test data for the London Clay outcrop were also considered.

The analysis revealed that the majority of the boreholes in Table 1 are located in areas with A to D shrink-swell hazard rating, indicating ground conditions ranging from non-plastic (A) to high plasticity (D). It is worth noting that since the VCP refers to the mean plasticity index at each sample location and GeoSure hazard ratings mainly to surface geology, it is crucial to consider the effect of the different thickness of the clay deposit at the specified locations when analysing the resulting errors. For those piezometers showing a predominant rating of D and presence of thicker clay deposits, the occurrence of shrink-swell in the active zone (i.e. generally, the first ~1.5 m; Jones & Terrington 2011) where soil moisture changes are more likely to occur, could partly justify the higher errors observed after the simulation.

To simulate the hydraulic head changes based on the observed ground motion, additionally Equation (4) at piezometer 4988 was inverted (Figure 5) as:

$$\Delta h = \Delta d / S \qquad (8)$$

This approach could be used to infer groundwater level changes based on satellite ground motion data and aquifer storativity in areas of London where no observation boreholes are available.

The relative error between the simulated hydraulic head changes and the measured groundwater level variations is 25% of the hydraulic head change.

The 1D ground motion modelling also allowed the estimation of the cumulated vertical displacement occurred between the last ERS-1/2 image (31/07/2000) and the first ENVISAT image (13/12/2002) at the nine piezometers. The ENVISAT ground motion time series in Figure 5 were indeed adjusted for the position of the ground on 13/12/2002 to match with the modelled ground motion time series based on the ERS data. A vertical displacement of -5 mm was observed for piezometer 14149, 4 mm for piezometer 4979 and -2 mm for piezometer 14265.

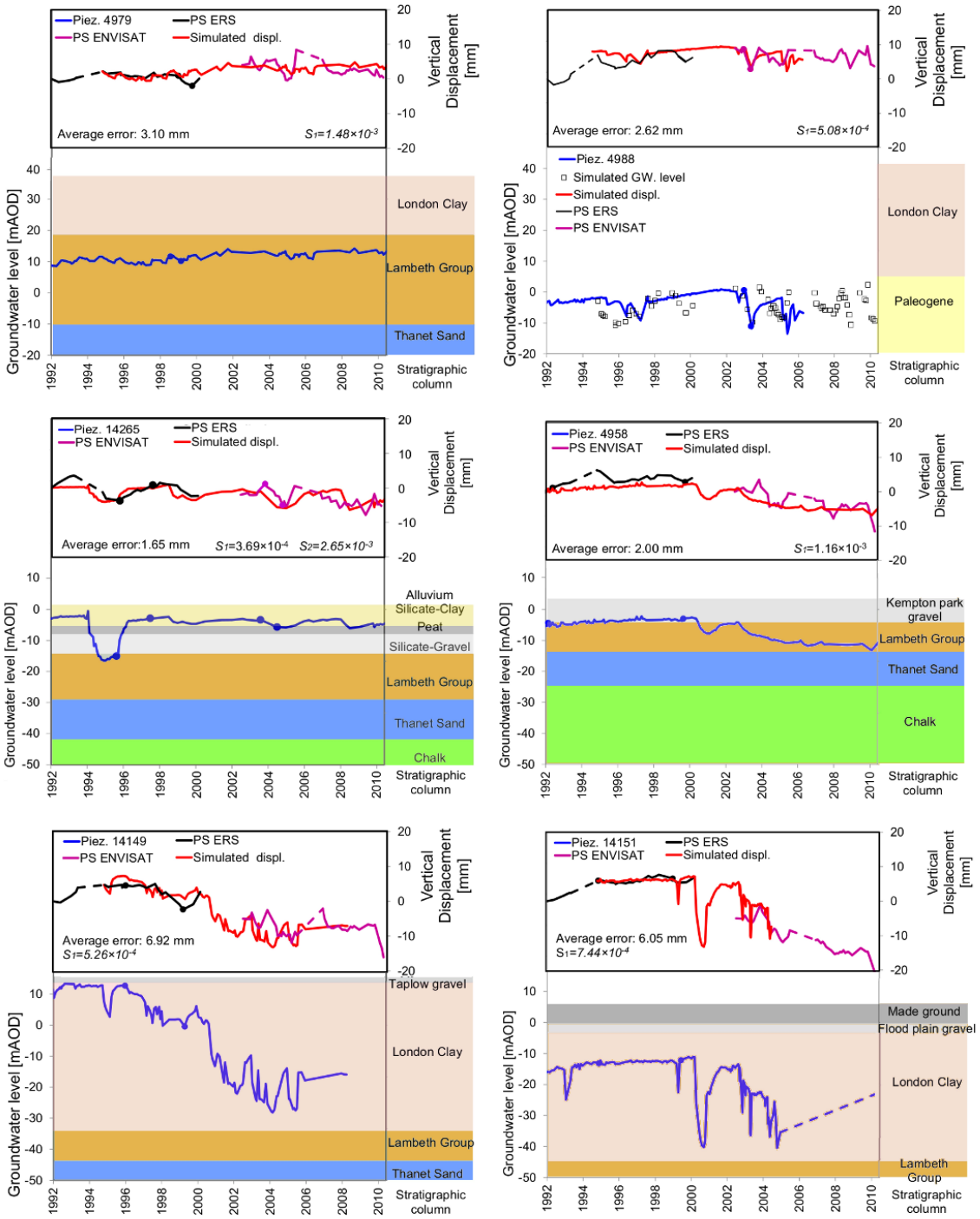

Figure 5. Comparison of InSAR ground motion data for 1992-2000 and 2002-2010 and simulated displacements [mm] with the groundwater level variations [m]. In addition, the stratigraphic column is represented. The dots represent the start and the end of the calibration period for the simulation. Piezometer localization is in figure 1. For piezometer 4988, the simulated groundwater (GW) level is also reported.

Table 1. Summary of the piezometers where displacements were simulated. *Piez.ID*, unique code of each piezometer. *S*, storage coefficient. Note that the calibration period was chosen based on visual identification of good fit between groundwater level and displacement time series. Shrink-swell hazard ratings are from BGS GeoSure dataset, and refer to the predominant ratings observed within the 500 m buffer area around each borehole. Volume Change Potential (VCP) ratings and plasticity index (I_p) values for the London Clay are from Jones & Terrington (2011) and do not account for plasticity variations with depth. VCP indicates the relative change in volume to be expected with soil moisture content changes.

Location	**Piez. ID**	**Calibration period**	**Aquifer condition**	**Geological unit within which the hydraulic head fluctuates**	**Groundwater level change [m]**	**Ground level change [mm]**	**S**	**Average Error [mm]**	**Thickness of the Lambeth Group [m]**	**Thickness of clay deposits [m]**	**Shrink-swell hazard**	**VCP (I_p)**
Northern London Basin	4979	04/03/99-09/09/99	Semi-confined	Lambeth Group	-1.98	-2.93	1.48×10^{-3}	3.10	29.10	17.00	D	High (45)
	4988	26/06/03-17/11/03	Confined	Lambeth Group	-11.50	-5.85	5.08×10^{-4}	2.62	-	37.00	D	High (45)
	5022	17/10/97-05/03/98	Confined	London Clay	1.47	0.74	5.05×10^{-4}	3.15	9.80	8.00	D and A	High (50)
Central London Basin	14265	01/02/96-12/12/97	Confined	Silicate-gravel	12.16	4.49	3.69×10^{-4}	1.65	15.60	6.70	C	-
		14/01/04-13/12/04	Semi-confined	Alluvium Silicate-clay	-2.32	-6.14	2.65×10^{-3}					
	4970	02/04/96-14/12/98	Confined	London Clay	6.43	2.93	4.55×10^{-4}	2.34	16.40	24.70	D and A	Medium (37)
	4958	15/07/92-30/03/00	Semi-confined	Lambeth Group	2.45	2.85	1.16×10^{-3}	2.00	8.23	0	A and B	-
Southern London Basin	14149	07/06/96-27/09/99	Confined	London Clay	-13.16	-6.92	5.26×10^{-4}	6.92	9.50	47.00	D	High (47)
	14151	03/05/95-20/12/99	Confined	London Clay	1.04	0.77	7.44×10^{-4}	6.05	8.50	39.00	C and D	High (40)
	4957	15/02/08-15/10/08	Confined	London Clay	-5.77	-2.76	4.78×10^{-4}	1.40	24.00	30.00	D and A	High (49)

4.2. Chalk aquifer properties derived from PSI data

The aim of this study is to understand the aquifer ground motion response to hydraulic head changes in the London Basin, using PSI data which spanned the periods 1992-2000 and 2002-2010. The groundwater observation network of the Environment Agency was exploited. Of the available 440 piezometers sampling the aquifer, only ~200 have got hydraulic head measurements from 1992 to 2010 (i.e. the time span of the PSI data) and were used for the comparison with the ground motion time series.

4.2.1 Confined and semi-confined aquifer properties

For this analysis, first the groundwater level changes for the periods 1992-2000 and 2002-2010 from the borehole observation network was quantified. Secondly, the average ground motion change in the two periods, detected by the PS included in a 500 m buffer area around each piezometer, was computed to account for the zone of influence of pumping. For each of these buffer areas, on average, ~200 PS were found, and the standard deviation of their vertical displacements reached maximum values of 5×10^{-2} mm, confirming the high consistence of the considered time series around each borehole.

Then, the storage coefficient was estimated using Equation (4) for each of these boreholes by comparing the observed ground motion changes in 1992-2000 and 2002-2010 versus the hydraulic head changes measured for the same periods. Only piezometers for which a correlation between deformation and hydraulic head changes was evident were used for the following analysis. In particular, the piezometers where either groundwater level decline corresponded to observed subsidence in the ground motion data, or groundwater level rise corresponded to uplift were selected. Conversely, the piezometers where the correlation was not evident were those where ground motion is caused by others factors, such as the compressible soil compaction, neo-tectonics and near-surface fault displacements, or loading from new buildings that were documented in the literature (Aldiss *et al.* 2014, Cigna *et al.* 2015, Bingley *et al.* 2007). Note that no time-lag for each geological unit to compact/expand in response to the decline/increase in groundwater levels was accounted for, because none was identified during the comparison between groundwater level variations and ground motion changes for the analysed boreholes in the semi-confined and confined aquifer conditions.

By using this approach, the storage coefficient at 56 and 23 piezometers, respectively for the period 1992-2000 and 2002-2010 was obtained. Figure 6 shows the interpolated maps of the storage coefficient, using the Inverse Distance Weighting approach. The resulting storage coefficient estimated in 1992-2000 ranged from 4.51×10^{-5} to 7.31×10^{-3}, and in 2002-2010 from 1.30×10^{-4} to 1.03×10^{-2}.

In the period 1992-2000, the storage distribution highlights a mean value of 1.18×10^{-3} and median of 4.99×10^{-4}, and the 25 and 75 percentiles are 3.03×10^{-4} and 1.20×10^{-3}. The storage in the period 2002-

2010 detains a mean value of 1.68×10^{-3} and median of 1.35×10^{-3}, and the 25 and 75 percentiles are 4.39×10^{-4} and 2.13×10^{-3} respectively.

The values of the PSI-derived storativity maps were compared with the storage coefficient obtained by pumping tests performed in the Chalk aquifer by Allen *et al.* (1997) during the 1990s (see the localization in Figure 6). The map of the storage coefficient estimated in the period 1992-2000 was compared with the storage coefficient measured by 19 pumping tests and the second one was cross-compared by 18 pumping tests that matched with the extension of the PSI-based storage coefficient maps. The storage coefficient measured by pumping tests ranged from 9.00×10^{-5} to 5.17×10^{-2}. The storage distribution highlights a mean value of 6.85×10^{-3} and median of 2.00×10^{-3}, and the 25 and 75 percentiles are 5.00×10^{-4} and 5.40×10^{-3}. The comparisons were performed by extracting values from the PSI-based storage coefficient map values at the pumping tests locations. Table 2 cross-compares the values from the pumping tests and PSI-based assessment. PSI-based storage values for the analysed pumping test locations are between 3.53×10^{-4} and 4.88×10^{-3}, and their absolute differences with respect to the values obtained by pumping tests range between 2.20×10^{-5} and 4.91×10^{-2}. In most cases, the storage measured by pumping tests and the corresponding PSI-based values also show the same order of magnitude as confirmed by their ratios, and only a few outliers from this pattern can be observed.

Pumping tests of high reliability were used for this analysis. Indeed, only the values obtained from constant rate tests carried out for more than a day were considered, in order to minimize the error of the measured storage coefficient. It is worth noting, however, that some of the pumping tests may have been conducted within the aquifer in unconfined conditions, whereas at the present the water levels have risen and in the large part of the London Basin the aquifer is confined or semi-confined. Therefore, local differences between the two storage coefficient estimations may be justified by the change in aquifer conditions.

Taking into account that the water storage was assumed negligible, the PSI-derived storage coefficient is in good agreement with those obtained by pumping tests.

Using the method outlined previously the aquifer state and geological interval over which the change in piezometric head occurred was determined for each of the 56 piezometers used to calculate storage over the period 1992-2000. In doing so the spatial correlation between storage coefficient and aquifer condition is further assessed. Where the chalk is confined by the London Clay a storage coefficient of 1.00×10^{-4} to 1.00×10^{-5} is typically observed. The exception to this occurring near Battersea where the storage coefficient for a cluster of sites is unusually high and of the order of 1.00×10^{-3} this area coincides with the location of a number of anomalous buried hollows where ground disturbance due to peri-glacial processes is observed (Hutchinson 1980; Banks *et al.* 2015). Where the chalk is overlain

by the Lambeth Group and semi-confined conditions may persist higher storage values in the range 1.00×10^{-3} to 1.00×10^{-4} were observed.

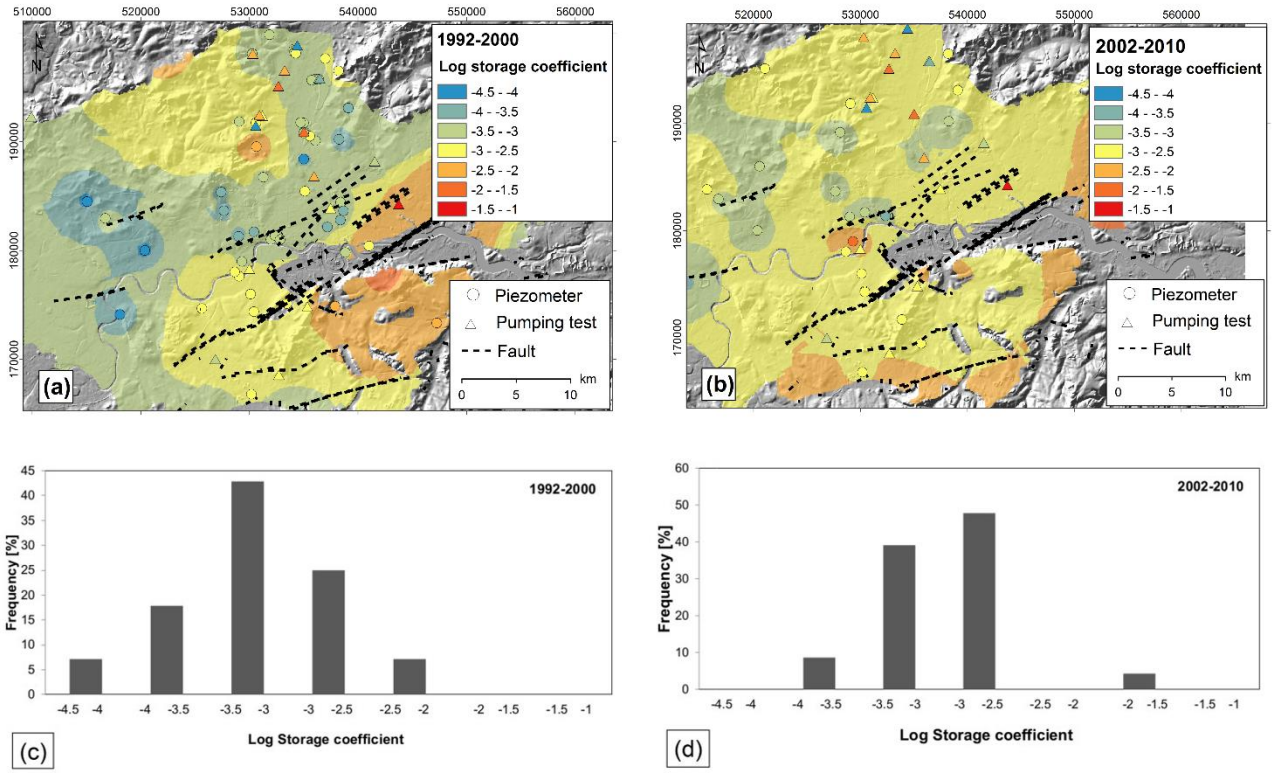

Figure 6. Maps of the aquifer storage coefficient in **(a)** 1992-2000 and **(b)** 2002-2010 (BGS ©NERC. All Rights Reserved. 2016) overlapped onto shaded relief of NEXTMap® DTM at 50 m resolution. British National Grid. Projection: Transverse Mercator. Datum: OSGB 1936. NEXTMap® Britain © 2003, Intermap Technologies Inc., All rights reserved. Distribution of aquifer storage coefficient data in 1992-2000 **(c)** and 2002-2010 **(d)** within the London Basin.

Table 2. Storage coefficient estimated by pumping test (S_{pt}) and by PSI-based method (S_{PSI}).

Name	S_{pt}	S_{PSI} (1992-2000)	S_{PSI} (2002-2010)	Absolute difference (S_{pt} - S_{PSI}) 1992-2000	Absolute difference (S_{pt} - S_{PSI}) 2002-2010	Ratio (S_{pt} / S_{PSI}) 1992-2000	Ratio (S_{pt} / S_{PSI}) 2002-2010
Vauxhall bridge rhm	1.91×10^{-3}	1.29×10^{-3}	4.88×10^{-3}	6.25×10^{-4}	2.97×10^{-3}	1.49	3.91×10^{-1}
Ponders end abh no.1	3.20×10^{-4}	4.21×10^{-4}	1.65×10^{-3}	1.01×10^{-4}	1.33×10^{-3}	7.60×10^{-1}	1.93×10^{-1}
Ponders end abh no.2	3.00×10^{-4}	4.32×10^{-4}	1.67×10^{-3}	1.32×10^{-4}	1.37×10^{-3}	6.94×10^{-1}	1.80×10^{-1}
Park ps	2.00×10^{-2}	4.42×10^{-4}	1.76×10^{-3}	1.96×10^{-2}	1.82×10^{-2}	45.25	11.38
Hadley road	3.60×10^{-3}	6.93×10^{-4}	1.32×10^{-3}	2.91×10^{-3}	2.28×10^{-3}	5.19	2.72
Merton abbey ps	1.00×10^{-3}	1.53×10^{-3}	3.02×10^{-3}	5.27×10^{-4}	2.02×10^{-3}	6.55×10^{-1}	3.31×10^{-1}
East ham ps	5.17×10^{-2}	4.04×10^{-3}	2.63×10^{-3}	4.77×10^{-2}	4.91×10^{-2}	12.80	19.66
Old ford ps	3.00×10^{-3}	1.10×10^{-3}	2.72×10^{-3}	1.90×10^{-3}	2.82×10^{-4}	2.73	1.10
Selhurst well	2.00×10^{-3}	2.10×10^{-3}	3.13×10^{-3}	9.80×10^{-5}	1.13×10^{-3}	9.53×10^{-1}	6.39×10^{-1}
Lee bridge well no.2	5.00×10^{-3}	1.17×10^{-3}	2.26×10^{-3}	3.83×10^{-3}	2.74×10^{-3}	4.26	2.21
Honor oak	2.40×10^{-3}	3.03×10^{-3}	3.40×10^{-3}	6.29×10^{-4}	1.00×10^{-3}	7.92×10^{-1}	7.05×10^{-1}
Myddleton road	9.00×10^{-5}	2.56×10^{-3}	2.03×10^{-3}	2.47×10^{-3}	1.94×10^{-3}	3.52×10^{-2}	4.44×10^{-2}
Wanstead	5.00×10^{-4}	1.81×10^{-3}	2.04×10^{-3}	1.31×10^{-3}	1.54×10^{-3}	2.77×10^{-1}	2.45×10^{-1}
Turkey brook	1.00×10^{-4}	8.19×10^{-4}	1.55×10^{-3}	7.19×10^{-4}	1.45×10^{-3}	1.22×10^{-1}	6.46×10^{-2}
Southbury road	5.40×10^{-3}	8.86×10^{-4}	1.44×10^{-3}	4.51×10^{-3}	3.96×10^{-3}	6.09	3.74
Oakthorpe road	1.90×10^{-3}	2.07×10^{-3}	1.92×10^{-3}	1.73×10^{-4}	2.20×10^{-5}	9.17×10^{-1}	9.89×10^{-1}
Knap arms bridge	1.00×10^{-2}	2.16×10^{-3}	1.98×10^{-3}	7.84×10^{-3}	8.02×10^{-3}	4.64	5.05
Bush hill road	2.00×10^{-2}	9.81×10^{-4}	1.46×10^{-3}	1.90×10^{-2}	1.85×10^{-2}	20.39	13.73
Hms warrior no.2	1.00×10^{-3}	3.53×10^{-4}	-	6.47×10^{-4}	-	2.83	-

Furthermore, the specific storage was calculated by inverting equation (2) as follows:

$$S_s = S/b \qquad (9)$$

To this aim, the thickness of the Chalk (which ranges from 75 to 200 m in the region of interest) as calculated by BGS based on borehole data, was used. The resulting specific storage reaches values higher than 3.00×10^{-5} m^{-1} near the Greenwich fault (see the location in Figure 1). The average specific storage that was estimated for the London Basin is of 7.50×10^{-6} and 1.00×10^{-5} m^{-1} respectively for the period 1992-2000 and 2002-2010. These values show good agreement with those that can be computed by using equation (5) and for values of matrix porosity (n_m) of 0.29, porosity contributed by the discontinuities (n_f) of 1.00×10^{-2}, compressibility of the aquifer resulting from the discontinuities (α_f) of 5.00×10^{-10} Pa^{-1}, compressibility of the unfractured matrix (α_m) of 8.10×10^{-11} Pa^{-1} and fluid compressibility (β) of 4.90×10^{-10} Pa^{-1}, resulting in 7.00×10^{-6} m^{-1} specific storage (Price 1987).

The aquifer compressibility varies from 2.60×10^{-11} to 8.60×10^{-9} Pa^{-1} with an average of 7.70×10^{-10} Pa^{-1} in the period 1992-2000, whilst in 2002-2010, the values range from 6.40×10^{-11} to 5.70×10^{-9} Pa^{-1}, with an average of 1.20×10^{-9} Pa^{-1} (Figure 7).

The estimated values in the first period agree with the range obtained by using the Young modulus derived from seismic surveying: 3.10×10^{-10} – 8.00×10^{-10} Pa^{-1} (Abbiss 1979). The average value obtained for the second period is also comparable with the results derived from tank test: 4.80×10^{-10} - 1.20×10^{-9} Pa^{-1} (Ward *et al.* 1968).

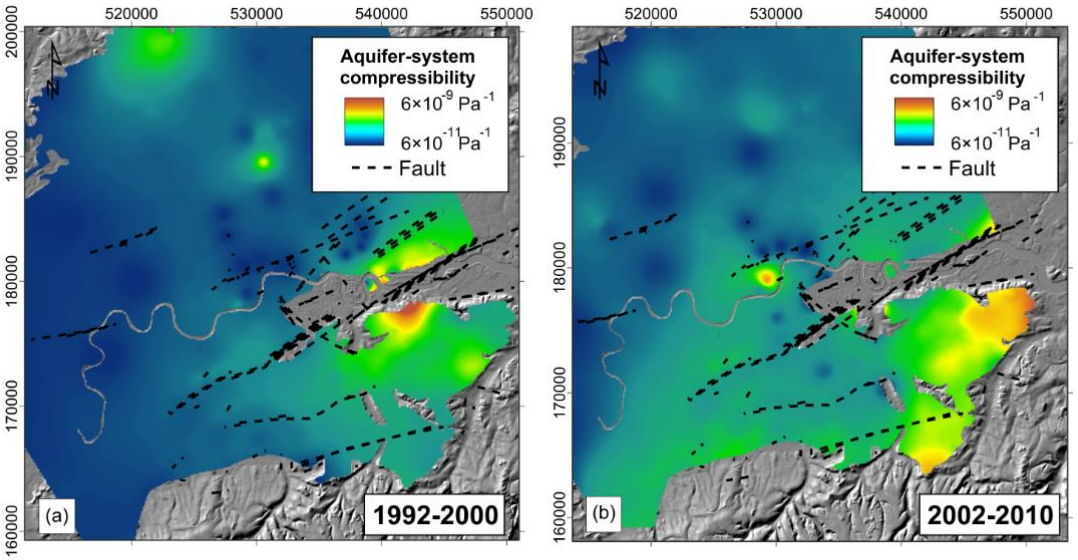

Figure 7. Maps of the aquifer compressibility in the periods **(a)** 1992-2000 and **(b)** 2002-2010 (BGS ©NERC. All Rights Reserved. 2016), overlapped onto shaded relief of NEXTMap® DTM at 50 m resolution. British National Grid. Projection: Transverse Mercator. Datum: OSGB 1936. NEXTMap® Britain © 2003, Intermap Technologies Inc., All rights reserved.

4.2.2 Unconfined aquifer properties

In order to analyse the ground motion response to hydraulic head changes in the unconfined condition of the Chalk aquifer, local comparisons for the piezometers located in the Chilterns and North Down areas were carried out. In the Chiltern Hills (see figure 8; piezometer 14796) the long-term seasonal trend of the water table is related to the wet and dry periods. The rise and/or fall of the water table of around 2 m correspond to 4 mm in ground motion. Around five months of time lag can be observed between the water table variations and ground motion changes at two piezometer locations (See figure 1; piezometers 14795 and 14796) in the Chiltern area. This time lag could be caused by the presence of a thick unsaturated zone and deposits with a low vertical hydraulic conductivity at these locations, which delays groundwater recharge. However, based on the temporal sampling frequency of the processed ERS-1/2 and ENVISAT radar imagery and the resulting time series, there is insufficient evidence to confirm the presence of this lag in other locations and its persistence across the entire monitored period 1992-2010. The observed time lag at these two piezometers could therefore simply be due to intrinsic characteristics of the satellite data time series.

In the North Downs, where the Chalk aquifer outcrops, significant seasonal rises and falls of the groundwater level are evident (see figure 8; piezometer 14844). Two seasonal components due to 1) short-term variations (from March to November) and to 2) long-term variation (multi-annual) were recognised. The hydraulic change of 20 m corresponds to approximately 3 mm of surface displacements.

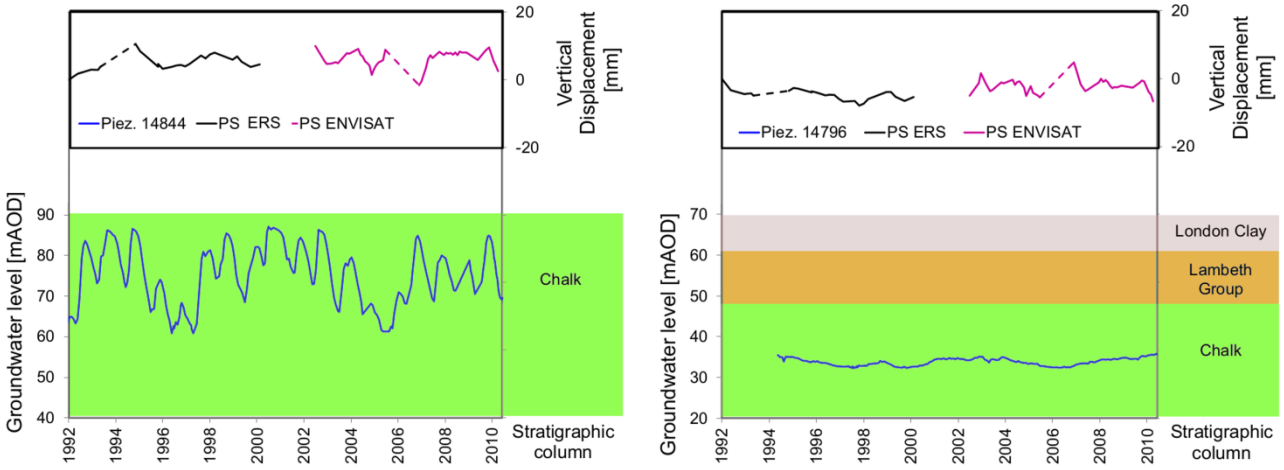

Figure 8. Comparison of water table changes with ground motion changes at piezometers station 14844 and 14796. See figure 1 for the localization. Groundwater level data © Environment Agency copyright and/or database rights 2015. All rights reserved.

5. Conclusions

The hydraulic properties of the Chalk aquifer have been previously investigated by several authors with traditional field and laboratory measurements and experiments (Ward *et al.* 1968; Carter & Mallard 1974; Bell 1977; Abbiss 1979; Price 1987; Barker 1991; Lewis *et al.*1993; Price *et al.* 1993; Allen *et al.*1997). Although the characterization of the Chalk aquifer properties resulting from the presence of discontinuities ideally requires estimation *in situ* over wide areas, the high costs of such campaigns only permitted to carry out investigations at limited spatial or temporal scales.

In this study, the combined analysis of hydrological information with displacement maps and time-series retrieved from multi-sensor and multi-temporal SAR images and PSI analysis has allowed the derivation of:

1) the Chalk aquifer storage coefficient maps over an area of ~1,360 km^2 in the periods 1992-2000 and 2002-2010; and
2) the 1D modelling of the ground motion response to hydraulic head changes at nine piezometers.

The resulting storage coefficient estimated in the period 1992-2000 ranged from 4.51×10^{-5} to 7.31×10^{-3}, and in the period 2002-2010 ranged from 1.30×10^{-4} to 1.03×10^{-2}. Additionally, these maps were compared with the storage coefficient obtained by pumping test performed in the Chalk aquifer by Allen *et al.* (1997) during the 1990s. The maps of the storage coefficient estimated in the periods 1992-2000 and 2002-2010 were compared with the storage coefficient measured respectively by 19 and 18 pumping tests and an average absolute difference of around 6×10^{-3} was found. Correlation between the derived storage and the hydrogeological setting is observed. Where the chalk is overlain by the Lambeth Group and semi-confined conditions may persist the storage coefficient is typically 1×10^{-3} to 1×10^{-4}. Where the chalk is confined by the London Clay the storage coefficient is typically an order of magnitude lower and in the range 1×10^{-4} to 1×10^{-5}, though local geological effects associated with faulting and ground disturbance appear to have a bearing on these results and may warrant further investigation.

A 1D model based on the approach proposed by Tomás *et al.* (2010) was implemented in order to simulate the ground motion response to hydraulic head changes in the semi-confined and confined aquifer conditions. The results of the modelling revealed that the ground response to groundwater levels variations is not uniform across the London Basin. Spatio-temporal variations of the storage coefficient are related to the groundwater levels with respect to the lithological units, and to the fractures network in the aquifer, which are believed to cause compartmentalisation of the aquifer. In those areas where the water level was found in the Lambeth Group, a greater storage coefficient (1×10^{-3}) than that measured where the water level was in the London Clay (3×10^{-4} – 7×10^{-4}) was observed. The variability of the aquifer storage coefficient throughout the Basin as a consequence, requires

different policies and zonal planning for certain parts of London to manage the available resource and conflicting aquifer uses effectively.

The modelling has also been useful in filling the temporal gap between ERS and ENVISAT PSI data. The ENVISAT ground motion time series were adjusted for the position of the ground on 13/12/2002 to match with the modelled ground motion time series based on the ERS data, and a vertical displacement of -5 mm was observed for piezometer 14149, 4 mm for piezometer 4979 and -2 mm for piezometer 14265.

In addition, the ground motion response to hydraulic head changes in the unconfined condition of the Chalk aquifer was analysed. The comparisons between the water table variations and the ground motion changes, located in the Chilterns Hills revealed that water table variations of around 2 m correspond to 4 mm in ground motion. Around five months of time lag between water table variations and ground motion changes were observed at two piezometers locations (piezometer 14795 and 14796). This time lag may be due to the presence of low saturated hydraulic conductivity deposits, which eventually delay the horizontal flow. However, there is insufficient evidence in the displacement time series to confirm this five month lag which could be simply due to intrinsic characteristics of the input satellite data and their temporal sampling (monthly to yearly). In the North Downs Chalk, the hydraulic head change of 20 m corresponds to approximately 3 mm of surface displacements.

We believe that the application of satellite data to understand the relationship between the groundwater levels and the surface displacements will provide new opportunities to inform future approaches for monitoring groundwater levels variations over wide urban areas, such as the London Basin and for wider spatial assessment of aquifer properties. The PSI-derived storage coefficient maps could be used within the London Basin aquifer model for groundwater resource sustainable management and for accurate simulation of artificial recharge operations. More widely, the findings of this work confirmed that PSI analysis and data are capable of supporting the characterisation of aquifer properties of fractured aquifers over wide regions of interest.

Acknowledgements

This study was carried out by R. Bonì in the framework of her PhD project at the University of Pavia and during her research visit at the British Geological Survey (BGS) in June-September 2015, under the supervision of F. Cigna and S. Bricker. ERS-1/2 and ENVISAT data were processed by H. McCormack in the framework of the EC-FP7 project PanGeo (http://www.pangeoproject.eu/). Groundwater level data were provided by the Environment Agency (Licence Agreement no.A2719; non-commercial use). The authors thank Dr Andrew Hughes for his insightful comments on the manuscript, and Mark Whiteman for providing the groundwater level data. F. Cigna and S. Bricker publish with the permission of the Executive Director of BGS-NERC.

References

Abbiss, C.P. (1979). A comparison of the stiffness of the chalk at Mundford from a seismic survey and a large scale tank test. *Geotechnique*, *29*(4), 461-468.

Aldiss, D., Burke, H., Chacksfield, B., Bingley, R., Teferle, N., Williams, S., Blackman D., Burren R., Press, N. (2014). Geological interpretation of current subsidence and uplift in the London area, UK, as shown by high precision satellite-based surveying. *Proceedings of the Geologists' Association*, *125*(1), 1-13.

Aldiss, D.T. (2013). Under-representation of faults on geological maps of the London region: reasons, consequences and solutions. *Proceedings of the Geologists' Association*, 124 (6), 929-945.

Allen, D.J., Brewerton, L.J., Coleby, L.M., Gibbs, B.R., Lewis, M.A., MacDonald, A.M., Wagstaff, S.J. & Williams, A.T. (1997). The Physical Properties of Major Aquifers in England and Wales. *British Geological Survey Technical Report* WD/97/34.

Balkhair, K.S. (2002). Aquifer parameters determination for large diameter wells using neural network approach. *Journal of Hydrology*, *265*(1), 118-128.

Banks, V.J., Bricker, S.H., Royse, K.R., & Collins, P.E.F. (2015). Anomalous buried hollows in London: development of a hazard susceptibility map. *Quarterly Journal of Engineering Geology and Hydrogeology*, 48 (1). 55-70. 10.1144/qjegh2014-037

Barker, J.A. (1991). Transport in fractured rock. In: Downing, R. A. & Wilkinson, W. B. (eds) *Applied Groundwater Hydrology*, Clarendon Press, Oxford. 199-216.

Bateson, L.B., Barkwith, A.K.A.P., Hughes, A.G., & Aldiss, D.T. (2009). Terrafirma: London H-3 Modelled Product. Comparison of PS data with the results of a groundwater abstraction related subsidence Model. *British Geological Survey Commissioned Report*, OR/09/032: 47 pp.

Bell, F.G. (1977). A note on the physical properties of the chalk. *Engineering Geology*, *11*(3), 217-225.

Bell, J.W., Amelung, F., Ferretti, A., Bianchi, M., & Novali, F. (2008). Permanent scatterer InSAR reveals seasonal and long-term aquifer-system response to groundwater pumping and artificial recharge. *Water Resources Research*, *44*(2).

BGS, 2014. GeoSure: National Ground Stability Data. Available at: http://www.bgs.ac.uk/products/geosure/home.html, Accessed on: 05/11/2015.

Bingley, R., Teferle, F.N., Orliac, E.J., Dodson, A.H., Williams, S.D.P., Blackman, D.L., Baker, T.F., Riedmann, M., Haynes, M., Aldiss, D.T., Burke, H.C., Chacksfield, B.C., & Tragheim, D.G. (2007). Absolute Fixing of Tide Gauge Benchmarks and Land Levels: Measuring Changes in Land and Sea Levels around the coast of Great Britain and along the Thames Estuary and River Thames using GPS, Absolute Gravimetry, Persistent Scatterer Interferometry

and Tide Gauges. Joint DEFRA/EA Flood and Coastal Erosion Risk Management R&D Programme. In DEFRA/EA (Ed.), *R&D Technical Report FD2319/TR:* http://nora.nerc.ac.uk/1493/1/Absolutefixing.pdf

Bloomfield J.P., Brewerton L.J., & Allen D.J. (1995). Regional trends in matrix porosity and dry density of the chalk of England. *Quarterly Journal of Engineering Geology* 28: S–131-142.

Bloomfield, J.P., Bricker, S.H. & Newell, A.J. (2011). Some relationships between lithology, basin form and hydrology: a case study from the Thames basin, UK. *Hydrological Processes.*, 25: 2518–2530. doi:10.1002/hyp.8024

Bonì, R., Herrera, G., Meisina, C., Notti, D., Béjar-Pizarro, M., Zucca, F., González, P. J., Palano, M., Tomás, R., Fernández, J., Fernández-Merodo, J. A., Mulas, J., Aragón, R., Guardiola-Albert, C., & Mora, O. (2015). Twenty-year advanced DInSAR analysis of severe land subsidence: The Alto Guadalentín Basin (Spain) case study. *Engineering Geology, 198, 40-52*. doi:10.1016/j.enggeo.2015.08.014

Burbey, T.J. (2003). Use of time–subsidence data during pumping to characterize specific storage and hydraulic conductivity of semi-confining units. *Journal of Hydrology*, *281*(1), 3-22.

Carter, P.G. & Mallard, D.J. (1974). A study of the strength, compressibility and density trends within the Chalk of southeast England. *Quarterly Journal of Engineering Geology*, 7, 43-55.

Chaussard, E., Bürgmann, R., Shirzaei, M., Fielding, E.J., & Baker, B. (2014). Predictability of hydraulic head changes and characterization of aquifer-system and fault properties from InSAR-derived ground deformation. *Journal of Geophysical Research: Solid Earth*, *119*(8), 6572-6590.

Cigna, F., Jordan, H., Bateson, L., McCormack, H., & Roberts, C. (2015). Natural and anthropogenic geohazards in greater London observed from geological and ERS-1/2 and ENVISAT persistent scatterers ground motion data: results from the EC FP7-SPACE PanGeo Project. *Pure and Applied Geophysics*, 172 (11), 2965-2995.

Cigna, F., Osmanoğlu, B., Cabral-Cano, E., Dixon, T.H., Ávila-Olivera, J.A., Gardũno-Monroy, V.H., DeMets, C., & Wdowinski, S. (2012). Monitoring land subsidence and its induced geological hazard with Synthetic Aperture Radar Interferometry: a case study in Morelia, Mexico, *Remote Sensing of Environment*, 117, 146–161, doi:10.1016/j.rse.2011.09.005.

Cooper, H.H. (1966). The equation of groundwater flow in fixed and deforming coordinates. *Journal of Geophysical research*, *71*(20), 4785-4790.

De Freitas, M.H. (2009). Geology; its principles, practice and potential for Geotechnics. *Quarterly Journal of Engineering Geology and Hydrogeology*, *42*(4), 397-441.

EA (2007). Groundwater Levels in the Chalk-Basal Sands Aquifer of the London Basin. *Unpublished report*.

EA (2015). Management of the London Basin Chalk Aquifer. Status Report 2015. *Environment Agency of England and Wales, Thames Region Report.*

Ellison, R.A., Woods, M.A., Allen, D.J., Forster, A., Pharaoh, T.C., & King, C. (2004). *Geology of London: special memoir for 1: 50000 geological sheets 256 (north London), 257 (Romford), 270 (south London), and 271 (Dartford) (England and Wales)*. British Geological Survey.

ESA (2009). The Terrafirma Atlas. Terrain-motion across Europe. A compendium of results produced by the European space agency GMES service element project Terrafirma 2003–2009: 94.

European Environment Agency, EEA (2010). GMES Urban Atlas. Available online at: http://www.eea.europa.eu/data-and-maps/data/urban-atlas. Accessed on: 05/11/2015

Ezquerro, P., Herrera, G., Marchamalo, M., Tomás, R., Béjar-Pizarro, M., & Martínez, R. (2014). A quasi-elastic aquifer deformational behavior: Madrid aquifer case study. *Journal of Hydrology*, *519*, 1192-1204.

Ferretti, A., Prati, C., & Rocca, F. (2001). Permanent scatterers in SAR interferometry. *Geoscience and Remote Sensing, IEEE Transactions on*, *39*(1), 8-20.

Fetter, C.W., (2001). *Applied hydrogeology* (4th Edition). Upper Saddle River: Prentice hall.p.102. ISBN 0-13-088239-9

Ford, J.R., Mathers, S.J., Royse, K.R., Aldiss, D.T., & Morgan, D.J.R. (2010). Geological 3D modelling: scientific discovery and enhanced understanding of the subsurface, with examples from the UK. Z. *Dtsch. Ges. Geowiss.* 161, 205–218.

Freeborough, K., Kirkham, M., & Jones, L.D. (2006). Determination of the shrinking and swelling properties of the London Clay Formation: laboratory report. *British Geological Survey report* IR/06/058, 34 pp.

Fry, V.A. (2009). Lessons from London: regulation of open-loop ground source heat pumps in central London. *Quarterly Journal of Engineering Geology and Hydrogeology*, 42(3), 325-334.

Gabriel, A.K., Goldstein, R.M. & Zebker, H.A. (1989). Mapping small elevation changes over large areas: differential radar interferometry. *Journal of Geophysical Research: Solid Earth (1978–2012)*, *94*(B7), 9183-9191.Galloway, D.L. & Hoffmann, J. (2007). The application of satellite differential SAR interferometry-derived ground displacements in hydrogeology. *Hydrogeology Journal*, 15(1), 133-154.

Galloway, D. L., Hudnut, K. W., Ingebritsen, S. E., Phillips, S. P., Peltzer, G., Rogez, F., & Rosen, P. A. (1998). Detection of aquifer system compaction and land subsidence using interferometric synthetic aperture radar, Antelope Valley, Mojave Desert, California. *Water Resources Research*, 34 (10), 2573-2585.

Galloway, D., Jones, D. R., & Ingebritsen, S. E. (Eds.). (1999). Land subsidence in the United States (p. 177). *Reston, VA, USA: US Geological Survey*.

Helm, D.C. (1975). One-dimensional simulation of aquifer system compaction near Pixley, Calif. 1: constant parameters. *Water Resources Research,* 11 (3), 465–478.

Helm, D.C. (1976). One-dimensional simulation of aquifer system compaction nearPixley, Calif. 2: stress-dependent parameters. *Water Resources Research,* 1 (3), 375–391.

Herrera, G., Fernández, J.A., Tomás, R., Cooksley, G., & Mulas, J. (2009). Advanced interpretation of subsidence in Murcia (SE Spain) using A-DInSAR data-modelling and validation. *Nat. Hazards Earth Syst. Sci.*, *9* (3), 647-661.

Hoffmann, J., Galloway, D.L., &. Zebker, H.A. (2003). Inverse modelling of interbed storage parameters using land subsidence observations, Antelope Valley, California, *Water Resources Research*, 39, *1031*, *doi:*10.1029/2001WR001252, 2.

Hoffmann, J., Zebker, H.A., Galloway, D.L., & Amelung F. (2001), Seasonal subsidence and rebound in Las Vegas Valley, Nevada, observed by Synthetic Aperture Radar Interferometry, *Water Resources Researc*., 37*(*6*),* 1551–1566*, doi:*10.1029/2000WR900404*.*

Hooper, A., Zebker, H., Segall, P., & Kampes, B. (2004). A new method for measuring deformation on volcanoes and other natural terrains using InSAR persistent scatterers. *Geophysical research letters*, *31*(23).

Hutchinson, J.N. (1980). Possible late Quaternary pingo remnants in central London. *Nature* 284(5753): 253-255.

Jacob, C.E. (1940). On the flow of water in an elastic artesian aquifer. *Eos, Transactions American Geophysical Union*, *21*(2), 574-586.

Jones L. & Terrington R. (2011). Modelling Volume Change Potential in the London Clay. *Quarterly Journal of Engineering Geology and Hydrogeology*, 44, 109-122.

Jones, M.A., Hughes, A.G., Jackson, C.R., & Van Wonderen, J.J. (2012). Groundwater resource modelling for public water supply management in London. *Geological Society, London, Special Publications*, 364(1), 99-111.

Kaczmaryk, A., & Delay, F. (2007). Interference pumping tests in a fractured limestone (poitiers–france): Inversion of data by means of dual-medium approaches. *Journal of Hydrology*, *337*(1), 133-146.

Klemm, H., Quseimi, I., Novali, F., Ferretti, A., & Tamburini, A. (2010). Monitoring horizontal and vertical surface deformation over a hydrocarbon reservoir by PSInSAR. *first break*, *28*(5).

Lewis, M. A., Jones, H. K., Macdonald, D. M. J., Price, M., Barker, J. A., Shearer, T. R., Wesselink, A. J. & Evans, D. J. (1993). Groundwater storage in British aquifers: Chalk. National Rivers Authority R & D Note 128.

MacDonald, A.M & Allen, D.J. (2001). Aquifer properties of the Chalk of England. *Quarterly Journal of Engineering Geology and Hydrogeology* (November 2001), 34, Part 4:371-384

Mason PJ, Ghail RC, Bischoff C, &Skipper JA (2015). Detecting and monitoring small-scale discrete ground movements across London, using Persistent Scatterer InSAR (PSI). *XVI Geotechnical Engineering for Infrastructure and Development: XVI European Conference on Soil Mechanics and Geotechnical Engineering (ECSMGE)*, ICE Publishing. 9 pp.

Massonnet, D., & Rabaute, T. (1993). Radar interferometry: limits and potential. *Geoscience and Remote Sensing, IEEE Transactions on*, *31*(2), 455-464.

Mathers, S.J., Burke, H.F., Terrington, R.L., Thorpe, S., Dearden, R.A., Williamson, J.P., & Ford, J.R. (2014). A geological model of London and the Thames Valley, southeast England. *Proceedings of the Geologists' Association*, *125*(4), 373-382.

Morris, B.L., Lawrence, A.R., Chilton, P.J., Adams, B., Calow, R.C & Klink, B.A (2003). Groundwater and its susceptibility to degradation: A global assessment of the problem and options for Management. Early Warning and Assessment Report Series, RS.03-3. United Nations Environment Programme, Nairobi, Kenya.

Mortimore, R., Newman, T.G., Royse, K., Scholes, H., & Lawrence, U. (2011). Chalk: its stratigraphy, structure and engineering geology in east London and the Thames Gateway. *Quarterly Journal of Engineering Geology and Hydrogeology*, *44*(4), 419-444.

Newman, T. (2009). The impact of adverse geological conditions on the design and construction of the Thames Water Ring Main in Greater London, UK. *Quarterly Journal of Engineering Geology and Hydrogeology* 42, 5–21.

Notti, D., Mateos, R. M., Monserrat, O., Devanthéry, N., Peinado, T., Roldán, F. J., Fernández-Chacón, F., Galve, J. P., Lamas, F., & Azañón, J. M. (2016). Lithological control of land subsidence induced by groundwater withdrawal in new urban areas (Granada Basin, SE Spain). Multiband DInSAR monitoring. *Hydrological Processes.*

NRFA (2016). National River Flow Archive, 39001 Thames at Kingston http://nrfa.ceh.ac.uk/data/station/meanflow/39001. Accessed 10.02.2016.

O'Shea, M.J., & Sage, R. (1999). Aquifer Recharge: An Operational Drought-Management Strategy in North London. *Water and Environment Journal*, *13*(6), 400-405.

O'Shea, M.J., Baxter, K.M., & Charalambous, A.N. (1995). The hydrogeology of the Enfield-Haringey artificial recharge scheme, north London. *Quarterly Journal of Engineering Geology and Hydrogeology*, *28* (Supplement 2), S115-S129.

Osmanoğlu B., Dixon T.H., Wdowinski S., Cabral-Cano E., & Jiang Y. (2011). Mexico City Subsidence Observed with Persistent Scatterer InSAR. *International Journal of Applied Earth Observation and Geoinformation*, 13 (1), 1-12.

Poland, J.F., (1984). Guidebook to studies of land subsidence due to ground-water withdrawal. Unesco, Paris, France.

Price, M. (1987). Fluid flow in the Chalk of England. In: Goff, J. C. and Williams, B. P. J. (eds) Fluid Flow in Sedimentary Basins and Aquifers, Geological Society London Special Publications, 34, 141-156.

Price, M., Bird, M.J. & Foster, S.S.D. (1976). Chalk pore-size measurements and their significance. *Water Services*, October, 596-600.

Price, M., Downing, R.A. & Edmunds, W.M. (1993). The Chalk as an aquifer In: Downing, R. A., Price, M. & Jones, G. P. (eds), The hydrogeology of the Chalk of north-west Europe. Clarendon Press, Oxford.14-34.

Reeves, J.A., Knight, R., Zebker, H.A., Kitanidis, P.K., & Schreüder, W.A. (2014). Estimating temporal changes in hydraulic head using InSAR data in the San Luis Valley, Colorado. *Water Resources Research*, *50*(5), 4459-4473.

Riley, F.S. (1969). Analysis of borehole extensometer data from central California. In: Tison, L.J. (Ed.) Land subsidence. *Proceedings of the Tokyo Symposium*, September 1969, IAHS Pub. vol. 88, pp. 423–431. Available at: http://iahs.info/redbooks/a088/088047.pdf

Riley, F.S. (1998). Mechanics of aquifer systems—The scientific legacy of Joseph F. Poland, in Borchers, J.W., ed., Land subsidence case studies and current research: Proceedings of the Dr. Joseph F. Poland Symposium on Land Subsidence: Belmont, Calif., Star Publishing Co., *Association of Engineering Geologists Special Publication* 8, p. 13–27.

Royse, K.R., de Freitas, M., Burgess, W.G., Cosgrove, J., Ghail, R.C., Gibbard, P., King, C., Lawrence, U., Mortimore, R.N., Owen, H.G., & Skipper, J. (2012). Geology of London, UK. *Proceedings of the Geologists' Association* 123, 22–45.

Samieie-Esfahany, S., Hanssen, R., van Thienen-Visser, K., & Muntendam-Bos, A. (2009). On the effect of horizontal deformation on InSAR subsidence estimates. *Proceedings of The Fringe 2009 Workshop, Frascati, Italy* (Vol. 30).

Schad, H., & Teutsch, G. (1994). Effects of the investigation scale on pumping test results in heterogeneous porous aquifers. *Journal of Hydrology*, *159*(1), 61-77.

Sneed, M. & Galloway, D.L. (2000). Aquifer - System Compaction and Land Subsidence: Measurements, Analyses, and Simulations - the Holly Site, Edwards Air Force Base, Antelope Valley, California: *U.S. Geological Survey Water-Resources Investigation Report* 00-4015, 70p. (Available online at http://ca.water.usgs.gov/archive/reports/wrir004015/)

Sumbler, M.G. (1996). British Regional Geology: London and the Thames Valley, fourth ed. HMSO for the British Geological Survey, London.

Terzaghi, K. (1943). Theory of Consolidation (pp. 265-296). John Wiley & Sons, Inc..

Thames Water, (Undated), Final Water Resources Management Plan 2015-2040, Executive Summary. Available online at: https://www.thameswater.co.uk/tw/common/downloads/wrmp/WRMP14_Section_0.pdf. Accessed on 22 December 2015.

Tomás, R., Herrera, G., Cooksley, G., & Mulas, J. (2011). Persistent Scatterer Interferometry subsidence data exploitation using spatial tools: The Vega Media of the Segura River Basin case study. *Journal of Hydrology*, *400*(3), 411-428.

Tomás, R., Herrera, G., Delgado, J., Lopez-Sanchez, J.M., Mallorquí, J.J., & Mulas, J. (2010). A ground subsidence study based on DInSAR data: calibration of soil parameters and subsidence prediction in Murcia City (Spain). *Engineering Geology*, *111*(1), 19-30.

Tomás, R., Lopez-Sanchez, J.M., Delgado, J., & Mallorquí, J.J. (2006). Hydrological Parameters of the Vega Media of the Segura River Aquifer (SE Spain) obtained by Means of Advanced DInSAR. *Proceedings of the IEEE Intl. Geoscience and Remote Sensing Symposium, 2006. IGARSS 2006.* Vol. 3, pp. 1553-1556.

UK Groundwater Forum (1998). *Groundwater our hidden asset*. British Geological Survey, Keyworth. Thames Water Authority, 1978. *The Thames Groundwater Scheme*. Institution of Civil Engineers, London.

Ward, W.H., Burland, J.B., & Gallois, R.W. (1968). Geotechnical assessment of a site at Mundford, Norfolk, for a large proton accelerator. *Geotechnique*, *18*(4), 399-431.

Werner, C., Wegmüller, U., Wiesmann, A., & Strozzi, T. (2003). Interferometric point target analysis with JERS-1 L-band SAR data. *Proceedings of the IEEE Intl. Geoscience and Remote Sensing Symposium, 2003. IGARSS 2003.* Vol. 7, pp. 4359-4361. IEEE.

Wolf L., Morris, B., & Burn, S (2006). AISUWRS: Urban Water Resources Toolbox, 2006 IWA Publishing, London UK.

Chapter VII. Conclusions

In this thesis, a multidisciplinary approach was adopted, by combining geological, geotechnical, hydrogeological and A-DInSAR data to gain insight into the ground motion identification, monitoring and modelling. Major findings are described below.

7.1. Ground motion areas identification

A novel methodology to detect and to disentangle the contributions of different geohazards, by analysing multi-sensors and multi-temporal A-DInSAR data has been developed and tested in different areas such as: the Oltrepo Pavese, the valley bottom of the Oglio river, Ravenna and the Piemonte Region (Italy). The principal novelty of the proposed approach is the exploitation of full time series, which enables the detection of ground motion areas affected by linear, non-linear, and seasonal movements. The proposed methodology consists of three phases:

1. Post processing elaborations; disentanglement of the vertical and horizontal components of motion and displacements time series accuracy assessments, performed by selecting the most coherent (>0.9) targets with an average LOS velocity in the range ±0.5 mm/yr., where no significant movements are expected.
2. Identification of ground motion areas; application of two approaches for automatic A-DInSAR time series analyses. First, principal components analysis of the time series is performed, implementing a matrix organization of location versus time (T-mode). Then, PS-time software is used to find the kinematic behaviour of the time series (i.e., uncorrelated, linear and non-linear trend). Finally, ground-motion areas were identified using a spatial cluster with a buffer zone of 50 m around the targets, characterized by a significant correlation with the principal components of motion. The results of both approaches are overlapped to distinguish linear and non-linear and seasonal ground motion areas.

3. Mechanism recognition: comparison between ground motion areas and ancillary data (i.e., geological, geotechnical, hydrogeological, and land use information) in order to preliminary interpret the driving forces of the subsidence mechanisms.

Regarding the Oltrepo Pavese, which is a representative of moderate subsidence of the Po Plain characterized by swelling/shrinkage of clayey soils, the methodology allowed to disentangle natural and human-induced ground motion. By the use of ERS-1/2 and RADARSAT SAR a time span of around twenty years was monitored. By the adopted approach, a better understanding of the spatial and temporal evolution of different geohazards has been reached. The results gave insight into swelling–shrinkage of clayey soils, land subsidence due to the load of new buildings, moderate tectonic uplift, seasonal ground motion due to seasonal groundwater level variations.

The developed methodology was applied along the valley bottom of the Oglio river (Italy) which is a representative site of pre-Alpine and Alpine valley bottom subsidence with both natural and anthropic components. In this case, the approach applied on ERS-1/2 and RADARSAT data, gave insight into the geomorphologic control of the subsidence pattern; the stronger subsidence rate occurs in correspondence to a slope change. Subsidence due to dissolution of evaporitic rocks will also be investigated, and further *in situ* investigations are necessary to assess the occurrence of this process.

Finally, the approach was tested in Ravenna, which is a representative of natural and human high-moderate ground motion, in a coastal area. In this case, the procedure was applied using ERS1/2, Envisat, TerraSAR-X, and Sentinel-1 SAR. The priority areas for further investigations were identified in Porto Corsini, the Industrial area, Lido Adriano, Lido di Dante, Southwest of Ravenna, Mezzano and Savarna.

Furthermore, the reproducibility of the procedure was assessed in a wide area, the Piemonte Region. In this case, the same methodology was applied to detect slope instabilities.

The methodology allowed to identify two parts of the landslide with different behaviours (linear and non-linear trend) and to detect large unstable area that can be considered as a predisposing factor for the activation of rockfalls.

Results confirm its high capability of the methodology for detecting the temporal evolution of deformation patterns due to very different geohazards, not recognizable by conventional analyses of the average LOS velocity alone (i.e., seasonal components of motion). The approach is able to identify various deformational behaviours despite the use of A-DInSAR acquired by different sensors

and processed by different algorithms: linear, non-linear (accelerations and decelerations of the movements), and seasonal components of motion. The proposed methodology has been developed using open-source software and it can be easily applied to others geological contexts, using different A-DInSAR data. New opportunities will be provided by the improvement of the time series acquired by new sensors of ESA Sentinel missions. The procedure will also identify the priority area where to address prevention activities, in order to optimize the costs and benefits and to draw a management plan of land use and groundwater resources, at regional and local scales. Furthermore, the approach may also be used in land subsidence studies to discern the contributions of the seasonal components of motion from others processes, such as soil consolidation and solid and fluid extraction or injection.

7.2. Mechanism of ground motion

The combined analysis of geological and hydrological information with displacement maps and time-series retrieved from multi-sensor and multi-temporal SAR images had provided new insights about mechanisms of ground motion due to groundwater level change.

A-DInSAR analysis were performed in the Alto Guadalentín Basin (Spain) for the analysis of the mechanisms. The findings in this work confirmed that the combination of A-DInSAR time series analysis and hydrogeological data is capable of supporting the knowledge of the relationship between groundwater level fluctuations and deformations, and to provide fundamental information about the aquifer state conditions. The approach allowed to understand that very thick soft soil layer with low permeability that has been drained since the 1960s, are involved in slow consolidation process due to aquifer overexploitation. The negative gradient is maintained in this layer, which creates a delayed consolidation process wherein the maximum settlement has yet to be reached.

The achieved results, advise about the mechanisms of ground motion that affect this site and inform the scientific community about the lag that can occur between the exploitation of the groundwater resources and the response in ground motion at the surface. The lesson learned in the selected test area is applicable to other worldwide areas.

The mechanisms of ground motion were also investigated in the Oltrepo Pavese. In this case, first the ground motion areas were identified with the methodology described in Section 5.1. and then

these were cross-compared with the engineering geological unit's map, geological model, the land use change, the climatic data, the thickness of the unsaturated zone, and the database of damaged buildings. The main natural and man-induced processes were disentangled. Evidences of swelling–shrinkage of clayey soils, land subsidence due to the load of new buildings, moderate tectonic uplift, and seasonal ground motion due to seasonal groundwater level variations were retrieved. Clear correlation between the seasonal ground motions and the phreatic condition of the aquifer was observed. Results for this study also highlight that ground motion areas that record low average LOS velocities, in the range of ±1.5 mm/yr can be affected by geohazards (i.e. swelling/shrinkage of clayey soils) that may impact public safety.

7.3. Modelling ground motion caused by groundwater level change

Due to the large availability of geological, hydrogeological and geotechnical data, the area of London Basin has been selected to model the ground motion due to groundwater level change by applying 1D model. The combined analysis of hydrological information with displacement maps and time-series retrieved from multi-sensors and multi-temporal SAR images and A-DInSAR analysis has allowed the derivation of:

- the Chalk aquifer storage coefficient maps over an area of 1,360 km^2 in the periods 1992–2000 and 2002–2010;
- the 1D modelling of the ground motion response to hydraulic head changes at nine piezometers.

Correlation between the derived storage and the hydrogeological setting was observed. A 1D model based on the approach proposed by Tomás *et al.* (2010) was implemented in order to simulate the ground motion response to hydraulic head changes in the semi-confined and confined aquifer conditions. The results of the modelling revealed that the ground response to groundwater levels variations is not uniform across the London Basin. Spatio-temporal variations of the storage coefficient are related to the groundwater levels with respect to the lithological units, and to the fractures network in the aquifer, which are believed to cause compartmentalisation of the aquifer.

The variability of the aquifer storage coefficient throughout the Basin as a consequence, requires different policies and zonal planning for certain parts of London to manage the available resource and conflicting aquifer uses effectively. The application of satellite data to understand the relationship between the groundwater levels and the surface displacements, will provide new opportunities to inform future approaches for monitoring groundwater levels variations over wide urban areas of interest, such as the London Basin and for wider spatial assessment of aquifer properties.

7.4. Conclusions remarks

In the Introduction, Section 1.2. scientific questions have been raised and here the answers to each one are explained.

With the reference to the first question, a systematic and reproducible methodology to ground motion areas detection, was developed. A significant number of case histories were provided to test the methodology for different types of natural and human-induced processes. The reliability of the procedure was assessed using A-DInSAR images acquired by different sensors C-Band (ERS-1/2, Envisat, RADARSAT and Sentinel-1) and X-Band (Cosmo-SkyMed and TerraSAR-X) and characterized by different spatio-temporal resolution. In addition, the methodology was applied with data processed using different algorithms (PSInSAR^{TM}, Small Baseline Subset, Coherence Pixel Technique, Persistent scatterer pairs method, SqueeSAR^{TM}).

To distinguish different components of motion (Question 2, in Section 1.2.), Principal Component Analysis was applied to A-DInSAR data and the approach allowed to identify multiyear and seasonal component of motion.

The application of the methodology in different case of studies highlights the capability to detect natural and human-induced ground motion such swelling–shrinkage of clayey soils, landslides, land subsidence due to the load of new buildings, moderate tectonic uplift, and seasonal ground motion due to seasonal groundwater level variations (Question 3, in Section 1.2.).

The results obtained by the methodology was assessed in a wide area of 25,000 km^2 in Piemonte Region (Italy) and in this case, the approach proves the capability to detect different portion of the landslide characterized by different behaviours and to detect large unstable area that can be considered as a predisposing factor for the activation of rockfalls (Question 4, in Section 1.2.).

Furthermore, the combination of A-DInSAR with hydrogeological and geological proves to be fundamental to characterize the properties of fractured aquifer such as in the case of the London Basin, where the presence of discontinuities ideally requires investigations *in situ* over wide areas (Question 5, in Section 1.2). The high costs of such campaigns only permitted to carry out investigations at limited spatial or temporal scales. The approach allows the derivation of hydrogeological and geotechnical properties at large scale (i.e. the Chalk aquifer storage coefficient has been computed over an area of ~1,360 km^2 in the periods 1992-2000 and 2002-2010).

The A-DInSAR data were integrated with hydrogeological and geotechnical data to calibrate and validate a 1D model in the London Basin, based on the approach proposed by Tomás *et al.* (2010). The results of the modelling revealed that the ground response to groundwater levels variations is not uniform across the London Basin. Spatio-temporal variations of the storage coefficient are mainly related to the groundwater levels with respect to the lithological units (Question 6, in Section1.2.)

The outcomes of this thesis emphasize the fact that the improvement in the A-DInSAR technique can provide new insights into ground deformation investigations.

Furthermore, some considerations emerged by the SAR images acquired by different sensors and processed by the different algorithms (PSInSAR^{TM}, Small Baseline Subset, Coherence Pixel Technique, Persistent scatterer pairs method, SqueeSAR^{TM}) exploited in this thesis.

Overall, the use in conjunction of multi-sensor A-DInSAR data is fundamental to reconstruct the long-term evolution of ground motion due to the groundwater management. One the other hand, different benefits can be reached by the exploitation of the different sensors and processing-techniques.

It can be noted how the exploitation of C-band sensor is suggested to monitor the deformation over wide areas, meanwhile better benefits can be reached using X-band sensor for site-specific analysis at higher spatial resolution. In addition, A-DInSAR data acquired by L-band sensor are preferable for analysis at higher resolution, but they are not common. Regarding the processing techniques, the PSInSAR^{TM} and PSP-IFSAR are specifically addressed to monitor the motion of single buildings or outcrops where the full pixel resolution is necessary. Instead, in the case of rural scenarios (i.e. Oltrepo Pavese) characterized by lower coherence, the SqueeSAR^{TM} algoritm is preferable, thank to the detection of Distributed Scatterers (DS). SBAS, CPT and SPN approaches that work better than PS in lower coherence areas can be suggested for medium and large-scale phenomena to monitor slow deformation over wide areas, by allowing an accurate estimation of the deformation and, to remove the atmospheric and topographic residuals. The StaMPS approach allows an accurate estimation of the deformation. The IPTA technique that improves the parameters estimation in the interferometric phase, it is suggested for urban areas characterized by slow deformation. Thus, taking into account the different *pro* and *cons* for the different A-DInSAR data, the *priori* knowledge of the geological processes is fundamental to choose the most appropriate monitoring-system for deformation.

Furthermore, the higher temporal sampling of the recent satellite missions (i.e. Sentinel-1) makes it possible to study the temporal evolution of a mechanism providing time series and rate of the deformation process at higher precision.

Notwithstanding the profuse efforts, some topics discussed in this thesis have not yet been investigated in detail. For instance, the discovered time delay, in the Alto Guadalentín Basin, between the extraction of groundwater and the resulting subsidence, has not be quantified. The 3D coupled hydrogeological and geomechanical model is required to fill the gap. Additionally, the results inevitably indicated gaps worthy of further research, including the contribution in depth of the deformation. The understanding of the contribute in depth of deformation is still a challenging issue, especially in the case of complex geological and hydrogeological (multilayers aquifer-system) contexts where the overlapping of driving mechanisms makes more difficult the interpretation of the processes. In this case, *in situ* instrumentation such as extensometers combined with remote sensing tools may overcome the limitations in order to obtain the 4D deformation field (surficial and deep) monitoring.

However, this thesis offers detaileted investigations of ground motion processes headed in conjunction with a multi-disciplinary approach including geological, geotechnical, hydrogeological and A-DInSAR data. Following this standpoint, the proposed approach represents a valuable asset for a wide spectrum of natural and human-induced processes applications, at regional and local scale. A detailed understanding of ground motion processes is much needed, particularly for land use planning, for performing remediation/mitigation actions and for a sustainable management of the available resources. The approaches proposed through this study may be of high relevance for best practices and future project. Only the comprehensive understanding of the ground surface dynamics will allow to reduce the social, environmental, infrastructural and economic impacts of this silent hazard.

Appendix

Multi-sensors Advanced DInSAR analysis of the land subsidence pattern from 1992 to 2016 in the Ravenna area (Italy)

R. Bonì[1], S. Fiaschi[2], C. Meisina[1], A. Ibrahim[3], D. Calcaterra[4], D. Di Martire[4], M. Ramondini[5], S. Tessitore[4], S. Borgstrom[6], V. Siniscalchi[6], V. Achilli[7], M. Floris[2]

[1]Dept. of Earth and Environmental Science, University of Pavia, Pavia, Italy

[2]Dept. of Geosciences, University of Padua, Padua, Italy

[3]Dept., Faculty of Science, South Valley University, Qena, Egypt

[4]Dept. of Earth, Env. and Resources Sc., Federico II Univ. of Naples, Naples, Italy

[5]Dept. of Civil, Arch. and Env. Eng., Federico II University of Naples, Naples, Italy

[6]INGV, Osservatorio Vesuviano, Naples, Italy

[7]Dept. of Civil, Env. and Architectural Engineering, University of Padua, Padua, Italy

The results have been presented in the 2nd International Workshop on Coastal Subsidence (May 30th – June 1st, 2016; Arsenale, Tesa 102; ISMAR-CNR; Venice, Italy)

The methodology described in Section 5.1. was applied on datasets acquired by the ERS-1/2, ENVISAT, TerraSAR-X and Sentinel-1 satellites and processed using the SBAS algorithm in the Ravenna area, in Italy.

1. Study area

Ravenna is located on the south-eastern portion of the Po River plain (Italy) covering an area of about 391 km^2. The study area is located along the Adriatic coast, where land subsidence of natural and anthropogenic origin occurs since the last century. From the geological point of view, the area is bounded by two mountain ranges, the Alps to the North and the Apennines to the South. These mountains range are related to two subduction zones: the Alps results from the subduction of the

European plate beneath the Adriatic plate, and the Apennines from the subduction of the Adriatic plate under the Tyrrhenian lithosphere. The buried tectonic structures underlain around 2000 m of Quaternary sediments of Alpine and Apennines origin deposited under different environments, from continental to marine (Carminati *et al.,* 2003). Sediment accumulation is more pronounced in the areas of large tectonic subsidence, the so-called depocenter, which corresponds to the Po River delta. The pre-Quaternary basement is characterized by a complex structure of folds and faults which develop parallel to the main Apennine tectonic lines forming natural traps for the methane gas. Several Pliocene and Pleistocene gas fields are located in thrusted anticlines, with depths ranging between 1000 m and 4500 m, simple drape structures and stratigraphic traps (Gambolati *et al.*, 1991). A typical feature of this basin is that gas accumulation occurs in multiple zone reservoirs with thickness ranging from centimetres to a few tens of meters. The Quaternary sequence is made of normally consolidated layers of alternating silty-clay, sand and sandy silt. A multi-layer aquifer system is located in the first 500 m of sediments accumulated since the Pleistocene. The aquifer-system is characterized by an upper hydro-stratigraphic unit, named A, and a lower unit, named B (Figure 1c). The upper A unit belongs to the Sintema Emiliano-Romagnolo Superiore (AES) and is made of four main aquifer complexes, from A1 to A4. The deeper hydro-stratigraphic unit (B), also made of four different complexes (from B1 to B4), belongs to the Sintema Emiliano-Romagnolo Inferiore (AEI), the oldest part of the Supersynthem (Figure 1). This multi-layer aquifer system is characterized by sediments deposited during transgressive and regressive stages: the aquifers are mainly constituted by sandy layers, while the aquitard by silty-clayey layers. The recharge area is located in the thick coarse Apennine foothills as well as in the beds of the major rivers crossing the plain (Farina *et al.,* 2014).

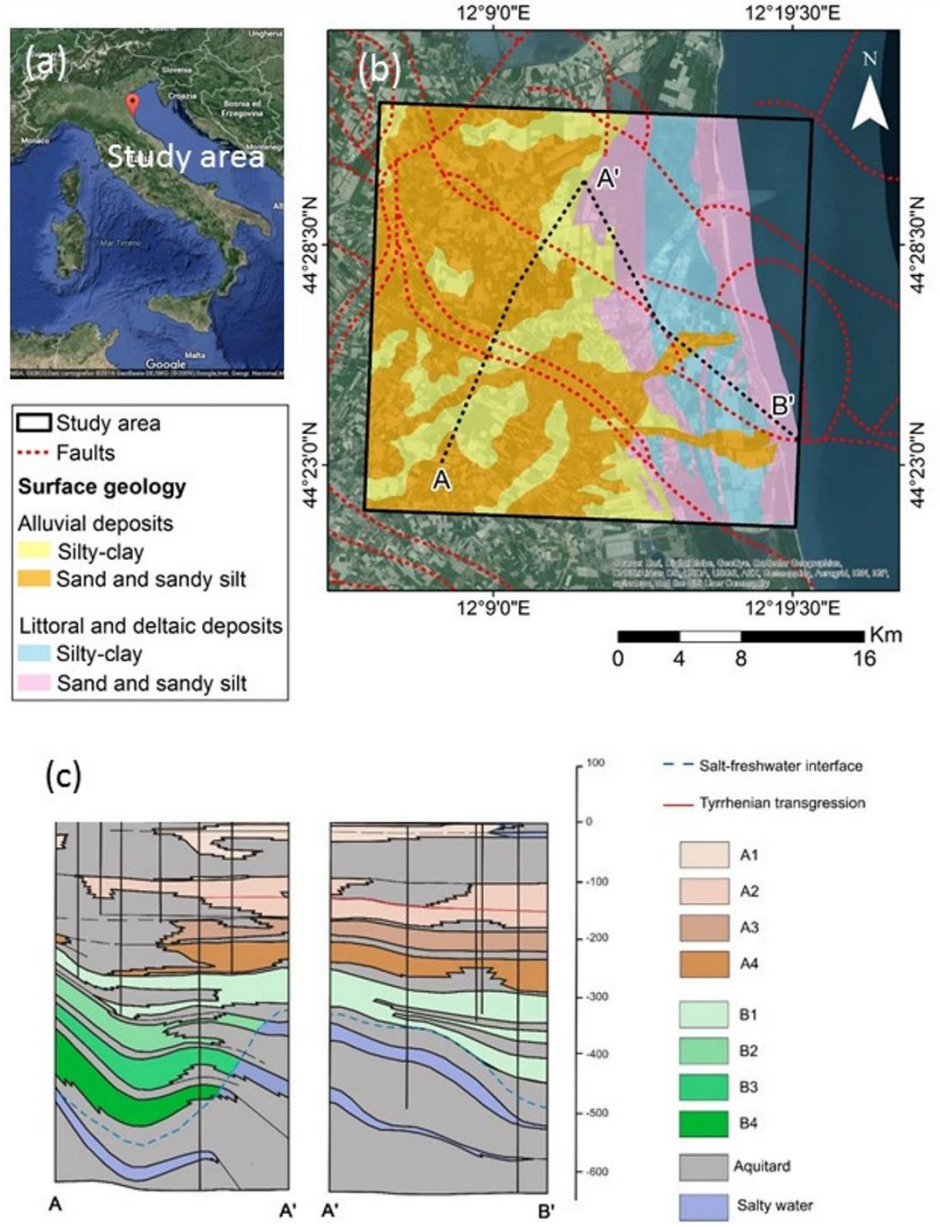

Figure 1. (**a**) Location of the study area. (**b**) Geological setting of the study area (CARG from Emilia Romagna). (**c**) Hydro-geological sections; their location is reported in Figure 1.c. (redrawn from AGIP, Regione Emilia Romagna, 1998).

2. A-DInSAR data

A-DInSAR techniques have been used to get twenty-four years (1992-2016) of ground displacement monitoring in the Ravenna area exploiting four SAR datasets acquired by C- and X-band SAR satellites. Specifically, 57 ERS-1/2 (C-band), 60 ENVISAT (C-band), 53 TerraSAR-X StripMap (X-

band) and 30 Sentinel-1A Interferometric Wide Swath (C-band) images acquired in descending geometry have been processed with using the SBAS algoritm (Figure 2).

Additional details are listed in table 1.

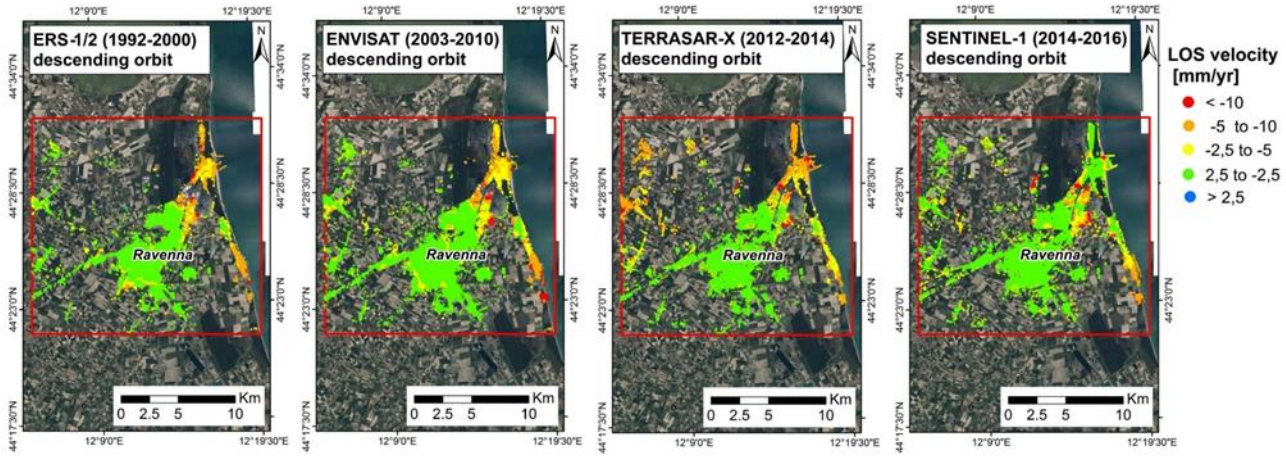

Figure 2. Advanced DInSAR data processed by University of Padua using SBAS algorithm (SARscape© software) Ortophoto AGEA 2011 (http://geoportale.regione.emilia-romagna.it/). ERS-1/2 ½, ENVISAT and Sentinel-1 images were provided by ESA (respectively, CAT-1 Project and free-downloadable the last ones) TerraSAR-X images provided by DLR (Proposals GEO2478 and GEO3016).

Table 1. Details of the available SAR images.

Satellite	**ERS-1/2**	**ENVISAT**	**TerraSAR-X**	**Sentinel-1**
Time span	10/05/1992-13/12/2000	02/04/2003-22/09/2010	25/02/2012-05/04/2014	12/10/2014-11/01/2016
Track	122	122	2	95
N° images	57	60	53	30
λ (cm)	5.6	5.6	3	5.6
Incidence angle (°)	23	23	29	39

3. Results

The results reveal that ERS-1/2 and Envisat data are characterized, respectively, by one and two components of motion (Figure 3). Conversely, TerraSAR-X and Sentinel-1 data reveal three components of motion. The principal component of the movement (PC1) explains about the 80-90% of the variance for all datasets. The second (PC2) and third (PC3) components of motion, that had been detected using ENVISAT, TerraSAR-X and Sentinel-1 data, explain a percentage of variance in the range from 1% to 10%. The first component of motion (PC1) is a movement away from the satellite, conversely the second one (PC2) is a movement toward the satellite, and the third one (PC3) shows a seasonal component of motion (Figure 3).

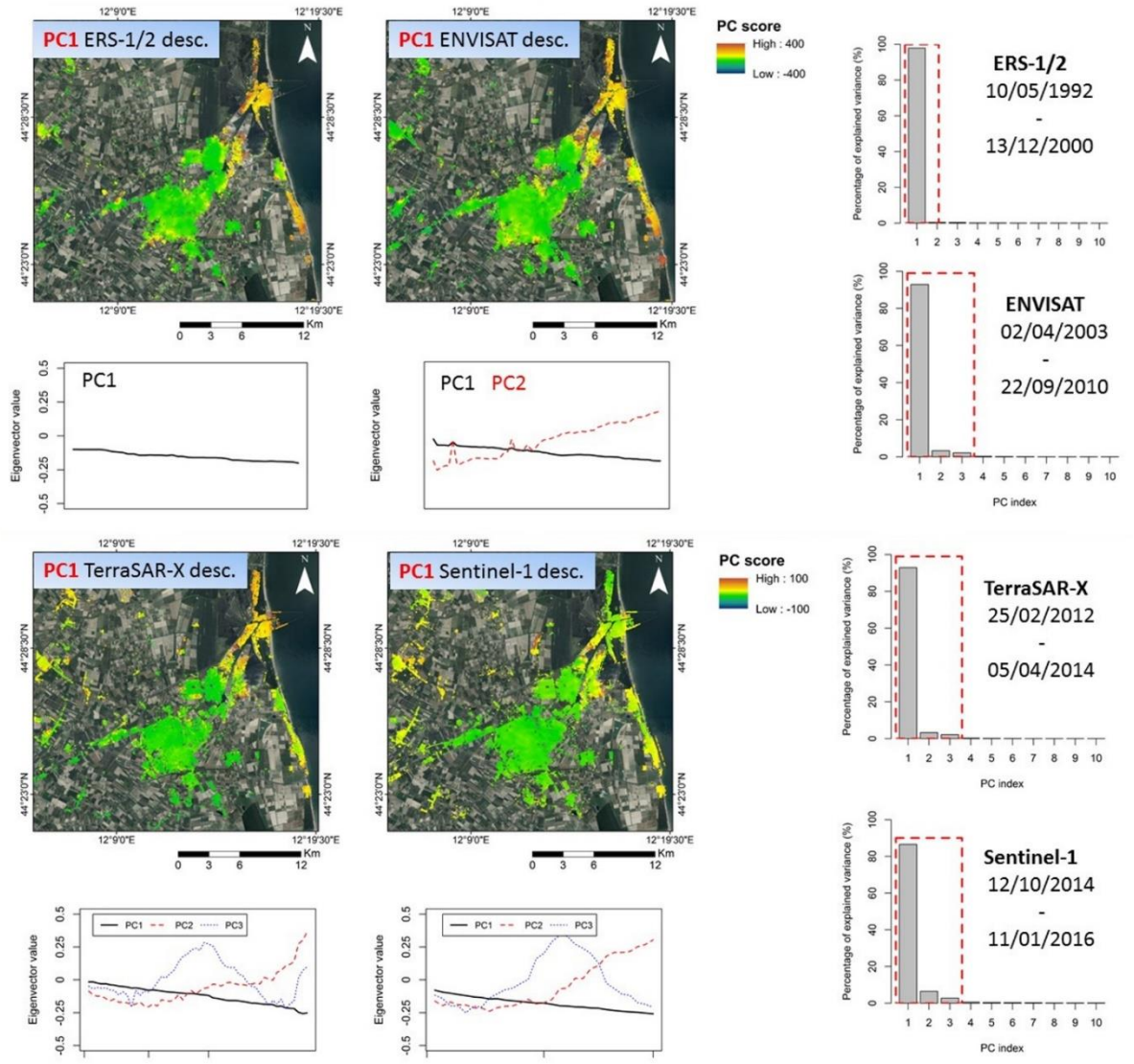

Figure 3. Principal component score maps of the first component of motion, eigenvectors and percentage of the variance, for each dataset.

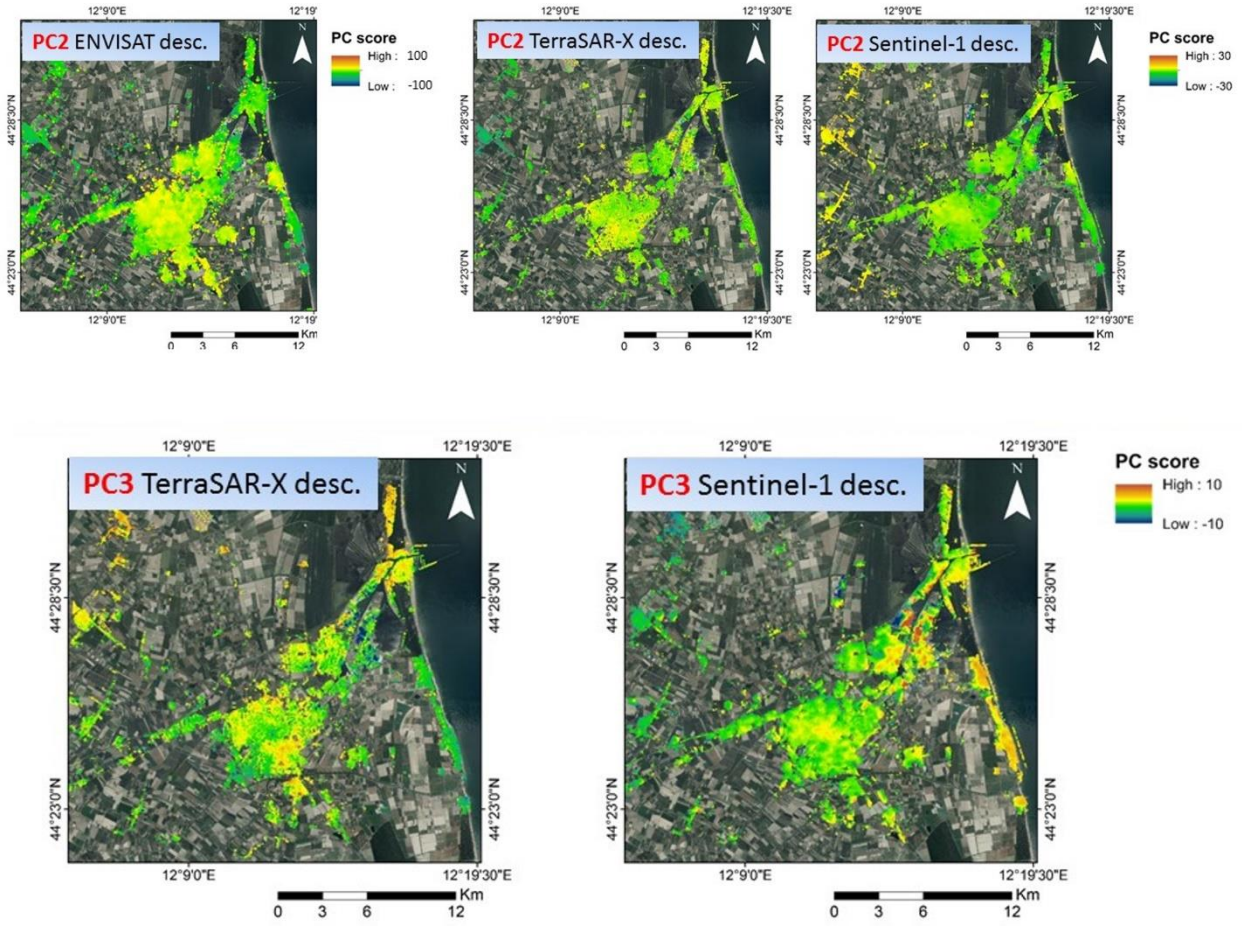

Figure 4. Principal component score maps of the second and third components of motion, for each dataset.

4. Discussion

In this work, a preliminary interpretation of first component of motion (PC1) that represents the land subsidence, was carry out. Since the scarcity of ancillary data, at this step of the research, the analysis was performed on this component which is the prevalent (about the 80-90% of the variance for all datasets was explained by the land subsidence process). Figure 5 shows the spatial distribution of the ground-motion areas detected using the PC1 of the four datasets. The application of the methodology gave insight into six main areas (Figure 5):

- Porto Corsini (A1);
- Industrial area (A2);

- Lido Adriano (A3);
- Lido di Dante (A4);
- Southwest of Ravenna (A5);
- Mezzano and Savarna (A6).

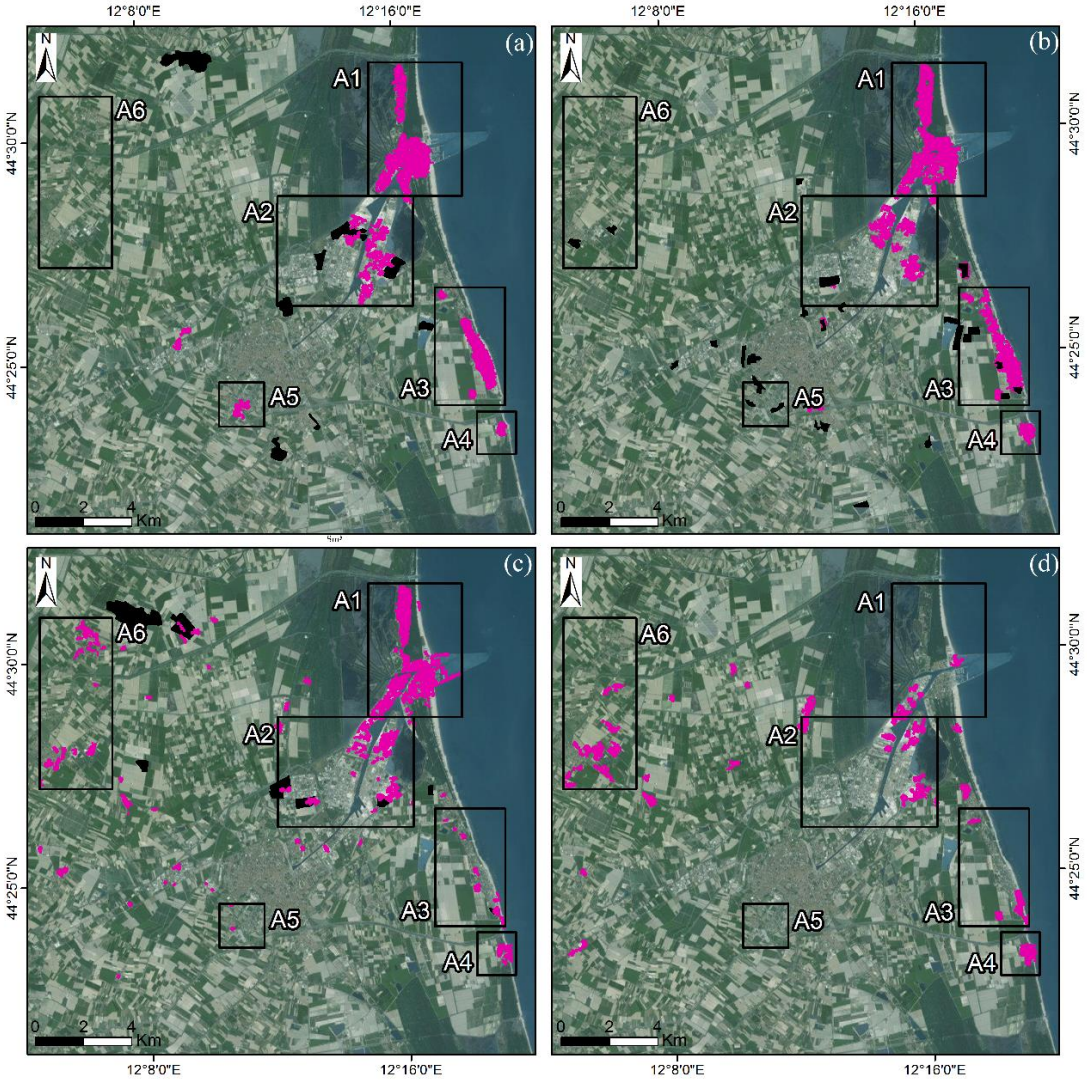

Figure 5. Ground motion areas detected using the PC1.

Regarding the kinematic model, the results highlight that 40-50% of the points measured using the ERS-1/2 and ENVISAT datasets is characterized by linear trend, 30-40% show non-linear trend and 20-30% show uncorrelated trend. Most of the measure points (around 43%) resulted from the TerraSAR-X data processing shows non-linear trend, while the 30% is characterized by linear trend and the 27% by uncorrelated trend. Unfortunately, the time interval covered by the Sentinel-1 dataset cannot be analysed using the automatic procedure.

Then, such statistics were carry out on the rates of displacement detected in the ground motion areas. More precisely, the average velocity was computed using the measurements along the line of sight (LOS) of the satellites. The vertical average velocity (V_{vert}) was computed by dividing the V_{LOS} for the incidence angle of each satellite. Obviously, it is an approximation since the available data did not made possible the estimation of the horizontal component of motion. The procedure was applied to extract comparable values about the evolution of the movements. The results of this analysis are showed in table 2.

Table 2. Average LOS (V_{LOS}) and vertical (V_{vert}) velocity, and standard deviation (Std) calculated in the six different ground motion areas for each dataset.

Period		10/05/1992-13/12/2000	02/04/2003-22/09/2010	25/02/2012-05/04/2014	12/10/2014-11/01/2016
Dataset		ERS-1/2	Envisat	TerraSAR-X	Sentinel-1
A1 (Porto Corsini)	V_{LOS} (mm/yr)	-6.65	-5.68	-6.88	-1.63
	V_{vert} (mm/yr)	-7.23	-6.17	-7.91	-2.09
	Std (mm/yr)	2.34	1.31	0.85	0.85
A2 (Industrial area)	V_{LOS} (mm/yr)	-5.86	-7.72	-8.74	-11.89
	V_{vert} (mm/yr)	-6.37	-8.39	-10.05	-15.25
	Std (mm/yr)	2.17	3.35	4.49	9.46
A3 (Lido Adriano)	V_{LOS} (mm/yr)	-6.29	-6.55	-6.15	-6.65
	V_{vert} (mm/yr)	-6.83	-7.12	-7.07	-8.52
	Std (mm/yr)	1.24	2.07	1.27	0.90
A4 (Lido di Dante)	V_{LOS} (mm/yr)	-7.30	-11.72	-6.48	-8.33
	V_{vert} (mm/yr)	-7.94	-12.74	-7.45	-10.68
	Std (mm/yr)	0.92	1.47	0.94	1.12
A5 (Southwest of Ravenna)	V_{LOS} (mm/yr)	-5.61	-4.81	-4.55	-2.12
	V_{vert} (mm/yr)	-6.10	-5.23	-5.23	-2.72
	Std (mm/yr)	2.27	0.87	0.94	0.43
A6 (Mezzano and Savarna)	V_{LOS} (mm/yr)	-3.40	-3.38	-8.80	-2.58
	V_{vert} (mm/yr)	-3.70	-3.68	-10.11	-3.31
	Std (mm/yr)	0.78	0.69	0.72	1.76

It is worth noting that the Industrial area (A2) records the highest average vertical velocity of -15.25 mm/yr in the period 2014-2016 (Table 2). The average vertical velocity in A2 shows an increase in the displacement rate from -6.37 mm/yr in the first monitored period (1992-2000) up to -15.25 mm/yr in the last one (2014-2016).

The contribution that land-use changes may have on the detected displacement rates were evaluated by overlapping the six ground-motion areas with the CORINE Land Cover (CLC) inventory corresponding to the period covered by each dataset. The ground-motion areas extracted from the ERS-1/2 results were compared with the CLC changes 1990-2000. Most of the subsidence affects areas which land use changes from salt marshes and non-irrigated arable land to industrial or commercial unit. The displacement observed with the ENVISAT dataset matches with the CLC changes 2000-2006.

4.1. Porto Corsini (A1)

A correlation between land use changes from non-irrigated arable land to industrial/commercial unit and from construction site to industrial/commercial unit, was detected in the A1 area. Even if the ground-motion area observed at Porto Corsini (A1) insists on the coastline like in the case of Lido Adriano (A3) and Lido Dante (A4), it seems to be affected by subsidence with a different temporal evolution. More precisely, area A1 shows an increase of the average vertical velocity from 2012-2014 to 2003-2010, while in 2014-2016 the velocity rapidly decreased till -2.09 mm/yr. The increase of the average velocity found in 2012-2014 may correspond to the gas production activity at the Porto Corsini mare reservoir (Figure 6) that reached its maximum of approximately 132 M Smc in 2011.

4.2. Industrial area (A2)

By comparing the CLC changes 2012-2013 with the TerraSAR-X results, the same correlation was observed in A2 where the same land-use change occurred. Therefore, in A2 most of the subsidence seems to be correlated to the sediments compaction caused by the load of the new constructions.

4.3 Lido Adriano (A3) and Lido di Dante (A4)

Regarding the evolution of the movements detected in the areas of A3 and A4, it is evident an increase in the subsidence rates in the period 2003-2010 in respect to 1992-2000, and in the period

2014-2016 in respect to 2012-2014. The average vertical velocity is higher in area A4 than in area A3. These areas are located in proximity of the offshore Angela-Angelina reservoirs (around 2 km from the coastline), and a quite good correlation is observed with the gas production management. The increase of the average velocity, detected using the Envisat sensor, in these areas seem to be connected with the activation in 1997 of gas extraction from the Angela-Angelina gas field. In the period monitored by the TerraSAR-X sensor, the decrease of the average vertical velocity in respect to the previous period (2003-2010) seems to be correlated with a decrease in the methane gas production from an annual average of 734 M Smc (2003-2010) to 377 M Smc (2012-2014). Conversely, the increase average velocity detected in the period monitored by the Sentinel-1 sensor seems not to be correlated with the methane gas production management.

4.4. Southwest of Ravenna (A5)

The ground-motion area detected in A5 highlights a decrease of the average vertical velocity from -6.10 mm/yr (1992-2000) to -2.72 mm/yr (2014-2016).

4.5. Mezzano and Savarna (A6)

The ground-motion area detected at Mezzano and Savarna (A6) is characterized by a high increase of the average vertical velocity in the period 1992-2010 from around -3.7 mm/yr to -10.11 mm/yr in the 2012-2014 period; it follows a rapid decrease in 2014-2016 with -3.3 mm/yr. In this case, a correlation between the land-use change from non-irrigated arable land to industrial/commercial unit, was detected by comparing the CLC 2012-2013 and the TerraSAR-X results. As observed in A2, even in this area the loading produced by the construction of new buildings may locally affects the observed ground displacements.

5. Conclusions

Different components of motion have been recognized in the period from 1992 to 2016 in the Ravenna through PCA analysis. The application of the methodology proves the capability to identify priority areas where further investigations have to be performed to identify the mechanisms of ground motion.

AQUARISK Project

AQUARISK is a coordinated project by the Geological Survey of Spain (IGME) that aims to provide new products and services for the analysis, management and mitigation of the geological-geotechnical risks associated with the exploitation of aquifers in urban areas. For this purpose, multi-sensor ((ERS & ENVISAT, ALOS PALSAR, Sentinel, PAZ) satellite DInSAR and GPS data fusion will be performed at regional scale to determine the 3D deformation field of the Mediterranean arc (Southeast Spain). This analysis will permit to detect the temporal evolution of subsidence in those hydrographic basins that suffer the greatest exploitation (e.g. Guadalentin-Segura river basin). In these areas, new in situ monitoring systems will be developed and implemented to monitor automatically and in real time (robotised sytem connected with GPRS) the temporal evolution of ground water level and the aquifer deformation in depth. These measurement data will be integrated with EO data to determine the 4D deformation field (surficial and deep), and to define future climate change based scenarios of the aquifer system response. All this effort will permit to develop, calibrate and validate advanced numerical geomechanical models that will simulate the past-present-future aquifer system response, and to analyze the impact of subsidence on urban structures and infrastructures.

During the period of the Erasmus traineeship (12/01/15-13/03/15) at the Geological Survey of Spain (IGME) under the supervision of the Dr. Herrera, two main activities were performed in the framework of the AQUARISK Project:

1. Drilling borehole perforated until about 300 m in depth in the Alto Guadalentín Basin (Figure), in order:

- to reconstruct the stratigraphic column until 300 m in depth;
- for the installation of piezometers at different depths;
- for the installation of a robotised system of magnetic ring and sensors to obtain automatically and in real time the aquifer deformation at different depths and for interpreting the causes of ground motion;

2. Building the stationary Model of the Alto Guadalentín Aquifer (Spain) using MODFLOW software, in order:
   - to reconstruct the 3D geometries of the aquifer-system involved in the compaction;
   - to understand the hydraulic behaviour of the aquifer-system;
   - to implement further coupled fluid flow and geomechanical deformation modelling.

1. Drilling borehole in the Alto Guadalentín Basin

The drilling was performed in Lorca, in the Alto Guadalentín Basin (Figure 1a), using the wireline coring (Figure 1b) and, more precisely, until 140 m in depth was used the PQ wireline drill bit and from 140 m to 300 m in depth the HQ wireline drill bit. Then, the borehole was drilled using a tricone with diameter of 120.6 mm and by using a mixed fluid of bentonite clay and water, to keep the borehole from collapsing.

The boreholes had to be instrumented with piezometer ad different depth and robotized system of magnetic ring and sensors (Figure 1c,d) to obtain automatically and in real time the aquifer deformation in depth. Unfortunately, the difficulties encountered during the installation did not allowed to complete the borehole instrumentation. The installation problem seems to be related uplift buoyancy force on the casing, lifting the casing out of the borehole (Figure 1e).

However, the drilling permitted to reconstruct the stratigraphic column until 300.5 m in depth as shown in Figure 2.

Figure 1. (**a**) Localization of the drilling borehole. (**b**) Equipment for the wireline drilling. (**c**) Magnetic ring and sensors for the vertical displacement rates at different depth. Detail of the design of the corrugated sheat and settlement rings included in the robotised system before (**e**) and after (**b**) the attempt of installation.

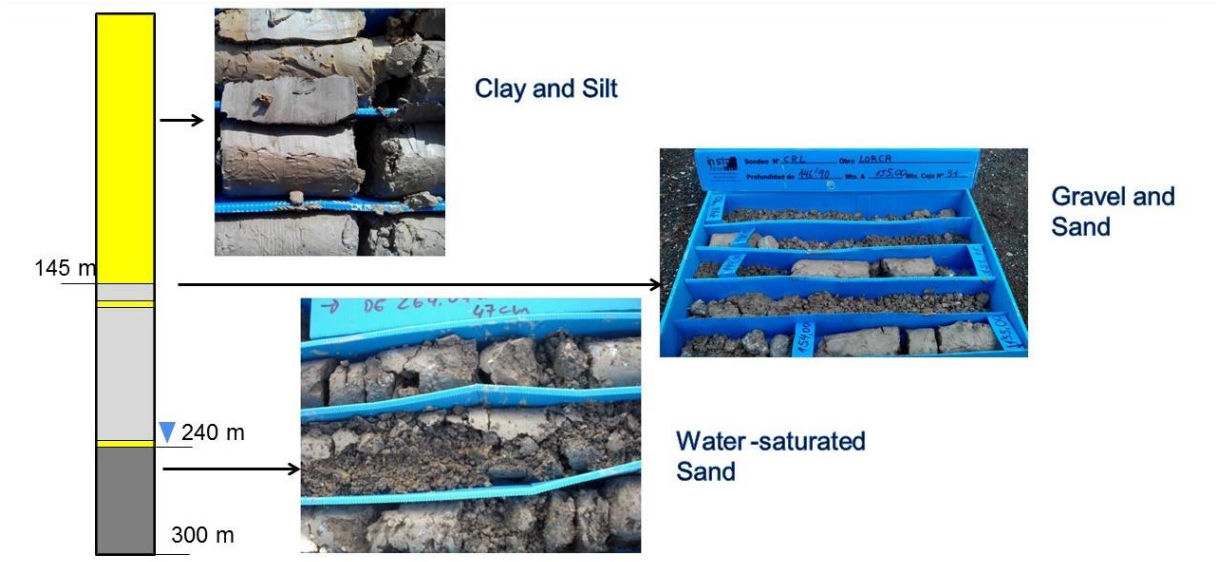

Figure 2. Schematic stratigraphic column of the borehole and details of the sampled soils.

2. Building the stationary Model of the Alto Guadalentín Aquifer (Spain)

The stationary 3D model of the Alto Guadalentín Aquifer was implemented using ModelMuse 3.8. that is an open-source graphical User Interface for MODFLOW-2005. The work has been performed under the supervision of Dr. Carolina Guardiola-Albert, hydrogeologist of the Geological Survey of Spain (IGME).

First, the data collection was carried out by the collaboration with the section of the IGME in Murcia (Spain), Prof. Ramón Aragón Rueda, Dr. Jorge Enrique Hornero Díaz and thanks to the *Confederación Hidrográfica del Segura*.

Following, the phase to build the model are listed:

1. Conceptual model of the aquifer-system
2. Aquifer-system geometry
3. Calibration of the hydraulic parameters

First, previous groundwater flow models of the Alto Guadalentín Aquifer were analysed. More precisely, different models were implemented by the Geological Survey of Spain (IGME 1994) and by the *Confederación Hidrográfica del Segura* (CHS 1990, CHS 2005). The table synthetize the main details of the models.

Table 1. Characteristics of the previous models of the Alto Guadalentín Aquifer.

Model IGME 1994	**Model CHS 1990**	**Model CHS 2005**
Implemented by: Geological Survey of Spain (IGME)	*Implemented by:* Dept. Ingeniería Hidráulica y Medio Ambiente de la Universidad Politécnica de Valencia	*Implemented by:* Dept. Ingeniería Hidráulica y Medio Ambiente de la Universidad Politécnica de Valencia
Area: Alto Guadalentín	*Area:* Alto, Medio and Bajo Guadalentín	*Area:* Alto, Medio and Bajo Guadalentín
N° layer: 1 (Plio-Quaternary sediments and only for two localized areas even the Miocene sediments were included in the aquifer	*N° layer:* 2 (Plio-Quaternary layer and Miocene layer)	*N° layer:* 22 (Plio-Quaternary layer and Miocene layer)
Type of Model: Integrated finite difference method	*Type of Model:* Finite difference method (cellsize 1000x500 m)	*Type of Model:* Finite difference method (cellsize 500x500 m)
Calibration: Transmissivity	*Calibration:* Conductivity	*Calibration:* Conductivity
*Time span:*1961-1993	*Time span:*1982-1989	*Time span:* 1982-1989 and 2004

The model implemented by the IGME in 1994 included only the Plio-Quaternary sediments and is calibrated using the values of transmissivity. The models introduced by the Confederación

Hidrográfica del Segura includes also the Miocene sediments in the model and are calibrated with the values of conductivity. Here, the implemented model is a fusion of the main advantages of both these models. Indeed, the geometry of the aquifer-system has been built including two layers:

- Plio-Quaternary detrital and alluvial material including clays, sands and conglomerates with clay and/or silt matrix;
- Miocene detritical with conglomerate and sand deposits;

The model was implemented using a cellsize of 500x500m. The hydrogeological parameter that has been implemented in the model, is the transmissivity (range from 5 to 300 m^2/h) obtained by drilling boreholes in the study area (Figure 3 and 4). The stationary model was calibrated with piezometric level in 1960 (IGME 1994).

In the future, the nonstationary model will be implemented and the hydrogeological model will be coupled with the 3D geomechanical model implemented with the GEHOMADRID finite element code.

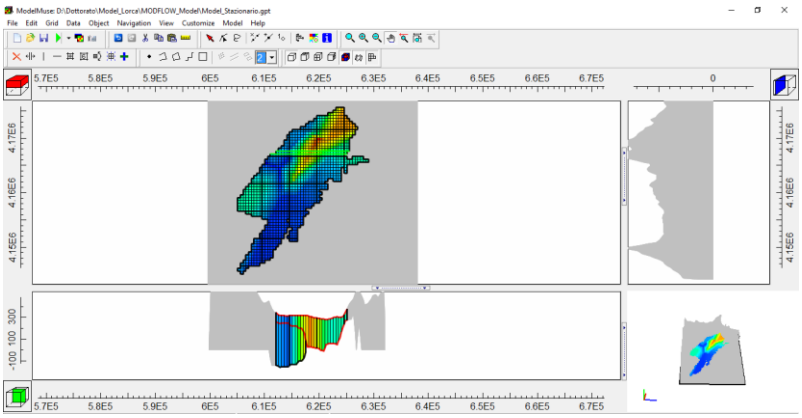

Figure 3. Model set up of the 1st layer (red represents high transmittivity values and blu high transmittivity values).

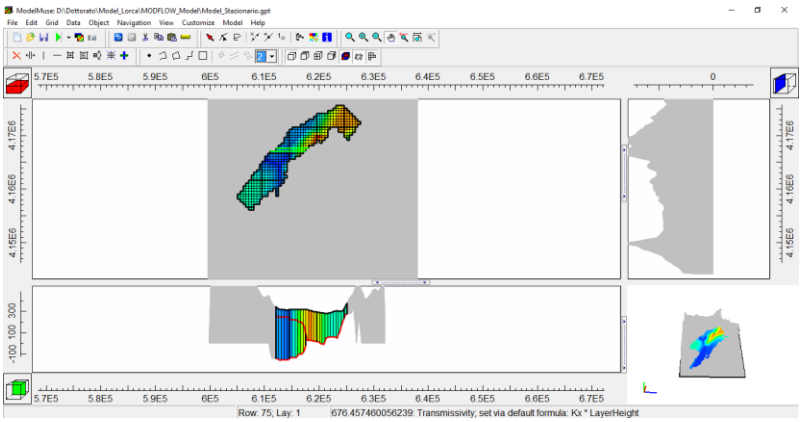

Figure 4. Model set up of 2nd layer (red represents high transmittivity values and blu high transmittivity values).

References

Abidin, H. Z., Andreas, H., Gumilar, I., Sidiq, T. P., and Gamal, M. (2015). Environmental Impacts of Land Subsidence in Urban Areas of Indonesia, in: Proceedings of the FIG Working Week 2015, TS 3 – Positioning and Measurement, Sofia, Bulgaria, Paper no. 7568, 17–21 May, 2015c.

Arnaud A., Adam, N., Hanssen, R., Inglada, J., Duro, J., Closa, J. Eineder M. (2003). ASAR ERS interferometric phase continuity. *International Geoscience and Remote Sensing Symposium*, 21-25 July 2003, Toulouse (France).

Bateson, L.; Cuevas, M.; Crosetto, M.; Cigna, F.; Schijf, M.; Evans, H. PANGEO: enabling access to geological information in support of GMES: deliverable 3.5 production manual. 2012, Version 1.

Available at: http://www.pngeoproject.eu/sites/default/files/pangeo_other/D3.5-PanGeo-Production-Manual-v1.3.pdf, Accessed on: 26/06/2016.

Berardino, P., Fornaro, G., Lanari, R., Sansosti, E. (2002). A new algorithm for surface deformation monitoring based on small baseline differential SAR interferograms. *Geoscience and Remote Sensing, IEEE Transactions* on, 40 (11), 2375-2383.

Berti, M., Corsini, A., Franceschini, S., Iannacone, J.P. (2013). Automated classification of Persistent Scatterers Interferometry time series. *Natural Hazards and Earth System Science*. 13(8), 1945-1958, doi:10.5194/nhess-13-1945-2013.

Bianchini, S., Cigna, F., Righini, G., Proietti, C., and Casagli, N. (2012). Landslide hotspot mapping by means of persistent scatterer interferometry. *Environmental Earth Sciences*, 67(4), 1155-1172.

Bini, A., Corbari, D., Falletti, P., Fassina, M., Perotti, C. R., & Piccin, A. (2007). Morphology and geological setting of Iseo Lake (Lombardy) through multibeam bathymetry and high-resolution seismic profiles. *Swiss Journal of Geosciences*, 100(1), 23-40.

Bloomfield, J.P., Bricker, S.H. & Newell, A.J. (2011). Some relationships between lithology, basin form and hydrology: a case study from the Thames basin, UK. *Hydrological Processes*., 25: 2518–2530. doi:10.1002/hyp.8024

Boni, A., Boni, P., Peloso, G.F., Gervasoni, S. Dati sulla neotettonica del foglio di Pavia (59) e di parte dei fogli voghera (71) ed alessandria (70). CNRPF Geodin. Pubbl. 1980, 356, 1199–1223.

Bourgois, J., Mauffret, A., Ammar, A., Demnati, A. (1992). Multichannel seismic data imaging of inversion tectonics of the Alboran Ridge (Western Mediterranean Sea). *Geo-Marine Letters*, 12 (2-3), 117-122.

Bozzano, F., Esposito, C., Franchi, S., Mazzanti, P., Perissin, D., Rocca, A., & Romano, E. (2015). Understanding the subsidence process of a quaternary plain by combining geological and hydrogeological modelling with satellite InSAR data: The Acque Albule Plain case study. *Remote Sensing of Environment*, 168, 219-238.

Braga, G., Cerro, A. Le strutture sepolte della pianura pavese e le relative influenze sulle risorse idriche sotterranee. Atti Tic. Sci. Terra 1988, 31, 421–433.

Brambilla G. Prime considerazioni cronologico-ambientali sulle filliti del Miocene superiore di Portalbera (Pavia-Italia settentrionale). Nuove ricerche archeologiche in provincia di Pavia. In Proceedings of Convegno di Casteggio, Casteggio, Italy, 14 October 1990; Civico Museo Archeologico di Casteggio e dell'Oltrepò Pavese, Casteggio, Italy, 1992; pp. 109–113.

Burbey, T. J. (2001). Stress-Strain Analyses for Aquifer-System Characterization. *Ground Water*, 39(1), 128-136.

Burbey, T. J. (2003). Use of time–subsidence data during pumping to characterize specific storage and hydraulic conductivity of semi-confining units. *Journal of Hydrology*, 281(1), 3-22.

Calderhead, A. I., Therrien, R., Rivera, A., Martel, R., and Garfias, J. (2011). Simulating pumping-induced regional land subsidence with the use of InSAR and field data in the Toluca Valley, Mexico. *Advances in Water Resources*, 34(1), 83-97.

Carminati, E., G., Martinelli, and P. Severi. (2012). "Influence of glacial cycles and tectonics on natural subsidence in the Po Plain (Northern Italy): insights from 14C ages". *Geochemistry Geophysics Geosystems Journal* 4: 1082-1096.

Cavanna, F., Marchetti, G., Vercesi, P.L. Idrogeomorfologia e insediamenti a rischio ambientale. Il caso della pianura dell'Oltrepò Pavese e del relativo margine collinare. Ricerche & Risultati, Valorizzazione dei progetti di ricerca 1994/97. Fondazione Lombardia Ambiente, Isabel Litografia, Gessate, Italy, 1998; pp. 14–72.

Cerón, J.C., and Pulido-Bosch, A. (1996). Groundwater problems resulting from CO2 pollution and overexploitation in Alto Guadalentín aquifer (Murcia, Spain). Environmental Geology, 28 (4) 223–228, doi:10.1007/s002540050096.

Chaussard, E., Amelung, F., Abidin, H., and Hong, S. H. (2013). Sinking cities in Indonesia: ALOS PALSAR detects rapid subsidence due to groundwater and gas extraction. *Remote Sensing of Environment*, 128, 150-161.

Chen, M., Tomás, R., Li, Z., Motagh, M., Li, T., Hu, L., Gong, H., Li, X., Yu, J., Gong, X. (2016). Imaging Land Subsidence Induced by Groundwater Extraction in Beijing (China) Using Satellite Radar Interferometry. *Remote Sensing*, 8(6), 468.

CHS (1990), Estudio y redacción del Plan de ordenación del acuífero Alto Guadalentín, Tech. rep.

CHS (2005), Estudio de cuantificación del volumen anual de sobreexplotación de los acuíferos de la unidad hidrogeológica 07.28 Alto Guadalentín y 07.33 Águilas, Tech. rep. (ftp://ftp.chsegura.es/oph/phcsegura/borrador/anejo12docs/FichaSub_070_057_AltoGuadalentin.pdf)

CHS (2006), Plan especial ante situaciones de alerta y eventual sequia en la cuenca del Segura: 238 Confederacion hidrografica del Segura, Tech. rep., 298 p., 239.

Cigna, F., Osmanoğlu, B., Cabral-Cano, E., Dixon, T.H., Ávila-Olivera, J.A., Gardũno-Monroy, V.H., DeMets, C., and Wdowinski, S. (2012). Monitoring land subsidence and its induced geological hazard with Synthetic Aperture Radar Interferometry: a case study in Morelia, Mexico, *Remote Sensing of Environment*, 117, 146–161, doi:10.1016/j.rse.2011.09.005.

Costantini M., Falco S., Malvarosa F., Minati F., (2008). "A new method for identification and analysis of persistent scatterers in series of SAR images," in *Proc. Int. Geosci. Remote Sensing Symp.(IGARSS)*, Boston MA, USA, 7-11 July 2008, pp. 449-452.

Crosetto, M., Biescas, E., Duro, J., Closa, J., Arnaud, A., (2008). Generation of advanced ERS and Envisat interferometric SAR products using the stable point network technique. *Photogram. Eng. Remote Sens.* 74 (4), 443–450.

Crosetto, M., Monserrat, O., Cuevas-González, M., Devanthéry, N., and Crippa, B. (2016). Persistent scatterer interferometry: A review. *ISPRS Journal of Photogrammetry and Remote Sensing*, *115*, 78-89.

De Freitas, M.H. (2009). Geology; its principles, practice and potential for Geotechnics. *Quarterly Journal of Engineering Geology and Hydrogeology*, 42(4), 397-441.

Di Martire, D., Tessitore, S., Brancato, D., Ciminelli, M.G., Costabile, S., Costantini, M., Graziano, G.V., Minati, F., Ramondini, M., Calcaterra, M., (2016). Landslide detection integrated system (LaDIS) based on in-situ and satellite SAR interferometry measurements. *Catena* 137, 406–421.

Duro J., Closa J., Biescas E., Crosetto M., Arnaud A., (2005). High Resolution Differential Interferometry using time series of ERS and ENVISAT SAR data. Proc. of the 6th. Geomatic Week Conference, February 2005, Barcelona, Spain (CDROM).

Ellison, R.A., Woods, M.A., Allen, D.J., Forster, A., Pharaoh, T.C., & King, C. (2004). Geology of London: special memoir for 1: 50000 geological sheets 256 (north London), 257 (Romford), 270 (south London), and 271 (Dartford) (England and Wales). British Geological Survey.

Ezquerro, P., Herrera, G., Marchamalo, M., Tomás, R., Béjar-Pizarro, M., & Martínez, R. (2014). A quasi-elastic aquifer deformational behavior: Madrid aquifer case study. *Journal of Hydrology*, 519, 1192-1204.

Farina M., Marcaccio M., Zavatti A. (2014). Esperienze e prospettive nel monitoraggio delle acque sotterranee. Il contributo dell'Emilia-Romagna. Pitagora Editrice, Bologna, 560 pp. (ISBN 88-371-1859-7).

Ferretti, A., Fumagalli, A., Novali, F., Prati, C., Rocca, F., and Rucci, A. (2011). A new algorithm for processing interferometric data-stacks: SqueeSAR. IEEE Transactions on Geoscience and Remote Sensing, 49(9), 3460-3470.

Ferretti, A., Prati, C., and Rocca, F. (2001). Permanent scatterers in SAR interferometry. IEEE Transactions on geoscience and remote sensing, 39 (1), 8-20.

Fokker, P. A., Wassing, B. B. T., van Leijen, F. J., Hanssen, R. F., and Nieuwland, D. A. (2016). Application of an ensemble smoother with multiple data assimilation to the Bergermeer gas field, using PS-InSAR. *Geomechanics for Energy and the Environment*, 5, 16-28.

Ford, J.R., Mathers, S.J., Royse, K.R., Aldiss, D.T., & Morgan, D.J.R. (2010). Geological 3D modelling: scientific discovery and enhanced understanding of the subsurface, with examples from the UK. Z. Dtsch. Ges. Geowiss. 161, 205–218.

Fry, V.A. (2009). Lessons from London: regulation of open-loop ground source heat pumps in central London. Quarterly Journal of Engineering Geology and Hydrogeology, 42(3), 325-334.

Galloway, D., Jones, D. R., and Ingebritsen, S. E. (Eds.). (1999). Land subsidence in the United States (p. 177). Reston, VA, USA: US Geological Survey.

Galloway, D., Jones, D. R., and Ingebritsen, S. E. (Eds.). (1999). Land subsidence in the United States (p. 177). Reston, VA, USA: US Geological Survey.

Gambolati, G., G. Ricceri, W. Bertoni, G. Brighenti, and E. Vuillermin. (1991). "Mathematical simulation of the subsidence of Ravenna". *Water Resources Research* 27: 2899-2918.

Goovaerts, P. (1997). Geostatistics for natural resources evaluation. Oxford University Press on Demand.

Helm, D.C. (1975). One-dimensional simulation of aquifer system compaction near Pixley, Calif. 1: constant parameters. *Water Resources Research*, 11 (3), 465–478.

Helm, D.C. (1976). One-dimensional simulation of aquifer system compaction near Pixley, Calif. 2: stress-dependent parameters. *Water Resources Research*, 1 (3), 375–391.

Herrera, G., Fernández, J. A., Tomás, R., Cooksley, G., and Mulas, J. (2009). Advanced interpretation of subsidence in Murcia (SE Spain) using A-DInSAR data-modelling and validation. *Nat. Hazards Earth Syst. Sci.*, 9(3), 647-661.

Higgins, S. A., Overeem, I., Steckler, M. S., Syvitski, J. P., Seeber, L., & Akhter, S. H. (2014). InSAR measurements of compaction and subsidence in the Ganges-Brahmaputra Delta, Bangladesh. *Journal of Geophysical Research: Earth Surface*, 119(8), 1768-1781.

Hoffmann, J., Galloway, D. L., and Zebker, H. A. (2003). Inverse modelling of interbed storage parameters using land subsidence observations, Antelope Valley, California. *Water Resources Research*, 39(2).

Holzer, T. L. (1981). Preconsolidation Stress of Aquifer Systems. *Water Resources Research*, 17(3), 693-704.

Hooper A., Zebker H., Segall P., Kampes B. (2004). A new method for measuring deformation on volcanoes and other natural terrains using InSAR persistent scatterers, *Geophys. Res. Lett*., 31, L23611, doi:10.1029/2004GL021737.

Hooper, A. (2008). A multi-temporal InSAR method incorporating both persistent scatterer and small baseline approaches. *Geophys. Res. Lett*. 35(16), L16302, doi:10.1029/2008GL034654.

Hu, B., Wang, H. S., Sun, Y. L., Hou, J. G., and Liang, J. (2014). Long-term land subsidence monitoring of Beijing (China) using the small baseline subset (SBAS) technique. *Remote Sensing*, 6(5), 3648-3661.

IGME (1981). Mapa Geologico de España, 1:50.000, Sheet Lorca (953). Servicio de Publicaciones Ministerio de Industria, Madrid.

IGME (1994) Estudio para la regulación y apoyo a la gestión de los recursos hídricos subterráneos del Alto Guadalentín. IGME internal report

Jones, M.A., Hughes, A.G., Jackson, C.R., & Van Wonderen, J.J. (2012). Groundwater resource modelling for public water supply management in London. *Geological Society, London, Special Publications*, 364(1), 99-111.

Kerle, N., Janssen, L. L., and Huurneman, G. C. (2004). Principles of remote sensing. ITC, Educational textbook series, 2.

Lanari R., Mora O., Manunta M., Mallorqui J.J., Berardino P., Sansosti E. (2004). A small baseline approach for investigating deformations on full resolution Differential SAR Interferograms. IEEE Transactions on Geoscience and Remote Sensing, 42: 1377–1386

Liu, Y., Huang, H., and Dong, J. (2015). Large-area land subsidence monitoring and mechanism research using the small baseline subset interferometric synthetic aperture radar technique over the Yellow River Delta, China. *Journal of Applied Remote Sensing*, 9(1), 096019-096019.

Lofgren, B. E. (1969). Field Measurement of Aquifer-system Compaction, San Joaquin Valley, California, USA. US Geological Survey.

Lu, P., Casagli, N., Catani, F., and Tofani, V. (2012). Persistent Scatterers Interferometry Hotspot and Cluster Analysis (PSI-HCA) for detection of extremely slow-moving landslides. *International Journal of Remote Sensing*, 33(2), 466-489.

Martín, V. J. M., Espinosa, G. J. S., Pérez, R. A. (1973). Mapa geológico de España: E. 1:50,000. Madrid: Servicio de Publicaciones, Ministerio de Industria y Energía. Instituto geológico y minero de España (IGME).

Martínez-Díaz, J. J., Bejar-Pizarro, M., Álvarez-Gómez, J. A., Mancilla, F. D. L., Stich, D., Herrera, G., Morales, J. (2012). Tectonic and seismic implications of an intersegment rupture: The damaging May 11th 2011 Mw 5.2 Lorca, Spain, earthquake. *Tectonophysics* 546, 28-37.

Matheron, G. (1963). Principles of geostatistics. *Economic geology*, 58(8), 1246-1266.

Mathers, S.J., Burke, H.F., Terrington, R.L., Thorpe, S., Dearden, R.A., Williamson, J.P., & Ford, J.R. (2014). A geological model of London and the Thames Valley, southeast England. Proceedings of the Geologists' Association, 125(4), 373-382.

Meisina, C., Zucca, F., Notti, D., Colombo, A., Cucchi, A., Savio, G., Giannico, C., Bianchi, M. (2008). Geological interpretation of PSInSAR data at regional scale. *Sensors.*, 8(11):7469–7492, doi:10.3390/s8117469.

Meisina. C. Engineering geological mapping for urban areas of the Oltrepo Pavese plain (Northern Italy). In Proceedings of 10th Congress of the International Association for Engineering Geology and the Environment (IAEG), Nottingham, UK, 6–10 September 2006.

Modoni, G., Darini, G., Spacagna, R. L., Saroli, M., Russo, G., & Croce, P. (2013). Spatial analysis of land subsidence induced by groundwater withdrawal. *Engineering geology*, 167, 59-71.

Mora, O., Mallorqui, J.J., Broquetas, A. (2003). Linear and nonlinear terrain deformation maps from a reduced set of interferometric SAR images. IEEE Trans. Geosci. Remote Sens. 41(10), 2243-2253.

National Research Council, 1991, Mitigating losses from land subsidence in the United States: Washington, D. C., National Academy Press, 58 p.

Notti, D., Calò, F., Cigna, F., Manunta, M., Herrera, G., Berti, M., Meisina, C., Tapete, D., Zucca, F. A User-Oriented Methodology for DInSAR Time Series Analysis and Interpretation: Landslides and Subsidence Case Studies. *Pure and Applied Geophysics*. 2015, 172(11), 3081-3105, doi:10.1007/s00024-015-1071-4.

O'Shea, M.J., & Sage, R. (1999). Aquifer Recharge: An Operational Drought-Management Strategy in North London. *Water and Environment Journal*, 13(6), 400-405.

O'Shea, M.J., Baxter, K.M., & Charalambous, A.N. (1995). The hydrogeology of the Enfield-Haringey artificial recharge scheme, north London. *Quarterly Journal of Engineering Geology and Hydrogeology*, 28 (Supplement 2), S115-S129.

Peduto, D., Cascini, L., Arena, L., Ferlisi, S., Fornaro, G., Reale, D. A general framework and related procedures for multiscale analyses of DInSAR data in subsiding urban areas. ISPRS *Journal of Photogrammetry and Remote Sensing*. 2015, 105, 186-210, doi:10.1016/j.isprsjprs.2015.04.001.

Pellegrini, L., Vercesi, P.L. (1995). Considerazioni morfotettoniche sulla zona a sud del Po tra Voghera (PV) e Sarmato (PC). *Atti Tic. Sci. Terra*, 38, 95–118.

Pilla, G., Sacchi, E., Ciancetti G. (2007). Studio idrogeologico, idrochimico ed isotopico delle acque sotterranee del settore di pianura dell'Oltrepò Pavese (Pianura lombarda meridionale). G. *Geol. Appl.*, 5, 59–74.

Poland, J. F. (1976). Land subsidence stopped by artesian-head recovery, Santa Clara Valley, California. In Proceedings of the Anaheim Symposium December 1976: International Association of Hydrologic Sciences Publication (No. 121).

Prati C., A. Ferrett, Perissin D. (2010). Recent advances on surface ground deformation measurement by means of repeated space-borne SAR observations, J. Geodyn., 49, 161–170.

Regione Emilia Romagna and ENI S.p.A.-AGIP. Riserve Idriche Sotterranee della Regione Emilia Romagna. (1998).

Riley, F.S. (1969). Analysis of borehole extensometer data from central California. In: Tison, L.J. (Ed.) Land subsidence. Proceedings of the Tokyo Symposium, September 1969, IAHS Pub. vol. 88, pp. 423–431. Available at: http://iahs.info/redbooks/a088/088047.pdf

Riley, F.S. (1998). Mechanics of aquifer systems—The scientific legacy of Joseph F. Poland, in Borchers, J.W., ed., Land subsidence case studies and current research: Proceedings of the Dr. Joseph F. Poland Symposium on Land Subsidence: Belmont, Calif., Star Publishing Co., Association of Engineering Geologists Special Publication 8, p. 13–27.

Rosen P.A., Hensley S., Joughin I.R., Li F.K., Madsen S.N., Rodríguez E., Goldstein R.M., 2000. SyntheticAperture Radar Interferometry. Proceedings of the IEEE, v.88: 333-382.

Royse, K.R., de Freitas, M., Burgess, W.G., Cosgrove, J., Ghail, R.C., Gibbard, P., King, C., Lawrence, U., Mortimore, R.N., Owen, H.G., & Skipper, J. (2012). Geology of London, UK. Proceedings of the Geologists' Association 123, 22–45.

Sumbler, M.G. (1996). British Regional Geology: London and the Thames Valley, fourth ed. HMSO for the British Geological Survey, London.

Syvitski, J., & Higgins, S. (2012). Going under: The world's sinking deltas. *New Scientist*, 216(2893), 40-43.

Teatini, P., Castelletto, N., Ferronato, M., Gambolati, G., Janna, C., Cairo, E., Marzorati, D., Colombo, D., Ferretti, A., Bagliani, A. and Bottazzi, F. (2011). Geomechanical response to

seasonal gas storage in depleted reservoirs: A case study in the Po River basin, Italy. Journal of *Geophysical Research: Earth Surface*, 116(F2).

Terzaghi, K. (1925). Principles of soil mechanics, IV—Settlement and consolidation of clay. *Engineering News-Record*, 95(3), 874-878.

Terzaghi, K. 1943, Theoretical Soil Mechanics, John Wiley & Sons, New York.

Tolman, C. F., and Poland, J. F. (1940). Ground-water, salt-water infiltration, and ground-surface recession in Santa Clara Valley, Santa Clara County, California. *Eos, Transactions American Geophysical Union*, 21(1), 23-35.

Tomás, R., Herrera, G., Delgado, J., Lopez-Sanchez, J. M., Mallorquí, J. J., and Mulas, J. (2010a). A ground subsidence study based on DInSAR data: calibration of soil parameters and subsidence prediction in Murcia City (Spain). *Engineering geology*, 111(1), 19-30.

Tomas, R., Herrera, G., Lopez-Sanchez, J. M., Vicente, F., Cuenca, A., and Mallorquí, J. J. (2010b). Study of the land subsidence in Orihuela City (SE Spain) using PSI data: distribution, evolution and correlation with conditioning and triggering factors. *Engineering Geology*, 115(1), 105-121.

Tosi, L., Teatini, P., and Strozzi, T. (2013). Natural versus anthropogenic subsidence of Venice. Scientific reports, 3.

Tralli, D. M., Blom, R. G., Zlotnicki, V., Donnellan, A., and Evans, D. L. (2005). Satellite remote sensing of earthquake, volcano, flood, landslide and coastal inundation hazards. *ISPRS Journal of Photogrammetry and Remote Sensing*, 59(4), 185-198.

Werner, C., Wegmuller, U., Strozzi, T., Wiesmann, A. (2003). Interferometric point target analysis for deformation mapping. In: Geoscience and remote sensing symposium, IGARSS ‘03. Proceedings. 2003 IEEE International, 21–25 July 2003 pp 4362–4364 vol.4367.

Zhang, Y., Xue, Y-Q, Wu, J-C, Ye, S-J, Wei, Z-W, Li, Q-F, Yu, J. (2007a). Characteristics of aquifer system deformation in the Southern Yangtse Delta, China. *Eng. Geol.* 90, 160-173